

<sup>1</sup>

# TOWARD A NOVEL TRACK

<sup>2</sup>

## RECONSTRUCTION

<sup>3</sup>

### ALGORITHM FOR THE FUTURE ATLAS ITk

Thèse n. 1234 2011

présenté le 15 Mars 2025

à la Faculté de Physique

programme doctoral en Physique

pour l'obtention du grade de Docteur de Sciences

par

MINH-TUAN PHAM

acceptée sur proposition du jury:

Prof Name Surname, président du jury

Prof Name Surname, directeur de thèse

Prof Name Surname, rapporteur

MADISON, WISCONSIN, 2025

<sup>4</sup>



**WISCONSIN**  
UNIVERSITY OF WISCONSIN-MADISON

## 5 TABLE OF CONTENTS

	Page
6 List of figures . . . . .	4
7 LIST OF FIGURES . . . . .	4
8 List of tables . . . . .	12
9 LIST OF TABLES . . . . .	12
10 1 Introduction . . . . .	15
11 I Search for dark matter interpreted in a Two-Higgs-Doublet 12 Model with a pseudoscalar mediator using $139 \text{ fb}^{-1}$ of $\sqrt{s} = 13$ 13 TeV proton-proton collision data at the ATLAS detector	18
14 2 Theoretical background . . . . .	19
15    2.1 The Standard Model of Particle Physics . . . . .	19
16    2.2 Electroweak symmetry breaking and the Higgs mechanism . . . . .	20
17    2.3 Standard Model Higgs boson production and decay . . . . .	24
18    2.4 Extension of the Standard Model Higgs sector . . . . .	28
19 3 The ATLAS experiment . . . . .	30
20    3.1 The ATLAS detector . . . . .	30
21      3.1.1 The Inner Detector . . . . .	32
22      3.1.2 The Calorimeter system . . . . .	36
23      3.1.3 The muon spectrometer . . . . .	38
24 4 Combination of dark matter searches interpreted in 2HDM+ $a$ . . . . .	40
25    4.1 Theoretical considerations . . . . .	40
26    4.2 Benchmark scenarios . . . . .	44
27      4.2.1 Scenario 1: Exploration of two $m_a - m_A$ planes . . . . .	45
28      4.2.2 Scenario 2: Exploration of two $m_A - \tan\beta$ planes . . . . .	45
29      4.2.3 Scenario 3: Exploration of two $m_a - \tan\beta$ planes . . . . .	46

30	4.2.4	Scenario 4: Variation of the pseudo-scalar mixing angle $\sin \theta$	46
31	4.2.5	Scenario 5: Variation of the Dark Matter mass $m_\chi$	46
32	4.2.6	Scenario 6: Variation of the $m_a - m_\chi$	47
33	4.3	Data and simulated event samples	48
34	4.4	Experimental signatures	52
35	4.4.1	$E_T^{\text{miss}} + Z(\ell\ell)$ signature	54
36	4.4.2	$E_T^{\text{miss}} + h(b\bar{b})$ signature	56
37	4.4.3	$E_T^{\text{miss}} + h(\gamma\gamma)$ signature	59
38	4.4.4	$E_T^{\text{miss}} + h(\tau\tau)$ signature	60
39	4.4.5	$E_T^{\text{miss}} + tW$ signature	61
40	4.4.6	$E_T^{\text{miss}} + j$ signature	63
41	4.4.7	$h \rightarrow$ invisible signature	64
42	4.4.8	Additional searches using $36 \text{ fb}^{-1}$ of $\sqrt{s} = 13 \text{ TeV}$ $pp$ collision data	65
43	4.4.9	$tbH^\pm(t\bar{b})$ signature	66
44	4.4.10	$t\bar{t}t\bar{t}$ signature	67
45	4.4.11	Exotic Higgs boson decays $h \rightarrow aa \rightarrow f\bar{f}f'\bar{f}'$	68
46	4.5	Systematic uncertainties	70
47	4.6	Statistical combination of results	71
48	4.6.1	Statistical analysis	71
49	4.6.2	Uncertainties and their correlations	73
50	4.6.3	The impact of uncertainties	73
51	4.7	Results on combined constraints on the 2HDM+ $a$	74
52	4.7.1	Scenario 1: $m_a - m_A$ planes	74
53	4.7.2	Scenario 2: $m_A - \tan\beta$ planes	79
54	4.7.3	Scenario 3: $m_a - \tan\beta$ planes	81
55	4.7.4	Scenario 4: Variation of $\sin\theta$	82
56	4.7.5	Scenario 5: Variation of $m_\chi$	85
57	4.7.6	Scenario 6: $m_a - m_\chi$ plane	87
58	4.8	Conclusion	89

59 II Track reconstruction with geometric deep learning in the  
60 ATLAS ITk 91

61 5 The High Luminosity Large Hadron Collider . . . . . 92

62 6 The ATLAS Inner Tracker . . . . . 95

63	6.1 Overview of the Inner Tracker . . . . .	95
64	6.2 Simulation of the Inner Tracker . . . . .	99

	Page
65            6.2.1    Simulation of the Pixel Detector . . . . .	100
66            6.2.2    Simulation of the Strip Detector . . . . .	102
67            6.3      Particle interaction with detector material . . . . .	103
68            6.3.1    Energy loss of heavy particles . . . . .	104
69            6.3.2    Energy loss of electrons and positrons . . . . .	107
70            6.3.3    Multiple Coulomb scattering . . . . .	110
71            6.4      Simulated samples . . . . .	113
72 <b>7   The ATLAS track reconstruction chain</b> . . . . .	114
73            7.1      Clusterization and space point formation . . . . .	114
74            7.2      The least-square fit . . . . .	119
75            7.3      Iterative track fit . . . . .	122
76            7.4      Combinatorial Kalman Filter . . . . .	124
77            7.5      Computational cost of track reconstruction . . . . .	126
78 <b>8   Track reconstruction with Graph Neural Networks</b> . . . . .	129
79            8.1      Overview . . . . .	130
80            8.2      Target, non-target particles and evaluation metrics . . . . .	131
81            8.3      Graph construction methods . . . . .	135
82            8.3.1    The Module Map Method . . . . .	135
83            8.3.2    The Metric Learning approach . . . . .	139
84            8.4      Result . . . . .	143
85 <b>9   Edge classification</b> . . . . .	147
86            9.1      Introduction to graph neural networks . . . . .	147
87            9.2      The filter network . . . . .	148
88            9.2.1    Method . . . . .	148
89            9.2.2    Results . . . . .	155
90            9.3      The Interaction Network . . . . .	158
91            9.3.1    Methods . . . . .	158
92            9.3.2    Results . . . . .	162
93 <b>10   Graph segmentation</b> . . . . .	171
94            10.1     Connected components . . . . .	171
95            10.2     The Walkthrough algorithm . . . . .	175

	Page
96 <b>11 Track reconstruction performance</b> . . . . .	180
97     11.1 Extraction of track parameters . . . . .	181
98     11.2 Track matching and performance metrics . . . . .	184
99     11.3 Results . . . . .	186
100        11.3.1 Reconstruction performance of the GNN-based algorithm under nom-	
101        inal and relaxed track selections . . . . .	189
102        11.3.2 Reconstruction efficiency . . . . .	192
103        11.3.3 Track fake rate . . . . .	196
104        11.3.4 Parameter resolution . . . . .	197
105 <b>12 Computational performance</b> . . . . .	208
106     12.1 An inference pipeline . . . . .	209
107     12.2 Neural Network optimization techniques . . . . .	209
108        12.2.1 Automatic mixed precision (AMP) . . . . .	210
109        12.2.2 Ahead-Of-Time (AOT) compilation . . . . .	211
110     12.3 Optimized performance . . . . .	212
111     12.4 Pipeline computational performance . . . . .	217
112     12.5 Toward computational performance in production environment . . . . .	219
113 <b>13 Conclusion</b> . . . . .	221
114 <b>APPENDIX   Definition of hit-level training variables</b> . . . . .	224
115 <b>APPENDIX   Track fit</b> . . . . .	225
116 <b>Bibliography</b> . . . . .	251

## <sup>117</sup> LIST OF FIGURES

	Figure	Page
<sup>118</sup> 2.1	Production cross-section of the Standard Model Higgs boson produced by $pp$ collision as a function of $M_H$ at $\sqrt{s} = 13$ TeV . . . . .	<sup>119</sup> 24
<sup>120</sup> 2.2	Leading-order Higgs boson production mechanisms . . . . .	<sup>121</sup> 26
<sup>121</sup> 2.3	Leading-order Higgs boson decay mechanisms . . . . .	<sup>122</sup> 27
<sup>122</sup> 3.1	The ATLAS detectors and its components [142] . . . . .	<sup>123</sup> 31
<sup>123</sup> 3.2	The ATLAS pixel detector and detector module. Figures taken from reference [87]	<sup>124</sup> 34
<sup>124</sup> 3.3	Overview of the strip module of the SCT in the barrel layers. Figures taken from reference [148] . . . . .	<sup>125</sup> 35
<sup>126</sup> 3.4	(a) Layout of the ATLAS calorimetry system, and (b) sketch of a barrel module of the electromagnetic calorimeter [93]. . . . .	<sup>127</sup> 37
<sup>128</sup> 3.5	(a) Layout of the ATLAS Muon Spectrometer system, and (b) a sideview of one quadrant of the MS [20]. . . . .	<sup>129</sup> 39
<sup>130</sup> 4.1	Representative production mechanisms and final state of the $E_T^{\text{miss}} + Z(\ell\ell)$ signature, including gluon-gluon fusion resonant (a) and non-resonant production, and (c) $b$ -initiated production. . . . .	<sup>131</sup> 54
<sup>133</sup> 4.2	Production mechanisms and final state of the $E_T^{\text{miss}} + h(b\bar{b})$ signature including gluon-gluon fusion resonant (a) and non-resonant production, $b\bar{b}$ -associated production (c) and $b\bar{b}$ -initiated production (d). . . . .	<sup>134</sup> 57
<sup>136</sup> 4.3	Production mechanisms and final state of the $E_T^{\text{miss}} + tW$ signature. . . . .	<sup>137</sup> 63
<sup>137</sup> 4.4	Production mechanisms and final state of the $E_T^{\text{miss}} + j$ signature, including gluon-gluon fusion production (a) and $b\bar{b}$ -initiated production (b). . . . .	<sup>138</sup> 63
<sup>139</sup> 4.5	Production mechanisms and final state of the $t b H^\pm (tb)$ signature. . . . .	<sup>139</sup> 67

Figure	Page
140 4.6 Production mechanisms and final state of the $t\bar{t}t\bar{t}$ , $E_T^{\text{miss}} + b\bar{b}$ , and $E_T^{\text{miss}} + t\bar{t}$ signatures. . . . .	67
142 4.7 Production mechanisms and final state of the $h \rightarrow aa \rightarrow f\bar{f}f'\bar{f}'$ signature. . . . .	68
143 4.8 Observed and expected exclusion regions at 95% CL over the $(m_a, m_A)$ plane evaluated at 2HDM+ $a$ mixing angles $\sin\theta = 0.35$ (subfigures (a), (c)), and $\sin\theta = 0.7$ (subfigures (b), (d)). The observed and expected contours are respectively shown in solid and dashed lines in all subsequent figures. In (a) and (b), the observed and expected exclusion limits from each of the three statistically combined signatures are shown along with the combined limits. The green and yellow shared bands respectively correspond to the $\pm 1$ and $\pm 2$ standard deviation uncertainty in the combined expected limits. In (c) and (d), the combined exclusion contours are overlaid along those of additional channels not included in the statistical combination. In all subfigures, a dashed grey region indicates the region where the width of any of the Higgs boson exceeds 20% of its mass [90]. . . . .	77
155 4.9 Observed and expected exclusion regions at 95% CL over the $(m_A, \tan\beta)$ plane evaluated at 2HDM+ $a$ mixing angles $\sin\theta = 0.35$ (a), and $\sin\theta = 0.7$ (b). The statistical combined contours are shown along with those from individual searches. In both subfigures, a dashed grey region indicates the region where the width of any of the Higgs boson exceeds 20% of its mass [90]. . . . .	80
160 4.10 Observed and expected exclusion regions at 95% CL over the $(m_a, \tan\beta)$ plane evaluated at 2HDM+ $a$ mixing angles $\sin\theta = 0.35$ (a), and $\sin\theta = 0.7$ (b). The statistical combined contours are shown along with those from individual searches. In both subfigures, a dashed grey region indicates the region where the width of any of the Higgs boson exceeds 20% of its mass [90]. . . . .	81
165 4.11 Observed and expected exclusion limits at 95% CL for the 2HDM+ $a$ as a function of $\sin\theta$ plane evaluated under benchmark scenarios 4. In subfigures (a) and (b), the results are derived at $\tan\beta = 1$ , while in (c) and (d) they are derived at $\tan\beta = 0.5$ or $\tan\beta = 50$ . (a) and (c) represent the sensitivity at low pseudo-scalar mass, in particular $m_A = 600$ GeV and $m_a = 200$ GeV, and (b) and (d) the high-mass regime, namely $m_A = 1.0$ TeV and $m_a = 350$ GeV. The combined exclusion is shown along with individual searches. In all subfigures, a dashed grey region indicates the region where the width of any of the Higgs boson exceeds 20% of its mass [90]. . . . .	83

## Figure

## Page

174	4.12 Observed and expected exclusion limits at 95% CL for the 2HDM+ $a$ as a function 175 of the dark matter particle mass $m_\chi$ evaluated under benchmark scenario 5 176 following $m_A = 1.0$ TeV, $m_a = 400$ GeV, $\tan\beta = 1.0$ , and $\sin\theta = 0.35$ . The 177 limits are expressed in terms of the ratio of the excluded cross-section to the 178 nominal cross-section of the signal model. The results from several individual 179 searches are shown along with the combined limits. The relic density for each 180 $m_\chi$ assumption, calculated with MADDM [10], is superimposed on the plot in 181 dashed line [90]. . . . .	86
182	4.13 Observed and expected exclusion limits at 95% CL for the 2HDM+ $a$ as a function 183 of $m_a$ and $m_\chi$ evaluated under benchmark scenario 6 following $m_A = 1.2$ TeV, 184 $\tan\beta = 1.0$ , and $\sin\theta = 0.35$ . The relic density contour for the case $\Omega_c h^2 = 0.12$ , 185 calculated with MADDM [10], is superimposed on the plot in dashed line. The 186 shaded regions mark the region where the model predicts a relic density greater 187 than the observed value $\Omega_c h^2 = 0.12$ . The island around ( $m_\chi \approx 100$ , $m_a \approx 100$ ) 188 GeV corresponds to the resonant enhancement of the process $\chi\bar{\chi} \rightarrow ah \rightarrow \text{SM}$ 189 that depletes the relic density [90]. . . . .	88
190	5.1 Distribution of pile-up multiplicity ( $\mu$ ) in proton–proton collision at the ATLAS 191 interaction point during Run 2 and the data taking period in 2022 of Run 3. 192 The dashed line represents a rescaled Run 2 distribution such that its integral is 193 the same as that of the Run 3 distribution. $\langle\mu\rangle$ denotes the distribution mean. 194 Figure taken from reference [92]. . . . .	93
195	6.1 A schematic view of the ITk layout (a), and of the pixel detector layout (b), 196 both in one quadrant. Only active elements are visible in both figures. Pixel and 197 strip elements are respectively shown in green and blue. The IP is located at the 198 origin. The horizontal axis is parallel to the beam line, and the vertical axis is 199 the radius measured from the IP [95]. . . . .	96
200	6.2 Overview of the endcap petal (upper) and barrel stave (lower) in the strip detector. 201 Sensor modules shown in blue are mounted directly on a rigid carbon-fiber 202 sandwich structure. Only one half of a stave is shown [19]. . . . .	100
203	6.3 Location of the materials for one quadrant of the ITk layout 03-00-00. The pixel 204 subsystem is shown in green and surrounded by the strip subsystem shown in 205 blue. The location of the materials are indicated by black regions [1]. . . . .	101
206	6.4 An illustration of the GEANT4 geometry model of the outer barrel longeron stave 207 with mounted inclined and flat modules. Figure taken from reference [18]. . . . .	102

Figure	Page
208 6.5 Displays of the GEANT4 geometry model of the strip barrel staves (left) and the 209 endcap petals (right). Figure taken from reference [18]. . . . .	103
210 6.6 The mass stopping power of positive muons in copper as a function of the muon 211 momentum spanning nine orders of magnitude. The solid curves indicate the 212 total stopping power of all dissipative effects. The region of interest in HEP 213 ranges from 100 MeV to 100 GeV, well within the so-called Bethe region, in 214 which the stopping power is strongly dependent on $\beta$ (see text for definition). 215 Figure taken from reference [140]. . . . .	106
216 6.7 Contribution of radiative and collisional components in the total energy loss of 217 electrons in copper as functions of electron energy. At a critical value $E_c = 19.63$ 218 MeV, radiative loss becomes the dominant mechanism. The energy range of 219 electrons in HEP detectors is well within the Bremsstrahlung regime [140]. . . .	109
220 6.8 Integrated material budget encountered on a particle's path in unit of radiation 221 length as a function of pseudorapidity based on (a) the ITk and (b) the ID. The 222 particle assumes a straight trajectory from the origin. (c) is a comparison between 223 the amount of material that must be traverse before the particle accumulates 224 enough hits to be deemed reconstructible. . . . .	111
225 6.9 Schematic of the calculation of macroscopic mean deflection angle caused by 226 multiple scattering [140]. . . . .	112
227 7.1 Formation of a pixel clusters from multiple cells. The particle deposits its energy 228 in 7 cells, 5 of which receive charges exceeding the detection threshold and enter 229 the clusterization [111]. . . . .	115
230 7.2 The passage of a particle through a pixel sensor segmented in two dimensions. 231 The energy deposit in each sensor cell is measured as a signal when it exceeds a 232 measurement threshold. The true intersection point is estimated from the signal 233 cells grouped together, called a cluster [111]. . . . .	116
234 7.3 A pair of strip sensors are used to reconstruct a 3-dimensional estimate of the 235 particle's true impact point (a). Ambiguity arises when more than one particle 236 hit a strip module, leading to more combinations than particles (b) [111]. . . .	117
237 7.4 Average number of lone strip clusters per track as a function of the particle 238 pseudorapdity $\eta$ . . . . .	118

Figure	Page
239 7.5 Tracking efficiency (left) and track parameter resolution (right) as functions of 240 the truth particle's pseudorapidity, evaluated at $\langle \mu \rangle = 200$ . The bottom plots 241 show the ratio of the corresponding metric observed in the fast chain to that in 242 the default chain [28]. . . . .	128
243 8.1 The GNN4ITk algorithm consists of three distinct stages. The first stage constructs a graph from the set of space points in an event, each acting as a node. 244 The second stage identifies edges connecting consecutive nodes on a particle 245 tracks from other edges. The last stage construct track candidates by segmenting 246 the graph using the output of the second stage. The algorithm's output 247 consists of individual track candidates each as a set of space points believed to 248 belong to the same particle. . . . .	131
250 8.2 Distributions of the production vertex position on the transverse plane (a) and 251 along the $z$ -axis (b) of simulated particles in $t\bar{t}$ -events at $\langle \mu \rangle = 200$ for non- 252 primary and primary particles. Primary vertices are restricted to a small region 253 around the interaction point, whereas non-primary vertices can occur throughout 254 the detector. . . . .	132
255 8.3 Distributions of transverse momentum $p_T$ (a) and pseudorapidity (b) of simulated 256 particles in $t\bar{t}$ -events at $\langle \mu \rangle = 200$ separated according into hard-scattering and 257 pile-up particles. Soft pile-up particles have low $p_T$ , whereas hard-scattering 258 particles have a wider $p_T$ distribution. The former is two orders of magnitude 259 more abundant than the latter. . . . .	134
260 8.4 Principle of the Module Map method for graph construction. By observing the 261 trajectory of target particles in 90000 $t\bar{t}$ events, a list of all pairs of detector 262 modules sequentially traversed by a particle is built. During event reconstruction, 263 the space points residing on the pairs of modules which appear in the module 264 map are connected by an edge. A set of selections are applied to reduce the 265 number of edges and eliminate outliers. . . . .	136
266 8.5 Principle of deep metric learning. Starting from (a) labelled data which are 267 difficult to separate in real space, (b) a distance metric is defined to measure 268 the similarity between data points in an embedding space, in this case a simple 269 Euclidean distance. (c) A transformation from real to embedding space is learned, 270 such that examples of the same class are close together, whereas those of different 271 classes are pushed away from each other. (d) The transformation is a simple feed- 272 forward network applied to to all instances of the dataset. (e) After training, 273 examples of different classes are well-separated, and clusterizable [124]. . . . .	140

Figure	Page
274 8.6 Graph construction efficiency of the Module Map approach as a function of $\eta$ (upper) and $p_T$ (lower), using the MinMax selection (left) and MeanRMS selection (right). . . . .	144
277 8.7 Graph construction efficiency of the Metric learning approach as a function of $\eta$ (a) and $p_T$ (b), averaged over 1000 $t\bar{t}$ events. . . . .	145
279 9.1 GRAPH SAGE sampling and aggregation mechanism. [118] . . . . .	150
280 9.2 Edge efficiency of the Filter network on graphs constructed by the Metric Learning method as a function of $\eta$ (a) and $p_T$ (b). . . . .	156
282 9.3 Edge efficiency (a) and purity (b) of the Filter network on graphs constructed by the Metric Learning method as functions of the $(z, r)$ -coordinates of the inner hit. . . . .	166
284 9.4 The number of space points per $(z, r)$ -bin averaged over 50 $t\bar{t}$ events. The bin-width is 15 mm in both $z$ - and $r$ -direction. . . . .	167
286 9.5 Edge efficiency of the INTERACTIONGNN as a function of $\eta$ (left) and $p_T$ (right), evaluated on graphs created using the Module Map method with MeanRMS (upper) and MinMax selections (lower). . . . .	168
289 9.6 Edge efficiency of the INTERACTIONGNN on graphs constructed by the <b>Module Map MeanRMS</b> as a function of the $(z, r)$ -coordinates of the inner hit. . . . .	169
291 9.7 Edge purity of the INTERACTIONGNN on graphs constructed by the <b>Module Map MeanRMS</b> as a function of the $(z, r)$ -coordinates of the inner hit. . . . .	170
293 10.1 A distribution of the GNN edge classification scores. 200 graphs constructed using the Metric Learning approach are used. . . . .	172
295 10.2 Illustration of the Connected Component method. (a) The input graph contains two particle tracks and a single hits, all color-coded. The three objects are merged by two fake edges in red. (b) Edges whose score falls under a threshold is eliminated. (c) The remaining connected components are considered as track candidates. . . . .	174

Figure	Page
--------	------

300 10.3 Different scenarios encountered by the Walkthrough algorithm. (a) A starting 301 node as a single outgoing edge. (b) The starting node has several outgoing edges 302 $\{e_{12}, e_{13}, e_{14}\}$ . Edge $e_{12}$ has the highest score, and neither lower-score edges 303 exceed the minimum score $s_{add}$ to create an alternative path. Only edge $e_{12}$ 304 is admitted. (c) The starting node has several outgoing edges $\{e_{12}, e_{13}, e_{14}\}$ , in 305 which $e_{12}$ and $e_{13}$ exceed $s_{add}$ . Two candidate paths stemming from the junction 306 are considered, the longer of which is admitted. . . . .	178
307 10.4 An ambiguity occurs when two candidate paths have equal lengths. The path 308 stemming from the higher edge score at the junction is selected. . . . .	179
309 11.1 A track represented in two different parametrizations, both being particular in- 310 stances of the general ATLAS parametrization in equation (11.1). The perigee 311 parametrization (left) is defined with respect to the global $z$ -axis, while the planar 312 parametrization (right) is defined with respect to the coordinate axes of a 313 local measuring surface [97]. . . . .	182
314 11.2 A comparison of the GNN-based track candidates selected by the nominal and 315 the relaxed criteria in representative performance metrics. Top plots show the 316 efficiency as functions of the truth pseudorapidity $\eta$ (a) and transverse momen- 317 tum $p_T$ (b). Bottom plots show the rate of fake tracks as functions of $\eta$ (c) and 318 the pile-up level $\mu$ (d). . . . .	190
319 11.3 Tracking efficiency as functions of the truth pseudorapidity $\eta$ (a) and transverse 320 momentum $p_T$ (b). The bottom plots show the ratio of the GNN-based curves 321 to the CKF-based curve. . . . .	193
322 11.4 Tracking efficiency as a function of the pile-up level $\langle \mu \rangle$ . The bottom plots show 323 the ratio of the GNN-based curves to the CKF-based curve. . . . .	195
324 11.5 The proportion of reconstructed tracks reconstructed by the GNN4ITk and CKF 325 chains having matching probability less than 0.5 as a function of the track pseu- 326 dorapidity $\eta$ (a) and the truth pile-up (b). The bottom plots show the ratio of 327 the GNN-based curves to the CKF-based curve. . . . .	202
328 11.6 Transverse (a) and longitudinal (b) impact parameter resolution shown as his- 329 tograms of $\sigma(d_0)$ and $\sigma(z_0)$ respectively. Note that the resolution of parameter 330 $x$ is inversely proportional to $\sigma(x)$ . . . . .	203
331 11.7 The number of hits from the inner most pixel layer as a function of reconstructed 332 pseudorapidity $\eta$ . . . . .	204

Figure	Page
--------	------

333 11.8 Transverse impact parameter resolution $\sigma(d_0)$ of as a function of truth $\eta$ , evaluated on tracks reconstructed by the GNN4ITk and the CKF chains. The bottom plots show the ratio of the GNN-based curves to the CKF-based curve. . . . .	204
336 11.9 Longitudinal impact parameter resolution $\sigma(z_0)$ of as a function of truth $\eta$ , evaluated on tracks reconstructed by the GNN4ITk and the CKF chains. The bottom plots show the ratio of the GNN-based curves to the CKF-based curve. . . . .	205
339 11.10 Transverse momentum resolution shown as a histogram of $\sigma(p_T)$ (a) and a function of the truth pseudorapidity $\eta$ (b). . . . .	206
341 11.11 Hit content of selected track candidates, demonstrated by the average number pixel clusters (a), pixel holes (b), strip clusters (c) and strip holes (d). These quantities are shown as functions of the reconstructed pseudorapidity $\eta$ . . . . .	207
344 12.1 Computational efficiency of the INTERACTIONGNN in terms of the execution time (left vertical axis) and peak memory (right vertical axis), measured using the baseline configuration, and configuration optimized with automated mixed precision (AMP), Ahead-of-time computation (AOT), and a combination of the two techniques. All measurements use graphs constructed with the Module Map MinMax method. . . . .	213
350 12.2 GPU time of the INTERACTIONGNN as a function of the number of space points in a $t\bar{t}$ event (a) and as a histogram (b), measured using the baseline configuration, and configurations optimized with automated mixed precision (AMP), AOT compilation, and a combination of both techniques. Each dashed line in (a) displays the best-fit second-order polynomial to the corresponding configuration. The fitted coefficients are exhibited in table 12.2. All measurements are performed on an NVIDIA-A100 GPU with 80 GB of memory, using graphs constructed with the Module Map MeanRMS method. . . . .	215

## Appendix

### Figure

## Appendix

### Figure

## 358 LIST OF TABLES

	Table	Page
359    2.1 Standard Model Higgs boson decay branching ratios and uncertainty at $M_H =$		
360    125.09 GeV . . . . .		27
361    4.1 Summary of the parameter settings for the different 2HDM+ $a$ benchmark sce-		
362    narios explored in this summary . . . . .		49
363    4.2 Details of the MADGRAPH5_AMC@NLO generation set-up used for the 2HDM+ $a$ sig-		
364    nals, for the signatures considered in this publication. The Pseudoscalar_2HDM		
365    UFO model is used for all simulated samples except those for the $tbH^\pm(tb)$		
366    search, which relies on the UFO of reference [99]. The $h \rightarrow$ invisible and		
367 $h \rightarrow aa \rightarrow f\bar{f}f'\bar{f}'$ signatures are not listed here as no signal samples are re-		
368    quired for the re-interpretation, which in those cases relies on the branching		
369    ratio limits [90]. . . . .		50
370    4.3 Summary of input analyses used in the different benchmark scenarios [90]. . . . .		53
371    4.4 Selection criteria used to defined resolved and merged signal regions for the		
372 $E_T^{\text{miss}} + h(b\bar{b})$ signature [49]. . . . .		58
373    4.5 Selection criteria used to define low- and high- $m_R$ signal regions for the $E_T^{\text{miss}} +$		
374 $h(\tau\tau)$ signature [46]. . . . .		62
375    4.6 Impact from different sources of uncertainties on the best-fit signal strength ex-		
376    press in $\Delta\mu$ on the signal at ( $m_A = 800$ GeV, $m_a = 450$ GeV, $\tan\beta = 1$ , $\sin\theta =$		
377    0.35), estimated by fixing the corresponding NPs to their best-fit values, and		
378    subtracting the resulting uncertainty from the total uncertainty in quadrature.		
379    The statistical uncertainty component is obtained by fixing all NPs except the		
380    floating background normalization factors, and quantifies the impact of the limit		
381    data yields in the signal and control regions. The total uncertainty is not the		
382    quadratic sum of the individual contribution due to correlations between system-		
383    atic uncertainties [90]. . . . .		75

Table	Page
384 5.1 The integrated luminosity delivered to the ATLAS detector by the LHC as of 385 September 2, 2024. . . . .	92
386 6.1 Representative parameters of the pixel flat barrel and inclined rings in the ITk 387 layout 03-00-00. Note that while all pixel layers have rings, only the OB features 388 inclined rings. The fifth column provides the number of flat sensors mounted on 389 a complete stave in the central barrel of each layer. The number of inclined rings 390 is given by $2 \times$ the number of rings on each of the barrel [95]. . . . .	98
391 6.2 Representative parameters of the pixel endcaps in the ITk layout 03-00-00. The 392 radius in the second column refers to the radius of the circle formed by the 393 innermost point of the sensors on each ring. The number of rings is twice the 394 number of rings on each of the barrel [95]. . . . .	99
395 6.3 Characterization of the strip barrel, including the number of staves, radius, tilt 396 angle, and strip length in the ITk layout 03-00-00 [95]. . . . .	101
397 7.1 The CPU required in $\text{HS06} \times$ seconds to reconstruct a Run 2 data event using the 398 corresponding software release at average pile-up 90 using. The total reconstruction 399 time is broken down into inner tracking, Calorimeter and Muon Spectrometer 400 reconstruction, and Monitoring. Numerical figures taken from reference [86]. . .	126
401 7.2 The CPU required in $\text{HS06} \times$ seconds to reconstruct a $t\bar{t}$ MC event with $\langle\mu\rangle = 140$ 402 and 200 in the ITk. The total track reconstruction time, evaluated for both the 403 default and an optimized CKF-based chains, is broken down into individual steps, 404 most significant of which are clustering, space point formation, CKF-based track 405 finding and ambiguity resolution. An Intel Xeon E5-2620v2 processor with 2.1 406 GHz and six physical cores per CPU was used. The CPU time is multiplied by 407 an HS06 factor of 17.8 for single-thread running. Numerical figures taken from 408 reference [28]. . . . .	127
409 8.1 Input features into the Metric Learning model. See Appendix A for definitions 410 of the variables. . . . .	142
411 8.2 Hyperparameters used to train the Metric Learning model. . . . .	143
412 9.1 Hyperparameters used to train the Filter network. . . . .	155
413 9.2 Comparison of graphs entering the INTERACTIONGNN . . . . .	157
414 9.3 Hand-engineered edge features . . . . .	159

Table	Page
415 9.4 INTERACTIONGNN model specification . . . . .	162
416 9.5 Performance of the INTERACTIONGNN across three graph construction methods.	165
417 10.1 Edge efficiency and fake reduction rate at representative values of GNN edge score cut. . . . .	173
419 11.1 Nominal track selection criteria featured in reference [95]. . . . .	187
420 11.2 Relaxed selections adapted to GNN-based tracks. Modified criteria with respect to those in table 11.1 are highlighted in boldface. The rest is identical to reference [95]. . . . .	188
423 11.3 The total number of reconstructed tracks by the GNN4ITk and the CKF chains having matching probability less than 0.5 over 1000 $t\bar{t}$ events. . . . .	191
425 11.4 Minimally modified selections adapted to GNN-based tracks. Modified criteria with respect to those in table 11.1 are highlighted in boldface. The rest is identical to reference [95]. . . . .	192
428 12.1 Latency improvement over eager computation at full precision of each optimization, measured using the baseline configuration, and configurations optimized with automated mixed precision (AMP), AOT compilation, and a combination of both techniques. All measurements use graphs constructed with the Module Map MeanRMS method. . . . .	214
433 12.2 The coefficients of a second-order polynomial fit to the GPU time shown in figure 12.2 for each optimization technique. The GPU time $t$ in units of seconds is assumed to depend on $x = \frac{ V }{10^6}$ , where $V$ is the set of nodes, as $t = Ax^2 + Bx + C$ .216	216
436 12.3 Per-event run time of each stage in the GNN4ITk algorithm. The latency of graph construction and edge classification is evaluated on an NVIDIA-A100 GPU with 80GB of memory, and of graph segmentation on the AMD EPYC 7763 CPU, using graphs constructed with the Module Map MeanRMS method. . . . .	218

Appendix  
Table

Appendix  
Table

## 440 Chapter 1

### 441 Introduction

442 The existence of Dark Matter (DM) enjoys well-established acceptance among particle  
443 physicists and cosmologists, supported by a wealth of evidence from astrophysical observa-  
444 tions [96, 152, 69, 121, 145, 159, 70, 105]. Although DM accounts for an estimated 85% of  
445 the mass in the universe, it has no obvious particle candidate in the Standard Model. Thus,  
446 an explanation of its nature is a central focus of the physics programme in the collider exper-  
447 iments such as ATLAS and CMS [4]. Among the proposed hypotheses, Weakly-Interacting  
448 Massive Particles (WIMPs)  $\chi$  gain much interest for experimental detection of DM, which  
449 typically targets the associated production of a visible mediator decaying to stable particles  
450 and a large missing transverse momentum with magnitude  $E_T^{\text{miss}}$ . The result of these indirect  
451 searches is usually interpreted in the context of a simplified model that involves a fermionic  
452 DM particle connected to the visible sector via a vector, axial-vector, scalar, or pseudo-scalar  
453 mediator  $a$ . It contains a minimal set of free parameters, including the masses and coupling  
454 strength of the DM and mediator particles.

455 The Two-Higgs-Doublet model (2HDM) plus a pseudo-scalar mediator  $a$  is the simplest  
456 gauge-invariant and renormalizable extension of the simplified pseudo-scalar DM model,  
457 offering a rich phenomenology and a more complete benchmark. It is identified by the LHC  
458 Dark Matter Working Group along with a set of recommended scans to explore its parameter

459 space through LHC searches. A variety of analyses using  $137 \text{ fb}^{-1}$  of proton-proton collision  
 460 data collected at the center-of-mass energy up to 13 TeV by the ATLAS detector during  
 461 LHC Run 2 and targetting diverse visible signatures provide constraints on the 2HDM+ $a$ .  
 462 The first part of this thesis presents a statistical combination of the three most sensitive  
 463 analyses and a summary of the remaining searches. The statistical combination considers  
 464  $E_T^{\text{miss}} + X$ -type signatures where  $X$  is either a SM Higgs boson decaying into a pair of  $b$ -  
 465 quarks [49] or a  $Z$ -boson decaying into a pair of leptons [42], and a search for associated  
 466 production of a top and a bottom quark with a charged Higgs boson decaying into a top  
 467 and a bottom quark [43]. The result from searches targeting signatures are summarized in  
 468 the result. Overall, this work represents the most comprehensive set of constraints on the  
 469 model obtained by the ATLAS Collaboration to date.

470 These searches for DM leave a sizeable part of the parameter space unexcluded and await  
 471 more data to derive better constraints on the 2HDM+ $a$ . In general, searches for exotic  
 472 phenomena at the LHC are often statistically limited, motivating a significant boost in the  
 473 rate of data collection. The High-Luminosity phase of the Large Hadron Collider will help  
 474 quench this thirst for data with up to 3-fold increase in instantaneous luminosity  $\mathcal{L}$ , reaching  
 475  $7.5 \times 10^{34} \text{ cm}^{-2}\text{s}^{-1}$  [3]. The integrated luminosity delivered to each of the general-purpose  
 476 detectors will total  $4000\text{fb}^{-1}$  at the end of Run 5,  $\sim 10$  times the amount of data collected  
 477 during the nominal LHC runs. This upgrade will bring unprecedented opportunities for  
 478 physics discovery and precision measurements, and at the same time many challenges to all  
 479 aspects of data processing, from simulation to reconstruction.

480 In particular, the elevated luminosity leads to an increased number of proton-proton  
 481 interactions in a bunch crossing. As a result, events characterized by a large momentum  
 482 transfer and often producing interesting physics, or hard scatters, are more likely to occur,  
 483 they are accompanied by a larger background of soft inelastic collisions, or pile-up. The  
 484 expected pile-up  $\langle \mu \rangle$  will increase from  $\sim 50$  in Run 3 to 140 at the end of Run 4, peaking  
 485 at 200 in Run 5, and with it a steep increase in event complexity as well as the necessary

486 CPU resources to for event reconstruction. The computing budget dedicated to reconstruc-  
487 tion is typically dominated by inner tracking, which is why both many LHC experiments  
488 are investigating methods based on hardware accelerators (GPUs, FPGAs) as a potential  
489 solution to this problem. In this direction, a tracking algorithm centered on Graph Neural  
490 Networks (GNNs) is identified as a promising approach whose development and evaluation  
491 are reported in the second part of this thesis.

492

# Part I

493

Search for dark matter interpreted in

494

a Two-Higgs-Doublet Model with a

495

pseudoscalar mediator using  $139 \text{ fb}^{-1}$  of

496

$\sqrt{s} = 13 \text{ TeV}$  proton-proton collision

497

data at the ATLAS detector

<sup>498</sup> **Chapter 2**

<sup>499</sup> **Theoretical background**

<sup>500</sup> This chapter presents an overview of the Standard Model (SM) of Particle Physics which  
<sup>501</sup> describes the particle nature of visible matter in the universe and unifies the electromagnetic,  
<sup>502</sup> weak and strong interactions. Since a complete account of this monumental achievement far  
<sup>503</sup> exceeds the scope of this document, only aspects of the theory most relevant to the rest  
<sup>504</sup> of the thesis will be introduced. Interested readers are invited to peruse classic texts on  
<sup>505</sup> the subject for further details [143, 117, 154]. We describe at the end some of the SM's  
<sup>506</sup> limitations, which motivate the exploration of the extended Higgs sector, part of what is  
<sup>507</sup> known as Beyond Standard Model (BSM) physics.

<sup>508</sup> **2.1 The Standard Model of Particle Physics**

<sup>509</sup> Elementary particles in the SM are typically grouped by their spin. There are three  
<sup>510</sup> generations of spin- $\frac{1}{2}$  particles called fermions, several spin-1 gauge bosons which mediate  
<sup>511</sup> their interaction, and a spin-0 Higgs boson to account for other particles' mass. Two types of  
<sup>512</sup> fermions exist; the first is the leptons, which include the electron ( $e$ ), the muon ( $\mu$ ) and the  
<sup>513</sup> tau lepton ( $\tau$ ), and their associated neutrinos, denoted ( $\nu_e, \nu_\mu, \nu_\tau$ ). The second type consist  
<sup>514</sup> of three generations of quarks, each consisting of a pair, namely up ( $u$ ) and down ( $d$ ), charm  
<sup>515</sup> ( $c$ ) and strange (also sideways) ( $s$ ), and top ( $t$ ) and bottom ( $b$ ).

516 With the exception of neutrinos, all SM fermions carry an electric charge and couple  
517 to the *electromagnetic* field via the photon. Leptons carry integer charge  $\pm 1$ , while quarks  
518 carry fractional charges  $\mp \frac{1}{3}e$  and  $\mp \frac{2}{3}e$ .

519 Unlike leptons, quarks also carry  $SU(3)$  color charge and couple to the gluon field, just  
520 like electrically charged particles coupling to the electromagnetic field. The spin-1 gluon also  
521 carries color charges and mediate the strong force between quarks and other gluons. It is  
522 due to the strong interaction that quarks always appear in bound states of a pair or a triplet  
523 called hadron, of which the proton and the neutron are examples, despite having same-sign  
524 electric charges. The color charge of bound quarks in hadrons cancel each other, so hadrons  
525 are color-neutral.

526 All fermions participate in the weak interaction mediated by the  $W^\pm$  and the  $Z$  bosons  
527 and responsible for decays of the muon and the tau lepton to the electron, and of quarks  
528 to lighter quarks, the most well-known example of which in nuclear physics is  $\beta$  decay, and  
529 the top quark decaying to the bottom quark in particle physics. Unlike the photon and  
530 the gluon, the weak vector bosons are massive particles, whose mass is generated by their  
531 interaction to the Higgs field whose quantized particle is the Higgs boson. The discovery of  
532 the Higgs boson in 2012 grants the SM its completeness and self-consistency.

## 533 2.2 Electroweak symmetry breaking and the Higgs mechanism

534 In the standard model, the left-handed leptons transform as an  $SU(2)$  doublet, and the  
535 right-handed leptons transform as an  $SU(2)$  singlet. Their Lagrangian must be invariant  
536 under the corresponding generic transformation

$$E_L \rightarrow e^{\frac{i}{2}(\alpha^a(x)\sigma^a + \beta(x))} E_L, \quad E_R \rightarrow e^{i\beta(x)/2} E_R, \quad (2.1)$$

537 where  $\alpha^a(x)$  and  $\beta(x)$  are arbitrary differentiable functions, and  $\sigma^a$  the Pauli matrices. To  
538 account for lepton masses, a scalar field invariant under local  $SU(2) \otimes U(1)$  transformation

<sup>539</sup> is introduced

$$\phi = \begin{pmatrix} \phi^+ \\ \phi^- \end{pmatrix}, \quad \phi \rightarrow e^{\frac{i}{2}(\alpha^a(x)\sigma^a + \beta(x))} \phi, \quad (2.2)$$

<sup>540</sup> from which its covariant derivative follows

$$D_\mu = \partial_\mu - i\frac{g_2}{2}W_\mu^a\sigma^a - i\frac{g_1}{2}B_\mu, \quad (2.3)$$

<sup>541</sup> where  $A_\mu^a$  and  $B_\mu$  are the  $SU(2)$  and  $U(1)$  gauge bosons. The most general Lagrangian for  
<sup>542</sup> a renormalizable scalar field respecting these symmetries can be written as

$$\mathcal{L}_{\text{Higgs}} = |D_\mu|^2 + \mu^2\phi^\dagger\phi - \frac{\lambda}{2}(\phi^\dagger\phi)^2. \quad (2.4)$$

<sup>543</sup> The configuration which minimizes the Higgs potential, assuming  $\mu^2 > 0$ , is such that

$$\phi^\dagger\phi = \frac{\mu^2}{\lambda} = v^2. \quad (2.5)$$

<sup>544</sup> The number  $v$  is known as the vacuum expectation value (VEV) of the Higgs field. Selecting  
<sup>545</sup> the simplest configuration, and adding a fluctuation field around the minimum, we get

$$\langle\phi\rangle = \frac{1}{\sqrt{2}} \begin{pmatrix} 0 \\ v \end{pmatrix}, \quad \phi = \frac{1}{\sqrt{2}} \begin{pmatrix} 0 \\ v + H(x) \end{pmatrix}, \quad (2.6)$$

<sup>546</sup> and evaluating the kinetic term in (2.4), we obtain terms suggestive of the mass eigenstates  
<sup>547</sup> of the electroweak bosons

$$|D_\mu\phi|^2 = \frac{1}{2}(\partial_\mu H)^2 + \frac{g_2^2}{8}(v + H)^2|W_\mu^1 + iW_\mu^2|^2 + \frac{1}{8}(v + H)^2|g_2W_\mu^3 - g_1B_\mu|^2. \quad (2.7)$$

<sup>548</sup> By defining the mass eigenstates as

$$W_\mu^\pm = \frac{1}{\sqrt{2}}(W_\mu^1 \mp iW_\mu^2), \quad Z_\mu = \frac{g_2W_\mu^3 - g_1B_\mu}{\sqrt{g_1^2 + g_2^2}}, \quad A_\mu = \frac{g_2W_\mu^3 + g_1B_\mu}{\sqrt{g_1^2 + g_2^2}} \quad (2.8)$$

<sup>549</sup> and the corresponding masses as

$$M_W = \frac{g_2 v}{2}, \quad M_Z = \frac{v\sqrt{g_1^2 + g_2^2}}{2}, \quad m_A = 0 \quad (2.9)$$

550 and writing (2.7) as

$$|D_\mu \phi|^2 = \frac{1}{2}(\partial_\mu H)^2 + M_W^2 \left(1 + \frac{H}{v}\right)^2 W_\mu^+ W^{\mu-} + \frac{M_Z^2}{2} \left(1 + \frac{H}{v}\right)^2 Z_\mu Z^\mu + \frac{M_A^2}{2} A_\mu A^\mu, \quad (2.10)$$

551 we “create” mass for the vector bosons, while maintaining a massless photon. It is convenient  
552 to introduce the electroweak mixing angle  $\theta_W$  such that

$$\tan \theta_W = \frac{g_1}{g_2} \Rightarrow \cos \theta_W = \frac{m_W}{m_Z}, \quad (2.11)$$

553 and that

$$\begin{pmatrix} Z_\mu \\ A_\mu \end{pmatrix} = \begin{bmatrix} \cos \theta_W & -\sin \theta_W \\ \sin \theta_W & \cos \theta_W \end{bmatrix} \begin{pmatrix} W_\mu^3 \\ B_\mu \end{pmatrix}. \quad (2.12)$$

554 We can rewrite the covariant derivative in (2.4) using the mass eigenstates

$$D_\mu = \partial_\mu - i \frac{g_2}{2} W_\mu^a \sigma^a - i \frac{g_1}{2} B_\mu \quad (2.13)$$

$$= \partial_\mu - \frac{ig_2}{\sqrt{2}} (W_\mu^+ T^+ + W_\mu^- T^-) - i \frac{1}{\sqrt{g_1^2 + g_2^2}} Z_\mu (g_2^2 T^3 - g_1^2 Y) \quad (2.14)$$

$$- i \frac{g_1 g_2}{\sqrt{g_1^2 + g_2^2}} A_\mu (T^3 + Y) \quad (2.15)$$

555 where  $T^a = \sigma^a/2$ ,  $T^\pm = (T^1 \pm iT^2)$ ,  $Y$  a general  $U(1)$  charge. Defining the coefficient  
556 of the electromagnetic interaction  $e = \frac{g_1 g_2}{\sqrt{g_1^2 + g_2^2}}$ , and the electric charge quantum number  
557  $Q = T^3 + Y$ , we retrieve a covariant derivative where the couplings of all electroweak bosons  
558 can be described by the familiar electric charge and the mixing angle

$$D_\mu = \partial_\mu - \frac{ig_2}{\sqrt{2}} (W_\mu^+ T^+ + W_\mu^- T^-) - \frac{ig_2}{\cos \theta_W} (T^3 - \sin \theta_W Q^2) - ie A_\mu Q \quad (2.16)$$

559 By spontaneously breaking the symmetry  $SU(2)_L \times U(1)_Y \rightarrow U(1)_Q$ , three Goldstone bosons  
560 (three degrees of freedom) are absorbed by the  $W^\pm$  and  $Z$  boson, making them massive. The  
561 remaining  $U(1)_Q$  symmetry is unbroken, so its generator, the photon, remains massless.

562 Fermion mass is generated by treating the same scalar field  $\phi$  and its isodoublet  $\tilde{\phi} =$   
563  $i\sigma^2\phi*$ . Take for example the first generation of fermion, introduce the  $SU(2)_L \times U(1)_Y$   
564 invariant Yukawa Lagrangian

$$\mathcal{L}_F = -\lambda_e \bar{L} \phi e_R - \lambda_d \bar{Q} \phi d_R - \lambda_u \bar{Q} \tilde{\phi} u_R + h.c., \quad (2.17)$$

<sup>565</sup> and repeat the same procedure, we get

$$\mathcal{L}_F = -\frac{1}{\sqrt{2}}\lambda_e(v + H)\bar{e}_L e_R + \dots, \quad (2.18)$$

<sup>566</sup> and the fermion mass

$$m_f = \frac{\lambda_f v}{\sqrt{2}} \quad (2.19)$$

<sup>567</sup> After symmetry breaking, the Higgs Lagrangian can be written as

$$\mathcal{L}_H = \frac{1}{2}(\partial_\mu H)^2 - \lambda v^2 H^2 - \lambda v H^2 - \frac{\lambda}{4}H^4, \quad (2.20)$$

<sup>568</sup> from which the Higgs boson mass reads

$$M_H^2 = 2\lambda v^2 = -2\mu^2. \quad (2.21)$$

<sup>569</sup> The triple and quartic terms give rise to the Higgs self-interaction vertices with coupling  
<sup>570</sup> strength given in terms of its mass and VEV by

$$g_{HHH} = \frac{3M_H^2}{v}, \quad g_{HHHH} = \frac{3M_H^2}{v^2}. \quad (2.22)$$

<sup>571</sup> The Higgs coupling to gauge bosons can easily be read from terms in (2.10) following  
<sup>572</sup>  $M_V(1 + \frac{H}{v})^2$ , and hence,

$$g_{HV} = \frac{2M_V^2}{v}, \quad g_{HHV} = \frac{2M_V^2}{v^2}. \quad (2.23)$$

<sup>573</sup> Similarly, the Higgs coupling to fermion is proportional to the fermion mass

$$g_{Hff} = \frac{m_f}{v} \quad (2.24)$$

<sup>574</sup> In addition, the vacuum expectation value  $v$  is fixed in terms of the Fermi constant  $G_F$ ,  
<sup>575</sup> experimentally determined from muon decay

$$M_W = \frac{g_2 v}{2} = \left( \frac{\sqrt{2}g_2^2}{8G_F} \right)^{1/2} \Rightarrow v = \sqrt{\frac{1}{\sqrt{2}G_F}} \approx 246 \text{ GeV}. \quad (2.25)$$

### 576 2.3 Standard Model Higgs boson production and decay

577 From the Higgs coupling structure derived from 2.2, we can examine the main production  
 578 mechanisms of the Higgs boson in  $pp$  collision at the LHC. Figure 2.1a shows the production  
 579 cross sections of the SM Higgs boson during  $pp$  collision at center-of-mass energy  $\sqrt{s} = 13$   
 580 TeV as a function of the Higgs mass. The most important production mechanisms include  
 581 gluon-gluon fusion ( $ggF$ ), vector boson fusion ( $qqH$ ), associated production with a vector  
 582 boson  $VH$ , ( $V = W, Z$ ), associated production with a pair of top (bottom) quarks  $t\bar{t}H$  ( $b\bar{b}H$ ),  
 583 and associated production with a single top quark ( $tH$ ).

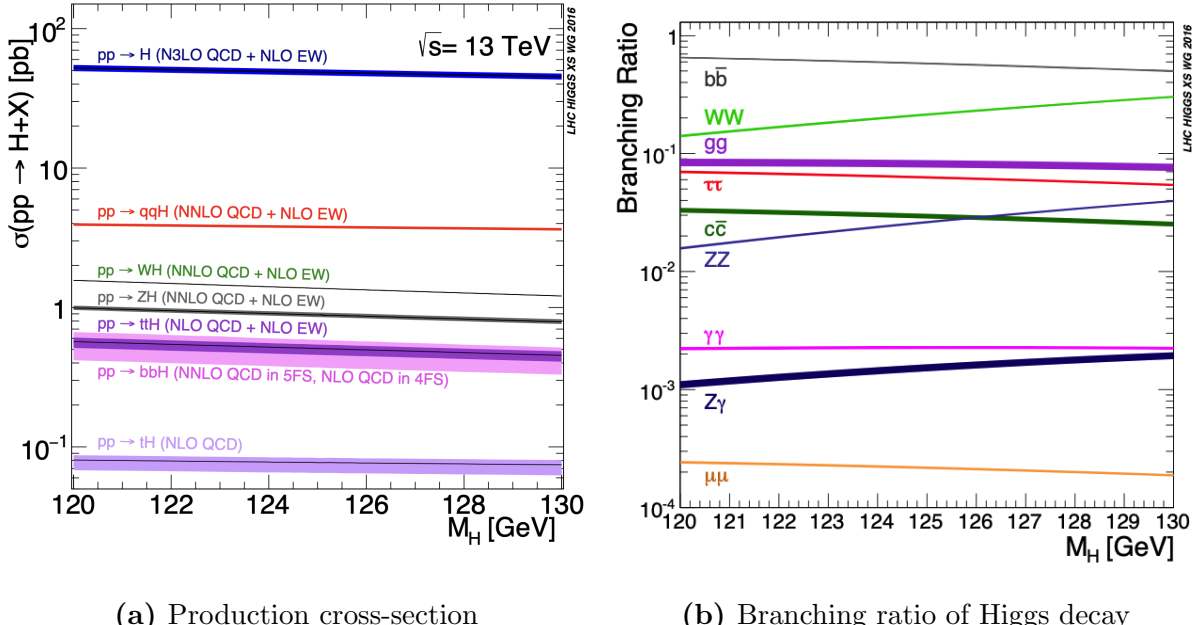


**Figure 2.1:** Production cross-section of the Standard Model Higgs boson produced by  $pp$  collision as a function of  $M_H$  at  $\sqrt{s} = 13$  TeV

584 The most dominant production mechanism is gluon-gluon fusion, whose cross-section  
 585 far exceeds those of other mechanism. The Feynman diagram for this process is shown in  
 586 figure 2.2a. The gluon is massless and only indirectly couples to the Higgs boson through  
 587 a triangular heavy quark loop, to which the largest contribution comes from the top quark.

588 The diagram still has a large magnitude, thanks to the strong coupling of the Higgs boson  
589 and the gluon to the top quark at this energy scale.

590 Production via vector boson fusion (*VBF*) sees the second largest cross-section, thanks  
591 to large couplings between the Higgs and the  $W/Z$  bosons and between the vector bosons  
592 to heavy quarks, albeit an order of magnitude smaller than  $\sigma_{ggF}$ . Its tree-level diagram is  
593 shown in figure 2.2b. The final state is characterized by two forward jets from hadronized  
594 heavy quarks, along with products from various Higgs decay signatures. This process is  
595 particularly important in measurements of the  $g_{HVV}$  coupling.

596 The leading diagram for associated Higgs production with a vector boson initiated by  
597 a pair of quarks ( $qq \rightarrow VH$ ) is shown in figure 2.2c. Another much smaller  $gg$ -initiated  
598 production also contribute at next-to-leading order. The Higgs boson is produced via Hig-  
599 gsstrahlungs from the vector boson. The latter can decay leptonically or hadronicall, but  
600 analyses in the leptonic channel often benefit from efficient lepton triggers, and high-quality  
601 lepton reconstruction.

602 Finally, we mention the mechanism of associated production with a top quark pair, shown  
603 in figure 2.2d, which is small but of paramount importance in probing the Higgs coupling  
604 to the top quark. Unlike the case of other third-generation fermions, namely the tau lepton  
605 and the bottom quark, the Higgs decay to the top quark is kinematically forbidden due to  
606 the latter's large mass. Therefore, the top quark Yukawa coupling  $y_t$  can only be measured  
607 through the  $pp \rightarrow t\bar{t}H$  production process.

608 Another consequence of the Higgs coupling structure described in 2.2 equally important  
609 to the study of the Higgs boson at the LHC is the consideration of its decay channels.  
610 Being one of the heaviest SM particles, the Higgs boson has a lifetime of approximately  
611  $10^{-22}s$ . Tree-level Higgs boson decay is induced by its coupling to quarks, whose primary  
612 channels include  $H \rightarrow b\bar{b}/c\bar{c}$ , to leptons, namely  $H \rightarrow \tau\bar{\tau}/\mu\bar{\mu}$ , and to vector bosons, namely  
613  $H \rightarrow WW/ZZ$ . In addition, notable loop-induced decays include  $H \rightarrow gg/\gamma\gamma/Z\gamma$ . Figure

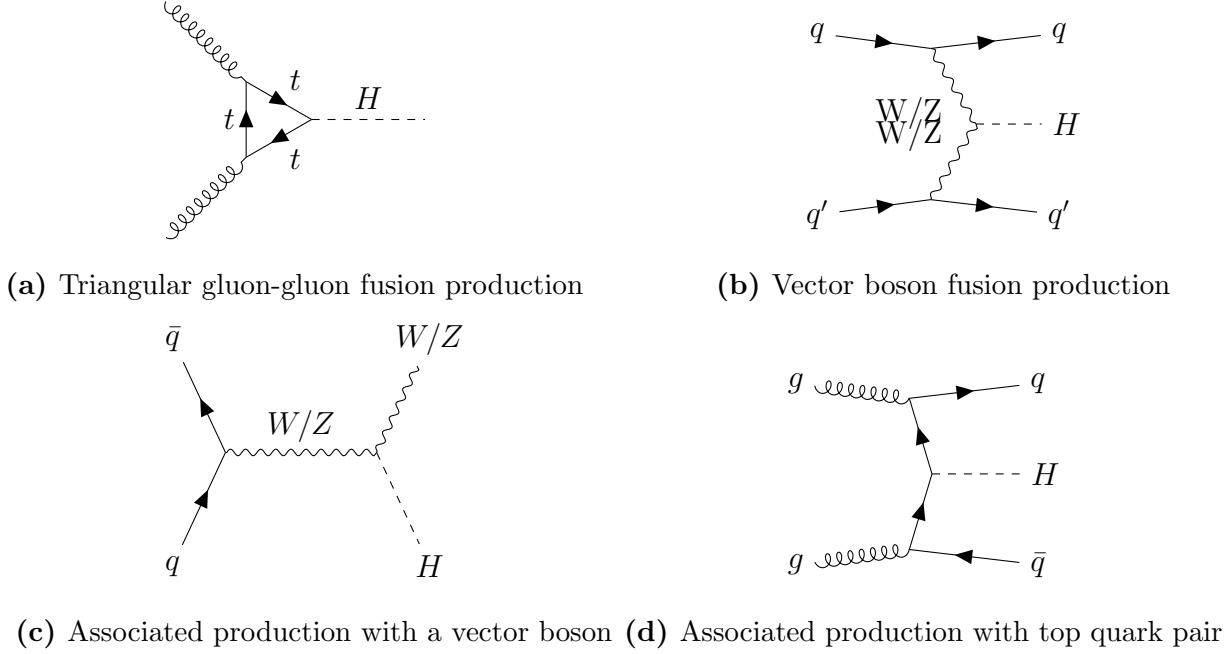


**Figure 2.2:** Leading-order Higgs boson production mechanisms

614 2.1b shows the branching ratios of primary Higgs decay channels as a function of the Higgs  
 615 mass near  $m_H = 125$  GeV. Table 2.1 specifies the branching ratio measured at Higgs mass  
 616  $M_H = 125.09$  GeV.

617 Since a decay to the top quark is forbidden, it is not surprising that the most dominant  
 618 decay mode is via Yukawa coupling to the second heaviest quark,  $H \rightarrow b\bar{b}$ , whose branching  
 619 ratio is 57.5% at  $m_H = 125.09$  GeV. Among other fermions, decay into a pair of tau leptons  
 620 is the second largest, followed by decays into second-generation fermions (figure 2.3a). The  
 621 decay to a pair of vector boson proceeds through tree-level processes (figure 2.3b), whereas  
 622  $H \rightarrow \gamma\gamma$  is mediated by a  $W$  boson (figure 2.3d) or a heavy quark loop (figure 2.3c). Despite  
 623 having a small branching ratio,  $H \rightarrow \gamma\gamma$  is an important channel for precision measurement  
 624 of the Higgs mass due to the high resolution of the reconstructed photon invariant mass.

Decay channel	Branching ratio (%)
$H \rightarrow b\bar{b}$	$57.5 \pm 1.9$
$H \rightarrow WW$	$21.6 \pm 0.9$
$H \rightarrow gg$	$8.56 \pm 0.86$
$H \rightarrow \tau\bar{\tau}$	$6.30 \pm 0.36$
$H \rightarrow c\bar{c}$	$2.9 \pm 0.35$
$H \rightarrow ZZ$	$2.67 \pm 0.11$
$H \rightarrow \gamma\gamma$	$0.228 \pm 0.011$
$H \rightarrow Z\gamma$	$0.155 \pm 0.014$
$H \rightarrow \mu\bar{\mu}$	$0.022 \pm 0.001$

**Table 2.1:** Standard Model Higgs boson decay branching ratios and uncertainty at  $M_H = 125.09$  GeV

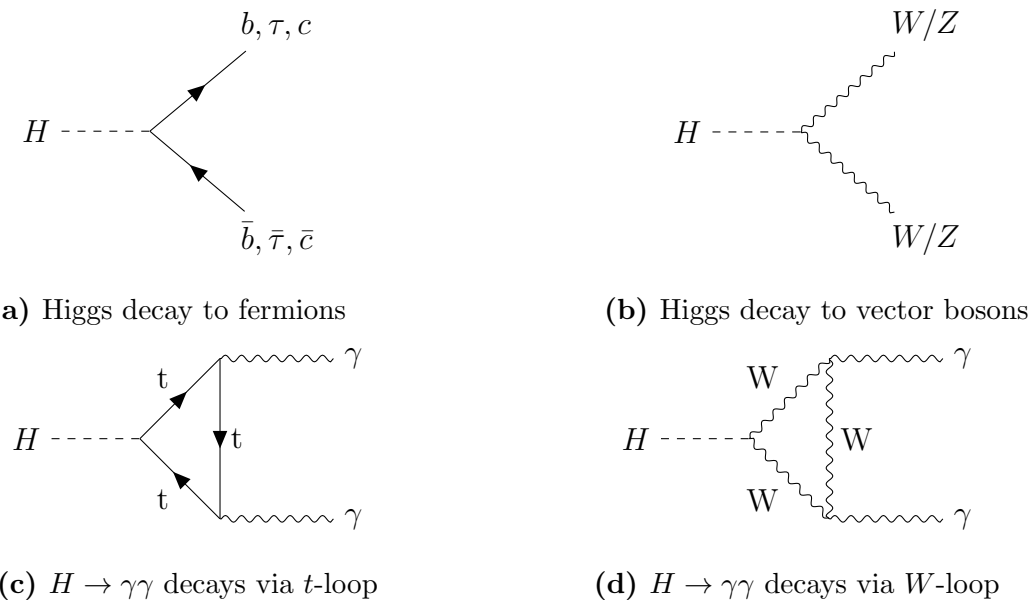


**Figure 2.3:** Leading-order Higgs boson decay mechanisms

## 625 2.4 Extension of the Standard Model Higgs sector

626 Until now, we have given a theoretical description of the simplest possible scalar struc-  
 627 ture of the Higgs field, namely a single  $SU(2)$  doublet  $\phi$ . This assumption is motivated  
 628 almost entirely by simplicity, and there exist a number of extensions to the SM Higgs sector  
 629 which satisfy the experimental constraint on its scalar structure [140]. The simplest of such  
 630 extensions consists of an additional scalar Higgs doublets—known as the Two-Higgs-Doublet  
 631 Model (2HDM).

632 The model is motivated by several considerations, the best known of which is supersymme-  
 633 try, which is explored in reference [114]. Briefly speaking, supersymmetric quarks of charges  
 634  $2/3$  and  $-1/3$  cannot acquire their mass through coupling to a single Higgs doublet. More-  
 635 over, the cancellation of anomalies requires the existence of an additional Higgs doublet.  
 636 Therefore, the Minimal Supersymmetric Standard Model (MSSM) must contain two Higgs  
 637 doublets, as prescribed by the 2HDM.

638 In addition, while the SM cannot account for the baryon-antibaryon asymmetry of the  
 639 early universe, the 2HDM, thanks to the flexibility of their scalar mass spectrum and ad-  
 640 ditional sources of CP violation, can provide stronger theoretical explanation of this phe-  
 641 nomenon. Aspects of electroweak baryogenesis in the 2HDM are explored in reference [122,  
 642 110, 83, 84, 127, 108]. A comprehensive review of the rich phenomenology of the 2HDM can  
 643 be found in reference [74].

644 In the context of dark matter (DM) searches at the LHC, the 2HDM extended by a  
 645 pseudo-scalar mediator  $a$ , denoted by 2HDM+ $a$ , constitutes an attractive benchmark model  
 646 [1]. The pseudo-scalar mediates the interactions between the visible sector of the 2HDM and  
 647 the dark sector, assumed to include a single fermionic DM particle  $\chi$ . Chapter 4 presents a  
 648 combination and summary of dark matter searches using  $139\text{ fb}^{-1}$  of  $pp$  collision data at  $\sqrt{s} =$   
 649  $13\text{ TeV}$  collected by the ATLAS detector throughout LHC Run 2. Relevant phenomenological

650 consideration of the 2HDM+ $a$  is presented in 4.1, along with important model parameters  
651 and experimental signatures to be examined by DM searches in ATLAS, many of which are  
652 introduced earlier in this chapter.

<sub>653</sub> **Chapter 3**

<sub>654</sub> **The ATLAS experiment**

<sub>655</sub> **3.1 The ATLAS detector**

<sub>656</sub> The ATLAS (A Toroidal LHC ApparatuS) detector is a general-purpose detector, along  
<sub>657</sub> with CMS, designed to observe any new physics phenomena that the LHC can discover. It  
<sub>658</sub> is a cylindrical structure constructed around the beam pipe at one of the collision points on  
<sub>659</sub> the LHC, comprised of an Inner Detector (ID), an electromagnetic calorimeter, a hadronic  
<sub>660</sub> calorimeter, and a muon spectrometer. Being the largest of the LHC detectors, it spans 44m  
<sub>661</sub> in length and 25m in height, as shown in figure 3.1.

<sub>662</sub> The detector's geometry facilitates the use of a right-handed cylindrical coordinate system  
<sub>663</sub> to describe locations and directions, with the nominal interaction point (IP) at the origin.  
<sub>664</sub> The  $z$ -axis points along the beam pipe, parallel to the direction of the incoming protons.  
<sub>665</sub> The  $x$ -axis points from the IP towards the center of the LHC. Any position is described  
<sub>666</sub> by  $(r, \phi, z)$ , where  $\phi \in [-\pi, \pi]$ . Particle momentum can be represented by a four-vector  
<sub>667</sub>  $p = (E, p_x, p_y, p_z)$ . In practice, however, the rapidity, define as

$$y = \frac{1}{2} \ln \left( \frac{E + p_z}{E - p_z} \right) \quad (3.1)$$

<sub>668</sub> is commonly used in lieu of the longitudinal momentum, because differences in rapidity is  
<sub>669</sub> invariant under a Lorentz boost along  $z$ . For massless or very energetic particles, the rapidity

<sup>670</sup> is well approximated by the pseudorapidity defined from the polar angle  $\theta$

$$\eta = -\ln \tan\left(\frac{\theta}{2}\right). \quad (3.2)$$

<sup>671</sup> Both  $y$  and  $\eta$  are symmetric about  $z = 0$ . A particle moving entirely on the transverse plane  
<sup>672</sup> has  $y = \eta = 0$ , and one moving parallel to the  $z$ -axis has  $\eta = \pm\infty$ . Obviously, no detector  
<sup>673</sup> can cover the entire  $4\pi$  steradians of solid angle around the IP. The range of pseudorapidity  
<sup>674</sup> observable by a detector is called the *acceptance*. Each subsystem of ATLAS has a different  
<sup>675</sup> acceptance, in particular,  $|\eta| < 2.5$  in the ID, and  $|\eta| < 4.8$  for the calorimeters. Since the  
<sup>676</sup> pseudorapidity represents the polar angle, it is sufficient to describe a particle by  $(E, p_T, \eta, \phi)$ ,  
<sup>677</sup> where  $p_T = \sqrt{p_x^2 + p_y^2}$  is the transverse momentum.

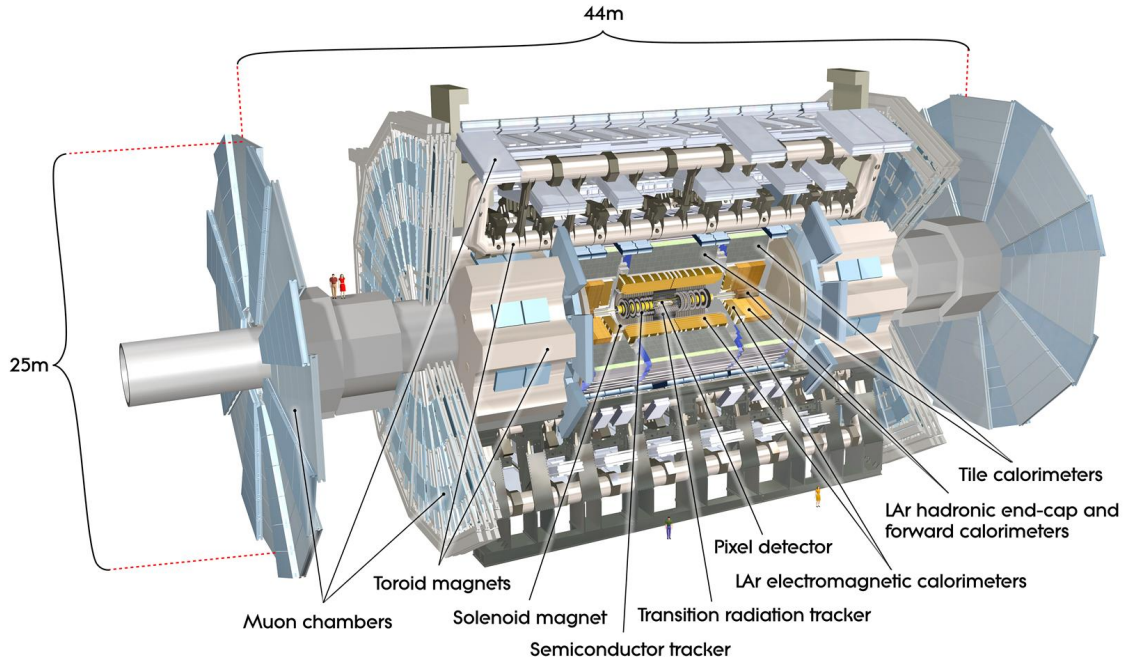


**Figure 3.1:** The ATLAS detectors and its components [142]

### 678 3.1.1 The Inner Detector

679 f Immediately surrounding the interaction point is the Inner Detector, consisting of 3  
 680 subsystems constructed from two sensor technologies. These subsystems include a Pixel  
 681 detector, a Semi-Conductor Tracker (SCT), and a Transition Radiation Tracker (TRT), in  
 682 order of increasing radial distance from the IP. The first two use silicon sensors to detect  
 683 the passage of a charged particle and the latter a collection of gas-filled straw tube and a  
 684 tungsten wire to collect the secondary radiation engendered from the particle.

685 The ID is responsible for precise measurements of discrete points along the path of a  
 686 charged particle, from which its trajectory (tracks) is reconstructed. Tracks are essential  
 687 inputs to reconstruct physics objects charged leptons, jets, as well as the identification of  
 688 jets from heavy quarks.

689 A crucial part of the ID's function is the estimation of particle momentum and impact  
 690 parameters. In the presence of a homogeneous magnetic field of 2T permeating the ID along  
 691 the  $z$ -axis, charged particles move in helical orbits, whose radius depends on the transverse  
 692 momentum  $p_T$

$$R = \frac{p_T}{qB}. \quad (3.3)$$

693 In principle, by fitting a helix through measurements on a track, one obtains an estimate of  
 694 the curvature and thus  $p_T$ . Extrapolating this helix to the point of closest approach to the  
 695 IP, called the *perigee*, yields an estimate of the primary and longitudinal impact parameters  
 696 ( $d_0, z_0$ ) respectively. This procedure is described in detail in chapter 7.

697 Being the first sub-detector to observe particles after they are created in the entire de-  
 698 tector, the ID has the best position to characterize their kinematics to the highest possible  
 699 resolution. In particular, the relative momentum resolution  $p_T\sigma(\frac{q}{p_T})$  is  $O(1\%)$ , while the  
 700 impact parameter resolutions can reach  $\sigma(d0) \approx 25\mu m$  and  $\sigma(z0) \approx 40\mu m$ . This level of

701 resolution is remarkable considering the physical dimensions of ATLAS, which can only be  
702 achieved through meticulous custom designs of the subsystems described below.

703 **3.1.1.1 The Pixel Detector**

704 The pixel detector (figure 3.2a) is the innermost part of the ID, consisting of 3 barrel  
705 layers extending from a radius of  $r = 50.5\text{ mm}$  up to  $r = 122.5\text{ mm}$ , and 3 end-cap disks  
706 on each sides of the barrel. Each of these physical layers provides a structure onto which  
707 detector modules are mounted. Each barrel layer consists of supporting staves, and each  
708 end-cap of 8 sectors circularly arranged around the  $z$ -axis. In total, the pixel detector has  
709 1744 identical modules, each composed of an array of silicon sensor and 16 front-end chips  
710 which read out the electrical signal created by the passage of a charge particle [73].

711 A sensor element is fabricated from a detector-grade n-type silicon wafer implanted with  
712 high positive ( $p^+$ ) and negative ( $n^+$ ) dose regions on each side. At the  $p^+ \text{-} n$  junction, holes  
713 from the  $p^+$  region neutralize free electrons in the  $n$ -typed bulk, creating a depletion zone  
714 devoid of free charge carriers. Operated in a reverse bias, this region is enlarged over the  
715 whole sensor bulk volume. Although containing no free charge carrier, the  $pn$ -junction is  
716 easily ionized by a traversing particle, creating electron-hole pairs. Primary electrons directly  
717 created by the traversing particle are often energetic enough to induce secondary ionization  
718 and amplify the signal. Electron-hole pairs are separated by the biasing electric field and drift  
719 toward their corresponding electrodes. As electrons approach the anode, they are multiplied  
720 and measured by the read-out chips.

721 The sensitive part of a pixel module is approximately  $2 \times 6\text{ cm}^2$  in size, segmented into  
722 highly granular pixels of dimensions  $50 \times 400\text{ }\mu\text{m}^2$ , totalling 47268 pixels. Nearly every pixel  
723 corresponds to a readout channel, providing the pixel detector approximately 80 million  
724 channels. With the inclusion of the Insertable B-Layer (IBL), the total number of channels

the smallest pixel dimension is reduced to  $50 \times 250 \mu\text{m}^2$ , and the total number of read-out channels increased to 94 million. This high level of granularity enables high precision measurements very close to the beam pipe.

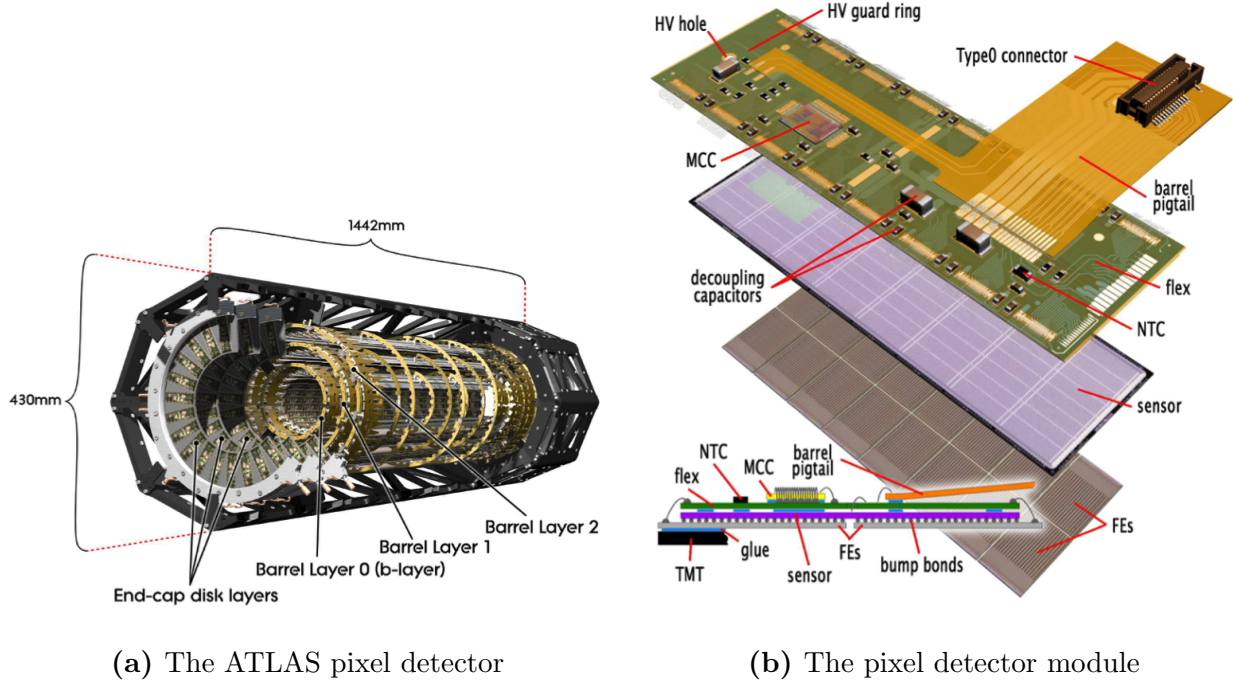


**Figure 3.2:** The ATLAS pixel detector and detector module. Figures taken from reference [87]

### 3.1.1.2 The Semi-Conductor Tracker

Surrounding the Pixel volume is the Semi-Conductor Tracker (SCT), consisting of four barrel layers and eighteen symmetric end-cap disks, both featuring a total of 4088 strip modules [16, 17]. Figure 3.3b provides an overview of a strip module used in the barrel layers. Each detector module consists of two pairs of single-sided microstrips with  $80 \mu\text{m}$  pitch. Each single strip sensor is capable of detecting particle intersection in one dimension, information from a pair of strips must be combined to provide three-dimensional point information with space-point resolution of  $16 \mu\text{m}$  in the  $(R - \phi)$  direction and  $580 \mu\text{m}$  in the  $z$ -direction [66].

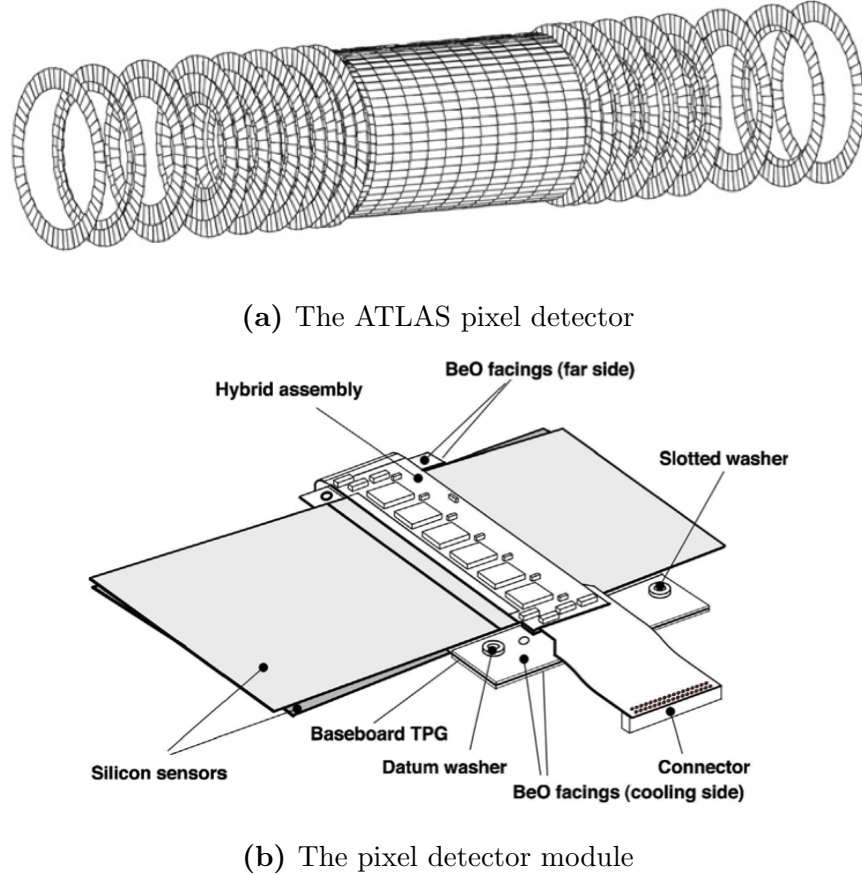


**Figure 3.3:** Overview of the strip module of the SCT in the barrel layers. Figures taken from reference [148]

### 736 3.1.1.3 The Transition Radiation Tracker

737 The Transition Radiation Tracker (TRT) is the outermost component of the Inner De-  
 738 tector. It comprises of approximately 300000 straw tubes that are 4 mm in diameter, and  
 739 covers up to  $|\eta| = 1$  in the barrel and  $|\eta| = 2$  in the end-cap layers. Each high  $p_T$  track  
 740 passing through the TRT leaves 30 – 36 hits and reach a resolution of 130  $\mu\text{m}$  in the  $(R - \phi)$   
 741 direction.

742 In each straw tube, a tungsten wire is located at the center and surrounded by a gas  
 743 mixture spreading the volume of the tube. When a charged particle passes through the

<sup>744</sup> tube, it ionizes the ambient gas and creates an pairs of electrons and positive gas ions. An  
<sup>745</sup> electric field exists between the outer tube and the central wire, which act as electrodes,  
<sup>746</sup> separating the charges. As they reach the wire, the charges are amplified and detected. To  
<sup>747</sup> enhance electron identification, the straw tubes are surrounded by polymer fibers (barrel)  
<sup>748</sup> and foils (end-caps), which facilitate transition radiation at the interface between materials.

### <sup>749</sup> 3.1.2 The Calorimeter system

<sup>750</sup> The second group of detector subsystems, the calorimeters, is dedicated to the measure-  
<sup>751</sup> ment of particle energies and directions. There exist two types of calorimeters: electromag-  
<sup>752</sup> netic and hadronic. They detect particle through alternating layers of passive and active  
<sup>753</sup> materials. In the passive layers, also called the absorber, an energetic particle deposits a  
<sup>754</sup> large portion of its kinetic energy and induces a large number of secondary particles, includ-  
<sup>755</sup> ing electrons, photons, and hadrons, depending on the type of calorimeter. These particles  
<sup>756</sup> are then stopped and measured by the active layers.

<sup>757</sup> The electromagnetic calorimeter targets electrons/positrons and photons, which create  
<sup>758</sup> electromagnetic showers as they interact with the inactive material. In the electric field near  
<sup>759</sup> the atomic nuclei that make up the material, electrons and positron undergo Bremsstrahlung  
<sup>760</sup> and emit secondary photons, which induces electron pair production and generates more  
<sup>761</sup> high-energy charged particles. A reaction chain in which Bremsstrahlung photons induce  
<sup>762</sup> electrons/positrons, which emits more Bremsstrahlung photons, creates a shower of charged  
<sup>763</sup> particles in the passive material.

<sup>764</sup> In the case of the hadronic calorimeters, a hadron interacts with the atomic nuclei of a  
<sup>765</sup> dense material through which it passes and produces secondary hadrons, mostly pions, which  
<sup>766</sup> then drive the reaction chain, similar to the electromagnetic counterpart. In addition, neutral  
<sup>767</sup> pion decays to high-energy photon and leptonic decays can also induce electromagnetic sub-  
<sup>768</sup> shower within a hadronic shower.

### 3.1.2.1 The electromagnetic (EM) calorimeter

The passive absorber material in the ATLAS electromagnetic calorimeter comprises of lead, and the active material of liquid argon. The passive layers are interspersed with active layers in an accordion pattern. The barrel covers a pseudorapidity range up to  $|\eta| = 1.475$  and the endcaps  $1.375 < |\eta| < 3.2$ . The central region of the EM calorimeter consists of three layers and a pre-sampler with a fine granularity ( $\eta \times \phi = 0.025 \times 0.1$ ). The first sampling layer features a segmentation of  $\eta \times \phi = 0.025/8 \times 0.1$ , while the second and third sampling layers are segmented into  $\eta \times \phi = 0.025 \times 0.025$  and  $\eta \times \phi = 0.025 \times 0.05$ , respectively. Angular segmentation allows measurements of particle directions, and depth segmentation measurements of shape. This information is useful in discriminating electrons and photons from jets. Figure 3.4b shows a sketch of the EM calorimeter module in the barrel.

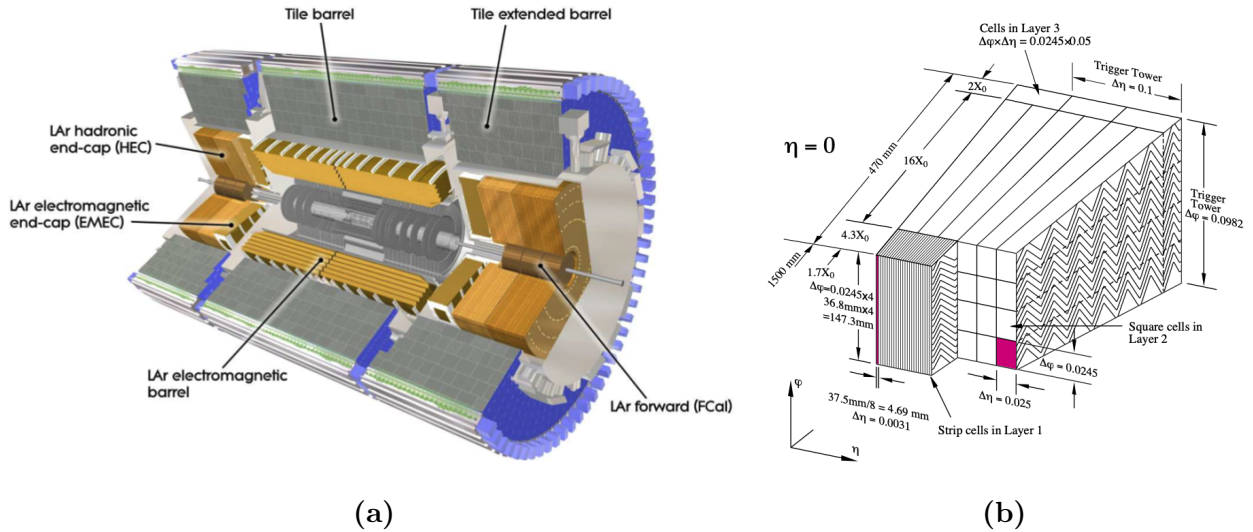


**Figure 3.4:** (a) Layout of the ATLAS calorimetry system, and (b) sketch of a barrel module of the electromagnetic calorimeter [93].

<sup>780</sup> **3.1.2.2 The hadronic calorimeter**

<sup>781</sup> The hadronic calorimeter uses iron absorbers and plastic scintillating tiles as active ma-  
<sup>782</sup> terial in the barrel region. It covers a pseudorapidity range of  $|\eta| < 1.0$  in the barrel and  
<sup>783</sup>  $0.7 < |\eta| < 1.7$  in the extended barrel. It also comprises of three layers of increasing radii.  
<sup>784</sup> The effective granularity varies between  $\eta \times \phi = 0.1 \times 0.1$  and  $0.2 \times 0.1$ .

<sup>785</sup> The endcap and forward regions (figure 3.4a) of the hadronic calorimeter uses cop-  
<sup>786</sup> per/tungsten as absorber and liquid argon as the active material. They cover a pseudo-  
<sup>787</sup> rapidity range of up to 4.9. The forward calorimeter is split into an electromagnetic and a  
<sup>788</sup> hadronic component.

<sup>789</sup> **3.1.3 The muon spectrometer**

<sup>790</sup> Unlike other particles, muons produced with energy in the range of 0.1–100 GeV typically  
<sup>791</sup> seen in ATLAS do not strongly interact with detector material in the detector subsystems  
<sup>792</sup> described in the previous sections. Despite leaving energy clusters in the ID, they traverse  
<sup>793</sup> the calorimeters intact are therefore measured by a dedicated muon system. The muon  
<sup>794</sup> spectrometer is composed of four subsystems that use different technologies to track muon  
<sup>795</sup> at high precision and perform fast triggers. It is immersed in a toroidal magnetic field  
<sup>796</sup> ranging from 2.0 to 6.0 T, providing enough bending power to resolve the muon transverse  
<sup>797</sup> momentum. Figure 3.5 shows the overall layout of and a side view of a quadrant of the MS,  
<sup>798</sup> including its subsystems.

<sup>799</sup> To measure the curvature of muon tracks along the bending direction of the toroidal  
<sup>800</sup> field, the MS uses a number of aluminum tubes 30 millimeters in diameter filled with Ar and  
<sup>801</sup> having a central tungsten/rhenium alloy wire, similar to the TRT. The outer surface and the  
<sup>802</sup> central wire of these Monitored Drift Tubes (MDTs) are kept at a potential difference of 3  
<sup>803</sup> kV to ensure a drifting time of less than 700 ns. The MDTs are divided into 1200 chambers

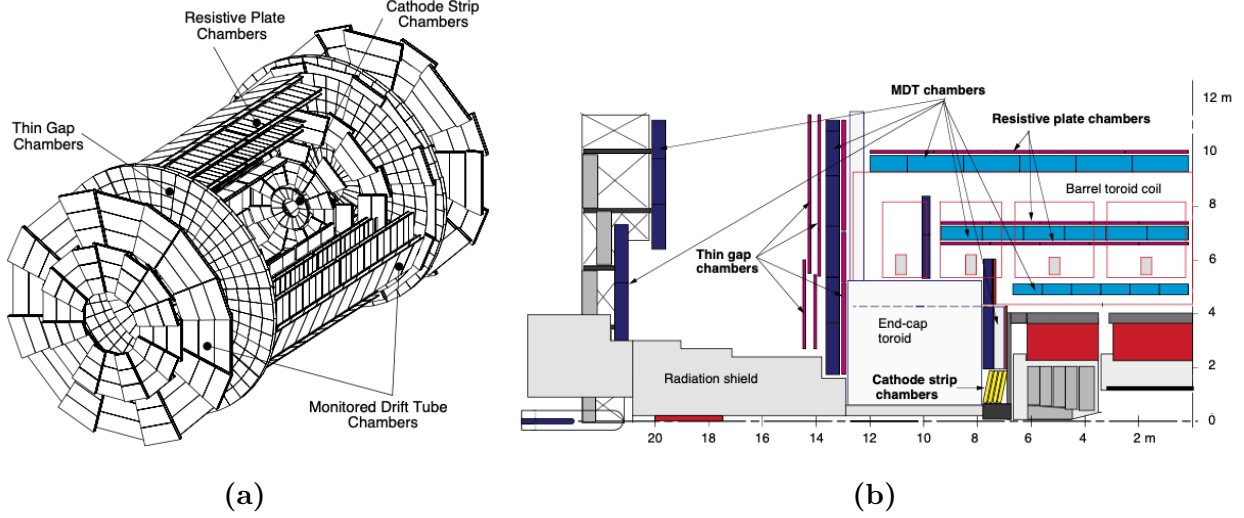


**Figure 3.5:** (a) Layout of the ATLAS Muon Spectrometer system, and (b) a sideview of one quadrant of the MS [20].

804 cover a pseudorapidity range up to  $|\eta| = 2.7$ , each chamber providing 6 to 8 measurements  
 805 along the track.

806 At larger  $|\eta|$ , the Cathode Strip Chambers (CSCs) have a higher granularity than the  
 807 MDTs to resolve large backgrounds in the forward region. They cover  $2.0 < |\eta| < 2.7$  and  
 808 have short drift times of around 40 ns. The CSCs provide 4 simultaneous measurements of  
 809  $\eta$  and  $\phi$ .

810 The Resistive Plate Chambers (RPCs), used in the barrel and the Thin Gap Chambers  
 811 (TGCs), used in the endcap regions are both gaseous detectors and together make up the  
 812 muon trigger system. They respectively cover  $|\eta| < 1.05$  and  $1.05 < |\eta| < 2.4$ .

813 **Chapter 4**

814 **Combination of dark matter searches interpreted in 2HDM+ $a$**

815 This chapter presents the combined searches for dark matter particles in the context of  
816 a Two-Higgs-Doublet Model (2HDM) extended by a pseudoscalar mediator  $a$  using proton-  
817 proton collision data collected at the ATLAS detector during LHC Run 2. We start with a  
818 discussion of the signal model as an extension of the Standard Model Higgs sector detailed  
819 in section 2.2, and introduce the fermionic dark matter particle  $\chi$  connected to the visible  
820 sector via  $a$ . In all analyses, no significant deviations from SM predictions are observed, and  
821 the data is used to derive exclusion limits on the signal model as functions of its parameters  
822 A statistical combination of the most sensitive channels carries out the limit setting over six  
823 benchmark scenarios given in section 4.2. An overview of the experimental signatures tar-  
824 geted by these searches, a description of systematic uncertainty, and the statistical method  
825 are provided in sections 4.4, 4.5 and 4.6, respectively. Finally, the results are presented  
826 in section 4.7. This analysis, in which the author is a contributor, has been published in  
827 reference [90].

828 **4.1 Theoretical considerations**

829 The benchmark model used to interpret the data extends the Standard Model with a  
830 second complex Higgs doublet, already postulated in several UV-complete BSM theories [75,  
831 2]. After electroweak symmetry breaking, the model contains 5 Higgs bosons: a light CP-  
832 even boson  $h$ , a heavier CP-even boson  $H$ , a CP-odd boson  $A$  and a two charged bosons

<sup>833</sup>  $H^\pm$ . The 2HDM allows some freedom in the choice of Higgs-fermion coupling structure, for  
<sup>834</sup> example, 2HDM type-I which couples only one Higgs doublet to fermions, and 2HDM type-  
<sup>835</sup> II, which couples the neutral member of one Higgs doublet to only up-type quarks and the  
<sup>836</sup> neutral member of the other to down-type quarks. This search assumes the type-II structure,  
<sup>837</sup> along with the alignment and decoupling limits, so that the lighter CP-even states  $h$  can be  
<sup>838</sup> identified with the SM Higgs boson [113]. The Lagrangian of the 2HDM can be written as

$$\mathcal{L}_{2HDM} = (D_\mu \Phi_1)^\dagger (D^\mu \Phi_1) + (D_\mu \Phi_2)^\dagger (D^\mu \Phi_2) - V(\Phi_1, \Phi_2) \quad (4.1)$$

where the covariant derivative  $D_\mu$  is given by

$$D_\mu = \partial_\mu - ig \frac{\tau^i}{2} W_\mu^i - i \frac{g'}{2} Y B_\mu,$$

<sup>839</sup> in which  $\tau^i$  are Pauli matrices and  $Y$  is the hypercharge. The potential is

$$\begin{aligned} V(\Phi_1, \Phi_2) &= m_{11}^2 \Phi_1^\dagger \Phi_1 + m_{22}^2 \Phi_2^\dagger \Phi_2 - (m_{12}^2 \Phi_1^\dagger \Phi_2 + h.c.) \\ &\quad + \frac{\lambda_1}{2} (\Phi_1^\dagger \Phi_1)^2 + \frac{\lambda_2}{2} (\Phi_2^\dagger \Phi_2)^2 + \lambda_3 (\Phi_1^\dagger \Phi_1)(\Phi_2^\dagger \Phi_2) + \lambda_4 (\Phi_1^\dagger \Phi_2)(\Phi_2^\dagger \Phi_1) \\ &\quad + \left\{ \frac{\lambda_5}{2} (\Phi_1^\dagger \Phi_2)^2 + [\lambda_6 (\Phi_1^\dagger \Phi_1) + \lambda_7 (\Phi_2^\dagger \Phi_2)] (\Phi_1^\dagger \Phi_2) + h.c. \right\} \end{aligned} \quad (4.2)$$

<sup>840</sup> The scalar field vacuum expectation values occur at

$$\langle \Phi_i \rangle = \frac{1}{\sqrt{2}} \begin{pmatrix} 0 \\ v_i \end{pmatrix}, \quad v_i \in \mathbb{R}, \quad (4.3)$$

<sup>841</sup> with the following conditions

$$\begin{aligned} m_{11}^2 &= m_{12}^2 t_\beta - \frac{1}{2} v^2 (\lambda_1 c_\beta^2 + \lambda_{345} s_\beta^2 + 3 \lambda_6 s_\beta c_\beta + \lambda_7 s_\beta^2 t_\beta) \\ m_{22}^2 &= m_{12}^2 (t_\beta)^{-1} - \frac{1}{2} v^2 (\lambda_2 s_\beta^2 + \lambda_{345} c_\beta^2 + \lambda_6 c_\beta^2 (t_\beta)^{-1} + 3 \lambda_7 s_\beta c_\beta), \end{aligned} \quad (4.4)$$

where

$$t_\beta = \frac{v_2}{v_1}, \quad \lambda_{345} = \lambda_3 + \lambda_4 + \lambda_5, \quad v = \sqrt{v_1^2 + v_2^2} = 246 \text{ GeV}$$

<sup>842</sup> After spontaneous symmetry breaking, three of the original eight scalar degrees of freedom  
<sup>843</sup> are absorbed by the  $W^\pm$  and the  $Z$  bosons, leaving five physical Higgs bosons as described

<sup>844</sup> above. The physical masses of the CP-odd and charged Higgs states are given by

$$\begin{aligned} m_A^2 &= \frac{m_{12}^2}{s_\beta c_\beta} - \frac{v^2}{2} \left( 2\lambda_5 + \frac{\lambda_6}{t_\beta} + \lambda_7 t_\beta \right) \\ m_{H^\pm}^2 &= m_A^2 + \frac{v^2}{2} (\lambda_5 - \lambda_5) \end{aligned} \quad (4.5)$$

<sup>845</sup> The two CP-even Higgs states mix according to the squared-mass matrix

$$\mathbf{M}^2 = m_A^2 \begin{pmatrix} s_\beta^2 & -s_\beta c_\beta \\ -s_\beta c_\beta & c_\beta^2 \end{pmatrix} + \mathbf{B}^2 \quad (4.6)$$

where

$$\mathbf{B}^2 = v^2 \begin{pmatrix} \lambda_1 c_\beta^2 + 2\lambda_6 s_\beta c_\beta + \lambda_5 s_\beta^2 & (\lambda_3 + \lambda_4) s_\beta c_\beta + \lambda_6 c_\beta^2 + \lambda_7 s_\beta^2 \\ (\lambda_3 + \lambda_4) s_\beta c_\beta + \lambda_6 c_\beta^2 + \lambda_7 s_\beta^2 & \lambda_2 s_\beta^2 + 2\lambda_7 s_\beta c_\beta + \lambda_5 c_\beta^2 \end{pmatrix}.$$

<sup>846</sup> Diagonalizing  $\mathbf{M}^2$  furnishes the physical CP-even Higgs states, whose squared-masses are

<sup>847</sup> the eigenvalues

$$m_{H,h}^2 = \frac{1}{2} \left[ \mathbf{M}_{11}^2 + \mathbf{M}_{22}^2 \pm \sqrt{(\mathbf{M}_{11}^2 - \mathbf{M}_{22}^2)^2 + 4\mathbf{M}_{12}^2} \right], \quad (4.7)$$

<sup>848</sup> and the mixing angle

$$s_{2\alpha} = \frac{2\mathbf{M}_{12}^2}{\sqrt{(\mathbf{M}_{11}^2 - \mathbf{M}_{22}^2)^2 + 4\mathbf{M}_{12}^2}}, \quad c_{2\alpha} = \frac{(\mathbf{M}_{11}^2 - \mathbf{M}_{22}^2)^2}{\sqrt{(\mathbf{M}_{11}^2 - \mathbf{M}_{22}^2)^2 + 4\mathbf{M}_{12}^2}}. \quad (4.8)$$

<sup>849</sup> The 2HDM, though being a BSM model, does not natively contain a dark sector. Therefore,  
<sup>850</sup> a fermionic dark matter particle  $\chi$  is included, and connected to the Higgs sector by a pseudo-  
<sup>851</sup> scalar CP-odd mediator  $a$ , with Yukawa-like couplings to both SM and DM fermions. The  
<sup>852</sup> mediator mixes with the pseudo-scalar  $A$  of the 2HDM with a mixing angle  $\theta$ .

<sup>853</sup> With the inclusion of the fermionic dark matter and the pseudo-scalar mediator, the  
<sup>854</sup> phenomenology of the model is fully determined by 14 independent parameters:

- <sup>855</sup> 1. the mass of Higgs bosons  $m_h$ ,  $m_H$ ,  $m_A$ ,  $m_{H^\pm}$ ,
- <sup>856</sup> 2. the mass of the pseudo-scalar mediator  $m_a$ ,

- 857        3. the mass of the dark matter particle  $m_\chi$  ,
- 858        4. the Yukawa coupling  $g_\chi$  between  $a$  and  $\chi$ ,
- 859        5. the electroweak VEV  $v$ ,
- 860        6. the ratio of the VEVs of the two Higgs doublets  $\tan \beta$  ,
- 861        7. the mixing angle  $\alpha$  of the CP-even Higgs states  $h$  and  $H$ ,
- 862        8. the mixing angle  $\theta$  of the CP-odd states  $A$  and  $a$ ,
- 863        9. the quartic coupling  $\lambda_3$  of the pure 2HDM potential,
- 864        10. the quartic couplings of the potential terms between the doublet and singlet fields  $\lambda_{P1}$ ,
- 865                  and  $\lambda_{P2}$

866        Some of these parameters are constrained by electroweak and flavour measurements, as well  
 867        as phenomenological considerations [68, 1]. Some parameters are chosen to simplify the  
 868        model and reduce the space of independent parameters. Reference [1] contains detailed  
 869        descriptions of the 2HDM+ $a$  benchmark scenarios recommended by the LHC Dark Matter  
 870        working group.

871        This analysis scans over a total of 5 parameters, including  $m_A$  ,  $m_a$  ,  $\tan \beta$  ,  $\sin \theta$  , and  
 872         $m_\chi$  . Other parameters are set to constant in all benchmark scenarios. The coupling  $g_\chi$  is  
 873        set to 1, having negligible effect on the shape of the kinematic distribution of interest. The  
 874        alignment and decoupling limits are assumed, effectively assigning  $m_h = 125$  Gev,  $v = 246$   
 875        GeV, and  $\cos(\beta - \alpha) = 0$ . The quartic coupling  $\lambda_3$  is set to 3 to guarantee the stability of  
 876        the Higgs potential for the chosen range of the heavy Higgs bosons. In addition, they are  
 877        fixed to the same value, i.e.  $m_A = m_H = m_{H^\pm}$ . The heavy CP-even Higgs  $H$  is chosen to  
 878        have the same mass as the charged Higgs to avoid the constraints from electroweak precision  
 879        measurements, and the same mass as the CP-odd Higgs to reduce the number of independent

parameters [68]. The other quartic couplings are also fixed at 3 to maximize the trilinear couplings between the CP-odd and the CP-even neutral sates.

The phenomenology of the 2HDM+ $a$  is particularly rich, and this analysis combines a large number of signatures as illustrated in table 4.3. These signatures can be broadly categorized into those involving invisible and visible mediator decays, the former being represented by  $E_T^{\text{miss}} + X$ . An overview of the signatures considered are given in section 4.4, and further details can be found in the referenced publications. The dominant production mode for the majority of signatures is  $gg$ -initiated production. Figures 4.1a, 4.1b respectively summarize  $gg$ -initiated resonant and non-resonant production mechanisms of the  $E_T^{\text{miss}} + Z(\ell\ell)$  final state. Similarly, the  $E_T^{\text{miss}} + h(b\bar{b})$  signature, as well as other  $E_T^{\text{miss}} + h$  signatures, can be produced both resonantly and non-resonantly via  $gg$  fusion, as seen on figures 4.2a and 4.2b. In addition,  $gg$ -initiated production of the  $E_T^{\text{miss}} + j$  signature is shown in figures 4.4a, and  $t\bar{t}$ - or  $b\bar{b}$ -associated resonant  $A/H$  production leading to  $t\bar{t}t\bar{t}$ ,  $b\bar{b}b\bar{b}$ ,  $t\bar{t}b\bar{b}$ ,  $E_T^{\text{miss}} + t\bar{t}$ , or  $E_T^{\text{miss}} + b\bar{b}$  signatures in Figure 4.6. Figure 4.5 shows the production of a charged Higgs associated with and decaying into a pair of  $tb$  quarks, designated  $tbH^\pm(tb)$ , and figure 4.7 shows loop-induced Higgs production of a SM Higgs boson decaying into a pair of mediators  $aa$  resulting in 2 pairs of fermionic DM or SM particles.

The second largest production mode is  $bb$ -initiated production, whose primary signatures include  $E_T^{\text{miss}} + Z(\ell\ell)$ ,  $E_T^{\text{miss}} + h(b\bar{b})$ , and  $E_T^{\text{miss}} + j$ . Representative Feynman diagrams are respectively shown in in figures 4.1c, 4.2d, 4.4b. Finally, the leading diagram for the  $E_T^{\text{miss}} + tW$  signature is shown in figure 4.3. The interplay between these signatures depends on the 2HDM+ $a$  model parameters.

## 4.2 Benchmark scenarios

The parameter space is examine through a total of 6 representative benchmark scenarios, in which one or two parameters are varied while the others are fixed. Table 1 summarizes

905 these scenarios, demarcated to demonstrate the rich phenomenology of the 2HDM+ $a$  and to  
 906 examine the interplay between the signatures described in the previous section.

### 907 4.2.1 Scenario 1: Exploration of two $m_a$ – $m_A$ planes

908 This scenario evaluates constraints on 2HDM+ $a$  as a function of the pseudo-scalar masses  
 909  $m_a$  and  $m_A$ , highlighting the complex dependence of the model phenomenology on the  
 910 pseudo-scalar mass hierarchy, which governs the production and decay modes that are kine-  
 911 matically accessible and favoured. In this scan,  $\tan \beta$  is fixed to 1.0 which favours couplings  
 912 to up-type quarks, particularly the top quark, while the  $a/A$  mixing angle is fixed to two  
 913 values  $\sin \theta = 0.35$  and  $\sin \theta = 0.7$ , and thus two parameter planes are explored. These  
 914 angles respectively correspond to low and almost maximal mixing between the CP-odd Higgs  
 915 and the pseudo-scalar mediator connected to the dark sector.

### 916 4.2.2 Scenario 2: Exploration of two $m_A$ – $\tan \beta$ planes

917 This scenario evaluates the constraints while simultaneously varying  $m_A$  and  $\tan \beta$  for  
 918 the same choices of mixing angle  $\sin \theta$  in 4.2.1. The pseudo-scalar mass  $m_a$  is fixed to  
 919 250 GeV to kinematically prevent on-shell decays of the mediator into a pair of top quarks  
 920 and enlarge the branching ratio of the decay into the fermionic DM particle  $a \rightarrow \chi\chi$  up  
 921 to 100%. This benchmark scenario highlights the dependence of the couplings of the CP-  
 922 odd Higgs  $A$  on the value of  $\tan \beta$  as a function of its mass. In particular, low values of  
 923  $\tan \beta$  correspond to stronger coupling to up-type quarks, while higher values of  $\tan \beta$  favour  
 924 couplings to down-type quarks and charged leptons. In addition, it examines the interplay  
 925 between  $gg$ -initiated, top-loop induced and  $b\bar{b}$ -initiated production modes.

### 926 4.2.3 Scenario 3: Exploration of two $m_a - \tan \beta$ planes

927 Similar to 4.2.2, constraints on 2HDM+ $a$  are evaluated as a function of the pseudo-  
 928 scalar mass  $m_a$  and Higgs doublet VEV ratio  $\tan \beta$ . The CP-odd Higgs mass is fixed at  
 929  $m_A = 600$  GeV, allowing for the decays  $A \rightarrow t\bar{t}$  and favouring it at low  $\tan \beta$ . The value of  
 930  $m_A$  is motivated by constraints on the mass of the charged Higgs  $m_{H^\pm} = m_A$  derived from  
 931 precision measurements of  $B$ -meson decays [134, 68]. Two parameter planes corresponding  
 932 to  $\sin \theta = 0.35$  and  $\sin \theta = 0.7$  are examined, similar to the previous scenarios.

### 933 4.2.4 Scenario 4: Variation of the pseudo-scalar mixing angle $\sin \theta$

934 This benchmark scenario highlights the interplay between the  $E_T^{\text{miss}} + Z$  and  $E_T^{\text{miss}} + h$   
 935 signatures arising from invisible mediator decays, and signatures that probe visible mediator  
 936 decays. The couplings  $g_{Aha}$ ,  $g_{HZa}$  which affect  $E_T^{\text{miss}} + h$  and  $E_T^{\text{miss}} + Z$  production scale with  
 937  $\sin \theta \cos \theta$  and  $\sin \theta$  respectively, and the coupling  $g_{at\bar{t}}$  which plays a dominant role in the  
 938 leading  $E_T^{\text{miss}} + X$  production modes, scales with  $\sin \theta$ . As  $\sin \theta \rightarrow 0$ , the sensitivity of the  
 939  $E_T^{\text{miss}} + X$  signatures vanishes.

### 940 4.2.5 Scenario 5: Variation of the Dark Matter mass $m_\chi$

941 The value of  $m_\chi$  has a strong effect on parameters in cosmological dark matter models,  
 942 such as the relic density, and on the sensitivity of direct and indirect detections of DM.  
 943 This benchmark scenario provides a basis to compare the sensitivity of collider searches to  
 944 those of non-collider experiments and cosmological observations in the context of 2HDM+ $a$ .  
 945 Constraints are evaluated by varying  $m_\chi$  and fixing other free parameters to  $\sin \theta = 0.35$ ,  
 946  $m_A = 600$  GeV,  $m_a = 400$  GeV, and  $\tan \beta = 1.0$ . A similar benchmark scenario was  
 947 examined in reference [1] under a different set of pseudo-scalar mass parameters, which is

948 fully excluded by a previous ATLAS publication [23]., The current choices of  $m_a$  and  $m_A$   
949 represent an unexplored region in the parameter space.

950 **4.2.6 Scenario 6: Variation of the  $m_a - m_\chi$**

951 This scenario illustrates the interplay between searches for invisible and exotic decays of  
952 the Higgs boson  $h$  in the context of 2HDM+ $a$ . Other free parameters are set to  $\sin \theta = 0.35$   
953 and  $\tan \beta = 1.0$  for consistency with other benchmark scans, and  $m_A = 1200$  to satisfy  
954 the constraint on the coupling  $g_{haa}$  from measurements of the total Higgs boson decay width  
955 [12]. This is a strong constraint for  $m_a < m_h/2$ , satisfied only by a relatively narrow range  
956 of  $m_A$  in the chosen subspace of other free parameters.

957 In all benchmark scenarios, unless varied, the DM mass is fixed at  $m_\chi = 10$  GeV to  
958 ensure a significant branching ratio for its decay from the pseudo-scalar  $a$  for  $m_a > 100$   
959 GeV. As long as  $m_\chi < m_a/2$ , the value of  $m_\chi$  has little impact on the sensitivity of the  
960 searches considered in this analysis. Consequently, it is possible to match the observed relic  
961 density across a range of model parameter space through an appropriate choice of  $m_\chi$   
962 without much effect on the experimental signatures.

963 Various theoretical constraints are considered in selecting the ranges of the parameters  
964 that are varied in these benchmark scenarios. First, in some regions of the parameter space, the  
965 scalar potential is not bounded from below at large  $m_A$ , occurring, for example, in scenario  
966 1a for  $(m_A \gtrsim 1250, m_a = 100)$  GeV and  $(m_A \gtrsim 1550, m_a = 1000)$  GeV. However, these  
967 constraints could be substantially relaxed if the quartic couplings take values closer to the  
968 perturbative limit or in more general 2HDM models [1, 68, 116]. Therefore, they should not  
969 be understood as a strong limit on the validity of the model predictions that were used to  
970 derive the exclusion contours. Second, given the parameter choices, the  $aah$  coupling exceeds  
971 the unitary limit of  $4\pi$  for large  $m_A$ , for instance, in scenario 1a, for  $(m_A \gtrsim 1250, m_a = 100)$   
972 GeV and  $(m_A \gtrsim 1550, m_a = 1000)$  GeV. In this region, the width of the additional heavy

973 Higgs bosons grows substantially and the theoretical predictions are subject to additional  
 974 uncertainties from the treatment of the width. Therefore, regions where the relative width  
 975  $\Gamma/m$  of at least one heavy Higgs boson or of the pseudo-scalar mediator  $a$  exceeds 20% are  
 976 marked as shaded areas in the summary plots in Section 4.2.6. This conservative approach  
 977 to large widths follows reference [23].

978 Table 4.1 summarizes the benchmark scenarios examined in this analysis. Scenarios 1a,  
 979 3a, 4a, 4b, and 5 are recommended by the LHC Dark Matter Working Group and appeared  
 980 in previous ATLAS analyses [23]. This work considers in addition scenarios 1b, 2, 3b, and  
 981 6, which are motivated by the studies in references [1, 139, 12]. In particular, the choice  
 982 of  $\sin \theta = 0.7$  or  $\theta \approx \pi/4$  corresponds to maximal mixing in the pseudo-scalar sector and  
 983 is relevant for the  $E_T^{\text{miss}} + tW$  search, which was designed specifically for 2HDM+ $a$  signal  
 984 processes [139]. Scenario 6 is included for the first time in this work to showcase the rich  
 985 phenomenology of the model.

986 This work also covers more production modes of the Higgs bosons and the pseudo-scalar  
 987 mediator. In the previous summary of dark matter searches by ATLAS [23], only  $gg$ -initiated  
 988 production was considered for the  $E_T^{\text{miss}} + Z$  signatures, and for the  $E_T^{\text{miss}} + h$  signatures,  
 989  $b\bar{b}$ -initiated production was considered only for  $\tan \beta > 10$ . In contrast, all  $E_T^{\text{miss}}$  signatures  
 990 take into account  $b\bar{b}$ -initiated production, which is relevant for the  $E_T^{\text{miss}} + Z$  and  $E_T^{\text{miss}} + h$   
 991 signatures not only at large  $\tan \beta$ , where it is more important, but also at more intermediate  
 992 values[90].

### 993 4.3 Data and simulated event samples

994 Proton–proton collision data collected with the ATLAS detector during the period 2015–  
 995 2018 at center-of-mass energy  $\sqrt{s} = 13$  TeV are used in the majority of analyses considered  
 996 in this summary. The data sample is equivalent to an integrated luminosity of  $139 \text{ fb}^{-1}$  after  
 997 ensuring good operational conditions of all detector sub-systems and high-quality data [14].

Scenario		Fixed parameter values			Varied parameters	
		$\sin \theta$	$m_A$ [GeV]	$m_a$ [GeV]	$m_\chi$ [GeV]	$\tan \beta$
1	a	0.35	—	—	10	1.0
	b	0.70	—	—	10	1.0
2	a	0.35	—	250	10	—
	b	0.70	—	250	10	—
3	a	0.35	600	—	10	—
	b	0.70	600	—	10	—
4	a	—	600	200	10	1.0
	b	—	1000	350	10	1.0
5		0.35	1000	400	—	1.0
6		0.35	1200	—	—	1.0
						$(m_a, m_\chi)$

**Table 4.1:** Summary of the parameter settings for the different 2HDM+ $a$  benchmark scenarios explored in this summary.

Monte Carlo simulation is used to model relevant background processes and predictions of the 2HDM+ $a$ . Details on MC generation of various background processes considered in this analysis can be found in the individual studies referenced in Section 4.4. The 2HDM+ $a$  benchmark is implemented in the Universal FeynRules Output (UFO) format [100] and is referred to as `Pseudoscalar_2HDM` throughout this discussion.

With the exception of the  $t b H^\pm(t b)$  process (Table 4.2), all signal processes are generated at leading order (LO) in the strong coupling constant. In this context, LO corresponds to loop-induced gluon-gluon fusion for the  $E_T^{\text{miss}} + X$  signatures, demonstrated for instance in figures 4.1a and 4.1b [90].

Event generation is performed using this UFO implementation with the `MADGRAPH5_AMC@NLO` [9] MC generator, which is interfaced with `PYTHIA 8`[157] to simulate the parton shower and

Analysis	Generator and Parton Shower	Cross-section	Further details
$E_T^{\text{miss}} + Z(\ell\ell)$	MADGRAPH5_AMC@NLO 2.4.3 (LO) + PYTHIA	LO 8.212	
$E_T^{\text{miss}} + h(b\bar{b})$	MADGRAPH5_AMC@NLO 2.6.0 (LO) + PYTHIA	LO 8.212	
$E_T^{\text{miss}} + h(\gamma\gamma)$	MADGRAPH5_AMC@NLO 2.7.3 (LO) + PYTHIA	LO 8.244	
$E_T^{\text{miss}} + h(\tau\tau)$	MADGRAPH5_AMC@NLO 2.7.3 (LO) + PYTHIA	LO 8.244	
$E_T^{\text{miss}} + j$	MADGRAPH5_AMC@NLO 2.7.3 (LO) + PYTHIA	LO 8.244	Section 4.4.6
$E_T^{\text{miss}} + tW$	MADGRAPH5_AMC@NLO 2.7.3 (LO) + PYTHIA	LO 8.244	
$t\bar{t}t\bar{t}$	MADGRAPH5_AMC@NLO 2.9.5 (LO) + PYTHIA	LO 8.245	Reference [68]
$tbH^\pm(tb)$	MADGRAPH5_AMC@NLO 2.2.2 (NLO) + PYTHIA 8.212	NLO, 4FS	Section 4.4.9

**Table 4.2:** Details of the MADGRAPH5\_AMC@NLO generation set-up used for the 2HDM+ $a$  signal samples, for the signatures considered in this publication. The `Pseudoscalar_2HDM` UFO model is used for all simulated samples except those for the  $tbH^\pm(tb)$  search, which relies on the UFO of reference [99]. The  $h \rightarrow$  invisible and  $h \rightarrow aa \rightarrow f\bar{f}f'\bar{f}'$  signatures are not listed here as no signal samples are required for the re-interpretation, which in those cases relies on the branching ratio limits [90].

hadronization. The parameter settings follow the ATLAS tune A14 [21]. Depending on the specific analysis, different versions of MADGRAPH5\_AMC@NLO (ranging from 2.6.0 to 2.9.5) and PYTHIA (from 8.212 to 8.245) were used, as summarized in Table 4.2. These version differences are not expected to impact the signal simulations. The NNPDF3.0NLO [158] parton distribution function (PDF) set, based on next-to-leading-order calculations in the five-flavor scheme, was used, assuming a massless  $b$ -quark and  $\alpha_s(m_Z) = 0.118$  [158].

1015 To maintain consistency, the five-flavor scheme with  $m_b = 0$  GeV was adopted for the  
 1016 matrix element (ME) computation in `MADGRAPH5_AMC@NLO` for  $b\bar{b}$ -initiated produc-  
 1017 tion. In contrast, the four-flavor scheme was used for  $gg$ -initiated production to incorporate  
 1018 top and bottom quark contributions in the production loop. These modelling choices align  
 1019 with the recommendations of the LHC Dark Matter Working Group [1].

1020 To account for pile-up effects, a number of interactions appropriate to the expected pile-  
 1021 up level of the data taking period were simulated using soft QCD processes in `PYTHIA 8.186`  
 1022 with the A3 tune[60] and the MSTW2008LO PDF [132]. These interactions were overlaid  
 1023 onto each simulated hard-scattering event. The generated samples were reweighted to match  
 1024 the instantaneous luminosity distribution observed in data. The simulations also incorporate  
 1025 the expected bunch train structure and include corrections to address related effects.

1026 Simulated events were processed using either a full detector simulation based on `GEANT4` [6,  
 1027 61] or a fast simulation[63] that parametrizes the calorimeter response while relying on  
 1028 `GEANT4` for the rest of the detector. Physics objects in all simulated data samples were  
 1029 reconstructed from detector response following identical procedures as those applied on real  
 1030 data. Additionally, corrections derived from data control samples were applied to the sim-  
 1031 ulations to account for differences between simulation and data in reconstruction efficiency,  
 1032 energy/momentum scale, and resolution of reconstructed electrons and muons. Analogous  
 1033 corrections were also made to account for differences in efficiency and false positive rate in  
 1034 the identification of jets containing  $b$ -hadrons. The energy scale and resolution of hadronic  
 1035 jets were adjusted to ensure consistency between data and simulation.

1036 To efficiently generate signal events across the extensive multi-dimensional parameter  
 1037 space of the 2HDM+ $a$ , the `MADGRAPH` reweighting module [133] was used to obtain pre-  
 1038 dictions for various signal model parameters from a minimal set of generated events by  
 1039 assigning new event weights based on the ratio of matrix elements of the generated and tar-  
 1040 get parameter points. These weights were computed dynamically during event simulation.

1041 The validity of this approach was confirmed by comparing weighted distributions with di-  
1042 rectly generated ones for select sample cases. This reweighting method significantly reduces  
1043 computational costs, as detector simulation only needs to be performed once.

1044 **4.4 Experimental signatures**

1045 A total of 13 searches in different final states targeting invisible or visible mediator  
1046 decays are included in this summary. No significant deviation from the SM predictions was  
1047 observed in all searches, and instead they are used to derive constraints on the 2HDM+ $a$  for  
1048 the benchmark scenarios introduced in section 4.2. Because the sensitivity of these searches  
1049 varies across different regions of the 2HDM+ $a$  parameter space, most of them are interpreted  
1050 in a subset of the current benchmark scenarios. Table 4.3 summarizes the scenarios in which  
1051 each search is interpreted, and some details are provided in this section. The searches using  
1052  $E_T^{\text{miss}} + h(b\bar{b})$ ,  $E_T^{\text{miss}} + Z(\ell\ell)$  and  $t b H^\pm(t b)$  signatures enter a statistical combination described  
1053 in section 4.6; limit contours from other relevant searches are overlaid on summary plots.

1054 Each analysis targets a different signature and therefore relies on a different set of key  
1055 physics objects identified by various subsystems of ATLAS. Jets are reconstructed from  
1056 particle-flow objects using the anti- $k_t$  algorithm [79, 78, 31]. The radius parameters are  $R =$   
1057 0.4 for small- $R$  jets and  $R = 1.0$  for large- $R$  jets [30]. Small- $R$  jets with  $|\eta| < 2.5$  containing  
1058  $b$ -hadrons are identified with multivariate algorithms [15, 13]. Photons and electrons are  
1059 reconstructed from topologically connected clusters of energy deposits in the electromagnetic  
1060 (EM) calorimeters, with electron showers additionally matched to a charged-particle track  
1061 in the Inner Detector (ID) [26, 27]. Muons are reconstructed by matching tracks in the ID  
1062 and the muon spectrometer (MS), and refining through a global fit using hits from both sub-  
1063 detectors[36]. Different lepton and photon selection criteria, and kinematic requirements are  
1064 employed for particle identification and isolation in the analyses.  $\tau$ -lepton reconstruction  
1065 relies on leptonic or hadronic  $\tau$ -lepton decay targeted by each analysis depending on the

Analysis/Scenario	1a	1b	2a	2b	3a	3b	4a	4b	5	6
$E_T^{\text{miss}} + Z(\ell\ell)$ [42]	x	x	x	x	x	x	x	x	x	x
$E_T^{\text{miss}} + h(b\bar{b})$ [49]	x	x	x	x	x	x	x	x	x	x
$E_T^{\text{miss}} + h(\gamma\gamma)$ [45]	x	x			x	x	x	x		
$E_T^{\text{miss}} + h(\tau\tau)$ [46]	x				x					
$E_T^{\text{miss}} + tW$ [47]	x	x	x	x	x	x	x	x		
$E_T^{\text{miss}} + j$ [56]	x	x			x	x	x	x		
$h \rightarrow \text{invisible}$ [22]	x	x			x				x	
$E_T^{\text{miss}} + Z(q\bar{q})$ [44]	x						x	x		
$E_T^{\text{miss}} + b\bar{b}$ [50]							x	x		
$E_T^{\text{miss}} + t\bar{t}$ [50, 58]							x	x		
$t\bar{t}t\bar{t}$ [41]	x	x	x	x	x	x	x	x	x	x
$tbH^\pm(tb)$ [43]	x	x	x	x	x	x	x	x	x	x
$h \rightarrow aa \rightarrow f\bar{f}f'\bar{f}'$ [51, 57, 54, 52, 53]									x	

**Table 4.3:** Summary of input analyses used in the different benchmark scenarios [90].

given signature [40, 34]. The visible part of hadronically decaying  $\tau$ -leptons is seeded by small- $R$  jets reconstructed from topological clusters, calibrated with a hadronic weighting scheme [32]. The missing transverse momentum  $p_T^{\text{miss}}$  is calculated from the negative vector sum of the transverse momenta  $p_T$  of electrons, muons, jet candidates, and an additional soft term which includes activity in the tracking system originating from the primary vertex but not matched with any reconstructed particle [39]. Some analyses may also consider photons and  $\tau$ -leptons in the  $E_T^{\text{miss}}$  reconstruction.

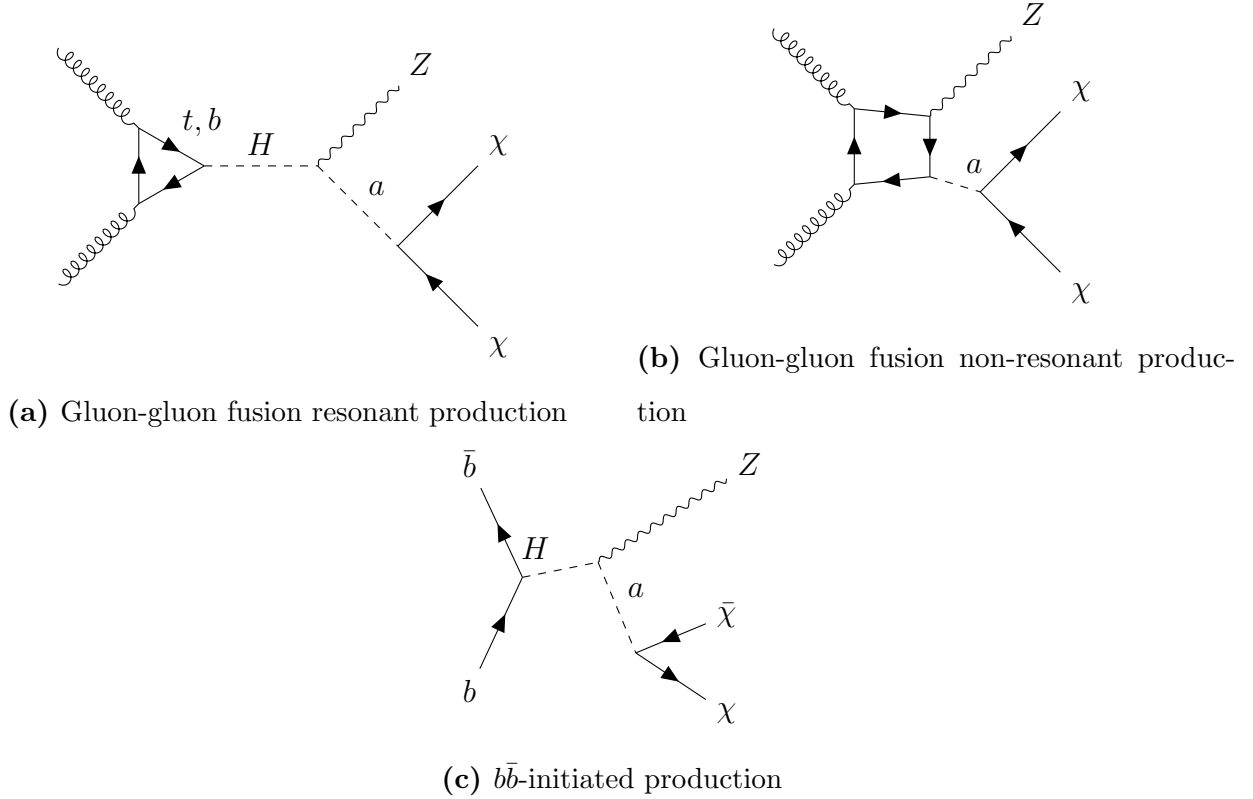


**Figure 4.1:** Representative production mechanisms and final state of the  $E_T^{\text{miss}} + Z(\ell\ell)$  signature, including gluon-gluon fusion resonant (a) and non-resonant production, and (c)  $b$ -initiated production.

#### 1073 4.4.1 $E_T^{\text{miss}} + Z(\ell\ell)$ signature

1074 The final state of this signature, shown on figure 4.1, is characterized by the presence of a  
 1075 large  $E_T^{\text{miss}}$  and a pair of high- $p_T$  electrons or muons [42]. Signal events must contain exactly  
 1076 a pair of oppositely charged electrons or muon, with an invariant mass consistent with the  
 1077  $Z$ -boson mass. The leptons are order in increasing  $p_T$ . The leading lepton is required to  
 1078 have  $p_T > 30$  GeV, and the sub-leading lepton  $p_T > 20$  GeV. The dilepton system must  
 1079 have an invariant mass  $m_{ll}$  in the range  $76 < m_{ll} < 106$  GeV, in accordance with the mass of  
 1080 the  $Z$  boson. The missing transverse momentum is required to have  $E_T^{\text{miss}} > 90$  GeV, and a  
 1081  $E_T^{\text{miss}}$  significance  $S_{E_T^{\text{miss}}} = \frac{E_T^{\text{miss}}}{\sigma_L \sqrt{1 - \rho_{LT}^2}} > 0$ , in which  $\sigma_L$  denotes the resolution of the  $pT$  of the

1082 system and  $\rho_{LT}$  a correlation factor between the resolutions of the parallel and perpendicular  
 1083 momentum components of the  $E_T^{\text{miss}}$  vector [37]. These quantities are calculated from MC  
 1084 simulation and shown to well describe the data. The requirements of  $E_T^{\text{miss}}$ , in addition to the  
 1085 constraints that the angular separation between the leptons  $\Delta R_{ll} < 1.8$  ensure consistence  
 1086 with invisible particles recoiling against the  $Z$  boson.

1087 The most abundant background is diboson production  $ZZ$ , followed by  $WZ$ ,  $Z + j$ , and  
 1088 non-resonant backgrounds ( $WW$ ,  $t\bar{t}$ , single top-quark,  $Z \rightarrow \tau\tau$ ). Additional backgrounds  
 1089 come from triboson production,  $t\bar{t} + V$ , and  $ZZ \rightarrow 4l$ , where a pair of leptons is not recon-  
 1090 structed.

1091 The  $ZZ$  background is estimated from MC simulation using a 4-lepton control region  
 1092 (CR), which is almost 100% pure in  $ZZ$  events. Events are required to contain two lepton  
 1093 pairs of the same flavour, opposite charge, and  $p_T > 7, 15, 15, 27$  GeV in increasing order  
 1094 of  $p_T$ . If all leptons in the final state are of the same flavour, they are grouped in pair by  
 1095 minimizing the quantity  $|m_{ll1} - m_Z| + |m_{ll2} - m_Z|$ , where the indices 1 and 2 denote the  
 1096 lepton pairs and  $m_Z = 91.19$  GeV. Similar to the signal region (SR), both lepton pairs must  
 1097 have  $76 < m_{ll} < 106$  GeV. The quantities  $E_T^{\text{miss}}$  and  $S_{E_T^{\text{miss}}}$  are calculated similarly as in the  
 1098 SR by treating a random pair of leptons as invisible and excluded from the calculation.

1099 The  $WZ$  background is constrained by a 3-lepton CR, in which two of the leptons have the  
 1100 same flavour and opposite charge to ensure their origin from a  $Z$  boson. This dilepton system,  
 1101 when ordered by increasing  $p_T$  must satisfy  $p_T^1 > 20$  GeV and  $p_T^2 > 30$  GeV, and  $76 < m_{ll} <$   
 1102 106 GeV. If there is ambiguity in selecting a dilepton pair, the pair closest to the  $Z$  boson  
 1103 in invariant mass is selected. The select events consistent with a  $W$  boson decay, the third  
 1104 lepton is required to have  $p_T > 20$  GeV, the event to have  $E_T^{\text{miss}} > 30$  GeV and  $S_{E_T^{\text{miss}}} > 3$ , and  
 1105 the transverse mass of the  $W$  boson candidate  $m_T^W = \sqrt{2p_T^l E_T^{\text{miss}}(1 - \cos \Delta\phi(l, E_R^{\text{miss}}))} > 60$   
 1106 GeV, where  $\Delta\phi(l, E_T^{\text{miss}})$  is the azimuthal angle between the third lepton and the  $E_T^{\text{miss}}$   
 1107 momentum.

1108 Finally, the non-resonant background is constrained primarily by a  $e\mu$  CR, defined simi-  
1109 larly to the SR, with the exception of the lepton flavour requirement. This CR includes  $t\bar{t}$ ,  
1110 single top quark,  $WW$  and  $Z \rightarrow \tau\tau$  events. The remaining backgrounds are estimated from  
1111 MC simulation.

1112 A profile likelihood fit in the  $ee$  and  $\mu\mu$  signal regions and the control regions is used to  
1113 estimate the signal strength. In the SRs and the  $e\mu$  CR, the observable of interest is the  
1114 transverse mass

$$m_T^{lep} = \sqrt{\left[ \sqrt{m_Z^2 + (p_T^{ll})^2} + \sqrt{m_Z^2 + (E_T^{\text{miss}})^2} \right]^2 - [\mathbf{p}_T^{ll} + \mathbf{p}_T^{\text{miss}}]^2}, \quad m_T^{lep} > 200 \text{ GeV} \quad (4.9)$$

1115 while the  $E_T^{\text{miss}}$  is used in the  $4l$ - and  $3l$ -CR. The transverse mass provides a good separation  
1116 between the 2DHM+a signal and the  $ZZ$  background.

#### 1117 4.4.2 $E_T^{\text{miss}} + h(b\bar{b})$ signature

1118 The final state of this signature, shown on figure 4.2, is characterized by a SM Higgs  
1119 boson decaying into two  $b$ -jets and a significant  $E_T^{\text{miss}}$  from the decay of the pseudo-scalar  $a$   
1120 [49]. Hence, selected events must contain at least two jets identified as  $b$ -jets and  $E_T^{\text{miss}} >$   
1121 150 GeV. The angular separation between the two  $b$ -jets is inversely proportional to the  
1122 transverse momentum of the Higgs boson, which is highly correlated to  $E_T^{\text{miss}}$ ; as such, at  
1123  $E_T^{\text{miss}} > 500$  GeV, the dijet system is reconstructed as a single large-radius jet. This motivates  
1124 splitting the events into merged regions and resolved regions, according to the decay topology  
1125 represented by the  $E_T^{\text{miss}}$ .

1126 In  $b$ -associated production (Figure 4.2c), an extra pair of  $b$ -jets is present in the final state  
1127 from gluon splitting. Therefore, the resolved and merged regions are split into a topology  
1128 containing two  $b$ -jets and one containing  $> 3$   $b$ -jets to enhance the sensitivity to both  
1129 production mechanisms, which are significant at different values of  $\tan\beta$ .

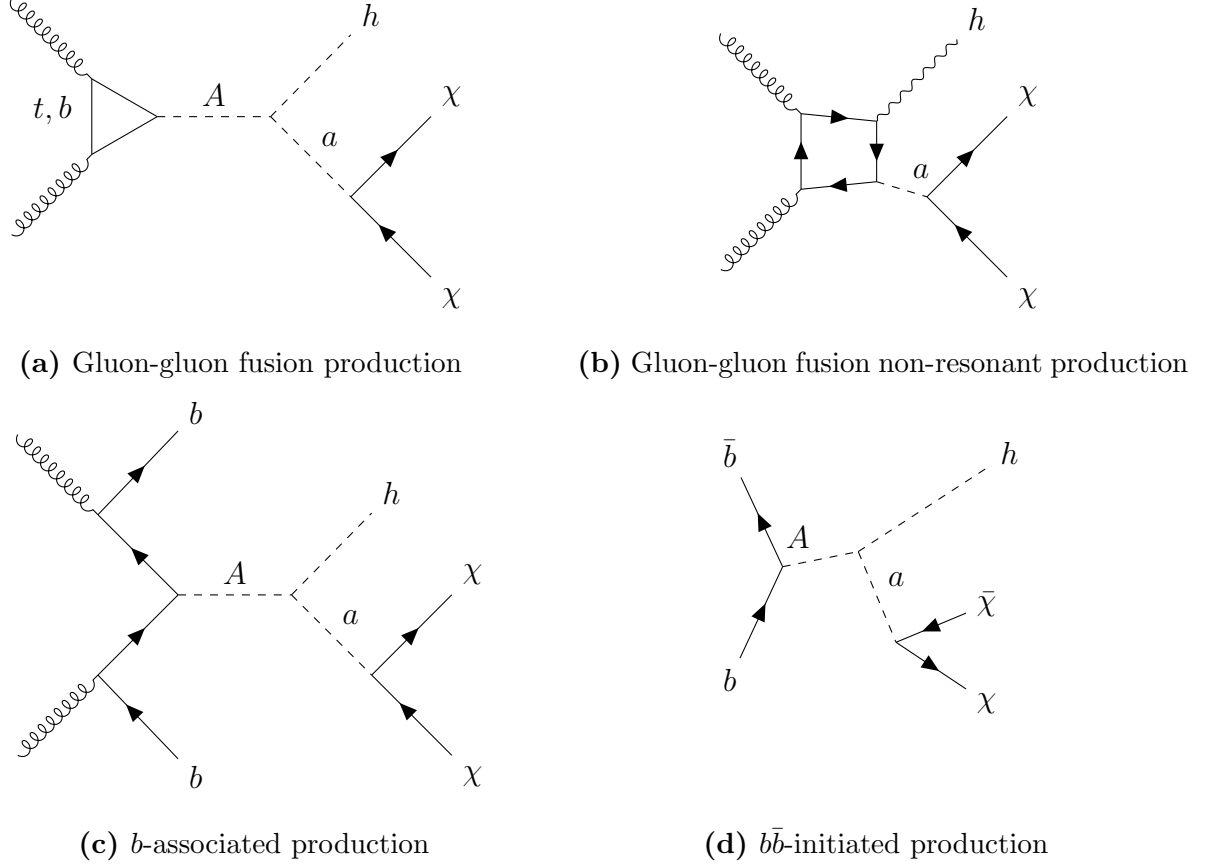


**Figure 4.2:** Production mechanisms and final state of the  $E_T^{\text{miss}} + h(b\bar{b})$  signature including gluon-gluon fusion resonant (a) and non-resonant production,  $b\bar{b}$ -associated production (c) and  $b\bar{b}$ -initiated production (d).

Table 4.4 summarizes the criteria used to select events in the signal regions. Owing to the complex topologies of the final state, event selection is carried out under several sets of selection criteria. First, all events are subjected to an “extended  $\tau$ -lepton veto” which consists of a baseline  $\tau$ -lepton veto, and a veto on small- $R$  jets whose multiplicity is within [1, 4] with  $\Delta\phi(\text{jet}, E_T^{\text{miss}}) < 22.5$  deg. Events in which any of the leading small- $R$  jets have  $\Delta\phi(\text{jet}, E_T^{\text{miss}}) < 20$  deg are also rejected. A loose selection on the Higgs mass  $m_h$ , defined from primary reconstructed object in each region, is applied.

Resolved	Merged
Primary $E_T^{\text{miss}}$ trigger	
Data quality selections	
$E_T^{\text{miss}} > 150 \text{ GeV}$	
Lepton and extended lepton vetos	
$\Delta\phi(jet_{1,2,3}, E_T^{\text{miss}}) > 20 \text{ deg}$	
$E_T^{\text{miss}} < 500 \text{ GeV}$	$E_T^{\text{miss}} > 500$
$\geq 2$ small- $R$ $b$ -tagged jets	$\geq 1$ large- $R$ jets, $\geq 2$ variable- $R$ $b$ -tagged jets
$p_{T_h} > 100 \text{ GeV}$ if $E_T^{\text{miss}} < 350$ , else $p_{T_h} > 300 \text{ GeV}$	
$m_T^{b,\min} > 170 \text{ GeV}$ , $m_T^{b,\max} > 200 \text{ GeV}$	
$S_{E_T^{\text{miss}}} > 12$	
$\leq 4$ small- $R$ jets (2 $b$ -tag)	
$\leq 5$ small- $R$ jets (3 $b$ -tag)	
$50 < m_h < 280 \text{ GeV}$	$50 < m_h < 270 \text{ GeV}$

**Table 4.4:** Selection criteria used to defined resolved and merged signal regions for the  $E_T^{\text{miss}} + h(b\bar{b})$  signature [49].

1137 In the resolved SRs, events required to have  $E_T^{\text{miss}} < 500 \text{ GeV}$ , and at least 2  $b$ -tagged  
 1138 small- $R$  jets, of which the 2 highest- $p_T$  jets reconstruct the Higgs boson candidate, whose  
 1139  $p_T$  must exceed 100 GeV. The dominant background in the resolved region is  $t\bar{t}$  production  
 1140 where one top quark decays leptonically but the lepton is misidentified or outright not  
 1141 reconstructed. To suppress this background, the transverse masses of the  $E_T^{\text{miss}}$ , defined for  
 1142 the  $b$ -jet closest to the  $E_T^{\text{miss}}$  in  $\phi$  (denoted  $m_T^{b,\min}$ ), and one furthest from it (denoted  $m_T^{b,\max}$ )  
 1143 as

$$m_T^{b,\min/\max} = \sqrt{2p_T^{b,\min/\max} E_T^{\text{miss}} (1 - \cos \Delta\phi(p_T^{b,\min/\max}, E_T^{\text{miss}}))} \quad (4.10)$$

1144 must satisfy  $m_T^{b,\min} > 170 \text{ GeV}$  and  $m_T^{b,\max} > 200 \text{ GeV}$ . The 2  $b$ -tag and  $\geq 3$   $b$ -tag regions are  
 1145 split into three bins according to  $E_T^{\text{miss}}$ , namely  $150 < E_T^{\text{miss}} < 200 \text{ GeV}$ ,  $200 < E_T^{\text{miss}} < 350$

<sub>1146</sub> GeV, and  $350 < E_T^{\text{miss}} < 500$  GeV, among which the highest  $E_T^{\text{miss}}$  bin is required to have  
<sub>1147</sub>  $p_{T_h} > 300$  GeV.

<sub>1148</sub> In the merge SRs, defined by  $E_T^{\text{miss}} > 500$  GeV, at least one large- $R$  jet is required and  
<sub>1149</sub> defined as the Higgs boson candidate, and 2 leading variable- $R$  track-jets must be  $b$ -tagged.  
<sub>1150</sub> Events are separated into those having no additional variable- $R$  track jets that are  $b$ -tagged,  
<sub>1151</sub> denoted 2  $b$ -tagged region, and those with at least one not associated with the Higgs boson  
<sub>1152</sub> candidate, denoted  $\geq 3$   $b$ -tagged region, the former of which is split into two  $E_T^{\text{miss}}$  bins,  
<sub>1153</sub> namely  $500 < E_T^{\text{miss}} < 750$  GeV and  $E_T^{\text{miss}} \geq 750$  GeV.

<sub>1154</sub> The most dominant backgrounds are  $t\bar{t}$  and  $W/Z$  boson production with jets from heavy  
<sub>1155</sub> flavour (HF) quarks. The the 2  $b$ -tag regions are dominated by  $t\bar{t}$  and  $Z + HF$  background,  
<sub>1156</sub> the latter of which becomes more important with increasing  $E_T^{\text{miss}}$ . In the 3  $b$ -tag regions,  
<sub>1157</sub> the main background is  $t\bar{t}$ , where the third jet, originating from a hadronic  $W$  decay, is  
<sub>1158</sub> mis-tagged as a  $b$ -jet. These backgrounds are modelled using MC simulation and corrections  
<sub>1159</sub> from data. Smaller backgrounds including single-top, diboson, and SM  $Vh$  production are  
<sub>1160</sub> modelled solely by simulation.

#### <sub>1161</sub> 4.4.3 $E_T^{\text{miss}} + h(\gamma\gamma)$ signature

<sub>1162</sub> The  $E_T^{\text{miss}} + h(\gamma\gamma)$  the  $E_T^{\text{miss}} + h(b\bar{b})$ , and the  $E_T^{\text{miss}} + h(\tau\tau)$  signatures in the next subsection  
<sub>1163</sub> share the same production mechanisms, shown in figure 4.2, differing only in the decay  
<sub>1164</sub> products of the SM Higgs boson. The  $h \rightarrow \gamma\gamma$  decay, despite a small branching ratio,  
<sub>1165</sub> benefits from excellent photon resolution and a clean Higgs signal [45]. The final state  
<sub>1166</sub> contains two photons and significant  $E_T^{\text{miss}}$ . Events must therefore pass a diphoton trigger  
<sub>1167</sub> with two reconstructed photon candidates having  $E_T^{\gamma, \text{lead}} \geq 35$  GeV and  $E_T^{\gamma, \text{sublead}} \geq 25$  GeV,  
<sub>1168</sub> and have  $E_T^{\text{miss}} > 90$  GeV. The Higgs boson candidate is constructed from the two photons  
<sub>1169</sub> with the largest  $E_T$ , if they satisfy  $E_T^{\gamma, \text{lead}}/m_{\gamma\gamma} > 0.35$  and  $E_T^{\gamma, \text{sublead}}/m_{\gamma\gamma} > 0.25$ . The  
<sub>1170</sub> invariant mass of the diphoton system must be compatible with the Higgs mass, such that

<sub>1171</sub>  $105 < m_{\gamma\gamma} < 160$  GeV. Events are separated into two categories, i.e. a low- $E_T^{\text{miss}}$  region with  
<sub>1172</sub>  $E_T^{\text{miss}} < 150$  GeV, and a high- $E_T^{\text{miss}}$  region with  $E_T^{\text{miss}} > 150$  GeV. A machine learning classifier  
<sub>1173</sub> based on Boosted Decision Trees (BDT) is trained to distinguish the 2HDM+ $a$  signal from  
<sub>1174</sub> non-resonant background. In each  $E_T^{\text{miss}}$  region, the BDT score spectrum is divided into two  
<sub>1175</sub> categories, whose boundary is optimized for the combined signal sensitivity.

<sub>1176</sub> SM Higgs boson production, QCD-induced non-resonant diphoton production, and re-  
<sub>1177</sub>ducible contributions from misidentified electrons or jets as photons and  $E_T^{\text{miss}}$  generated by  
<sub>1178</sub> particles outside of detector acceptance or by neutrinos constitute the primary background.  
<sub>1179</sub> In the low  $E_T^{\text{miss}}$  region, significant background arises from inaccurate  $E_T^{\text{miss}}$  reconstruction  
<sub>1180</sub> from high-energy objects and soft interactions in the ID. The photon invariant mass serves  
<sub>1181</sub> as the observable of interest to estimate various background contributions in each category  
<sub>1182</sub> using an analytic function.

#### <sub>1183</sub> 4.4.4 $E_T^{\text{miss}} + h(\tau\tau)$ signature

<sub>1184</sub> This search target a final state consisting of a Higgs boson decaying into a pair of  $\tau$ -  
<sub>1185</sub> leptons, which then decay hadronically, and a large  $E_T^{\text{miss}}$  [46]. The production mechanisms,  
<sub>1186</sub> similar to those of the  $E_T^{\text{miss}} + h(b\bar{b})$  and  $E_T^{\text{miss}} + h(\gamma\gamma)$ , are shown in figure 4.2. Selected  
<sub>1187</sub> events contain exactly two  $\tau$ -lepton objects of opposite charge that activate the di- $\tau_{had-vis}$   
<sub>1188</sub> trigger [62]. Event containing an electron or a muon are vetoed. Two SRs are defined to  
<sub>1189</sub> enhance the sensitivity to the 2HDM+ $a$  signal. Events are required to pass a set of common  
<sub>1190</sub> selections, shown in table 4.5, to reduce the dominant SM background processes. The limit  
<sub>1191</sub> on angular distance between the  $\tau$ -leptons suppresses the backgrounds involving  $\tau$ -leptons  
<sub>1192</sub> that do not come from a resonant decay (such as  $t\bar{t}$  and  $W+jets$ ). The event-level transverse  
<sub>1193</sub> mass is defined as

$$m_T^{tot} = \sqrt{(p_T^{\tau_1} + p_T^{\tau_2} + p_T^{\text{miss}})^2 - (p_{T,x}^{\tau_1} + p_{T,x}^{\tau_2} + p_{T,x}^{\text{miss}})^2 - (p_{T,y}^{\tau_1} + p_{T,y}^{\tau_2} + p_{T,y}^{\text{miss}})^2}, \quad (4.11)$$

1194 and the transverse mass of a  $\tau$ -lepton as

$$m_T^{\tau_i} = \sqrt{2p_T^{\tau_i} E_T^{\text{miss}} (1 - \cos \Delta\phi(\tau_1, p_T^{\text{miss}}))}. \quad (4.12)$$

1195 The sum of the  $\tau$  transverse mass is required to be larger than 100 GeV to reduce  $Z$  boson  
1196 decay background. The low- $m_A$  region is defined with  $m_A < 800$  GeV, in which the  
1197 angular distance between the  $\tau$ -leptons is limited to [0.6, 1.9], their visible invariant mass  
1198  $m_{\text{vis}}(\tau_1, \tau_2)$  to  $[75, \infty]$  GeV, and the individual transverse mass  $m_T^{\tau_1}, m_T^{\tau_2}$  to  $> 50$  GeV and  
1199  $> 25$  GeV, respectively. The high- $m_A$  corresponds to signal events with higher  $E_T^{\text{miss}}$  and  
1200 boosted Higgs boson, improving the sensitivity to 2HDM+ $a$  signal at high  $m_A$  masses. It  
1201 requires  $m_T^{\text{tot}} > 400$  GeV, and  $m_T^{\tau_1} + m_T^{\tau_2} > 400$  GeV. Both regions are binned according to  
1202 table 4.5

1203 Primary backgrounds include  $Z$  boson and multiboson production, and  $t\bar{t}$  production  
1204 decaying into two true  $\tau$ -leptons. Other background contributions arise from  $W$  boson and  
1205 multijet production, in which at least one reconstructed  $\tau$ -lepton is fake. These backgrounds  
1206 are estimated using both simulation and data-driven methods.

#### 1207 4.4.5 $E_T^{\text{miss}} + tW$ signature

1208 This search targets a final state with a  $W$  boson produced in association with a top  
1209 quark and a large  $E_T^{\text{miss}}$  resulting from invisible decay of the pseudo-scalar mediator  $a$  (figure  
1210 4.3) [47]. The primary top quark overwhelmingly to a  $W$  boson and a bottom quark, and  
1211 thus the final state is characterized by the decay channel of the two  $W$  bosons. The  $tW_{0L}$   
1212 channel target events in which both boson decay hadronically, and the  $tW_{1L}$  targets one  
1213 boson decaying leptonically and the other hadronically. The result from a previous search  
1214 targeting two charged leptons [48] in the final state is also included in the interpretation.  
1215 Zero-lepton and one-lepton signal regions enter the statistical combination.

Low $m_A$ SR	High $m_A$ SR
$\Delta R(\tau_1, \tau_2) < 2$	
$m_T^{tot} > 50$ GeV	
$40 < m_{vis}(\tau_1, \tau_2) < 125$ GeV	
$m_T^{\tau_1} + m_T^{\tau_2} > 100$ GeV	
$q(\tau_1)q(\tau_2) = -1$	
$N_{b-jet} = 0$	
$0.6 < \Delta R(\tau_1, \tau_2) < 1.9$	
	$m_T^{tot} > 400$ GeV
$m_T^{\tau_1} > 50$ GeV	
$m_T^{\tau_2} > 25$ GeV	
$m_{vis}(\tau_1, \tau_2) > 75$ GeV	$40 < m_{vis}(\tau_1, \tau_2) < 125$ GeV
$m_T^{\tau_1} + m_T^{\tau_2}$ bins $[100, 125, 400, 550, \infty]$ GeV	$[400, 750, \infty]$ GeV

**Table 4.5:** Selection criteria used to define low- and high- $m_R$  signal regions for the  $E_T^{\text{miss}} + h(\tau\tau)$  signature [46].

The search is sensitive to on-shell production of the charged Higgs bosons and their semi-visible decay. In both  $tW_{0L}$  and  $tW_{1L}$  channels, the hadronically decaying  $W$  boson is reconstructed as a single  $W$ -tagged large- $R$  jet due to its high  $p_T$ . Important background processes vary across different channels, but usually arise from genuine  $E_T^{\text{miss}}$  associated with neutrinos, or  $E_T^{\text{miss}}$  produced by particles which are misidentified, mismeasured, or outside of the detector's kinematic acceptance. For example,  $Z + \text{jet}$  in the  $tW_{0L}$  channel and  $W + \text{jet}$  in the  $tW_{1L}$  channel are both genuine  $E_T^{\text{miss}}$  background.  $t\bar{t}$  production and  $W + \text{jet}$  production in  $tW_{0L}$  are dominant background containing fake  $E_T^{\text{miss}}$ . Other significant contributions originate from  $t\bar{t}Z$  and single top quark production. These backgrounds are estimated from MC simulation via 6 dedicated control regions.

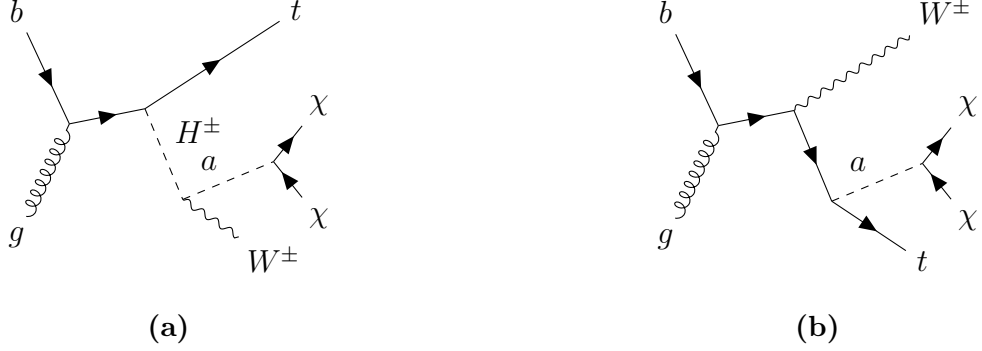


**Figure 4.3:** Production mechanisms and final state of the  $E_T^{\text{miss}} + tW$  signature.

#### 1226 4.4.6 $E_T^{\text{miss}} + j$ signature

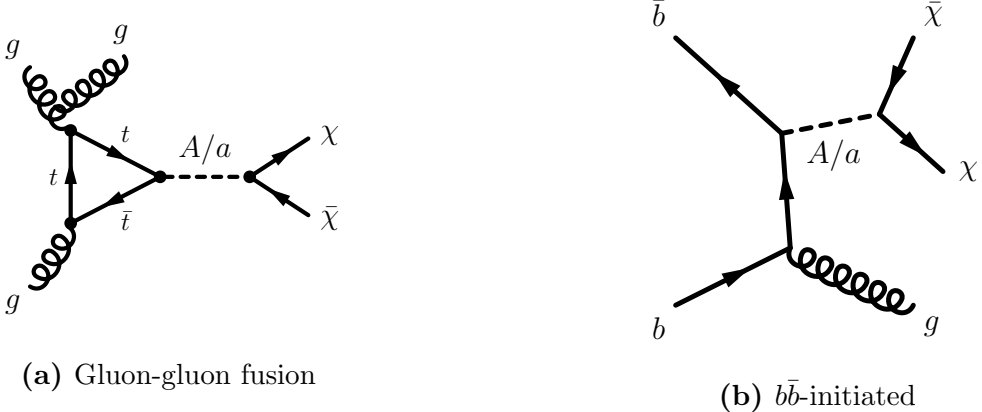


**Figure 4.4:** Production mechanisms and final state of the  $E_T^{\text{miss}} + j$  signature, including gluon-gluon fusion production (a) and  $b\bar{b}$ -initiated production (b).

1227 This search targets final states containing a single jet and a large  $E_T^{\text{miss}}$ , which must  
 1228 satisfy  $E_T^{\text{miss}} > 200$  GeV to guarantee full  $E_T^{\text{miss}}$  trigger efficiency for all selected events [56].  
 1229 Events must contain a leading jet with  $p_T > 150$  GeV,  $|\eta| < 2.4$ , up to three additional jets  
 1230 with  $p_T > 30$  GeV,  $|\eta| < 2.8$ , and no leptons or photons. The azimuthal angular separation  
 1231 between the  $E_T^{\text{miss}}$  vector and each jet is required to meet  $\Delta\phi(E_T^{\text{miss}}, \text{jet}) > 0.6$  for events  
 1232 with  $200 < E_T^{\text{miss}} < 250$  GeV, and  $\Delta\phi(E_T^{\text{miss}}, \text{jet}) > 0.4$  for those with  $E_T^{\text{miss}} > 250$  GeV to  
 1233 reduce multijet backgrounds.

1234 Dominant SM backgrounds include  $Z(\nu\nu)$  and  $W(l\nu)$  production, in which the  $W$  decays  
1235 into a  $\tau$ -lepton which later decays hadronically, or other leptons that are undetected. Other  
1236 contributions arise from  $t\bar{t}$ , single top quark, and diboson production, as well as non-collision  
1237 and multijet backgrounds. These background contributions are estimated using a profile  
1238 likelihood fit to the  $p_T$  distribution of the system recoiling against the reconstructed jets in  
1239 both signal and control regions.

1240 In this combination, the search is reinterpreted in the context of 2HDM+ $a$ , which is  
1241 not considered in the original search. Several signal contributions to this signature are  
1242 considered. In the low- $E_T^{\text{miss}}$  region, the production of a pair of DM particles with a jet is the  
1243 primary contribution at  $E_T^{\text{miss}} < 500 \text{ GeV}$   $m_a \leq 150 \text{ GeV}$ . Both  $gg$ -initiated and  $bb$ -initiated  
1244 productions are considered, the latter of which is relevant at large  $\tan\beta$ . For larger  $E_T^{\text{miss}}$   
1245 and smaller  $m_a$ , the production of two pairs of DM particles via  $h \rightarrow aa \rightarrow \chi\bar{\chi}\chi\bar{\chi}$  (figure 4.7)  
1246 is the dominant process. Smaller contributions come from  $E_T^{\text{miss}} + Z(q\bar{q})$  and  $E_T^{\text{miss}} + h(b\bar{b})$   
1247 productions which the invisible decays of the SM Higgs boson are kinematically forbidden.  
1248 Finally, minor contributions from  $pp \rightarrow t\bar{t} + a$ , and  $pp \rightarrow tW + a$  are also present.

#### 1249 4.4.7 $h \rightarrow$ invisible signature

1250 The invisible decays of the SM Higgs boson represented by a  $E_T^{\text{miss}}$  associated to other  
1251 visible signatures have been investigated in previous ATLAS publications and statistically  
1252 combined in reference [22]. The main production mechanisms include vector-boson fusion  
1253 (VBF) [55], VBF with an emitted photon [38], gluon-gluon fusion [56], associated production  
1254 with a vector boson [42], and associated production with a pair of top quarks [25]. The results  
1255 from Run 2 searches are combined statistically with constraints on invisible Higgs decays  
1256 obtained from searches with up to  $4.7 \text{ fb}^{-1}$  of  $pp$  collision data at  $\sqrt{s} = 7 \text{ TeV}$  and  $20.3 \text{ fb}^{-1}$   
1257 at  $\sqrt{s} = 8 \text{ TeV}$  [24].

1258 Among these searches,  $h \rightarrow$  invisible from VBF production from Run 2 is the most  
 1259 sensitive and sets an observed limit of 0.145 and an expected limit of 0.103 at 95% confidence  
 1260 level on the invisible branching ratio. Selected events are required to pass the  $E_T^{\text{miss}}$  trigger  
 1261 and have  $E_T^{\text{miss}} > 160$  GeV. They must also contain from two to four jets with  $p_T > 25$  GeV,  
 1262 among which the leading and sub-leading jets must have  $p_T^{\text{lead}} > 80$  GeV and  $p_T^{\text{sub-lead}} > 50$   
 1263 GeV and be well separated in  $\eta$ . In addition, lepton and  $b$ -jet vetoes are applied to reduce  $W +$   
 1264 *jets* and top quark backgrounds. By partitioning the  $E_T^{\text{miss}}$  spectrum, the jet multiplicity, and  
 1265 jet-invariant masses, sixteen orthogonal signal regions are defined. Dominant background  
 1266 processes include  $Z(\nu\nu) + \text{jet}$  and  $W(l\nu) + \text{jet}$  production, the latter of which the charged  
 1267 lepton is undetected or misidentified. The backgrounds are estimated from control regions  
 1268 in the one-lepton and two-lepton channels. The multijet background is directly estimated  
 1269 from data. An upper limit on the  $h \rightarrow$  invisible of  $0.113 (0.080^{+0.031}_{-0.022})$  is observed (expected)  
 1270 at 95% confidence level.

1271 **4.4.8 Additional searches using  $36 \text{ fb}^{-1}$  of  $\sqrt{s} = 13 \text{ TeV}$   $pp$  collision**  
 1272 **data**

1273 Three searches using  $36 \text{ fb}^{-1}$  of  $\sqrt{s} = 13 \text{ TeV}$  data are shown in this combination, the  
 1274 first of which targets  $E_T^{\text{miss}} + Z(q\bar{q})$  signature [44]. The final state contains a  $E_T^{\text{miss}} > 150$   
 1275 GeV and a hadronically decaying vector boson reconstructed as a single large- $R$  jet with  
 1276  $p_T > 250$  GeV in a boosted topology and two small- $R$  jets with  $p_T > 20$  GeV in a resolved  
 1277 topology. A lepton veto is applied in both cases. Signal regions are defined using the number  
 1278 of  $b$ -jets in the final state. The dominant backgrounds of  $t\bar{t}$  and  $W/Z + \text{jets}$  are estimated  
 1279 using a simultaneous fit to the  $E_T^{\text{miss}}$  distribution in the signal and control regions.

1280 The second search targets a  $E_T^{\text{miss}} + b\bar{b}$  signature. The final state contains at least two  $b$ -  
 1281 jets and  $E_T^{\text{miss}} > 180$  GeV [50]. The irreducible background from  $Z(\nu\nu) + b\bar{b}$  events separated  
 1282 from the signal events using the azimuthal separation between the  $b$ -jets and the  $E_T^{\text{miss}}$ . The

1283 results are extracted from a likelihood fit to the angular observable  $\cos\theta_{b\bar{b}} = |\tanh\Delta\eta_{n\bar{b}}/2|$ ,  
1284 in which  $\Delta\eta_{n\bar{b}}$  is the difference in pseudorapidity between the  $b$ -jets.

1285 The last group of searches targeting  $E_T^{\text{miss}} + t\bar{t}$  and differing the the number of final-state  
1286 leptons are included [50]. A search in the final state where both  $W$  bosons decay hadronically  
1287 selects events with at least four energetic jets, of which at least two are  $b$ -jets, and a large  
1288  $E_T^{\text{miss}}$ . Several requirements on the invariant mass of the large- $R$  jets are applied to identify  
1289 events with a boosted  $W$  boson or top quark decay. The main backgrounds are  $Z + \text{jets}$ ,  
1290  $t\bar{t}$ , and  $t\bar{t} + Z$  production, constrained using dedicated control regions. A search in the  
1291 one-lepton final state, resulting from a leptonically decaying  $W$  boson, selects events with at  
1292 least four energetic jets, at least one of which is a  $b$ -jet, an isolated lepton, and a large  $E_T^{\text{miss}}$   
1293 [58]. They must also have at least one hadronic top candidate with invariant mass close  
1294 to the top quark mass. The azimuthal separation between the lepton and  $E_T^{\text{miss}}$  and that  
1295 between the jets and  $E_T^{\text{miss}}$  are used to suppress the background contamination in the signal  
1296 regions. Dedicated control regions are used to estimate background processes involving top  
1297 quarks.

#### 1298 4.4.9 $tbH^\pm(tb)$ signature

1299 The leading-order Feynman diagram for the target signature of this search is shown in  
1300 figure 4.5 [43]. The charged Higgs boson is produced together with a top and a bottom  
1301 quark, and subsequently decays into a top and a bottom quark, in which one top quark  
1302 decays semi-leptonically. Events are preselected to contain exactly one electron or muon  
1303 with  $p_T > 27$  GeV and at least five jets with  $p_T > 25$  GeV. At least three jets must be  
1304  $b$ -tagged to reduce large backgrounds from multijet production. Selected events are divided  
1305 into four separate regions, namely  $5j3b$ ,  $5j \geq 4b$ ,  $\geq 6j3b$ , and  $\geq 6j \geq 4b$ , where  $j$  and  $b$   
1306 respectively stand for jets and  $b$ -jets. A neural network is trained to discriminate between  
1307 signal and background, whose output distributions are used to extract the signal in data.

1308 Dominant backgrounds include  $t\bar{t} + jets$ , and single top quark production in the  $Wt$   
1309 channel. The former is divided into  $t\bar{t} + \text{light}$ ,  $t\bar{t}+ \geq 1b$ , and  $t\bar{t}+ \geq 1c$ . These along with  
1310 other minor backgrounds are model using MC simulation and corrections obtained from an  
1311 additional  $\geq 5j2b$  region via a reweighting procedure [29, 35]. After the reweighting, the  
1312  $t\bar{t}+ \geq 1b$  and  $t\bar{t}+ \geq 1c$  normalizations factors are extracted from the fit to data.

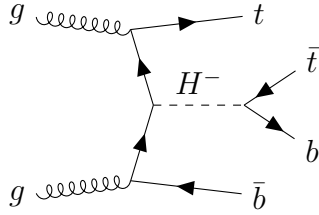


**Figure 4.5:** Production mechanisms and final state of the  $tbH^\pm(tb)$  signature.

1313 **4.4.10  $t\bar{t}t\bar{t}$  signature**

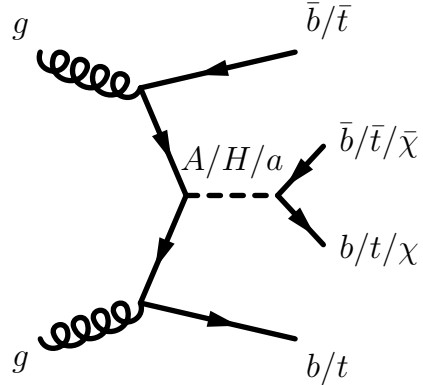


**Figure 4.6:** Production mechanisms and final state of the  $t\bar{t}t\bar{t}$ ,  $E_T^{\text{miss}} + b\bar{b}$ , and  $E_T^{\text{miss}} + t\bar{t}$  signatures.

1314 The targeted signature of this search, shown in figure 4.6, is a  $t\bar{t}$ -associated production  
1315 of a heavy scalar or pseudo-scalar Higgs boson in the 2HDM+ $a$ , which then decays into a  
1316 pair of top quarks[41]. The final state contains 2 pairs of top quarks, decaying into either  
1317 two leptons with the same-sign electric charge or at least three leptons, both with high  
1318 jet multiplicity. These leptons include electrons or muons from leptonic  $\tau$  decay, and are  
1319 required to have  $p_T > 28$  GeV. A baseline signal region is defined by requiring six jets with

1320  $p_T > 25$  GeV, among which at least two are  $b$ -tagged, and a scalar sum of the all transverse  
1321 momenta of jets and leptons  $H_T > 500$  GeV. First, a BDT is trained to separate SM  $t\bar{t}t\bar{t}$   
1322 production and background processes using event-level inputs. A second BDT, designated  
1323 BSM mass-parametrised BDT (BSM pBDT), is then trained to discriminate between BSM  
1324  $t\bar{t}t\bar{t}$  events and all background. It is parametrised as a function of the mass of the heavy  
1325 Higgs boson by introducing the mass as an input in the training [65].

1326 The major irreducible backgrounds arise from the top quark pair production with a boson  
1327 and jets ( $t\bar{t} + W + \text{jets}$ ,  $t\bar{t} + Z + \text{jets}$ , and  $t\bar{t} + h + \text{jets}$ ). These contributions are estimated  
1328 using MC simulations with data-driven corrections for  $t\bar{t} + W + \text{jets}$ . Minor, irreducible  
1329 backgrounds originate mostly from  $t\bar{t} + \text{jets}$  and  $tW + \text{jets}$  production with misidentified  
1330 charge, fake and non-prompt leptons, which are estimated from data using dedicated control  
1331 regions.

1332 **4.4.11 Exotic Higgs boson decays  $h \rightarrow aa \rightarrow f\bar{f}f'\bar{f}'$**

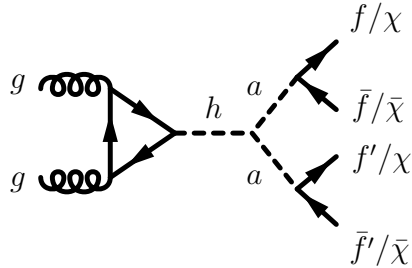


**Figure 4.7:** Production mechanisms and final state of the  $h \rightarrow aa \rightarrow f\bar{f}f'\bar{f}'$  signature.

1333 This set of searches target the decays of the SM Higgs boson into a pair of light pseudo-  
1334 scalar particles  $aa$ , which then decay into four fermions, as illustrated in figure 4.7. De-  
1335 pending on the type of fermion present in the final state, the searches provide sensitivity to  
1336 different pseudo-scalar mass ranges.

1337        The first search uses  $139 \text{ fb}^{-1}$  of  $\sqrt{s} = 13 \text{ TeV}$   $pp$  collision data, and targets the  $b\bar{b}\mu^+\mu^-$   
 1338        final state [51]. It is sensitive to pseudo-scalar mass in the range  $16 < m_a < 62 \text{ GeV}$ . The  
 1339        variable of interest is the dimuon invariant mass, chosen to probe for a resonant enhance-  
 1340        ment over the SM expectation. The dominant background is the Drell-Yan dimuon process  
 1341        together with  $b$  quarks and SM  $t\bar{t}$  production where both  $W$  bosons from the top quarks  
 1342        decay into a muon and a neutrino.

1343        A second search using  $36 \text{ fb}^{-1}$  of  $\sqrt{s} = 13 \text{ TeV}$   $pp$  collision data targeting  $b\bar{b}b\bar{b}$  final  
 1344        state provides sensitivity in the mass range  $20 < m_a < 60 \text{ GeV}$  [57]. The Higgs boson  
 1345        is produced in association with a leptonically decaying  $W$  boson (one-lepton channel) or  $Z$   
 1346        boson (two-lepton channel). Signal-background separation is performed with a BDT trained  
 1347        using event-level kinematic variables, notably the reconstructed pseudo-scalar masses. The  
 1348        dominant background process in the one-lepton channel is  $t\bar{t}$  production with additional  
 1349        jets, and  $Z + jet$  in the two-lepton channel. The BDT output distribution is used as the  
 1350        observable of interest in the final likelihood fit. This search is optimized for the resolved  
 1351        topology of the  $b\bar{b}$  dijet system, i.e. they are reconstructed as two small- $R$  jets.

1352        A third search on  $20.3 \text{ fb}^{-1}$  of  $\sqrt{s} = 8 \text{ TeV}$   $pp$  collision targeting  $\mu^+\mu^-\tau^+\tau^-$  probes the  
 1353        mass range  $3.7 < m_a < 50 \text{ GeV}$ . It probes resonant enhancement in the dimuon invariant  
 1354        mass spectrum [54].

1355        The last searches considered in this combination target final states with four charged  
 1356        leptons ( $l = e, \mu$ ) on  $36 \text{ fb}^{-1}$  and  $139 \text{ fb}^{-1}$  of  $\sqrt{s} = 13 \text{ TeV}$  [52, 53]. They probe two  
 1357        orthogonal pseudo-scalar mass regions, namely a low-mass region covering  $1 < m_a < 15$   
 1358        GeV range, excluding the mass ranges around the  $J/\psi$  and the  $\Upsilon$  resonances, and a high-mass  
 1359        region covering  $15 < m_a < 60 \text{ GeV}$ . The high-mass range is insensitive to 2HDM+ $a$  and  
 1360        therefore excluded from this combination. The final states containing at least four muons are  
 1361        exclusively considered thanks to their large branching ratio and the large selection efficiency  
 1362        of isolated muons relative to that of isolated electrons. The dominant background process is

<sub>1363</sub>  $ZZ^* \rightarrow \mu^+\mu^-\mu^+\mu^-$  and  $h \rightarrow ZZ^* \rightarrow \mu^+\mu^-\mu^+\mu^-$ . The observable of interest is the average  
<sub>1364</sub> dimuon invariant mass  $\langle m_{\mu^+\mu^-} \rangle = (m_{12} + m_{34})/2$ , in which the pairing is done to minimize  
<sub>1365</sub> the dimuon invariant mass difference.

<sub>1366</sub> Model-independent upper limit on the branching ratio of the  $h \rightarrow aa \rightarrow 4f$  are obtained.  
<sub>1367</sub> The upper limit is used directly to exclude parameter regions in the 2HDM+ $a$  based on  
<sub>1368</sub> the predicted  $h \rightarrow aa \rightarrow 4f$  branching ratio for each point considered in the benchmark  
<sub>1369</sub> scenarios in the previous section.

## <sub>1370</sub> 4.5 Systematic uncertainties

<sub>1371</sub> Systematic and statistical uncertainties depend on event selection, the considered phase  
<sub>1372</sub> space, and the background estimation strategy. Systematic uncertainties may be of experi-  
<sub>1373</sub> mental or theoretical origin. In general, experimental uncertainties may include uncertainties  
<sub>1374</sub> in the absolute jet energy scales and resolutions, jet quality requirements, pile-up corrections,  
<sub>1375</sub>  $b$ -jet identification efficiencies, and the soft contributions to  $E_T^{\text{miss}}$ . Uncertainties in lepton  
<sub>1376</sub> identification and reconstruction efficiencies, energy/momentum scale and resolution are con-  
<sub>1377</sub> sidered from events with selected or vetoed leptons. Uncertainties due to the finite size of the  
<sub>1378</sub> background MC samples and others related to the modelling of the background processes are  
<sub>1379</sub> also included in the analyses. A luminosity uncertainty of 1.7% is applied to backgrounds  
<sub>1380</sub> derived purely from MC simulation [33].

<sub>1381</sub> Theoretical uncertainties on the production cross-section or on the signal acceptance  
<sub>1382</sub> affect signal modelling. They include uncertainties related to the PDF and are evaluated  
<sub>1383</sub> following the PDF4LHC recommendations [77]. Other uncertainties pertain to the choice of  
<sub>1384</sub> renormalization and factorization scales. They are derived by varying independently such  
<sub>1385</sub> scales by a factor of 2.0 and 0.5 relative to the nominal values used for MC generation. In  
<sub>1386</sub> addition, for signatures entering the statistical combination, uncertainties in the modelling  
<sub>1387</sub> of initial- and final-state radiation and multi-parton interactions are taken into account.

## 1388 4.6 Statistical combination of results

1389 Three 2HDM+ $a$  signatures are selected to enter a statistical combination, namely  $E_T^{\text{miss}} +$   
1390  $h(b\bar{b})$ ,  $E_T^{\text{miss}} + Z(\ell\ell)$ , and  $tbH^\pm tb$ . They cover complementary regions of the model parameter  
1391 space, and are the most constraining signatures of those described in 4.4. These factors  
1392 simplify the statistical treatment and enhance the sensitivity to the 2HDM+ $a$  signal.

1393 These input analyses are statistically independent, due to their event selection. The  
1394  $E_T^{\text{miss}} + Z(\ell\ell)$  analysis vetoes events with  $b$ -jets, whereas the other analyses require the  
1395 presence of at least two jets. The  $tbH^\pm(tb)$  targets final states with a charged lepton, while  
1396  $E_T^{\text{miss}} + h(b\bar{b})$  vetoes the presence thereof. Therefore, the signal region of these analyses are  
1397 completely separated. A small event overlap ( $< 1\%$ ) is observed between  $tbH^\pm(tb)$  signal  
1398 region and the leptonic control region of the  $E_T^{\text{miss}} + h(b\bar{b})$  analysis, but has no impact on  
1399 the combination.

### 1400 4.6.1 Statistical analysis

1401 To statistically combine the results of these analyses, a combined likelihood function is  
1402 constructed and the corresponding profile likelihood ratio maximized [98]. The common  
1403 parameter of interest (POI) is the signal strength of a 2HDM+ $a$  signal at a particular point  
1404 in the parameter space, defined as the ratio of the observed number of signal event to  
1405 the signal cross-section times branching ratio. Systematic uncertainties are introduced to  
1406 the likelihood as constrained nuisance parameters (NPs), denoted by  $\theta_\mu$ , and modelled by  
1407 Gaussian, Poisson, or Log-normal probability density function. Background normalization  
1408 factors, denoted by  $\lambda_\mu$ , are floated without constraints in the fit to estimate the background  
1409 components in their corresponding control regions. The subscript  $\mu$  on these parameter is  
1410 in anticipation of their dependence on the best-fit signal strength.

1411 The combined likelihood is given by

$$L(\text{data}|\mu, \lambda_\mu, \theta_\mu) = \prod_{c=1}^{N_{cats}} L_c(\text{data}|\mu, \lambda_\mu, \theta_\mu) \prod_{k=1}^{N_{cons}} F(\tilde{\theta}_{\mu,k}|\theta_{\mu,k}), \quad (4.13)$$

1412 where  $N_{cats}$  is the number of categories,  $c$  the index of the event category,  $N_{cons}$  the number  
1413 of constrained NPs,  $k$  the index of the NP,  $\tilde{\theta}_{\mu,k}$  the global observable corresponding to  $\theta_k$ , and  
1414  $F$  the constraining probability distribution function corresponding to the type of uncertainty.

1415 The likelihood of observing  $m_c$  events in category  $c$  is

$$L_c(\text{data}|\mu, \lambda_\mu, \theta_\mu) = \frac{n_c^{m_c} e^{-n_c}}{m_c!}, \quad n_c = \mu s_c(\theta_\mu) + \lambda_\mu b_c(\theta_\mu), \quad (4.14)$$

1416 in which  $s_c$  and  $b_c$  are expected signal and background yields. The likelihood can be globally  
1417 maximized or conditional on a particular value of  $\mu$ .

1418 The 95% confidence level (CL) limits are obtained by the CLs frequentist formalism [146]

1419 using the profile likelihood ratio test statistics ( $q_\mu$ ) [98], defined as

$$q_\mu = \begin{cases} -2 \ln \frac{L(\text{data}|\mu, \hat{\lambda}_\mu, \hat{\theta}_\mu)}{L(\text{data}|0, \hat{\lambda}_0, \hat{\theta}_0)} & \hat{\mu} < 0, \\ -2 \ln \frac{L(\text{data}|\mu, \hat{\lambda}_\mu, \hat{\theta}_\mu)}{L(\text{data}|\hat{\mu}, \hat{\lambda}_\mu, \hat{\theta}_\mu)} & 0 \leq \hat{\mu} < \mu, \\ 0 & \hat{\mu} > \mu \end{cases} \quad (4.15)$$

1420 where the numerator is the likelihood maximized for a given fixed value of  $\mu$ , and the  
1421 denominator is the globally maximized likelihood. The single-hat quantities denote the global  
1422 optimum values, while the double-hat quantities denote the optima at  $\mu$ , i.e. a function of  
1423  $\mu$ . The confidence level is determined from the  $p$ -values of the  $b$ -only hypothesis and the  
1424 different  $s + b$  hypotheses,

$$\text{CL}_s = \frac{p_{s+b}}{1 - p_b}. \quad (4.16)$$

1425 Each signal hypothesis corresponds to a particular point in the parameter space. The  $p$ -  
1426 value of the null hypothesis  $p_b$  and the signal hypothesis is obtained by setting  $q_0 = 0$  and  
1427 evaluating  $q_1$  in equation (4.15) respectively and integrating over the corresponding sampling  
1428 distribution [98]. A signal model, i.e. a parameter point, is said to be excluded at 95% CL  
1429 when  $\text{CL}_s < 0.05$ .

### <sup>1430</sup> 4.6.2 Uncertainties and their correlations

<sup>1431</sup> Each of the three analyses treats a particular set of uncertainties. Often times, more  
<sup>1432</sup> than one analysis estimate the same systematic uncertainty, in which case it is correlated in  
<sup>1433</sup> the combination. This section describes this treatment. Most experimental uncertainties are  
<sup>1434</sup> correlated across search channels, namely they are modelled using the same observable in the  
<sup>1435</sup> combined likelihood. They include uncertainties related to the reconstruction of physics ob-  
<sup>1436</sup> jects, the integrated luminosity, and pile-up modelling. Physics object uncertainties include  
<sup>1437</sup> those from electrons, muons, and the jet energy response. Uncertainties from  $b$ -jet identi-  
<sup>1438</sup> fication depend on  $b$ -tagging algorithm and working point, which vary across the analyses.  
<sup>1439</sup> As a result, they are not correlated. Finally, several experimental systematic uncertainties  
<sup>1440</sup> are moderately constrained in a particular analysis, and hence not correlated to avoid phase-  
<sup>1441</sup> space biases. Different assumptions on the correlation of uncertainties related to jet,  $E_T^{\text{miss}}$ ,  
<sup>1442</sup> and  $b$ -jet identification, and other moderately constrained uncertainties are tested to gauge  
<sup>1443</sup> their impact on the observed exclusions, and found to have negligible impact.

<sup>1444</sup> Uncertainties on signal simulation and background modelling are assessed for each analy-  
<sup>1445</sup> sis. To each final state is dedicated a separate signal simulation, as they often probe different  
<sup>1446</sup> kinematic regions of the phase space. The theoretical uncertainties are found to be small  
<sup>1447</sup> and are considered to be uncorrelated. Uncertainties pertaining to background modelling  
<sup>1448</sup> are considered correlated amongst the analyses, motivated by their different sources of lead-  
<sup>1449</sup> ing background, different probed kinematic phase space, as well as different methods of  
<sup>1450</sup> background estimation.

### <sup>1451</sup> 4.6.3 The impact of uncertainties

<sup>1452</sup> Different 2HDM+ $a$  parameter values correspond to different signal kinematics and sen-  
<sup>1453</sup> sitivity delivered by each analysis, and thus see different levels of impact from uncertainties  
<sup>1454</sup> on the combined signal strength. As an example, the contributions to the uncertainty of the

best fit signal strength from statistical and systematic uncertainties are shown in table 4.6  
 for a parameter point at  $m_a = 450$  GeV,  $m_H = 800$  GeV,  $\tan \beta = 1.0$ , and  $\sin \theta = 0.35$ .  
 This signal is not excluded by any single input analysis, but is excluded by the combination.  
 The statistical uncertainty is slightly smaller than the systematic counterpart, which is bro-  
 ken into three categories: theoretical, experimental, and MC statistical uncertainties. The  
 impact of each category is estimated by fixing the uncertainties in that category in a fit, and  
 subtracting the resulting uncertainty in the signal strength from the total in quadrature.  
 Theoretical uncertainties arise mainly from uncertainties in background modelling and are  
 slight smaller than experimental ones. Among the experimental uncertainties originating  
 from reconstructed physics objects, those from jet and  $E_T^{\text{miss}}$  make the largest contributions.

For each input analysis, the most important uncertainties also make the largest con-  
 tribution to the combined uncertainty. For background modelling, the largest components  
 are  $ZZ$  modelling from  $E_T^{\text{miss}} + Z(\ell\ell)$ ,  $t\bar{t}$  uncertainties from  $E_T^{\text{miss}} + h(bb)$ , and uncertainties  
 from  $t\bar{t}$  production with additional  $b$  quarks from  $tbH^\pm(tb)$ . Among experimental systematic  
 uncertainties, the largest sources are lepton systematic uncertainties from  $E_T^{\text{miss}} + Z(\ell\ell)$ , un-  
 certainties related to jets and  $E_T^{\text{miss}}$  from  $E_T^{\text{miss}} + h(bb)$ , and those related to  $b$ -jet identification  
 from  $tbH^\pm(tb)$ .

## 4.7 Results on combined constraints on the 2HDM+ $a$

A summary of combined constraints on 2HDM+ $a$  across all benchmark scenarios intro-  
 duced in section 4.2 is presented in this section.

### 4.7.1 Scenario 1: $m_a - m_A$ planes

Figure 4.8 shows the exclusion contours from the  $m_a - m_A$  scans with the 2HDM mixing  
 angle fixed to  $\sin \theta = 0.35$  in 4.8a and 4.8c, and  $\sin \theta = 0.7$  in 4.8b and 4.8d. These choices

Uncertainty source	$\Delta\mu \cdot 100$
Statistical uncertainty	25.0
Systematic uncertainty	27.6
Theory uncertainties	16.2
Signal modelling	2.8
Background modelling	15.9
Experimental uncertainties (excl. MC stat.)	18.8
Luminosity, pile-up	3.9
Jets, $E_T^{\text{miss}}$	12.3
Identification of $b$ -jets	9.1
Electrons, muons	6.1
MC statistical uncertainty	9.3
Total uncertainty	37.2

**Table 4.6:** Impact from different sources of uncertainties on the best-fit signal strength express in  $\Delta\mu$  on the signal at ( $m_A = 800 \text{ GeV}$ ,  $m_a = 450 \text{ GeV}$ ,  $\tan\beta = 1$ ,  $\sin\theta = 0.35$ ), estimated by fixing the corresponding NPs to their best-fit values, and subtracting the resulting uncertainty from the total uncertainty in quadrature. The statistical uncertainty component is obtained by fixing all NPs except the floating background normalization factors, and quantifies the impact of the limit data yields in the signal and control regions. The total uncertainty is not the quadratic sum of the individual contribution due to correlations between systematic uncertainties [90].

of parameters correspond to benchmark scenarios 1a and 1b in section 4.2. The combined exclusion contours are shown along with those of the three individual channels entering the statistical combination in 4.8a and 4.8b, and with the remaining channels in 4.8b and 4.8d. Over the two benchmark parameter planes, the  $E_T^{\text{miss}} + Z(\ell\ell)$  and  $E_T^{\text{miss}} + h(b\bar{b})$  drive the sensitivity across a large region, due primarily to the resonant production of the scalar and pseudo-scalar according to the diagram in figures 4.1a and 4.2a. Their sensitivity varies widely with the pseudo-scalar Higgs boson and the mediator masses. At  $\sin \theta = 0.35$  and in the region where  $E_T^{\text{miss}} + Z(\ell\ell)$  and  $E_T^{\text{miss}} + h(b\bar{b})$  dominate, all pseudo-scalar mass is excluded up to a maximum  $m_a = 560$  GeV for  $m_A = 1.2$  TeV, while for  $m_a = 1.5$  GeV, all pseudo-scalar Higgs mass is excluded up to  $m_A = 1.55$  TeV. At  $\sin \theta = 0.7$ , all pseudo-scalar mass is excluded up to a maximum  $m_a = 550$  GeV for  $m_A = 1$  TeV, while for  $m_a = 400$  GeV, all pseudo-scalar Higgs mass is excluded up to  $m_A = 1.2$  TeV. For both choices of  $\sin \theta$ , the  $E_T^{\text{miss}} + Z(\ell\ell)$  contour reaches closer to the  $m_A = m_a$  limit than that of  $E_T^{\text{miss}} + h(b\bar{b})$ , because the former can probe lower  $E_T^{\text{miss}}$  values, whereas the latter is sensitive at higher  $E_T^{\text{miss}}$  due to the presence of a  $E_T^{\text{miss}}$  trigger in its selection and the mass difference between the  $Z$  and the Higgs bosons. In addition, the exclusion power of  $E_T^{\text{miss}} + h(b\bar{b})$  is increased relative to  $E_T^{\text{miss}} + Z(\ell\ell)$  at high  $m_A$  and low  $m_a$ , because of an increase in the cross-section of the non-resonant  $a^* \rightarrow ah$  process, without resonant  $A$  production, which has no equivalence in the latter's signature.

For both values of  $\sin \theta$ , the  $tbH^\pm(tb)$  channel excludes complementary regions where the other channels provide less exclusion power. For  $\sin \theta = 0.35$  all pseudo-scalar Higgs mass up to  $m_A \leq 700$  GeV is excluded, and for  $\sin \theta = 0.7$ , the upper bound of the excluded  $m_A$  ranges from 600 GeV to 700 GeV. The weak dependence on the mediator mass  $m_a$  is due to the absence of the mediator in its signature, such that its sensitivity is only indirectly affected by  $m_a$  via the competition from other possible decay modes, for instance  $H^\pm \rightarrow aW^\pm$ . The reduction in branching ratio is observed at  $\sin \theta = 0.7$ , where the limits from this channel weakens at lower  $m_a$ , where the aforementioned decay

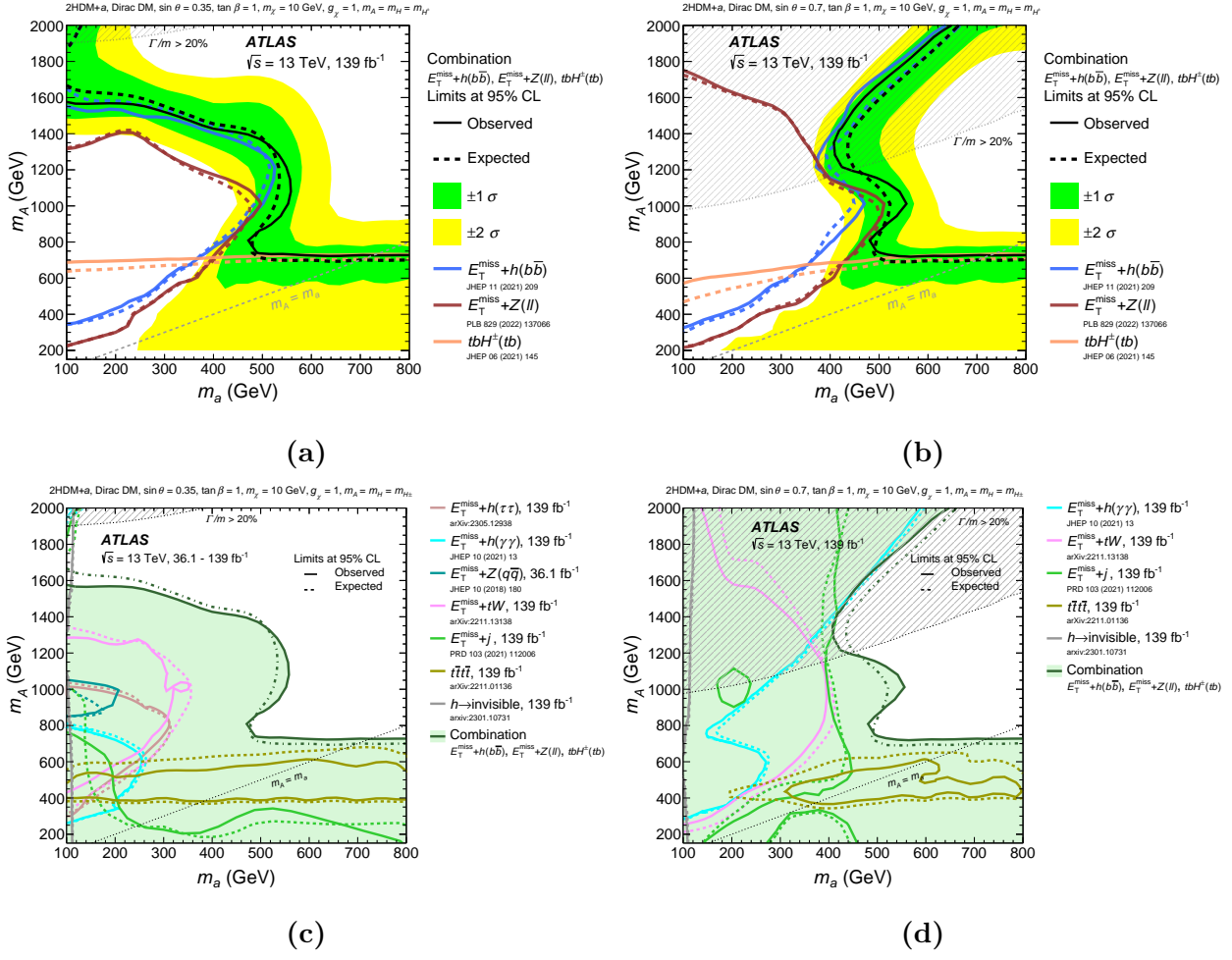


**Figure 4.8:** Observed and expected exclusion regions at 95% CL over the  $(m_a, m_A)$  plane evaluated at 2HDM+ $a$  mixing angles  $\sin \theta = 0.35$  (subfigures (a), (c)), and  $\sin \theta = 0.7$  (subfigures (b), (d)). The observed and expected contours are respectively shown in solid and dashed lines in all subsequent figures. In (a) and (b), the observed and expected exclusion limits from each of the three statistically combined signatures are shown along with the combined limits. The green and yellow shared bands respectively correspond to the  $\pm 1$  and  $\pm 2$  standard deviation uncertainty in the combined expected limits. In (c) and (d), the combined exclusion contours are overlaid along those of additional channels not included in the statistical combination. In all subfigures, a dashed grey region indicates the region where the width of any of the Higgs boson exceeds 20% of its mass [90].

1505 is kinematically possible. The statistical combination with  $tbH^\pm(t)$  augments the excluded  
 1506 parameter space above  $m_a = 500$  GeV and below  $m_A = 700$  GeV for both scenarios.

1507 The exclusion power of other channels not entering the statistical combination varies  
 1508 widely and is demonstrated on figures 4.8c and 4.8d. The  $E_T^{\text{miss}} + h(\gamma\gamma)$  search probes a  
 1509 region in the parameter space that is similar in shape to that of the  $E_T^{\text{miss}} + h(b\bar{b})$  search,  
 1510 only smaller due to the smaller branching ratio of the  $h \rightarrow \gamma\gamma$  decay relative to the  $h \rightarrow b\bar{b}$   
 1511 decay. At lower values of  $m_A$  however, it becomes more sensitive than  $E_T^{\text{miss}} + h(b\bar{b})$ , as it  
 1512 does not rely on the  $E_T^{\text{miss}}$  trigger and is capable of probing smaller values of  $E_T^{\text{miss}}$ , similar to  
 1513 the better sensitivity of  $E_T^{\text{miss}} + Z(\ell\ell)$  relative to  $E_T^{\text{miss}} + h(b\bar{b})$  in the same region. Similar to  
 1514 the  $E_T^{\text{miss}} + h(b\bar{b})$  search, the  $E_T^{\text{miss}} + h(\gamma\gamma)$  shows a significant boost in sensitivity at higher  
 1515  $m_A$  for  $\sin\theta = 0.7$ , due to an increase in the cross-section of the  $a \rightarrow ah$  process.

1516 The  $E_T^{\text{miss}} + h(\tau\tau)$  search is only interpreted at  $\sin\theta = 0.35$ , and its exclusion contour  
 1517 has a similar shape to that of other  $E_T^{\text{miss}} + h$  signatures, but is even smaller in coverage due  
 1518 to a small branching ratio relative to the  $h \rightarrow b\bar{b}$  final state.

1519 The exclusion contours of the  $E_T^{\text{miss}} + tW$  search have a similar shape to those of the  
 1520  $E_T^{\text{miss}} + Z(\ell\ell)$  search for both values of  $\sin\theta$ , albeit smaller in exclusion area. The observed  
 1521 exclusion consistently covers a smaller area of the phase space than the expected sensitivity,  
 1522 due to a small excess in the 2-lepton channel of less than  $2\sigma$  significance [48].

1523 The sensitivity of the  $E_T^{\text{miss}} + j$  search shows interesting features on the  $m_a - m_A$  plane.  
 1524 The signature does not contain resonant production as in the case of the  $Z/h$  boson in figures  
 1525 4.1a and 4.2a. Therefore, the exclusion contour differ significantly from the  $E_T^{\text{miss}} + Z$  and  
 1526  $E_T^{\text{miss}} + h$  signatures. In addition, the signal cross-section is affected by the inference between  
 1527 non-resonant contributions from the pseudo-scalars  $a$  and  $A$ , which depends on both  $m_a$   
 1528 and  $m_A$ , especially at the larger value of the mixing angle  $\sin\theta$  [68]. A small difference in  
 1529 pseudo-scalar mass ( $m_a \approx m_A$ ) leads to destructive interference, reducing the signal cross-  
 1530 section and thus the sensitivity to the 2HDM+ $a$ . This effect is observed for both values

of  $\sin \theta$ . At  $\sin \theta = 0.35$ , the  $E_T^{\text{miss}} + j$  search excludes values of  $m_a$  up to 600 GeV for  $m_A \approx 200$  GeV, and values of  $m_A$  up to 800 GeV for  $m_a \approx 100$  GeV. At  $\sin \theta = 0.7$ , stronger mixing leads to higher cross-sections for signal hypotheses with  $m_A > m_a$ . For  $m_A \approx 1300$  GeV, all values of  $m_a$  up to  $\approx 400$  GeV are excluded, comparable to the exclusion power of the  $E_T^{\text{miss}} + Z(\ell\ell)$  and  $E_T^{\text{miss}} + h(b\bar{b})$  searches.

The  $t\bar{t}t\bar{t}$  search is sensitive in regions where the  $E_T^{\text{miss}} + Z(\ell\ell)$  and  $E_T^{\text{miss}} + h(b\bar{b})$  searches have lower sensitivity, similar to the  $tbH^\pm(tb)$  search. However, unlike the latter, it is only sensitive to the 2HDM+ $a$  when either of the pseudo-scalar masses is above the production threshold of a top quark pair ( $m_{A/a} \geq 2m_t$ ). For  $\sin \theta = 0.35$ , the contour is almost independent of  $m_a$ , driven largely by the resonant production of the heavy Higgs bosons  $A/H$ . For  $\sin \theta = 0.7$ , the sensitivity is lowered for small  $m_a$  compared to the scenario with  $\sin \theta = 0.35$  due to a larger  $a/A$  and a forbidden  $a \rightarrow t\bar{t}$  decay.

The exclusion contours from the  $E_T^{\text{miss}} + Z(q\bar{q})$  search on 36  $\text{fb}^{-1}$  data are shown for scenario 1a [23]. The search provides the smallest sensitivity because it suffers from larger multijet production backgrounds and smaller data sample.

#### 4.7.2 Scenario 2: $m_A - \tan \beta$ planes

Figure 4.9 summarizes the exclusion limits over the  $m_A - \tan \beta$  parameter plane evaluated with  $\sin \theta = 0.35$  and  $\sin \theta = 0.7$ . In both scenarios, a large portion of the parameter plane is excluded by the combined contours. At  $\sin \theta = 0.35$  the combined sensitivity is driven primarily by the  $E_T^{\text{miss}} + Z(\ell\ell)$  search, which is also observed at lower pseudo-scalar mass at  $\sin \theta = 0.7$ . At higher values of  $m_A$ , the  $E_T^{\text{miss}} + h(b\bar{b})$  provides stronger constraints. In general, the sensitivity of these channels is influenced by the transition from  $gg$ - to  $bb$ -initiated production of the  $Z/h$  boson, and finds its minimum in the region around  $\tan \beta = 5$ .

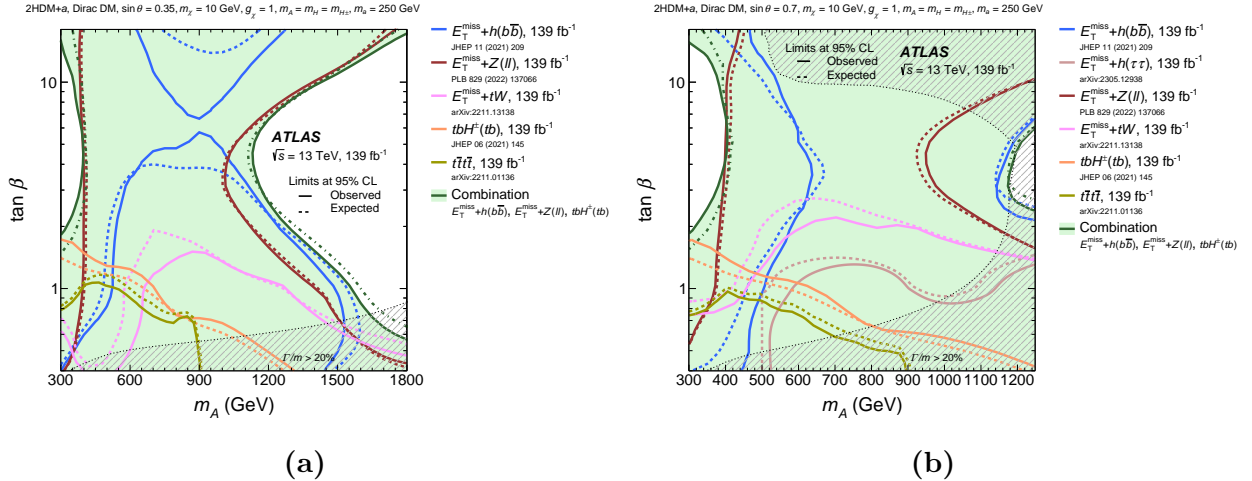


**Figure 4.9:** Observed and expected exclusion regions at 95% CL over the  $(m_A, \tan \beta)$  plane evaluated at 2HDM+ $a$  mixing angles  $\sin \theta = 0.35$  (a), and  $\sin \theta = 0.7$  (b). The statistical combined contours are shown along with those from individual searches. In both subfigures, a dashed grey region indicates the region where the width of any of the Higgs boson exceeds 20% of its mass [90].

1554      The  $E_T^{\text{miss}} + tW$  search excludes regions of the parameter space up to  $\tan \beta = 1.5$  for  
 1555       $\sin \theta = 0.35$  and  $\tan \beta = 2$  for  $\sin \theta = 0.7$ . The observed sensitivity in both scenarios  
 1556      is weaker than the expected counterpart because of a small excess in the two-lepton signal  
 1557      region of the search [48]. The larger mixing angle again shows better sensitivity to the  
 1558       $E_T^{\text{miss}} + tW$  signature [139].

1559      The exclusion contour from the  $E_T^{\text{miss}} + h(\tau\tau)$  search is evaluated as a function of  $m_A$   
 1560      and  $\tan \beta$  only at  $\sin \theta = 0.7$ . Because of the small branching ratio of the  $h \rightarrow \tau\tau$  decay, it  
 1561      has low sensitivity for the 2HDM+ $a$  signal.

1562      The  $t\bar{t}t\bar{t}$  and  $tbH^\pm(tb)$  searches provide sensitivity at low values of  $m_A$  and  $\tan \beta$ , due to  
 1563      enhanced production cross-section for smaller resonance masses and a preference for coupling  
 1564      to third generation quarks in this region.

### 1565 4.7.3 Scenario 3: $m_a$ – $\tan \beta$ planes

1566 Figure 4.10 summarizes the exclusion limits as a function of the  $m_a$  and  $\tan \beta$  evaluated  
 1567 at  $\sin \theta = 0.35$  (scenario 3a) and  $\sin \theta = 0.7$  (scenario 3b). In both scenarios, the  $E_T^{\text{miss}} +$   
 1568  $Z(\ell\ell)$  search drives the sensitivity over a large portion of the parameter plane. The  $E_T^{\text{miss}} +$   
 1569  $h(b\bar{b})$  and  $E_T^{\text{miss}} + h(\gamma\gamma)$  searches exclude analogous regions, albeit the latter covers a smaller  
 1570 area, due to the smaller  $h \rightarrow \gamma\gamma$  branching ratio. Both channels observe decreased sensitivity  
 1571 at  $\tan \beta \approx 5$  as the  $gg$ -initiated production transitions to the  $bb$ -initiated counterpart.

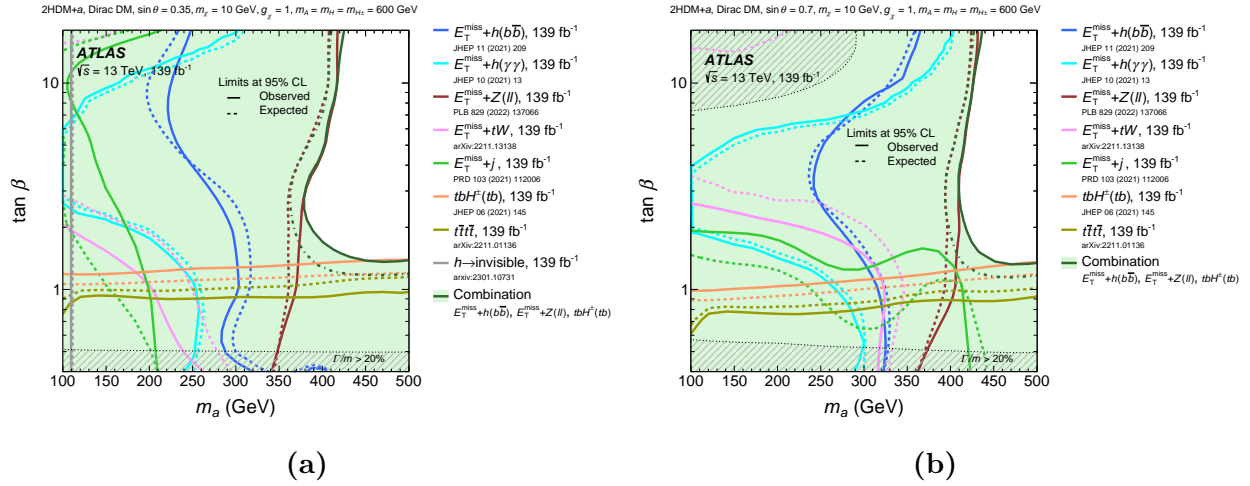


**Figure 4.10:** Observed and expected exclusion regions at 95% CL over the  $(m_a, \tan \beta)$  plane evaluated at 2HDM+ $a$  mixing angles  $\sin \theta = 0.35$  (a), and  $\sin \theta = 0.7$  (b). The statistical combined contours are shown along with those from individual searches. In both subfigures, a dashed grey region indicates the region where the width of any of the Higgs boson exceeds 20% of its mass [90].

1572 The  $E_T^{\text{miss}} + tW$  search excludes regions of the parameter space at low  $\tan \beta$  and low  
 1573  $m_a$ . Better sensitivity is observed for the larger  $A/a$  mixing angle.

1574 The  $E_T^{\text{miss}} + j$  search excludes signal hypotheses characterized by low values of  $m_a$  and  
 1575  $\tan \beta$ , and its sensitivity is enhanced at  $\sin \theta = 0.7$  due to more significant  $a/A$  mixing,  
 1576 enlarging the signal cross-sections for  $m_A > m_a$ .

1577        The  $h \rightarrow$  invisible decay suffers from small branching ratio and thus provides sensitivity  
1578 at low values of  $m_a$ , independent of  $\tan\beta$ .

1579        The  $t\bar{t}t\bar{t}$  and  $tbH^\pm(t)$  searches constrain regions complementary to the  $E_T^{\text{miss}} + X$  signa-  
1580 tures. It is sensitive at low  $\tan\beta$  and almost independent of  $m_a$ .

#### 1581 4.7.4 Scenario 4: Variation of $\sin\theta$

1582        Figure 4.11 summarizes the exclusion limits as a function of  $\sin\theta$  for the 2HDM+ $a$  under  
1583 both low- and high-mass mediator hypotheses. The upper row shows the results for the  
1584 baseline parameter choice of Scenario 4, in which  $\tan\beta = 1.0$ , and the lower row additional  
1585 results obtained for alternative values of  $\tan\beta$ , namely  $\tan\beta = 0.5$  and  $\tan\beta = 50$ .  
1586 Exclusion limits shown in the subfigures on the left are derived at  $m_A = 600$  GeV,  $m_a = 200$   
1587 GeV, corresponding to scenario 4a and the low-mass hypothesis, and those on the right at  
1588  $m_A = 1.0$  TeV,  $m_a = 350$  GeV, corresponding to scenario 4b and the high-mass hypothesis.  
1589 The exclusion limits are represented by the ratio of the excluded cross-section to the nominal  
1590 cross-section of the signal model.

1591        For the low-mass hypothesis at  $\tan\beta = 1.0$ , the most stringent limits in the region of  
1592 medium to high values of  $\sin\theta$  are set by the  $E_T^{\text{miss}} + Z(\ell\ell)$  and  $E_T^{\text{miss}} + h(b\bar{b})$  searches. The  
1593 sensitivity of the former increases monotonically with  $\sin\theta$ , as the cross-section of both non-  
1594 resonant and resonant production mechanisms, illustrated in figures 4.2 and 4.1, grows with  
1595  $\sin\theta$ . On the other hand, the production diagrams contributing to the  $E_T^{\text{miss}} + h$  signature  
1596 show a different dependence on  $\sin\theta$ , as discussed in references [68, 23]. The relative  
1597 contributions of each diagram are further affected by the different selections employed by  
1598 the  $E_T^{\text{miss}} + h(b\bar{b})$  and  $E_T^{\text{miss}} + h(\gamma\gamma)$  analyses, both of which reach a the maximum sensitivity  
1599 around  $\sin\theta = 0.5$ .

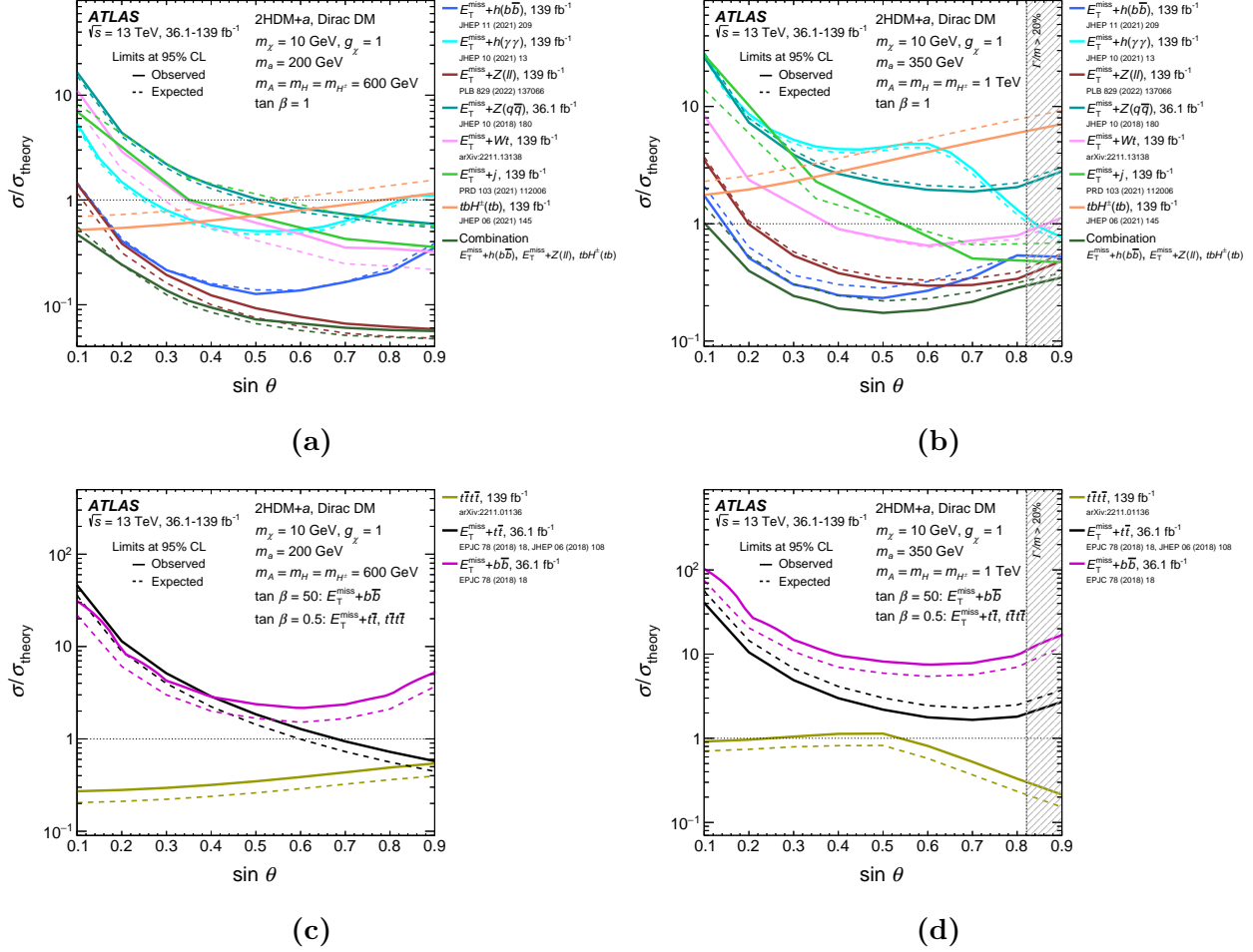


**Figure 4.11:** Observed and expected exclusion limits at 95% CL for the 2HDM+ $a$  as a function of  $\sin \theta$  plane evaluated under benchmark scenarios 4. In subfigures (a) and (b), the results are derived at  $\tan \beta = 1$ , while in (c) and (d) they are derived at  $\tan \beta = 0.5$  or  $\tan \beta = 50$ . (a) and (c) represent the sensitivity at low pseudo-scalar mass, in particular  $m_A = 600$  GeV and  $m_a = 200$  GeV, and (b) and (d) the high-mass regime, namely  $m_A = 1.0$  TeV and  $m_a = 350$  GeV. The combined exclusion is shown along with individual searches. In all subfigures, a dashed grey region indicates the region where the width of any of the Higgs boson exceeds 20% of its mass [90].

The sensitivity of both  $E_T^{\text{miss}} + h(b\bar{b})$  and  $E_T^{\text{miss}} + tW$  searches also monotonically increases with  $\sin \theta$ , similar to that of the  $E_T^{\text{miss}} + Z(\ell\ell)$  signature, albeit an order of magnitude lower than the latter. This is due to the smaller cross-sections of these processes. Meanwhile, the

1603  $tbH^\pm(tb)$  and  $t\bar{t}t\bar{t}$  signatures see a dependence on  $\sin\theta$  compared to other signatures, since  
1604 they are not directly sensitive to neutral boson production. They are particularly sensitive  
1605 at small mixing angle, with the sensitivity of  $tbH^\pm(tb)$  exceeding that of the  $E_T^{\text{miss}} + Z/h$   
1606 searches at  $\sin\theta < 0.2$ .

1607 For the high-mass hypothesis at  $\tan\beta = 1.0$ , the light pseudo-scalar mass is sufficiently  
1608 large to kinematically allow the  $a \rightarrow t\bar{t}$  decay, introducing an additional  $\sin\theta$  dependence  
1609 in the interpretation of the  $E_T^{\text{miss}} + Z/h$  searches. Consequently, the highest sensitivity for  
1610 these analyses is observed near or just below the maximal mixing condition  $\theta = \pi/4$ .

1611 In the case of the  $E_T^{\text{miss}} + h$  searches, there is a more complex dependence on  $\sin\theta$ , owing to  
1612 different contributions from the resonant and non-resonant productions of the Higgs boson  
1613 to the final selection of each analysis. In particular, the  $E_T^{\text{miss}} + h(b\bar{b})$  signature displays  
1614 in a broad peak at values of  $\sin\theta$  slightly below the maximal mixing. In contrast, the  
1615  $E_T^{\text{miss}} + h(\gamma\gamma)$  shows a local sensitivity minimum around  $\sin\theta \approx 0.6$ .

1616 The  $E_T^{\text{miss}} + tW$  search follows a similar  $\sin\theta$  dependence as the  $E_T^{\text{miss}} + Z(\ell\ell)$  and  
1617  $E_T^{\text{miss}} + h(b\bar{b})$  searches, but remains approximately an order of magnitude below the combined  
1618 sensitivity. On the other hand, the  $E_T^{\text{miss}} + j$  demonstrates a monotonic increase in sensitivity  
1619 and reaches a level similar to that of the  $E_T^{\text{miss}} + Z(\ell\ell)$  and  $E_T^{\text{miss}} + h(b\bar{b})$  searches at large  
1620  $\sin\theta$ . Results from the  $E_T^{\text{miss}} + V(q\bar{q})$  search are shown for completeness [23].

1621 Alternative values  $\tan\beta = 0.5$   $\tan\beta = 50$  are considered for Scenario 4 to illustrate the  
1622 strong dependence of the exclusion limits on  $\tan\beta$ , particularly in searches that are sensitive  
1623 to the Yukawa couplings of the neutral Higgs bosons and the mediator to fermions in a Type-II  
1624 2HDM. At low  $\tan\beta$ , the scalar and pseudo-scalar states couple primarily to top quarks,  
1625 whereas at high  $\tan\beta$ , they predominantly couple to bottom quarks. Therefore, the results  
1626 of the  $t\bar{t}t\bar{t}$  search are shown for  $\tan\beta = 0.5$ . The sensitivity of this search is generally  
1627 higher in the low-mass scenario relative to the high-mass counterpart, mainly due to the  
1628 reduced production cross-section of the heavy Higgs bosons  $A/H$  at higher  $m_{A/H}$ . However,

in the high-mass scenario, an enhancement in sensitivity is observed for  $\sin \theta > 0.5$ , and attributed to the increased  $a/A$  mixing and the fact that the mediator mass is sufficiently large to kinematically allow a decay into a pair of top quarks. At the same time, the mediator mass remains significantly below the masses of the heavy Higgs bosons, leading to the  $t\bar{t}t\bar{t}$  signal cross-section being dominated entirely by  $t\bar{t} + a(t\bar{t})$  production.

For completeness, results from the  $E_T^{\text{miss}} + t\bar{t}$  and  $E_T^{\text{miss}} + b\bar{b}$  searches reported in reference [23] are included for  $\tan \beta = 0.5$  and  $\tan \beta = 50$ , respectively.

#### 4.7.5 Scenario 5: Variation of $m_\chi$

In Figure 4.12, the sensitivity of various searches as a function of the fermion dark matter mass  $m_\chi$ , which has the strongest impact on the relic density predicted by the 2HDM+ $a$ , is shown. The sensitivity is evaluated as the observed exclusion limit on the ratio of the excluded cross-section to the nominal cross-section of the signal model. The relic density is overlaid on the plot as a long-dashed line. A notable feature of the relic density occurs around  $m_\chi = m_a/2 = 200$  GeV, known as the  $a$ -funnel region, where the predicted density is depleted by the resonant enhancement of the process  $\chi\bar{\chi} \rightarrow a \rightarrow \text{SM}$  [101, 64, 1]. A second resonant, occurring at  $m_\chi = m_A/2 = 500$  GeV, corresponding to a second funnel region, is not fully covered within the probed  $m_\chi$  range but nevertheless visible as a decrease in the predicted relic density for  $m_\chi > 400$  GeV. For  $m_\chi > 200$  GeV, the relic density reaches a plateau due to the increase in annihilation cross-section of the DM particles near the kinematic threshold of the processes  $\chi\bar{\chi} \rightarrow t\bar{t}$  (if  $m_\chi > m_t$ ) and  $\chi\bar{\chi} \rightarrow ah$  (if  $m_\chi > (m_a + m_h)/2$ ).

For all considered signatures, the sensitivity becomes independent of  $m_\chi$  as long as the pseudo-scalar mediator, whose mass is fixed at 400 GeV in this benchmark scenario, can decay into a pair of DM particles. The most stringent constraints in the region where  $m_\chi < 200$  GeV are provided by the  $E_T^{\text{miss}} + Z(\ell\ell)$  search. Together with the  $E_T^{\text{miss}} + h(b\bar{b})$ ,

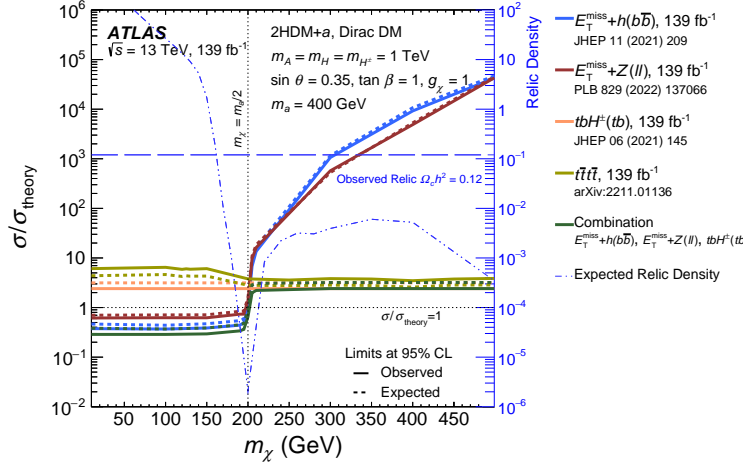


**Figure 4.12:** Observed and expected exclusion limits at 95% CL for the 2HDM+ $a$  as a function of the dark matter particle mass  $m_\chi$  evaluated under benchmark scenario 5 following  $m_A = 1.0$  TeV,  $m_a = 400$  GeV,  $\tan \beta = 1.0$ , and  $\sin \theta = 0.35$ . The limits are expressed in terms of the ratio of the excluded cross-section to the nominal cross-section of the signal model. The results from several individual searches are shown along with the combined limits. The relic density for each  $m_\chi$  assumption, calculated with MADDM [10], is superimposed on the plot in dashed line [90].

it excludes this part of the parameter space. However, at higher DM masses, the sensitivity of the  $E_T^{\text{miss}} + Z/h$  searches rapidly decreases, while that of the  $tbH^\pm(tb)$  and  $t\bar{t}t\bar{t}$  searches remains largely constant. This is because the corresponding leading-order signal processes do not involve the DM particle  $\chi$ , rendering their signal cross-sections independent of  $m_\chi$ .

For  $m_\chi > m_a/2$ , the  $tbH^\pm(tb)$  search provides the strongest constraints, probing cross-sections as low as  $\sigma = 2\sigma_{\text{theory}} - 3\sigma_{\text{theory}}$ . None of the searches exclude the 2HDM+ $a$  in this mass range under the chosen benchmark scenario. It is possible to match the observed relic density for  $m_\chi = 170$  GeV without changing the collider phenomenology, though this mass value is disfavored by the considered analyses.

It is important to emphasize that the relic density considerations primarily serve as a tool to assess 2HDM+ $a$  model predictions in the context of cosmological observations. They should not be interpreted as strict constraints on the model parameters, as the values of the

1666 parameters producing the correct relic density could shift if the model is modified to include  
1667 additional physics at high-energy scales or if an alternative cosmological history is assumed.

1668 **4.7.6 Scenario 6:  $m_a - m_\chi$  plane**

1669 Figure 4.13 presents exclusion limits as a function of  $m_a$  and  $m_\chi$  for Scenario 6. The  
1670  $h \rightarrow aa \rightarrow f\bar{f}f'\bar{f}'$  searches target the region characterized by  $m_a < m_h/2$  and  $m_a <$   
1671  $2m_\chi$ , which kinematically allows the  $h \rightarrow aa$  decay and forbids the  $a \rightarrow \chi\bar{\chi}$  decay. This  
1672 region is excluded almost entirely by these searches, except for two narrow bands where  $m_a$   
1673 approaches the masses of the  $J/\psi$  and  $\Upsilon$  mesons. Searches for dimuon final states near the  
1674  $J/\psi$  mass are experimentally challenging, as are searches for  $h \rightarrow aa \rightarrow 4g$ . The  $\mu^+\mu^-\tau^+\tau^-$   
1675 final state provides some sensitivity but is not sufficient to exclude the higher mass range  
1676 around  $m_a = 10$  GeV [54]. Similarly, searches for hadronic final states are complicated by  
1677 the collimation of the quark pairs, often necessitating dedicated techniques to enhance the  
1678 sensitivity of signatures such as  $b\bar{b}\gamma\gamma$  and  $b\bar{b}b\bar{b}$ . The  $h \rightarrow aa \rightarrow f\bar{f}f'\bar{f}'$  searches lose sensitivity  
1679 when  $m_a > m_A/2$ , as invisible mediator decays become dominant. For  $m_a < m_h/2$ , this  
1680 region is excluded by the  $h \rightarrow$  invisible search. For larger values of  $m_a$ , the region where  
1681  $m_a > m_\chi$  is excluded by the  $E_T^{\text{miss}} + h(b\bar{b})$  search up to  $m_a \approx 600$  GeV.

1682 The remaining high-mass region is not excluded, and can be probed by searches targeting  
1683 the mediator or heavy Higgs boson final states in  $t\bar{t}t\bar{t}$  and  $tbH^\pm(tb)$  signatures, which are  
1684 currently unable to exclude  $m_A = 1200$  GeV.

1685 The relic density contour for the case  $\Omega_c h^2 = 0.12$  is overlaid on figure 4.13 as a long-  
1686 dashed line. Regions above this line at low  $m_\chi$  and below it at high  $m_\chi$ , with an  
1687 exception of an island around  $(m_\chi \approx 100, m_a \approx 100)$  GeV, have a predicted relic density  
1688  $\Omega_c h^2 < 0.12$ .

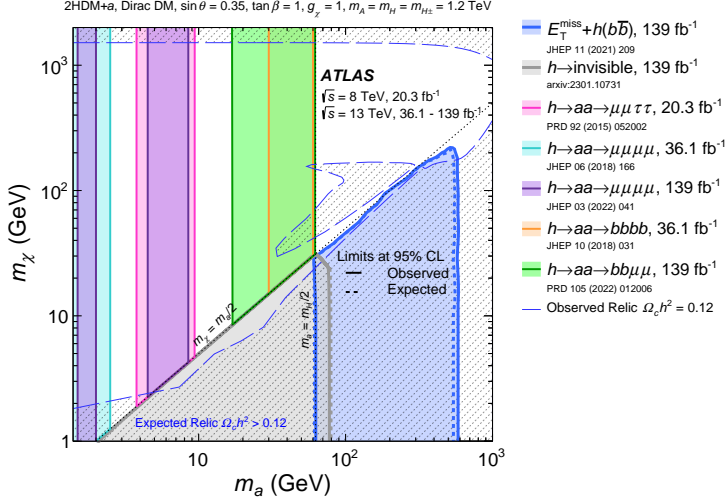


**Figure 4.13:** Observed and expected exclusion limits at 95% CL for the 2HDM+ $a$  as a function of  $m_a$  and  $m_\chi$  evaluated under benchmark scenario 6 following  $m_A = 1.2$  TeV,  $\tan\beta = 1.0$ , and  $\sin\theta = 0.35$ . The relic density contour for the case  $\Omega_ch^2 = 0.12$ , calculated with MADDM [10], is superimposed on the plot in dashed line. The shaded regions mark the region where the model predicts a relic density greater than the observed value  $\Omega_ch^2 = 0.12$ . The island around  $(m_\chi \approx 100, m_a \approx 100)$  GeV corresponds to the resonant enhancement of the process  $\chi\bar{\chi} \rightarrow ah \rightarrow \text{SM}$  that depletes the relic density [90].

1689 Due to the strong Yukawa coupling, the annihilation  $\chi\bar{\chi} \rightarrow t\bar{t}$  is highly efficient. However,  
 1690 in regions of small DM mass ( $m_\chi < m_t$ , the decay is kinematically forbidden, often leading  
 1691 to an overabundance of relic density unless alternative annihilation mechanisms are available.  
 1692 Key processes that help deplete the relic density include resonant annihilation when  $m_\chi \approx$   
 1693  $m_a/2$ , as well as other decay channels such as  $\chi\bar{\chi} \rightarrow aa$ , or  $\chi\bar{\chi} \rightarrow ah$  when they are allowed  
 1694 or kinematically enhanced. For small mediator mass, annihilation into fermions, such as  $b\bar{b}$ ,  
 1695  $c\bar{c}$ , and  $\tau\tau$  can be sufficiently efficient to compensate for their smaller couplings and deplete  
 1696 the relic density. Larger values of  $m_\chi$  can also satisfy the observed relic density, as these  
 1697 annihilations are suppressed.

## 1698 4.8 Conclusion

1699 A wide range of searches for new phenomena performed by the ATLAS Collaboration  
 1700 are summarized and interpreted in the context of a Two-Higgs-Doublet model extended by  
 1701 a pseudo-scalar mediator  $a$ , designated 2HDM+ $a$ . The model extends the Standard Model  
 1702 by introducing two Higgs doublets and an additional pseudo-scalar particle, which mediates  
 1703 interactions between dark matter and the SM particles. It predicts a wide variety of final  
 1704 states, of which the most relevant to DM searches consist of a large missing transverse energy  
 1705 originating from the decay of the mediator  $a$  into DM particles and a mono- $X$ , ( $X = Z, h$ )  
 1706 visible signatures. The majority of searches considered in this summary are based on up to  
 1707  $139 \text{ fb}^{-1}$  of proton-proton collision data at center-of-mass energy of  $\sqrt{s} = 13 \text{ TeV}$  collected  
 1708 by the ATLAS detector during the second run of the Large Hadron Collider. The results are  
 1709 in accordance with Standard Model predictions, as no significant excess is found. They are  
 1710 used to derive constraints on the 2HDM+ $a$  for a diverse selection of benchmark scenarios  
 1711 recommended by the LHC Dark Matter Working Group previously explored, as well as  
 1712 several benchmark scenarios which provide insights into the rich phenomenology of the model.  
 1713 Three searches targeting  $E_T^{\text{miss}} + Z(\ell\ell)$ ,  $E_T^{\text{miss}} + b(b\bar{b})$ , and  $t b H^\pm (tb)$  examine complementary  
 1714 regions of the parameter space, provide the most stringent constraints in many benchmark  
 1715 scenarios, and thus enter a statistical combination to derive an enhanced set of limits on the  
 1716 2HDM+ $a$ .

1717 All benchmark scenarios are simplified by assuming the mass degeneracy of the addi-  
 1718 tional Higgs bosons, namely  $m_A = m_{H^\pm} = m_H$ . The combined result excludes masses of  
 1719 the pseudo-scalar mediator  $a$  up to 560 GeV for  $m_{A/H/H^\pm} = 1.2 \text{ TeV}$ ,  $\sin \theta = 0.35$ , and  
 1720  $\tan \beta = 1.0$  (scenario 1a), and up to 640 GeV for  $m_{A/H/H^\pm} = 2.0 \text{ TeV}$ ,  $\sin \theta = 0.7$ , and  
 1721  $\tan \beta = 1.0$  (scenario 1b). In regions of large heavy Higgs mass ( $m_A$ ), the  $E_T^{\text{miss}} + Z(\ell\ell)$   
 1722 and  $E_T^{\text{miss}} + b(b\bar{b})$  searches are the most sensitive. The results from this benchmark see a

significant improvement over the same scan performed on  $36\text{ fb}^{-1}$  of  $\sqrt{s} = 13\text{ TeV}$  proton-proton collision data, which excludes values of  $m_a$  up to 340 GeV for  $m_{A/H/H^\pm} = 1.0\text{ TeV}$ ,  $\sin\theta = 0.35$ , and  $\tan\beta = 1.0$ . The improvement can be attributed to the full Run 2 dataset, as well as various improvements in the analysis strategies employed by individual searches, and a statistical combination of the most sensitive results.

The interpretation of the  $tbH^\pm(tb)$  in the combined limits represents a novel strategy previously not considered. This signature is the most sensitive of the three combined searches in the low- $m_A$  region where  $m_a > 400\text{ GeV}$ . It allows values of  $m_A$  up to 650 GeV to be excluded across the entire range of examined  $m_a$ , highlighting the importance of searches not classically interpreted in the context of DM in constraining more complex models such as the 2HDM+ $a$ . The statistical combination the  $E_T^{\text{miss}} + Z(\ell\ell)$ ,  $E_T^{\text{miss}} + h(b\bar{b})$ , and  $tbH^\pm(tb)$  searches extends the sensitivity to the 2HDM+ $a$  compared to that of individual analyses across different regions of the parameter space. In addition, the results of searches targeting  $h \rightarrow aa \rightarrow f\bar{f}f'\bar{f}'$  are used for the first time to constrain a part of the parameter space not previously probed. Overall, these results represent the most comprehensive set of constraints on the 2HDM+ $a$  obtained by the ATLAS collaboration to date.

1739

## Part II

1740

Track reconstruction with geometric  
deep learning in the ATLAS ITk

1741

<sub>1742</sub> **Chapter 5**

<sub>1743</sub> **The High Luminosity Large Hadron Collider**

<sub>1744</sub> At the time of writing this thesis in 2025, the LHC has been in operation for over 13  
<sub>1745</sub> years and delivered to each of its general-purpose detectors, ATLAS and CMS, approximately  
<sub>1746</sub>  $350 \text{ fb}^{-1}$  of proton–proton collision data at a peak center-of-mass energy of  $\sqrt{s} = 13 \text{ TeV}$ .  
<sub>1747</sub> Table 5.1 illustrates the energy and quantity of data collected over the LHC runs. An  
<sub>1748</sub> instantaneous luminosity of  $2 \times 10^{34} \text{ cm}^{-1} \text{s}^{-1}$  was achieved in 2018 and has been maintained  
<sub>1749</sub> until now, furnishing an integrated luminosity well above the initial goal of  $300 \text{ fb}^{-1}$ .

Run	Period	Integrated luminosity [ $\text{fb}^{-1}$ ]
1	2010 – 2012	29.2
2	2015 – 2018	159.8
3	2022 – 2025	160.4
Total		349.4

**Table 5.1:** The integrated luminosity delivered to the ATLAS detector by the LHC as of September 2, 2024.

<sub>1750</sub> Even before the nominal LHC operation, the High-Luminosity LHC (HL-LHC) project  
<sub>1751</sub> was established to fully exploit the collider’s discovery potential. The aim is to increase the  
<sub>1752</sub> instantaneous luminosity to  $5 \times 10^{34} \text{ cm}^{-1} \text{s}^{-1}$ , reaching up to  $7.5 \times 10^{34} \text{ cm}^{-1} \text{s}^{-1}$ , 3.75 times  
<sub>1753</sub> higher than the current rate. As such, the total integrated luminosity at the end of the  
<sub>1754</sub> HL-LHC will attain  $3000 \text{ fb}^{-1}$ , 10 times the data planned for the baseline LHC. Increasing

<sub>1755</sub> luminosity proportionately increases the rate of event production  $\langle N \rangle$ , since

$$\langle N_{pp \rightarrow X} \rangle = \mathcal{L} \sigma_{pp \rightarrow X} \quad (5.1)$$

<sub>1756</sub> where  $\mathcal{L}$  and  $\sigma_{pp \rightarrow X}$  are respectively the instantaneous luminosity and the production cross-  
<sub>1757</sub> section of the final state  $X$ . For example, the production cross-section of a Higgs boson  
<sub>1758</sub> is  $\sigma_{pp \rightarrow H} = 50 \text{ pb}$ , so the average Higgs production rate at the current luminosity  $\mathcal{L} =$   
<sub>1759</sub>  $2 \times 10^{34} \text{ cm}^{-1} \text{s}^{-1}$  is

$$\langle N_{pp \rightarrow H} \rangle = [2 \times 10^{34} \text{ cm}^{-1} \text{s}^{-1}] \times [50 \times 10^{-36} \text{ cm}^{-2}] = 1 \text{ Hz}, \quad (5.2)$$

<sub>1760</sub> i.e. one Higgs boson produced every second.

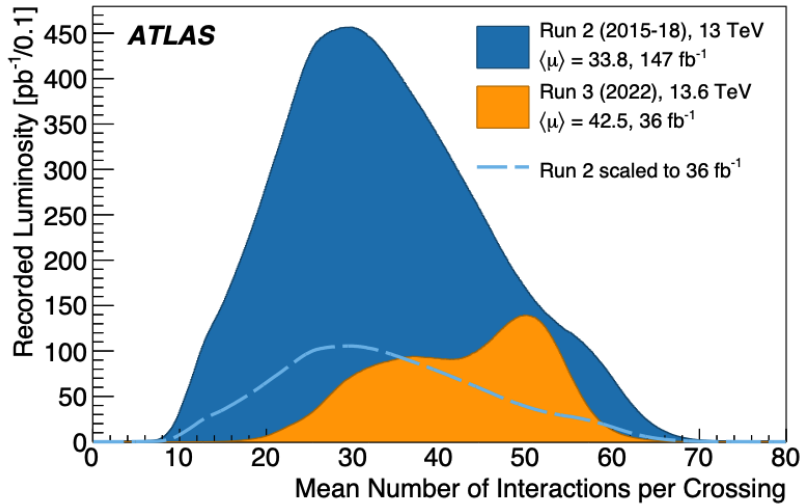


**Figure 5.1:** Distribution of pile-up multiplicity ( $\mu$ ) in proton–proton collision at the ATLAS interaction point during Run 2 and the data taking period in 2022 of Run 3. The dashed line represents a rescaled Run 2 distribution such that its integral is the same as that of the Run 3 distribution.  $\langle \mu \rangle$  denotes the distribution mean. Figure taken from reference [92].

<sub>1761</sub> All interactions that can occur in  $pp$  collision are boosted by higher luminosity. The  
<sub>1762</sub> rate not only of interesting collision events, but also of soft background events increases.  
<sub>1763</sub> The gross number of proton–proton interactions per bunch crossing, called the **pile-up**  
<sub>1764</sub> **multiplicity** and denoted  $\mu$ , can be estimated using equation (5.1) by noting that the total

1765  $pp$  cross-section is of order 100 mb. Figure 5.1 shows the distribution of the average pile-up  
1766 at the ATLAS interaction point during Run 2 and the first year of Run 3. While pile-up  
1767 primarily ranged from 20-40 in Run 2, it peaks around  $\mu = 50$  in a large fraction of events  
1768 recorded by ATLAS in Run 3. The HL-LHC is designed to achieve a peak luminosity of  
1769  $7.5 \times 10^{34} \text{ cm}^{-1} \text{s}^{-1}$ , corresponding to an average pile-up of  $\langle \mu \rangle = 200$ .

1770 To prepare for this major change in operating conditions, the accelerator as well as all  
1771 experiments at the LHC will undergo significant upgrades during the Long Shutdown after  
1772 Run 3, between 2026 and 2029. In the ATLAS Collaboration, both hardware and software  
1773 upgrades will take place, among which the most relevant to this thesis is the replacement  
1774 of the current Inner Detector described in section 3.1.1 by a new all-silicon **Inner Tracker**,  
1775 commonly known as the **ITk**. Chapter 6 describes the design and simulation of the ITk, and  
1776 chapter 7 the current track reconstruction chain, concluding with the challenges associated  
1777 with this process at high pile-up. This difficulty motivates the development of a novel,  
1778 accelerated tracking algorithm which constitutes the rest of this thesis.

1779 **Chapter 6**

1780 **The ATLAS Inner Tracker**

1781 The Inner Tracker (ITk) is the successor to the current Inner Detector (ID) in the High-  
1782 Luminosity era. It inherits many design features from the Pixel and SCT components of the  
1783 ID, but with significant improvements in granularity, geometry coverage, material budget  
1784 and expected parameter resolution. Understanding of its geometry and interaction with  
1785 charged particles is crucial to fully simulate its detector response, extract useful information  
1786 from track candidates, and interpret tracking results. This chapter describes aspects of the  
1787 ITk design and simulation, providing a foundation for the discussion in subsequent chapters.

1788 **6.1 Overview of the Inner Tracker**

1789 The Inner Tracker consists of two silicon-based sub-detectors, a Pixel Detector close to  
1790 the interaction point (IP) and a Strip Detector at a larger radius, and, unlike the Inner  
1791 Detector, without the Transition Radiation Tracker. They feature a total area of  $180\text{ m}^2$   
1792 with more than 5 billion readout channels, in comparison to  $63\text{ m}^2$  and 100 million channels  
1793 in the ID, translating to a significant increase in granularity. In the barrel region, the pixel  
1794 subsystem comprises five layers and the strip subsystem four layers. Each of the endcaps is  
1795 equipped with six strip rings featuring a petal design and many thin pixel rings. The layout  
1796 of the ITk, demonstrated in figure 6.1, is optimized to provide maximal hit coverage across  
1797 the pseudorapidity range.

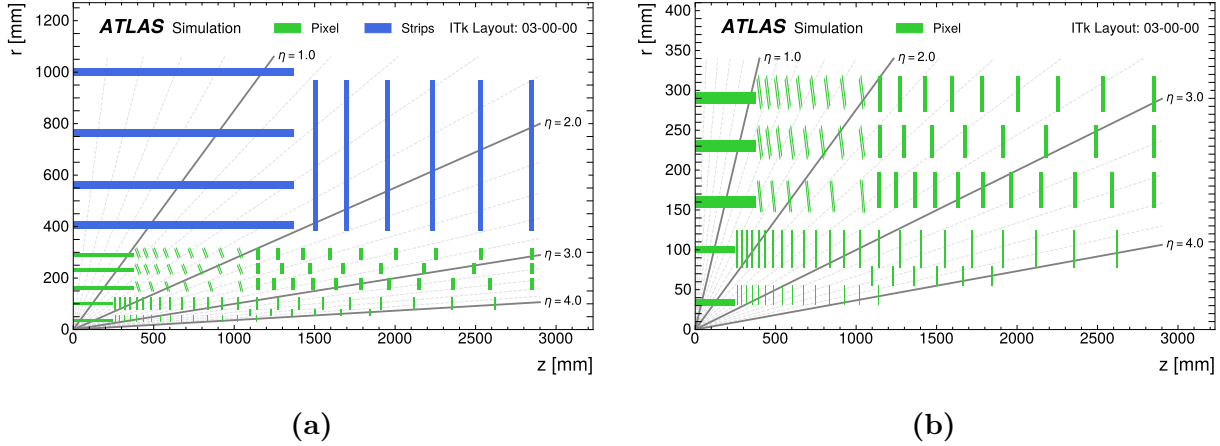


**Figure 6.1:** A schematic view of the ITk layout (a), and of the pixel detector layout (b), both in one quadrant. Only active elements are visible in both figures. Pixel and strip elements are respectively shown in green and blue. The IP is located at the origin. The horizontal axis is parallel to the beam line, and the vertical axis is the radius measured from the IP [95].

1798        The ITk is immersed in a solenoidal magnetic field of 2T, whose principal component  
 1799        lies largely along the  $z$ -axis. The bending power of the magnetic field creates a curvature in  
 1800        the trajectory of a charged particle, from which its transverse momentum  $p_T$  is deduced. In  
 1801        addition, the ITk produces tracking measurements in close proximity to the IP, which plays  
 1802        an important role in impact parameter estimation, vertex fitting and subsequent pile-up  
 1803        mitigation. In addition, the detector is designed to measure at least 9 hits per track in the  
 1804        barrel region and 13 in the endcaps, which provide strong constraints on the curvature of the  
 1805        track. Finally, pseudorapidity coverage is extended up to  $|\eta| = 4$ , in comparison to  $|\eta| < 2.5$   
 1806        in the ID.

1807        The ITk layout plays an important role in simulation and event reconstruction. It has  
 1808        undergone numerous refinements and evolutions since the first layout detailed in the technical  
 1809        design reports [19, 18], with the current edition designated 03-00-00. All subsequent results  
 1810        in this document are evaluated on data simulated using this version.

1811        The pixel system is divided into three subsystems: the Inner System, the Outer Barrel,  
 1812   and the Outer Endcap. The Inner System (IS) encompasses the two innermost layers of the  
 1813   pixel detector, the first of which is located at a radius of 34 mm from the beam pipe. Because  
 1814   of its proximity to the luminous region, the IS is exposed to the highest radiation damage of  
 1815   the entire ITk, and is thus designed to be replaced after  $2000 \text{ fb}^{-1}$  of data has been recorded,  
 1816   when its modules are anticipated to deteriorate. The Outer Barrel (OB) radially covers the  
 1817   IS in the central region at larger radii, and consists of three layers of modules and three  
 1818   sets of endcap rings. As seen on figure 6.1b, the inner rings of the OB are mounted at an  
 1819   incline angle to maximize the angular coverage while using less silicon, and to minimize the  
 1820   material length traversed by a particle having  $1.0 < |\eta| < 2.8$ . The third subsystem, the  
 1821   Outer End-cap (OE), contains three sets of double-sided rings located on each side of the  
 1822   OB at  $|z| \approx 3000 \text{ mm}$ .

1823        The pixel detector uses two different types of silicon sensors, namely 3D and planar  
 1824   sensors, depending on the radiation dose expected at different layers. The former is installed  
 1825   on the innermost layer and rings of the IS due to its radiation hardness, which is improved  
 1826   with respect to the 3D sensors employed in the ID. The rest of the pixel layers and rings  
 1827   uses planar sensors. The dimension of a pixel featured on the 3D sensor is  $25 \mu\text{m}$  in  $R\phi$   
 1828   direction and  $100 \mu\text{m}$  in the longitudinal direction, while the rest of the detector uses  $50 \times 50$   
 1829    $\mu\text{m}^2$  pixels. The small pixel size implies a better resolved cluster shape, and subsequently  
 1830   improves impact parameter resolution. The pixel detector layout in the barrel and endcaps is  
 1831   summarized in tables 6.1 and 6.2. In both tables, the triplet module features three connected  
 1832   read-out chips each processing electronic signals from a  $2 \times 2 \text{ cm}^2$  sensor, and the quad module  
 1833   features 4 connected chips processing signals from a single  $4 \times 4 \text{ cm}^2$  sensor.

1834        The strip detector is divided into two subsystems: the barrel region and two endcap  
 1835   regions with different arrangements of sensor modules. Figure 6.2 shows an overview of the  
 1836   support structure and the arrangement of strip modules in each subsystem. In the barrel  
 1837   region, four cylindrical barrel layers surround the beam line and cover  $|z| < 1.4 \text{ m}$ . Each

Barrel layer	Radius [mm]	Rows of sensors	Flat barrel $ z $ [mm]	Incl. rings per row	Incl. $ z $ [mm]	Module ring	Sensor type	Sensor dim. [ $\mu\text{m}^2$ ]
0	34	12	0-245	24			triplets	$25 \times 100$
1	99	20	0-245	12			quads	$50 \times 50$
2	160	32	0-372	18	380-1035	$2 \times 6$	quads	$50 \times 50$
3	228	44	0-372	18	380-1035	$2 \times 8$	quads	$50 \times 50$
4	291	56	0-372	18	380-1035	$2 \times 9$	quads	$50 \times 50$

**Table 6.1:** Representative parameters of the pixel flat barrel and inclined rings in the ITk layout 03-00-00. Note that while all pixel layers have rings, only the OB features inclined rings. The fifth column provides the number of flat sensors mounted on a complete stave in the central barrel of each layer. The number of inclined rings is given by  $2 \times$  the number of rings on each of the barrel [95].

1838 layer consists of staves running parallel to the  $z$ -axis, on each side of which 14 modules are  
 1839 mounted. The strips on each side of the stave are rotated with respect to the  $z$ -axis by  $\pm 26$   
 1840 mrad to form a stereo angle of 52 mrad between the microstrip on the two sides. Since each  
 1841 microstrip provides a one-dimensional measurement, the stereo angle allows an estimate of  
 1842 a second coordinate from combining the measurements on both side of the stave. The strips  
 1843 on the two inner cylinders are 24.1 mm long and those on the outer two are 48.2 mm long,  
 1844 designated respectively as short- and long-strips. The barrel sensors are tilted in the  $R\phi$   
 1845 plane to allow for an overlap between neighbouring sensors which ensures detection coverage  
 1846 over the entire azimuthal range ( $\phi$ -hermeticity). Table 6.3 shows the number of staves, tilt  
 1847 angle, and strip length on each barrel strip layer.

1848 The endcap region features six disks on each side, the outermost of which is located at  
 1849  $|z| = 3$  m. Each endcap disk is partitioned into 32 identical wedge-shaped petals, and each  
 1850 petal contains nine modules on each side organized into six subsegments referred to as rings  
 1851 (figure 6.2). The strips on each side are constructed with a stereo angle of  $\pm 20$  mrad with  
 1852 respect to the radial line that bisects the petal, achieving a total stereo angle of 40 mrad

Ring layer	Radius [mm]	$ z $ [mm]	Rings	Sensors per ring	Module type	Sensor dim. [ $\mu\text{m}^2$ ]
0	33.20	263-1142	$2 \times 15$	18	triplets	$50 \times 50$
0.5	58.70	1103-1846	$2 \times 6$	30	triplets	$50 \times 50$
1	80.00	263-2621	$2 \times 23$	20	quads	$50 \times 50$
2	154.50	1145.5-2850	$2 \times 11$	32	quads	$50 \times 50$
3	214.50	1145.5-2850	$2 \times 8$	44	quads	$50 \times 50$
4	274.60	1145.5-2850	$2 \times 9$	52	quads	$50 \times 50$

**Table 6.2:** Representative parameters of the pixel endcaps in the ITk layout 03-00-00. The radius in the second column refers to the radius of the circle formed by the innermost point of the sensors on each ring. The number of rings is twice the number of rings on each of the barrel [95].

<sub>1853</sub> between the two sides. Because of the increasing circumferences of the petal rings, each of  
<sub>1854</sub> them has a distinct sensor geometry and electronic arrangement. These features are detailed  
<sub>1855</sub> in the Technical Design Report [19].

## <sub>1856</sub> 6.2 Simulation of the Inner Tracker

<sub>1857</sub> The production of data samples used to study track reconstruction in the ITk proceeds  
<sub>1858</sub> through several steps: event generation, detector simulation using GEANT4 [6], and digitiza-  
<sub>1859</sub> tion of simulated energy deposits. Detector simulation is the costliest and the most difficult  
<sub>1860</sub> step, having to account for complex detector effects on the particle's trajectory. Charged par-  
<sub>1861</sub> ticles interact with the material through which they travel via several mechanisms. Because  
<sub>1862</sub> material interactions can change both the magnitude and direction of particle momentum,  
<sub>1863</sub> an accurate description of the material distribution in the detector is crucial to the modelling  
<sub>1864</sub> of particle trajectories as well as the extraction of track parameters from track candidates.  
<sub>1865</sub> Particular care was taken to describe the material at a high level of detail. The dimensions,

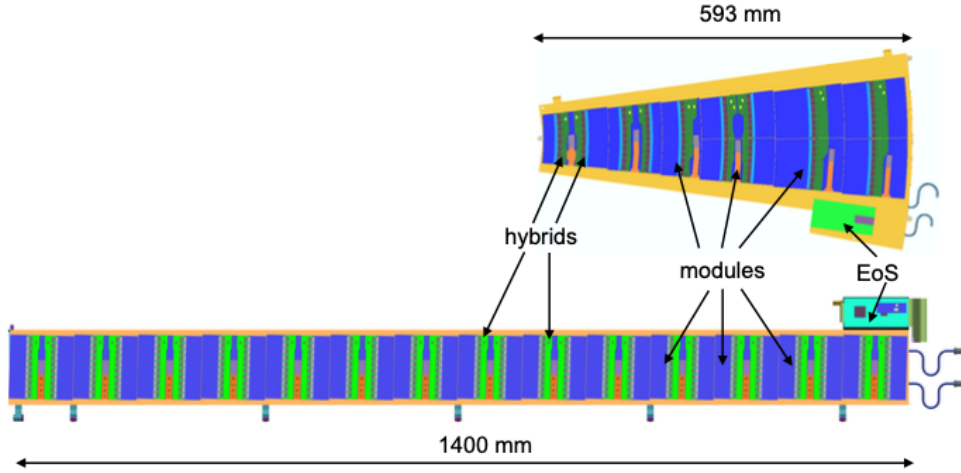


**Figure 6.2:** Overview of the endcap petal (upper) and barrel stave (lower) in the strip detector. Sensor modules shown in blue are mounted directly on a rigid carbon-fiber sandwich structure. Only one half of a stave is shown [19].

1866 location, and material of all detector elements are implemented in the simulation framework.  
 1867 The location of the material is shown in figure 6.3. The materials are defined in GEANT4 in  
 1868 terms of their chemical composition and density.

### 1869 6.2.1 Simulation of the Pixel Detector

1870 The Pixel Detector is divided into a barrel region and two identical endcaps. The outer  
 1871 barrel support structure is modelled using the longeron support structure, shown in figure  
 1872 6.4. The longeron truss structures are approximated as thin sheets of carbon fiber, and the  
 1873 main rails supporting the truss, accounting for 80% of the mass, are modelled by denser  
 1874 materials.

1875 The inner barrel support structure is modelled as truss double shells, with one shell per  
 1876 layer. The shells are modelled as a sheet of carbon fiber behind each row of modules. The  
 1877 total mass of each shell in the support structure is adjusted to match the corresponding

Barrel layer	Number of staves	Radius [mm]	Tilt angle [degree]	Strip length [mm]
0	56	399	13	2.5
1	80	562	12	2.5
2	112	762	12	5
3	144	1000	11	5

**Table 6.3:** Characterization of the strip barrel, including the number of staves, radius, tilt angle, and strip length in the ITk layout 03-00-00 [95].

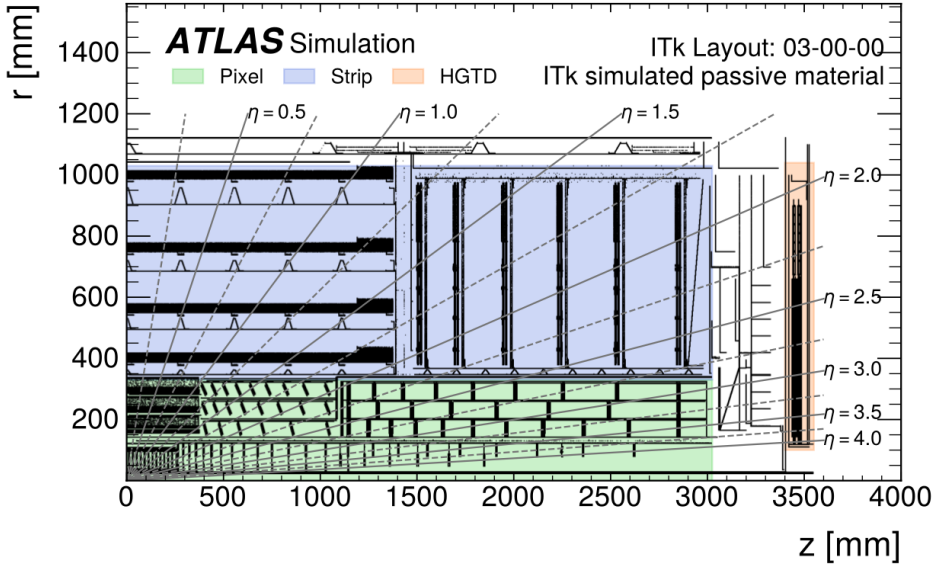


**Figure 6.3:** Location of the materials for one quadrant of the ITk layout 03-00-00. The pixel subsystem is shown in green and surrounded by the strip subsystem shown in blue. The location of the materials are indicated by black regions [1].

<sup>1878</sup> engineering estimate. The outer pixel endcaps are modelled as rings. Each layer of rings is  
<sup>1879</sup> also supported by a cylindrical carbon-fiber shell.

<sup>1880</sup> Pixel modules are modelled as an active sensor volume and a front-end (FE) chip. Layer  
<sup>1881</sup> 0 of both the barrel in the endcaps features 3D pixel sensors. The active part of the sensor

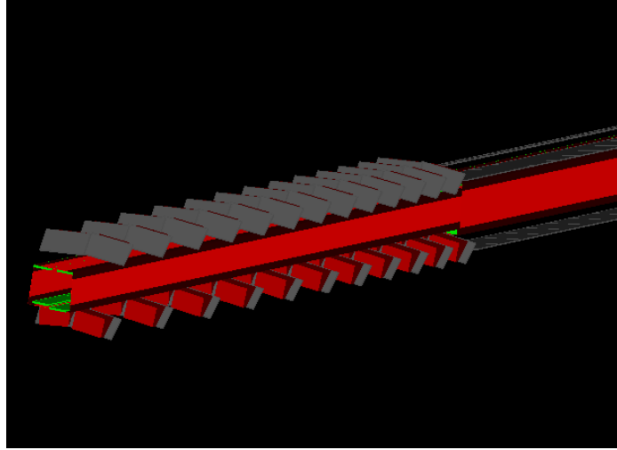


**Figure 6.4:** An illustration of the GEANT4 geometry model of the outer barrel longeron stave with mounted inclined and flat modules. Figure taken from reference [18].

1882 is implemented as a  $150\text{-}\mu\text{m}$  thick layer of silicon and the support wafer as a  $100\text{-}\mu\text{m}$  thick  
 1883 layer of inactive silicon. Other layers feature planar pixel sensors, modelled as  $100\text{-}\mu\text{m}$  and  
 1884  $150\text{-}\mu\text{m}$  thick active silicon respectively in layer 1 and layers 2-4.

1885 Front-end chips are modelled as a  $150\text{-}\mu\text{m}$  thick silicon wafer, with a  $1\text{-}\mu\text{m}$  thick copper  
 1886 layer to model its circuitry, and a Sn-Ag bump bond of  $20\text{-}\mu\text{m}$  in diameter per pixel channel.  
 1887 The material of each component in the FE chips is homogeneously distributed throughout  
 1888 its corresponding volume.

### 1889 6.2.2 Simulation of the Strip Detector

1890 In the strip barrel detector, each individual part is modelled separately, with masses and  
 1891 material compositions reflecting the mechanical designs. In the strip endcaps, materials and  
 1892 objects in close proximity with each other are not individually modelled, but instead as one  
 1893 homogeneous block of material adjusted to have the same radiation length as calculated  
 1894 based on engineering designs. Figure 6.5 displays the GEANT4 geometry model of barrel  
 1895 staves and endcap petals in the Strip detector.

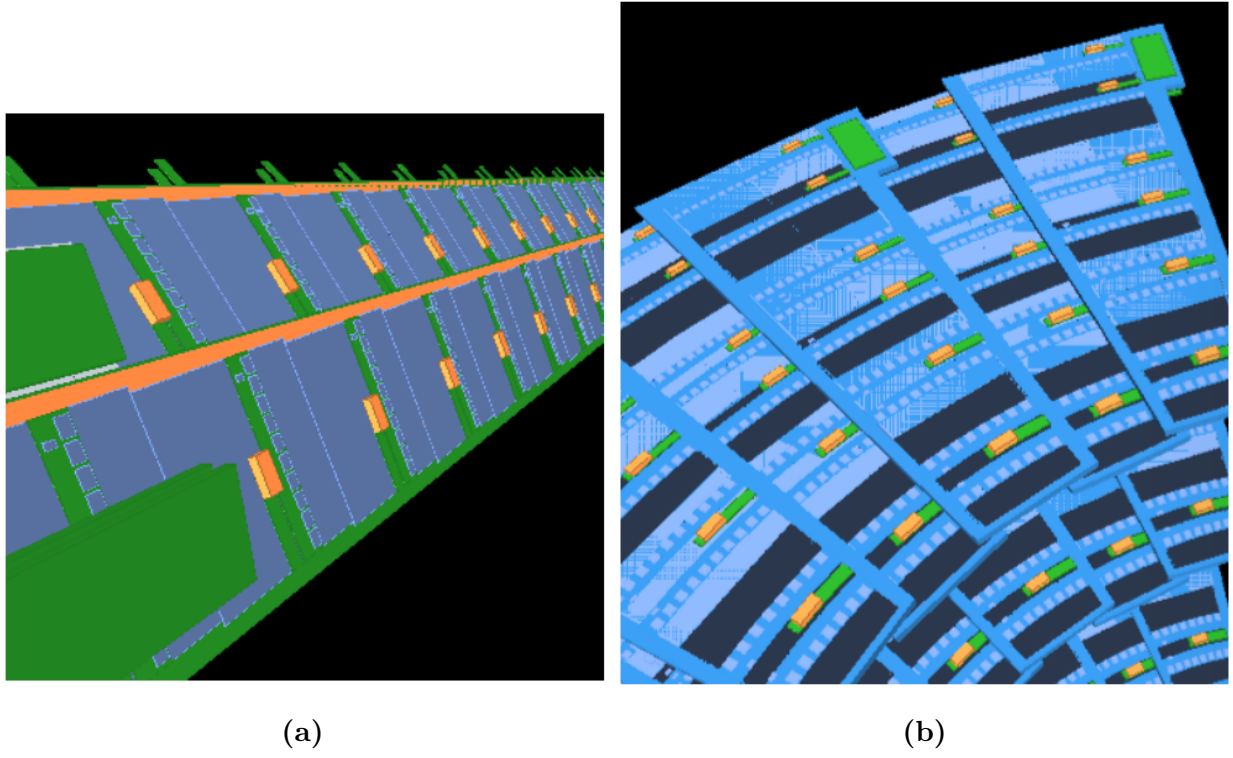


**Figure 6.5:** Displays of the GEANT4 geometry model of the strip barrel staves (left) and the endcap petals (right). Figure taken from reference [18].

1896        The global support of the detector in both the barrel and the endcaps is modelled in detail.  
 1897        Components include stave cooling pipes, carbon-foam, facesheets, cable bus, hybrids, and  
 1898        FE ASICs. Endcap sensors are individually modelled, while other components are modelled  
 1899        as a single edge-shaped object sandwiched between two silicon layers and uniformly filled  
 1900        with a generic material. The density of the material is adjusted to provide a radiation length  
 1901        of 0.02  $X_0$  per substructure.

### 1902        6.3 Particle interaction with detector material

1903        An important aspect of realistic detector simulation as well as track reconstruction is  
 1904        the treatment of interactions between high-energy particles and the materials they traverse.

1905 For charged particles at the energy range relevant to the Inner Tracker, these interactions  
 1906 are dominated by two processes: (i) inelastic collisions with atomic electrons, and (ii) elastic  
 1907 scattering against atomic nuclei. In turn, they result in two primary effects: (1) a loss in  
 1908 energy by the particle, and (2) a deflection from the original direction of incident. Of the  
 1909 two electromagnetic processes, inelastic collisions are responsible for the greater part of the  
 1910 energy loss from heavy particles in matter. Each collision transfers but a tiny fraction of  
 1911 the particle's energy to the incident atom, causing an ionization or excitation of the latter<sup>1</sup>.  
 1912 However, the number of collisions encountered by a particle per unit path length in dense  
 1913 materials is typically large enough that a non-negligible amount of its energy is lost to the  
 1914 environment.

### 1915 6.3.1 Energy loss of heavy particles

1916 The probability of an inelastic collision is described by the quantum mechanical scattering  
 1917 amplitude calculated for the corresponding process. In a macroscopic path length, a particle  
 1918 undergoes so many collisions that the distribution of total energy loss sharply peaks around  
 1919 an average value. Therefore, it is sufficient to compute the average energy loss per unit  
 1920 length, also called the stopping power or  $\frac{dE}{dx}$ . The stopping power of a material on an  
 1921 incident particle in the momentum range relevant to the ITk is given by the Bethe-Bloch  
 1922 formula [140]

$$-\frac{dE}{dx} = 2\pi N_a r_e^2 m_e c^2 \frac{Z}{A} \left( \frac{z^2}{\beta^2} \right) \left[ \log \left( \frac{2m_e \gamma^2 v^2 W_{max}}{I^2} \right) - 2\beta^2 - \delta \right], \quad (6.1)$$

1923 in which  $r_e = 2.817 \times 10^{-13}$  cm is the classical electron radius,  $m_e$  the electron mass,  $N_a$   
 1924 the Avogadro's number,  $I$  the mean excitation potential,  $Z$  and  $A$  the atomic number and  
 1925 atomic weight of the absorbing material,  $z$  the charge of the incident particle in units of  $e$ ,  
 1926  $\beta$  the  $\frac{v}{c}$  ratio,  $\gamma = (1 - \beta^2)^{-1/2}$  the relativistic  $\gamma$  factor,  $\delta$  the density correction, and  $W_{max}$   
 1927 the maximum energy transfer in a single collision. The maximum energy transfer depends

---

<sup>1</sup>To demonstrate the scale of each energy loss, note that atomic excitations are often measured in eV, while particle energy is often given in MeV or GeV.

<sup>1928</sup> on the ratio of the electron mass and the particle mass

$$W_{max} = \frac{2m_e c^2 \beta^2 \gamma^2}{1 + 2\gamma(m_e/M) + (m_e/M)^2}. \quad (6.2)$$

<sup>1929</sup> The left hand size of equation (6.1) is called the mass stopping power, which varies slowly  
<sup>1930</sup> with different materials. The average energy loss per unit length is simply given by  $\rho \left( \frac{dE}{dx} \right)$ .  
<sup>1931</sup> Shown in figure 6.6 is the mass stopping power computed for a positive muon in copper over  
<sup>1932</sup> 12 order of magnitude in muon momentum. The region corresponding to  $10 \text{ MeV} < p_{\mu^+} <$   
<sup>1933</sup>  $100 \text{ GeV}$ , most relevant in high-energy physics, is called the Bethe region where the stopping  
<sup>1934</sup> power is a function of  $\beta$  alone. At non-relativistic energies,  $\frac{dE}{dx}$  is dominated by the overall  
<sup>1935</sup>  $1/\beta^2$  factor (note the logarithmic scale in the vertical axis of 6.6). The stopping power  
<sup>1936</sup> reaches a minimum at  $\beta\gamma \approx 3$ , and slowly rises thanks to the logarithmic dependence up  
<sup>1937</sup> to  $\beta\gamma = 1000$ , a range equivalent to a muon momentum of  $1 - 100 \text{ GeV}$ . This minimum is  
<sup>1938</sup> broad and almost the same for all particles of the same charge. For this reason, particles at  
<sup>1939</sup> this point are called “minimum-ionizing”.

<sup>1940</sup> The stopping power in equation (6.1) is computed for pure elements. A non-elemental  
<sup>1941</sup> material can be considered as a mixture of elements, whose stopping power is approximated  
<sup>1942</sup> by a weighted mean of  $\frac{dE}{dx}$  over the elements in the compound. The weight is given by the  
<sup>1943</sup> fraction of electrons contributed by each element. In particular, the average mass stopping  
<sup>1944</sup> power is

$$\frac{dE}{dx} = \sum_i w_i \left( \frac{dE}{dx} \right)_i, \quad w_i = \frac{a_i A_i}{\sum_j a_j A_j} \quad (6.3)$$

<sup>1945</sup> where  $a_i$  is the number of atoms in the  $i$ -th element, and  $A_i$  the atomic weight. Knowing  
<sup>1946</sup> the stopping power of each element in a material and the molecular composition, one can  
<sup>1947</sup> easily compute the mean energy loss of an incident particle given its momentum.

<sup>1948</sup> Because of the statistical nature of inelastic collisions, the amount of energy deposited  
<sup>1949</sup> by a particle fluctuates around the mean calculated in equation (6.1). In a relatively thick  
<sup>1950</sup> absorber, the number of collisions is large, and, assuming each collision results in a small en-  
<sup>1951</sup> ergy loss  $\delta E$ , such that the particle velocity stays constant, the stopping power  $\frac{dE}{dx}$  negligibly

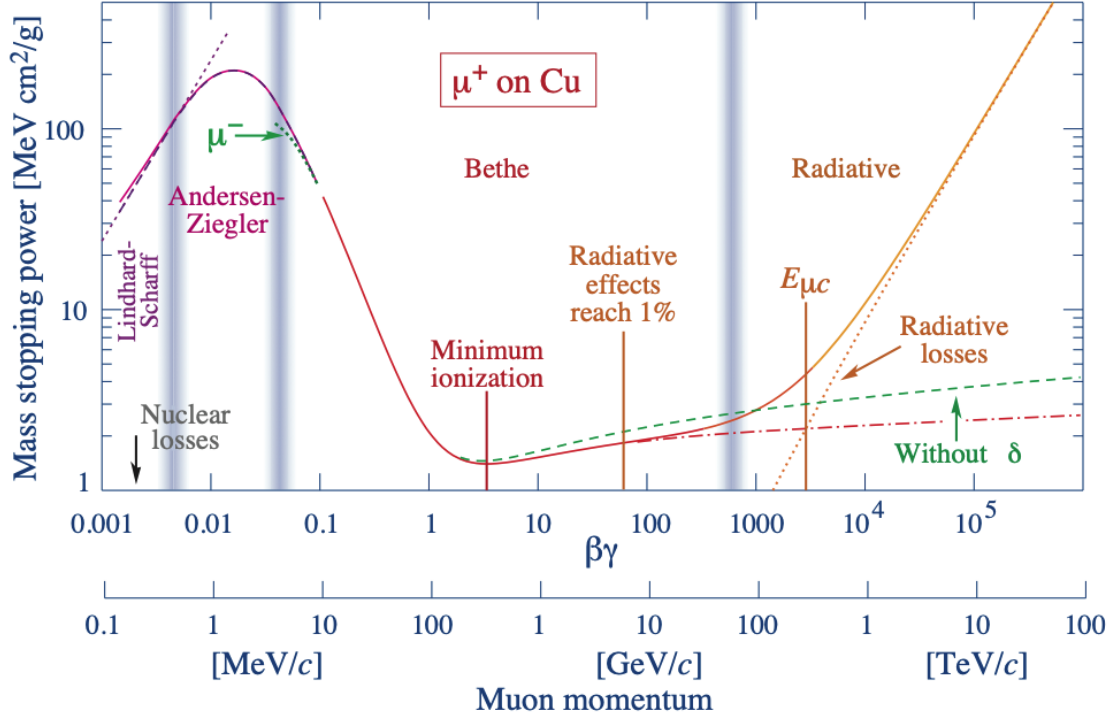


**Figure 6.6:** The mass stopping power of positive muons in copper as a function of the muon momentum spanning nine orders of magnitude. The solid curves indicate the total stopping power of all dissipative effects. The region of interest in HEP ranges from 100 MeV to 100 GeV, well within the so-called Bethe region, in which the stopping power is strongly dependent on  $\beta$  (see text for definition). Figure taken from reference [140].

1952 varies throughout the particle's path. The total energy loss is thus the sum of a large number  
 1953 of independent identically distributed random energy losses, which approaches a Gaussian  
 1954 as  $N \rightarrow \infty$

$$f(\Delta E; x) = \frac{1}{\sqrt{2\pi}\sigma} \exp \left[ \frac{-(\Delta E - \langle \Delta E \rangle)^2}{2\sigma^2} \right], \quad \langle \Delta E \rangle = \int_0^x \left( \frac{dE}{dx'} \right) dx'. \quad (6.4)$$

1955 with variance

$$\sigma = 0.1569\rho \left( \frac{Z}{A} \right) \frac{1 - \beta^2/2}{1 - \beta^2} x. \quad (6.5)$$

### 1956 6.3.2 Energy loss of electrons and positrons

1957 Light charged particles such as electrons and positrons undergo collisional energy loss  
 1958 in matter, just like heavy particles. However, because of their small mass, electromagnetic  
 1959 radiation in the electric field of atomic nuclei becomes a significant contribution to their  
 1960 overall rate of energy loss

$$\left( \frac{dE}{dx} \right) = \left( \frac{dE}{dx} \right)_{rad} + \left( \frac{dE}{dx} \right)_{col}, \quad (6.6)$$

1961 in which  $\left( \frac{dE}{dx} \right)_{rad}$  is the radiative component and  $\left( \frac{dE}{dx} \right)_{col}$  the collisional component already  
 1962 described.

1963 Even though the mechanism of collisional loss remains the same, because their mass is  
 1964 small, light particles could get deflected significantly from the original direction of incident.  
 1965 In addition, the collision occurs between identical particles, so several modifications to the  
 1966 Bethe equation are needed, starting with the maximum energy transfer  $W_{max} = T/2$  where  
 1967  $T$  is the kinetic energy of the incident particle. The collisional stopping potential becomes

$$-\left( \frac{dE}{dx} \right)_{col} = 2\pi N_a r_e^2 m_e c^2 \frac{Z}{A} \left( \frac{1}{\beta^2} \right) \left[ \log \frac{\tau^2(\tau+2)}{2(I/m_e c^2)^2} + F(\tau) - \delta \right], \quad \tau = \frac{T}{m_e c^2} \quad (6.7)$$

where the function  $F(\tau)$  modifies the  $\beta^2$  term in equation (6.1) to account for the interaction  
 between identical particles, resulting from crossing Feynman diagrams:

$$F_{e^-}(\tau) = 1 - \beta^2 + \frac{\tau^2/8 - (2\tau+1)\ln 2}{(\tau+1)^2},$$

and

$$F_{e^+}(\tau) = 2\ln 2 - \frac{\beta^2}{12} \left( 23 + \frac{14}{\tau+2} + \frac{10}{(\tau+2)^2} + \frac{4}{(\tau+2)^3} \right).$$

1968 Qualitatively, the radiative cross-section of bremsstrahlung is proportional to the inverse  
 1969 square of particle mass. Therefore, being far lighter than any other particle, electrons and,  
 1970 to a much lesser extent, muons lose a significant portion of their energy to this phenomenon.  
 1971 The radiative contribution to the mass stopping power can be written as

$$-\left( \frac{dE}{dx} \right)_{rad} = \frac{N_a}{A} E \Phi_{rad}, \quad (6.8)$$

<sup>1972</sup> where  $\Phi_{rad}$  is the total radiative cross section, approximated by

$$\Phi_{rad} = 4Z^2(e^2/m_e c^2)^2 \alpha^2 \left[ \ln(183Z^{-1/3}) + \frac{1}{18} - f(Z) \right], \quad (6.9)$$

<sup>1973</sup> where  $f(Z)$  is a small correction to the Born approximation accounting for the Coulomb

<sup>1974</sup> interaction between the electron and the nucleus.

<sup>1975</sup> It is straightforward to compare the two contributions of the total stopping power. Figure  
<sup>1976</sup> 6.7 demonstrates the the radiation and collisional energy losses for electron in copper as  
<sup>1977</sup> functions of the electron energy. Bremsstrahlung takes effect starting at 15 MeV, and at  
<sup>1978</sup> energy above a critical value of  $\approx 25$  MeV, its contribution quickly dominates the total  
<sup>1979</sup> energy loss. This observation is due to the fact that collisional loss rises logarithmically with  
<sup>1980</sup> energy, whereas radiative loss scales linearly, evidenced by equations (6.7) and (6.8). In the  
<sup>1981</sup> energy range from 1 – 100 GeV relevant to the ITk, the electron stopping power is composed  
<sup>1982</sup> almost entirely of radiative loss.

<sup>1983</sup> The critical energy at which the both components contribute equality to the total energy  
<sup>1984</sup> loss for a material is approximated by

$$E_c (\text{MeV}) = \frac{800}{Z + 1.2} \quad (6.10)$$

<sup>1985</sup> It is evident that the material energy loss of electrons and positrons is characterized  
<sup>1986</sup> by the Bremsstrahlung cross section. In practice, it is more convenient to characterize a  
<sup>1987</sup> material by its radiation length  $X_0$ , defined as the distance over which the average electron  
<sup>1988</sup> energy is reduced by a factor of  $1/e$  due to radiation loss. Equation (6.8) can be rewritten  
<sup>1989</sup> as

$$-\rho \left( \frac{dE}{dx} \right)_{rad} \frac{1}{E} = \frac{N_a \rho}{A} \Phi_{rad} = N \Phi_{rad} = \frac{1}{X_0} \quad (6.11)$$

<sup>1990</sup> or

$$E = E_0 \exp \left( -\frac{x}{X_0} \right), \quad (6.12)$$

<sup>1991</sup> where  $N$  is the volumetric density of atomic nuclei in the material.

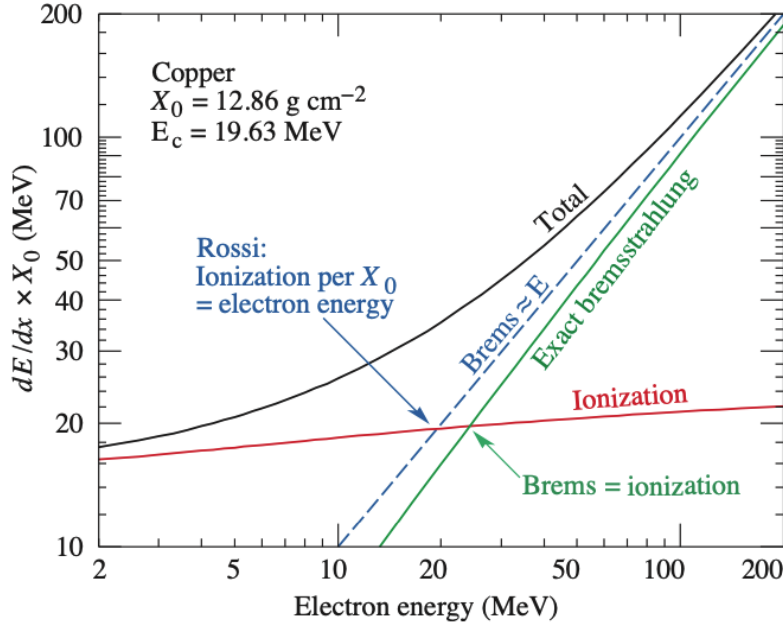


**Figure 6.7:** Contribution of radiative and collisional components in the total energy loss of electrons in copper as functions of electron energy. At a critical value  $E_c = 19.63 \text{ MeV}$ , radiative loss becomes the dominant mechanism. The energy range of electrons in HEP detectors is well within the Bremsstrahlung regime [140].

1992 In the ITk, material thickness is described in units of radiation length. Figure 6.8a shows  
 1993 the material thickness traversed by a straight track as a function of its pseudorapidity.  
 1994 Obviously, charged particles move in mostly helical orbits, whose curvature depends on the  
 1995 transverse momentum, because of the magnetic field, and thus the actual material length  
 1996 traversed by the particle is obtained by numerical integration. The central region has very  
 1997 little material, resulting from the light design of the sensor support. At higher  $\eta$ , a particle  
 1998 travels through progressively more layers and thus experiences almost linearly increasing  
 1999 material thickness. The largest contribution to the total radiation length comes from pixel  
 2000 services and cooling.

2001 For comparison, the material depth of the ID in Run 2, including the Pixel, SCT and  
 2002 TRT, is shown in figure 6.8b, and expected material thickness traversed by a particle until

it reaches the minimum number of hits required for track reconstruction in figure 6.8c. The linear ITk material budget is significantly smaller than that of the ID in the forward region, despite having more layers and better eta coverage. This is due to the adoption of serial powering in the ITk, among other design optimizations. A realistic particle experiences up to 50% more material before reaching the minimum number of hits for  $\eta < 1.5$  in the ITk than in the ID. Note, however that ID tracks are required to have only 8 hits in this region, compared to 9 hits for an ITk track. Beyond this point, the ITk becomes more transparent than the ID, by up to 50%.

### 6.3.3 Multiple Coulomb scattering

In addition to inelastic collision and radiation, charged particles undergo a large number of small-angle elastic scattering due to Coulomb interaction with atomic nuclei. Coulomb scatterings are governed by the Rutherford formula for non-relativistic collision, and the Mott formula for the relativistic counterpart. In both formulae, the scattering cross-section follows

$$\frac{d\sigma}{d\Omega} \propto \frac{1}{\sin^4(\theta/2)} \quad (6.13)$$

which favours a small scattering angle  $\theta$ . Assuming the material is sufficiently thick and the energy transfer to the nuclei is negligible, the particle suffers a large number of small deflections. The net effect can therefore be statistically represented by a probability distribution function of the total deflection which depends on the material thickness. A rigorous treatment of multiple scattering is complicated. Among the most commonly used approximations is the theory of Molière [136, 135], valid for the scattering of fast charged particles. The theory was expanded by Bethe [71] and later Scott [155] to account for Coulomb interactions with atomic electrons. Although it agrees well with data, especially at small angles and large target nuclear numbers, it relies on an unwieldy series expansion and is therefore inconvenient to use. Rossi and Greisen [151] developed a simple estimate of the root-mean-square scattering angle, which was improved by Highland [120] and Lynch and Dahl [130] to obtain

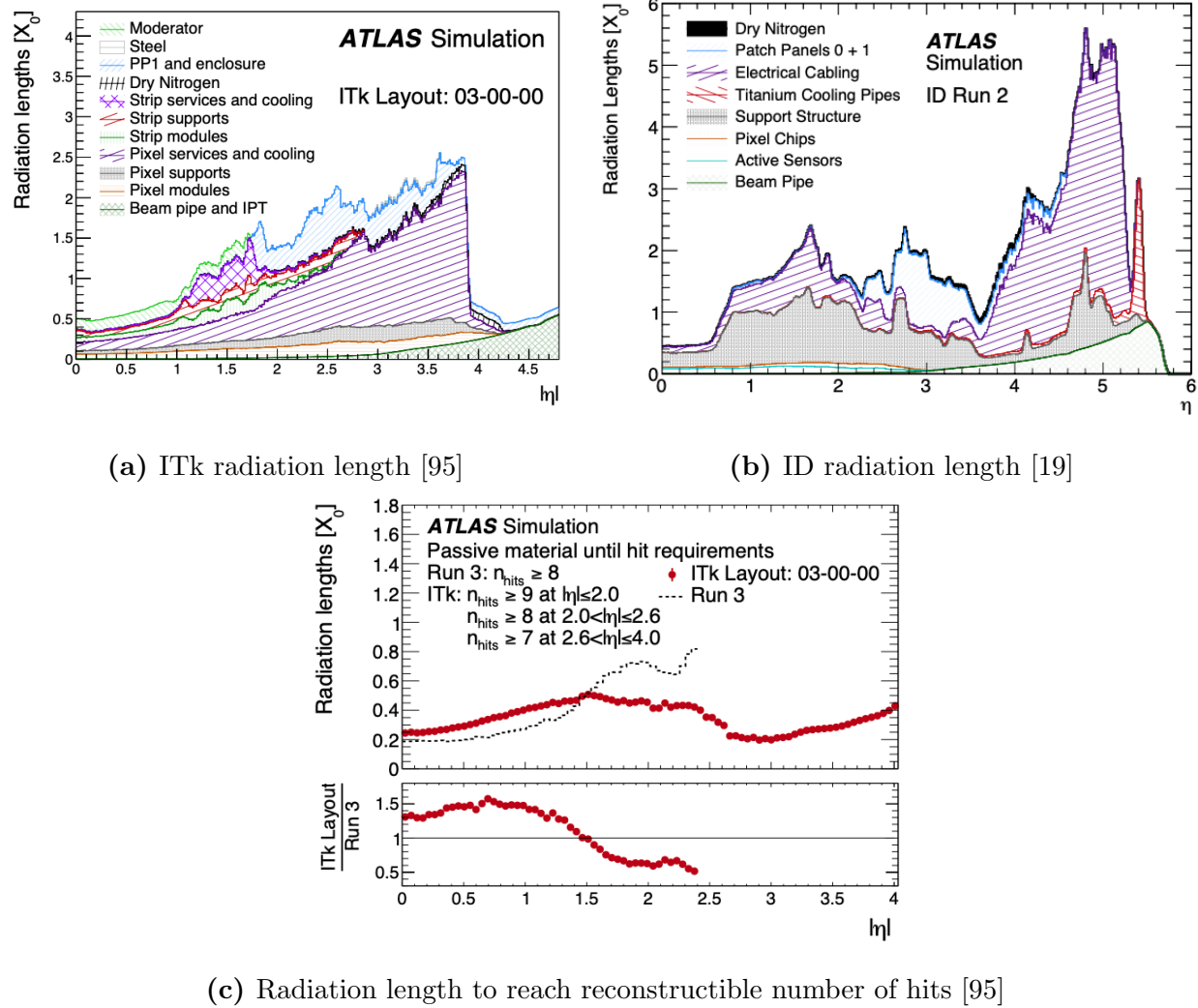


**Figure 6.8:** Integrated material budget encountered on a particle's path in unit of radiation length as a function of pseudorapidity based on (a) the ITk and (b) the ID. The particle assumes a straight trajectory from the origin. (c) is a comparison between the amount of material that must be traverse before the particle accumulates enough hits to be deemed reconstructible.

2028 the RSM width of the projected scattering angle distribution on a plane

$$\theta_0 = \frac{13.6z \text{ MeV}}{pc\beta} \sqrt{\frac{x}{X_0}} \left[ 1 + 0.038 \ln \frac{z^2(x/X_0)}{\beta^2} \right], \quad (6.14)$$

2029 where  $p$ ,  $\beta c$ , and  $z$  are the momentum, the velocity, and the charge of the incident particle.

2030  $x/X_0$  is the material thickness in radiation lengths. The scattering angle projected on a

2031 plane  $\theta_{plane}$  can be approximated by a Gaussian centered at  $\theta_{plane} = 0$

$$dP(\theta_{plane}) = \frac{1}{\sqrt{2\pi}\theta_0} \exp\left[-\frac{\theta_{plane}^2}{2\theta_0^2}\right] d\theta_{plane} \quad (6.15)$$

2032 The total angle  $\vartheta$  can be approximated by the quadratic sum of two small projected angles  
2033 on orthogonal planes

$$\vartheta^2 = \theta_{plane,x}^2 + \theta_{plane,y}^2, \quad d\vartheta = d\theta_{plane,x} d\theta_{plane,y} \quad (6.16)$$

2034 and with the assumption that the two projected angles are independent,  $\vartheta_{tot}$  is

$$dP(\vartheta) = \frac{1}{2\pi\theta_0^2} \exp\left[-\frac{\vartheta^2}{2\theta_0^2}\right] d\vartheta \quad (6.17)$$

2035 Figure 6.9 illustrates the quantities used to describe the effect of multiple scattering. The  
2036 total scattering angle is projected on a plane

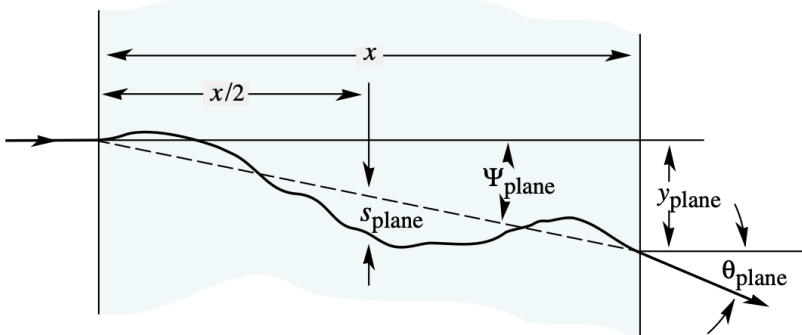


**Figure 6.9:** Schematic of the calculation of macroscopic mean deflection angle caused by multiple scattering [140].

2037 The material effects described in this section, sections 6.3.1 and 6.3.2, are sufficient for  
2038 Monte-Carlo simulations of the particle passage through material in the ITk. The overall  
2039 trajectory can be discretized into small segments. The mean energy loss and Coulomb  
2040 scattering angle over each segment can be estimated using equations (6.1), (6.12), (6.15) and  
2041 (6.17), along with the material distribution as shown in figure 6.8a. The actual energy loss  
2042 and scattering angle are then sampled from the corresponding distribution.

2043 **6.4 Simulated samples**

2044 The development and evaluation of the new tracking algorithm in this thesis is carried  
2045 out using a sample of simulated  $pp \rightarrow t\bar{t}$  events at center-of-mass energy  $\sqrt{s} = 14$  TeV, with  
2046 average pile-up ranging from 190 to 210. The actual number of pile-up interactions in each  
2047 event is randomly sampled from a Poisson distribution centred at the average pile-up. The  
2048 hard-scattering event is generated using the POWHEG Box v2 [107, 106, 137, 8] generator at  
2049 next-to-leading order in QCD with the NNPDF3.0NLO [158] Parton Distribution Functions  
2050 (PDFs). The  $h_{\text{damp}}$  parameter<sup>II</sup> is fixed to  $1.5m_{\text{top}}$  [59] and the top quark mass to  $m_{\text{top}} =$   
2051 172.5 GeV. Parton shower and hadronization are modeled using PYTHIA 8.230[157], with  
2052 the A14 set of tuned parameters [21] and using the NNPDF2.3LO [138] set of PDFs. A  
2053 semi-leptonic final state, in which one of the two  $W$ -bosons descending from the top quarks  
2054 decays to an electron or a muon, is enforced. The decay of bottom and charm hadrons are  
2055 performed by EVTGEN 1.6.0[129]. The simulation described here follows the procedure  
2056 detailed in reference [95].

2057 To simulate the pile-up background, a large pool of soft minimum-bias interactions is  
2058 generated. Each event is created by overlaying a number of min-bias sub-events on the hard-  
2059 scattering sub-event, and then digitizing the detector response. A feature of MC simulation  
2060 in ATLAS is that the pile-up sub-events are not uniquely generated for each events but ran-  
2061 domly sampled from the common pool, resulting in a dataset whose events are guaranteed to  
2062 feature different hard-scattering events, but may share a portion of their pile-up background.  
2063 A dataset of 100000  $t\bar{t}$  events are simulated, from which a subset of 10000 events is identified  
2064 to share no pile-up particles with the remaining 90000. This subset is dedicated to machine  
2065 learning training and performance evaluation. The hard-scattering particles of the 90000 are  
2066 used to train an algorithm to construct graphs from detector hits.

---

<sup>II</sup> $h_{\text{damp}}$  is a resummation damping factor and one of the parameters that controls the matching of POWHEG matrix elements to the parton shower and regulates the high- $p_T$  radiation against which the  $t\bar{t}$  system recoils.

2067 **Chapter 7**

2068 **The ATLAS track reconstruction chain**

2069 The High Luminosity era brings many challenges to event reconstruction in general and  
2070 charged-particle tracking in particular, due to increased pile-up level and detector granu-  
2071 larity. The current algorithm used in offline tracking scales super-linearly with pile-up and  
2072 struggles to meet the future operational requirements. This motivates the development of  
2073 an alternative algorithm that leverages modern hardware accelerators, such as the Graphic  
2074 Processing Unit (GPU) or the Field-Programmable Gate Array (FPGA), to boost the re-  
2075 construction speed. In this context, an understanding of the existing algorithm is necessary  
2076 to adequately compare its performance to that of the proposed algorithm. This chapter  
2077 describes the working principle of the Combinatorial Kalman Filter—the engine of charged-  
2078 particle tracking, and the challenges facing it in the High-Luminosity era. The Kalman  
2079 mechanism stems naturally from the least-square fit, which is also the basis of the discussion  
2080 in chapter 11.

2081 **7.1 Clusterization and space point formation**

2082 The first step of track reconstruction is the clusterization of the energy deposit on indi-  
2083 vidual sensor cells recorded by the detector. Figure 7.1 illustrates a particle passing through  
2084 a planar pixel sensor and depositing a small amount of its energy. Each sensor cell inde-  
2085 pendently measures this energy and, when the energy exceeds a certain threshold, records a  
2086 signal. Throughout an event, a sensor may experience multiple passages of different particle

2087 trajectories, as shown on figure 7.2, so its collection of cell read-outs must then be sorted into  
 2088 groups of neighbouring cells likely to originate from the same particle. This process, called  
 2089 clusterization, transforms low-level information from individual sensor cells to a higher-level  
 2090 and more compact objects, called **clusters**.

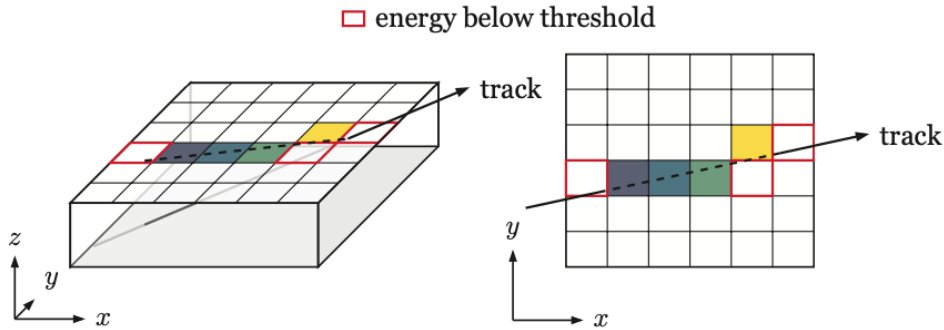


**Figure 7.1:** Formation of a pixel clusters from multiple cells. The particle deposits its energy in 7 cells, 5 of which receive charges exceeding the detection threshold and enter the clusterization [111].

2091 ATLAS traditionally uses a connected component analysis (CCA) [150], and more re-  
 2092 cently a neural network-based approach to clusterize cell read-outs[94]. The intersection  
 2093 point  $\mathbf{l}$  between the track and the sensor is estimated from the local coordinates  $\mathbf{l}_i$  of each  
 2094 cells in the clusters

$$\mathbf{l} = \begin{cases} \frac{1}{N} \sum_i \mathbf{l}_i \\ \frac{1}{\sum_i q_i} \sum_i q_i \mathbf{l}_i \end{cases}, \quad (7.1)$$

2095 where  $q_i$  is the charge deposit on cell  $i$ . The first formula computes a simple vector mean of  
 2096 the cell location, and the second a charge-weighted mean. In the neural network approach,  
 2097 the cluster position and uncertainty are both predicted by the network and found to be more  
 2098 accurate than the (weighted) mean approach.

2099 A cluster can be regarded as a measurement made in the local coordinate of the measuring  
 2100 surface<sup>I</sup>. From a cluster, the location of the hit in global coordinate, called the space point,

---

<sup>I</sup>For rest of this thesis, the terms “measurement” and “cluster” are interchangeable and refer to the same objects

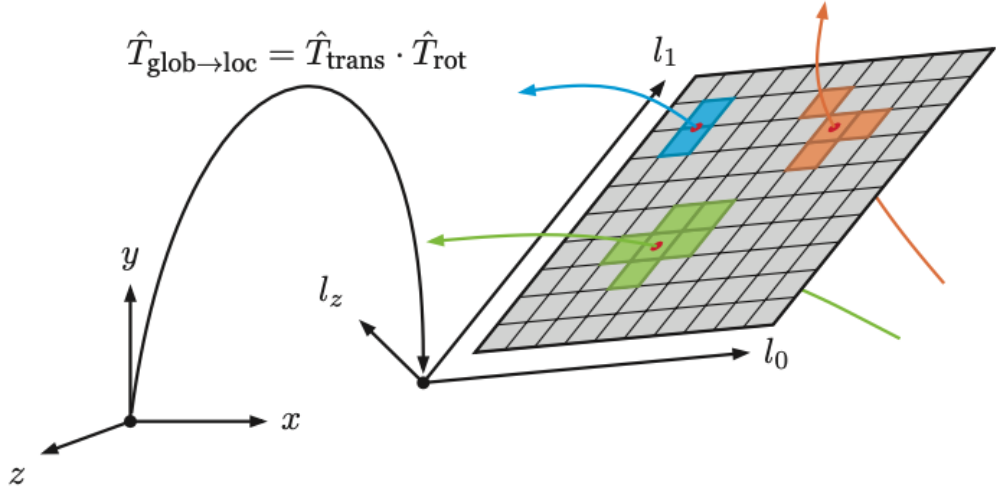


**Figure 7.2:** The passage of a particle through a pixel sensor segmented in two dimensions. The energy deposit in each sensor cell is measured as a signal when it exceeds a measurement threshold. The true intersection point is estimated from the signal cells grouped together, called a cluster [111].

can be derived. Figure 7.2 illustrates three particle tracks traversing a pixel sensor and inducing separate clusters. The true intersections are shown as red dots. An estimate of each of the true intersections between the trajectory and the sensor plane shown as red dots, is made in the clusterization step, and combined with the location and rotation of the sensor surface to obtain the space points. In this sense, pixel space point formation is obtained from a change in reference frame of the cluster coordinates via a series of translational and rotational transformations.

While there is a one-to-one correspondence between a pixel cluster and a pixel space point, the space point formation in the strip detector is more complicated. Strip modules are finely segmented in only one direction, rendering each measurement one-dimensional, in contrast to the two-dimensional measurements on a pixel module. To obtain a three-dimensional position estimate, two strip clusters from the same layer are combined, as shown in fig. 7.3. The local position of the hit along the thinly segmented dimension is estimated with high resolution. Thanks to the stereo angle between the modules, an estimate of the second

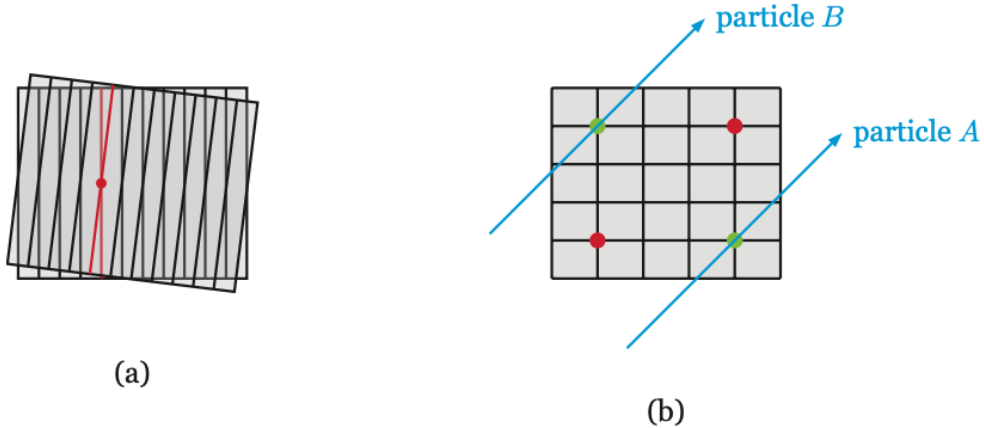


**Figure 7.3:** A pair of strip sensors are used to reconstruct a 3-dimensional estimate of the particle's true impact point (a). Ambiguity arises when more than one particle hit a strip module, leading to more combinations than particles (b) [111].

2115 coordinate is made from the intersection of the strip cells, albeit with lower resolution. These  
2116 measurements are then transformed to a global position estimate, as described above.

2117 In the current track reconstruction chain, space points are used to build track seeds, which  
2118 are small groups of hits likely to originate from the same particle. A dedicated seeding stage  
2119 creates large number of seeds each containing three space points and subsequently feeds them  
2120 to a track building algorithm. The latter extends the seed by iteratively adding clusters that  
2121 are compatible with the corresponding track state. A small number of clusters in the final  
2122 track candidate come from the seed space points, and the rest from individually incorporated  
2123 clusters on the track path.

2124 Finally, we note an important consequence of the 2-cluster composition of the strip space  
2125 point. Despite meticulous optimization of the detector layout, a particle does not always  
2126 leave two hits on a strip layer. Silicon sensors have inherent inefficiency, which means that a  
2127 particle may traverse a detector module without inducing a signal. This phenomenon occurs  
2128 in both sub-detectors of the ITk, but is very unlikely. A more important inefficiency comes  
2129 from the the strip detector, in which a particle may approach a layer in a direction such that

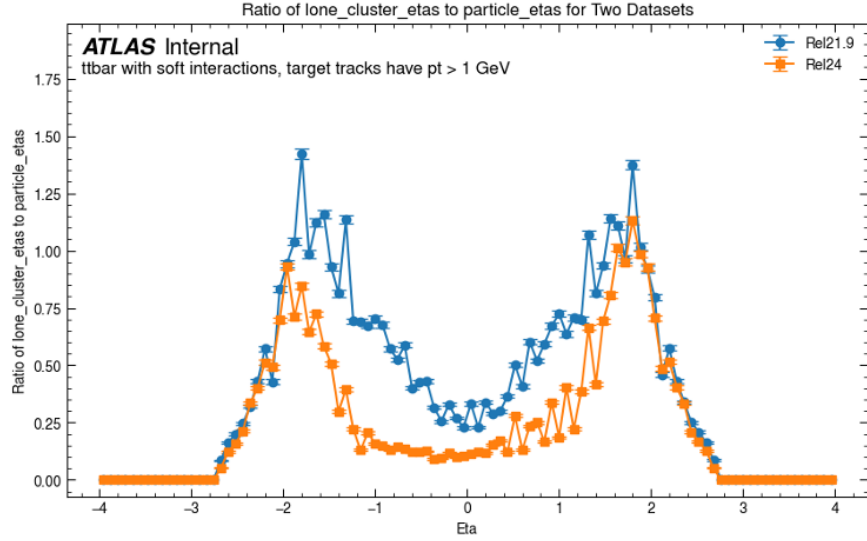


**Figure 7.4:** Average number of lone strip clusters per track as a function of the particle pseudorapidity  $\eta$ .

it intersects only one of two physical strip modules (see section 6.1 for a description of the strip detector). For any reason, when a strip layer records a *lone* cluster, it is ignored by the space point formation algorithm, resulting in its absence from the space point collection. On figure 7.4, we observe that particles leave lone clusters when their pseudorapidity falls under the coverage of the strip detector at  $|\eta| < 2.8$ , reaching up to one lone cluster per particle at  $|\eta| \simeq 1.8$ . This means that if we look at the space point record, every particle in this region effectively skips a strip layer. This hit inefficiency is inconsequential in the current ATLAS reconstruction chain, because space points are only used for track seeding, and there is enough redundancy to cover all true particle seeds. However, an algorithm that builds tracks from space points would not see lone clusters in the input, which may cause potential impacts on its performance. This issue will become important for the new algorithm and be described in chapter 11.

## 2142 7.2 The least-square fit

2143 A track candidate is a set of measurements made by sensitive detector elements on  
2144 the particle's trajectory. The latter is mathematically represented by a set of parameters  
2145 describing its position and momentum as it traverses the detector. Although in idealized  
2146 situations, the track may be parametrized by constants of motion, in a realistic detector,  
2147 even these constants vary over time, due to random material effects. Therefore, a necessary  
2148 ingredient to describe the trajectory is the solution to the equation of motion given the  
2149 detector setup. From an initial value and the precise magnetic field on a dense grid of  
2150 sampling points, the equation of motion is numerically integrated to obtain the a description  
2151 of that particle state as it evolves along the trajectory.

2152 Let  $\mathbf{x} \in \mathbb{R}^d$  represent the state of the particle and vary as a function of the arc length  $s$   
2153 along the trajectory<sup>II</sup>, so that

$$\mathbf{x} = \mathbf{x}(s) \quad (7.2)$$

2154 We will keep the discussion here general and note that any set of parameters from which the  
2155 instantaneous position and momentum of the particle can be derived is usable. The choice  
2156 of parametrization in ATLAS is discussed in section 11.1. In general, track parameters can  
2157 be regarded as the internal state of the particle, which is not directly measurable. Instead  
2158 the measurements are made at discrete points on the trajectory where a sensitive module  
2159 is present. Each measurement  $\mathbf{m}_i$  can then be modelled as a deterministic function of the  
2160 track state at that the measuring surface  $\mathbf{x}_i$  superimposed by a random experimental noise  
2161  $\epsilon_i$ .

$$\mathbf{m}_i = h_i(\mathbf{x}_i) + \epsilon_i. \quad (7.3)$$

2162 The function  $h_i : \mathbb{R}^d \rightarrow \mathbb{R}^n$ , called the *measurement model*, projects the  $d$ -dimensional state  
2163 vector  $\mathbf{x}_i$  on the  $i$ -th surface to an  $n$ -dimensional measurement vector. Its functional form  
2164 depends on the type of measuring surface, hence the subscript. For example, a measurement

---

<sup>II</sup>Since  $s = vt$ , this is equivalent to parametrization in time.

2165 on a pixel module is intrinsically different from one on a strip module<sup>III</sup>, so their measurement  
2166 models naturally differ.

2167 The experimental noise  $\epsilon_i$  also depends on the type of measuring surface. However, it is  
2168 generally assumed to be unbiased with finite variance, namely

$$E[\epsilon_i] = \mathbf{0}, \quad 0 < \sigma(\epsilon_i^{(j)}) < +\infty, \forall j \in [n], \quad (7.4)$$

2169 where the superscript denotes the  $j$ -th component of the  $n$ -dimensional error vector. The  
2170 covariance matrix of  $\epsilon$  is an important ingredient of the least-square fit, denoted by

$$\mathbf{V}_i = E[\epsilon_i \epsilon_i^T] \quad (7.5)$$

2171 As mentioned above, the state vector evolves along the trajectory, governed by the Equa-  
2172 tion of Motion (EOM), the solution to which is called the track model. The system evolution  
2173 can be written as a recursive process

$$\mathbf{x}_i = \mathbf{x}(s_i) = f_{i-1}(\mathbf{x}_{i-1}). \quad (7.6)$$

2174 The extrapolation function  $f_{i-1} : \mathbb{R}^d \rightarrow \mathbb{R}^d$  projects the track state from the previous  
2175 measuring surface  $\mathbf{x}_{i-1}$  to the current surface. Its functional form depends on the equation  
2176 of motion, which in turns depends on detector characteristics, such as its magnetic field  
2177 and layouts. As the EOM is in general a second-order non-linear differential equation, a  
2178 close-form solution, if it exists, is likely non-linear. However, in practice, the EOM is often  
2179 linearized and numerically integrated by, for example, Euler's method, allowing a linear,  
2180 albeit recursive and potentially expensive solution

$$\mathbf{x}(s_{i-1} + \Delta s) \approx \mathbf{x}(s_{i-1}) + \frac{\partial \mathbf{x}'}{\partial s'} \Big|_{s'=s_{i-1}} \Delta s + \mathcal{O}((\Delta s)^2), \quad (7.7)$$

2181 where the derivative is calculated from the dynamical equation of the system. More sophis-  
2182 ticated numerical methods can be used, but in principle, it is possible to approximate the

---

<sup>III</sup>A pixel cluster is a 2D measurement, while a strip cluster is 1D.

2183 transport equation (7.6) as a linear recursive relation. The benefit of such linearization is  
2184 that we can write the track state on any surface  $\mathbf{x}_i$  as a simple linear function of some initial  
2185 value on a reference surface  $\mathbf{x}_0$ ,

$$\mathbf{x}_i = f_{i-1}(x_{i-1}) = f_{i-1}(f_{i-2}(\mathbf{x}_{i-2})) = f_{i-1} \circ f_{i-2} \circ \dots \circ f_0(\mathbf{x}_0) = f_i(\mathbf{x}_0), \quad (7.8)$$

2186 and take  $\mathbf{x}_0$  as *the* estimated track parameters.

2187 Track fitting is now reduced to finding an estimator  $F$  from the set of measurements  
2188  $M = \{\mathbf{m}_1, \dots, \mathbf{m}_N\}$  to the parameter space, such that (1) the estimate  $\hat{\mathbf{x}}_0 = F(M)$  is  
2189 unbiased

$$E[\hat{\mathbf{x}}_0] = \mathbf{x}_0 \quad (7.9)$$

2190 and (2) of minimum variance

$$E[(F(M) - \mathbf{x}_0)^2] = \min_{F'} E[(F'(M) - \mathbf{x}_0)^2] \quad (7.10)$$

2191 The Gauss-Markov theorem [144] states that among the class of linear and unbiased esti-  
2192 mators, the Least Squares Estimator (LSE) has minimum variance, provided a linear track  
2193 model, purely statistical<sup>IV</sup>, unbiased and uncorrelated errors  $\epsilon_i$ . The LSE is obtained by  
2194 minimizing the  $\chi^2$ -function, defined as

$$\chi^2 = \sum_{i=1}^N [\mathbf{m}_i - h_i(f_i(\mathbf{x}_0))]^T \mathbf{V}_i^{-1} [\mathbf{m}_i - h_i(f_i(\mathbf{x}_0))], \quad (7.11)$$

2195 where both  $h_i$  and  $f_i$  are now assumed to be linear. The linearity of  $h_i$  can be achieved by a  
2196 careful choice of parametrization, such as the one used by ATLAS, discussed in section 11.1.  
2197 The estimator is simply the solution to

$$\nabla \chi^2(\mathbf{x}_0) = 0 \quad (7.12)$$

---

<sup>IV</sup>i.e. independent of  $\mathbf{x}$

<sub>2198</sub> **7.3 Iterative track fit**

<sub>2199</sub> Because the LSM considers all measurements at the same time, it is a global fitting  
<sub>2200</sub> method. It can be shown that in situations where the material effects described in section  
<sub>2201</sub> 6.3 cannot be ignored, the minimization of the  $\chi^2$ -function translates to the inversion of a  
<sub>2202</sub> non-diagonal covariance matrix whose dimension grows with the number of measurements  
<sub>2203</sub>  $N$ . This computation can become a significant bottleneck in complex and granular detectors  
<sub>2204</sub> (see chapter 3 of reference [147] for more details).

<sub>2205</sub> The Kalman formalism [131, 72, 109] offers a faster alternative to global fit that, cru-  
<sub>2206</sub> cially, yields optimal estimates for Gaussian measurement uncertainties. The track state still  
<sub>2207</sub> evolves as a linear dynamical system. Multiple scattering and energy loss due to material  
<sub>2208</sub> interactions are modelled as random process noise  $\mathbf{w}$  added to the transport equation

$$\mathbf{x}_i = \mathbf{F}_{i-1} \mathbf{x}_{i-1} + \mathbf{w}_{i-1}, \quad (7.13)$$

<sub>2209</sub> where the matrix  $\mathbf{F}_{i-1}$  is the track model given in equation (7.6) now written in the explicitly  
<sub>2210</sub> linear form. The process noise  $\mathbf{w}$  has a covariance denoted by

$$\mathbf{Q} = E[(\mathbf{w} - E[\mathbf{w}])(\mathbf{w} - E[\mathbf{w}])^T] \quad (7.14)$$

<sub>2211</sub> Instead of minimizing a  $\chi^2$ -function over all measurements, the Kalman procedure iteratively  
<sub>2212</sub> incorporates measurements into an existing estimate of the track parameters. Each iteration  
<sub>2213</sub> inverts a single  $n \times n$  matrix, so in total,  $N$  inversions of  $n \times n$ -matrices are needed, where  $n$   
<sub>2214</sub> is the number of measurement coordinates<sup>V</sup> and  $N$  the number of measurements, as opposed  
<sub>2215</sub> to inverting an  $(nN) \times (nN)$  matrix in the LSM. The information from the measurement  
<sub>2216</sub> is used to constrain the estimate and reduce the error. The procedure is carried out in the  
<sub>2217</sub> following 3-step recipe.

<sub>2218</sub> **Step 1: Prediction.** Suppose the measurement  $\mathbf{m}_i \in M$  is being incorporated. Let  $\mathbf{x}_{i-1}$   
<sub>2219</sub> and  $x_i^{i-1}$  denote the track state before the inclusion of  $\mathbf{m}_i$ , and its projection to the measuring

---

<sup>V</sup>In typical ATLAS parametrization,  $n = 2$

2220 surface of  $\mathbf{m}_i$  by the transport equation. In addition, denote the covariance of the estimate  
2221 as  $\mathbf{C}$ ,

$$\mathbf{C} = E[(\mathbf{x} - E[\mathbf{x}])(\mathbf{x} - E[\mathbf{x}])^T], \quad (7.15)$$

2222 so that the covariance before inclusion is  $\mathbf{C}_{i-1}$ . *Neither* of  $\mathbf{x}_{i-1}$  nor  $\mathbf{x}_i^{i-1}$  contains information  
2223 from  $\mathbf{m}_i$ , nor any material effect during the propagation,

$$\mathbf{x}_i^{i-1} = \mathbf{F}_{i-1}\mathbf{x}_{i-1}. \quad (7.16)$$

2224 The stochastic noise due multiple Coulomb scattering and energy loss corrections is instead  
2225 superimposed on the projected covariance,

$$\mathbf{C}_i^{i-1} = \mathbf{F}_{i-1}\mathbf{C}_{i-1}\mathbf{F}_{i-1}^T + \mathbf{Q}_{i-1}. \quad (7.17)$$

2226 **Step 2: Filtering.** The predicted track state in (7.16) is combined with the present mea-  
2227 surement  $\mathbf{m}_i$  to yield the updated estimate  $\mathbf{x}_i$

$$\mathbf{x}_i = \mathbf{x}_i^{i-1} + \mathbf{K}_i(\mathbf{m}_i - \mathbf{H}_i\mathbf{x}_i^{i-1}). \quad (7.18)$$

2228  $\mathbf{K}_i$  is called the Kalman gain matrix

$$\mathbf{K}_i = \mathbf{C}_i^{i-1}\mathbf{H}_i^T(\mathbf{V}_i + \mathbf{H}_i\mathbf{C}_i^{i-1}\mathbf{H}_i^T)^{-1}. \quad (7.19)$$

2229 Intuitively,  $(\mathbf{m}_i - \mathbf{H}_i\mathbf{x}_i^{i-1})$  represents the difference between the actual measurement and  
2230 the expected measurement given the predicted track state. If the measurement exactly  
2231 equals its predicted value, it supports the predicted track state, so the update track state  
2232 equals its predicted value. No new information is added to the filtered estimate in such a  
2233 case. Therefore, we can think of the Kalman matrix as the information gained from any  
2234 disagreement between the predicted and the actual measurement, hence its denomination.

2235 The covariance of the estimate is updated from its prediction as

$$\mathbf{C}_i = (\mathbf{I} - \mathbf{K}_i\mathbf{H}_i)\mathbf{C}_i^{i-1}. \quad (7.20)$$

2236 The uncertainty from stochastic noise and the measurement uncertainty are respectively  
2237 encoded in  $\mathbf{C}_i^{i-1}$  and  $\mathbf{K}_i$ . Both sources of uncertainty thus contribute to the filtered covari-  
2238 ance, as expected. Both the state vector and its covariance are updated by incorporating a  
2239 new measurement and the material effects from propagating the particle from its last known  
2240 position.

2241 Repeated applications of prediction and filtering incorporate all measurements to refine  
2242 the track state from its initial value  $\mathbf{x}_0$

2243 **3. Smoothing.** The prediction and filtering sequence refines the track state in the forward  
2244 direction. This means that an estimate at the end of the trajectory is better than one  
2245 at the beginning. It is, however, desirable that all estimates receive information from all  
2246 measurements, rather than those preceding them. The smoothing step achieves this goal by  
2247 working backward from the outermost measurement and updating a state vector at step  $i$   
2248 using the state vector at step  $i + 1$

$$\mathbf{x}_i^N = \mathbf{x}_i + \mathbf{A}_i(\mathbf{x}_{i+1}^N - \mathbf{x}_{i+1}^i), \quad (7.21)$$

2249 in which the superscript  $N$  signifies an estimate incorporating all  $N$  measurements.  $\mathbf{A}_i$  is  
2250 called the smoothing gain matrix, defined as

$$\mathbf{A}_i = \mathbf{C}_i \mathbf{F}_i^T (\mathbf{C}_{i+1}^i)^{-1}. \quad (7.22)$$

2251 Only after filtering through all measurements on track can the smoothing be effected. In  
2252 ATLAS terminology, the former is therefore referred to as the forward filter, while the latter  
2253 backward smoothing. The initial track state  $\mathbf{x}_0$ , or the state on any other surface, real or  
2254 imaginary, can be refined or extrapolated using the entire measurement set.

## 2255 7.4 Combinatorial Kalman Filter

2256 Thanks to its iterative mechanism, the Kalman formalism can be extended from track  
2257 fitting to track finding, called the Combinatorial Kalman Filter (CKF). From a track seed

2258 containing  $k$  measurements, it estimates the initial value  $\mathbf{x}_k$  and projects it to the next surface  
 2259 using equation (7.13). In the filtering stage, instead of incorporating a given measurement,  
 2260 as in the case of track fitting, it considers all measurements on the target surface falling  
 2261 into a search window defined by the projected measurement covariance. By filtering each  
 2262 candidate measurement  $l$ , it computes a filtered track state and measurement residual

$$\mathbf{r}_{k+1,l} = \mathbf{m}_{k+1,l} - \mathbf{H}_{k+1}\mathbf{x}_{k+1,l}. \quad (7.23)$$

2263 The increment in  $\chi^2$  is computed from the residual

$$\chi_{+,l}^2 = \mathbf{r}_{k+1,l}^T [(\mathbf{I} - \mathbf{H}_{k+1}\mathbf{K}_{k+1})\mathbf{V}_{k+1,l}]^{-1} \mathbf{r}_{k+1,l}. \quad (7.24)$$

2264 All candidate measurements  $l$  whose contribution to the global  $\chi^2$  falls before a certain  
 2265 threshold are admitted, creating the same number of branches from the track seeds. The  
 2266 procedure is repeated till no more measurements can be incorporated. The output from a  
 2267 given track seed is usually a large set of track candidates each originating from a combination  
 2268 of branching connections, hence the *combinatorial* denomination.

2269 The track candidate is characterized by a global  $\chi^2$  equal to the sum of the contributions  
 2270 from individual measurements in equation (7.24). Several candidates might be ruled out  
 2271 based on the mean  $\chi_{track}^2/|M_{track}|$ , as well as other quality cuts. To guarantee tracking  
 2272 efficiency, a large number of track seeds are produced and considered by the CKF. The  
 2273 number of considered track seeds combined with the number of combinations per seed results  
 2274 in significant track redundancy and overlapping measurements. An ambiguity resolution step  
 2275 globally sorts through the track candidates and assigns each measurement to mostly a unique  
 2276 track, effectively reducing them to a set of tracks of highest quality and compatibility to real  
 2277 particles.

## 2278 7.5 Computational cost of track reconstruction

2279 Inner tracking is one of the most expensive tasks of event reconstruction. For instance,  
2280 table 7.1 illustrates the CPU consumption in  $\text{HS06} \times \text{seconds}$  of each reconstruction stage  
2281 under Run 2 conditions but scaled to  $\langle \mu \rangle = 90$  [86]. Track reconstruction dominates the  
2282 computing budget, consuming 67% of the total reconstruction time. This contribution will  
2283 only get worse at pile-up 200, due to the strong scaling behaviour of the Combinatorial  
2284 Kalman Filter and the Ambiguity Resolution step which necessarily follows.

Detector	$\langle \mu \rangle$	Tracking	Calo and M.S	Combined Reco.	Monitoring	Total
Run 2	90	1137	149	301	106	1693

**Table 7.1:** The CPU required in  $\text{HS06} \times \text{seconds}$  to reconstruct a Run 2 data event using the corresponding software release at average pile-up 90 using. The total reconstruction time is broken down into inner tracking, Calorimeter and Muon Spectrometer reconstruction, and Monitoring. Numerical figures taken from reference [86].

2285 Within Inner Tracking, the tracking finding step described in this chapter consumes the  
2286 largest CPU resource. Listed in table 7.2 are the cost of each step in the tracking stage,  
2287 assuming the pile-up levels of 140 and 200. In the default tracking chain, the tracking finding  
2288 and ambiguity resolution steps dominate the total CPU consumption. Although listed as  
2289 separate items, the former's performance is severely degraded without the latter, so they  
2290 should be considered together as one item, which occupies 83% of the overall computing  
2291 consumption for inner tracking at pile-up 200.

2292 ATLAS has carried out major optimizations of the default CKF chain to improve its CPU  
2293 performance, shown in table 7.2 as Fast tracking. Track seeds used to initialize the CKF are  
2294 created exclusively from pixel space points, enabled by the increased number of expected  
2295 pixel hits thanks to an additional layer and the full  $\eta$ -coverage of the ITk compared to the  
2296 ID. A tighter track selection and precise cluster calibrations are used to remove duplicate and

$\langle \mu \rangle$	Algorithm	Decoding	Clustering	S.P. Formation	CKF	Am. Reso.	Total
140	Default	1.2	17.1	6.0	41.1	58.2	124
140	Fast	1.2	4.5	0.9	12.4		19.0
200	Default	1.6	26.3	8.6	85.8	92.0	214
200	Fast	1.6	6.3	1.2	22.6		31.7

**Table 7.2:** The CPU required in HS06×seconds to reconstruct a  $t\bar{t}$  MC event with  $\langle \mu \rangle = 140$  and 200 in the ITk. The total track reconstruction time, evaluated for both the default and an optimized CKF-based chains, is broken down into individual steps, most significant of which are clustering, space point formation, CKF-based track finding and ambiguity resolution. An Intel Xeon E5-2620v2 processor with 2.1 GHz and six physical cores per CPU was used. The CPU time is multiplied by an HS06 factor of 17.8 for single-thread running. Numerical figures taken from reference [28].

2297 fake tracks after the track finding step, in lieu of the costly ambiguity resolution step. These  
 2298 changes, along with other incremental improvements, allows running the track reconstruction  
 2299 pass approximately 8 times faster than the default chain, as illustrated in table 7.2, but with  
 2300 a loss in physics performance, as shown in figure 7.5 [28]. Despite the impressive acceleration,  
 2301 the fast track chain still is far from ready for production due to both latency and tracking  
 2302 performance.

2303 Along with optimizing the traditional event reconstruction algorithm, ATLAS is actively  
 2304 pursuing significant modernization of its analysis software, both online and offline. As out-  
 2305 lined in reference [88], the primary challenge of the HL-LHC era will be the effective use of  
 2306 General Purpose Graphics Processing Units (GP-GPUs), which are becoming ubiquitous in  
 2307 large High-Performance Computing (HPC) facilities and data centers. They can accelerate  
 2308 suitable applications by orders of magnitude, many of which have already been deployed  
 2309 in ATLAS. Examples include Fast Simulation [89], Particle Flow [91], and  $b$ -tagging graph

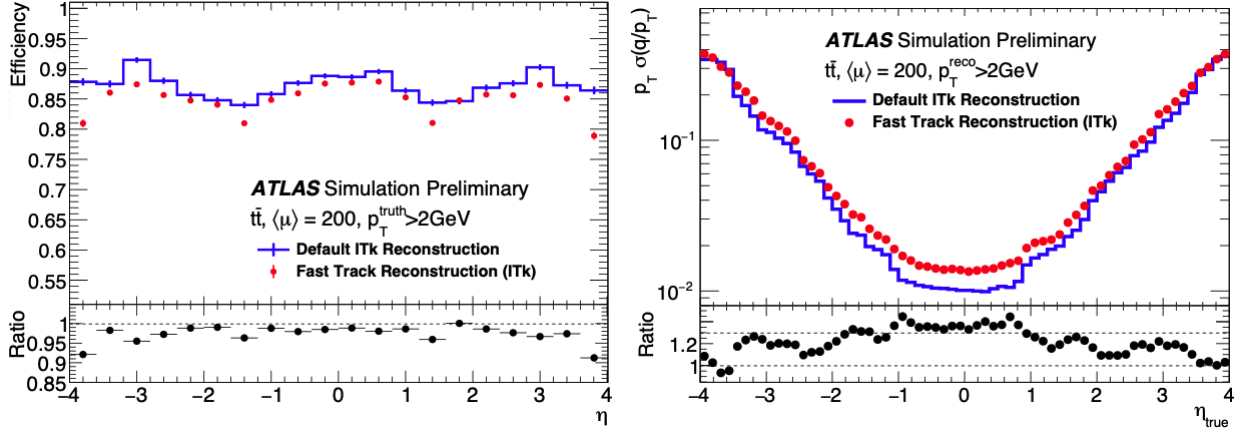


**Figure 7.5:** Tracking efficiency (left) and track parameter resolution (right) as functions of the truth particle’s pseudorapidity, evaluated at  $\langle\mu\rangle = 200$ . The bottom plots show the ratio of the corresponding metric observed in the fast chain to that in the default chain [28].

neural networks [102]. Exploiting this computing resource requires recasting current software on the hardware accelerators, for instance the TRACKCC project [153], or designing new algorithms inherently compatible with them. In addition, because of the increased track multiplicity in HL-LHC, online applications such as trigger and data acquisition will likely be migrated to accelerators, and thus, new hardware-accelerated algorithms are further incentivized for offline software to maintain synergies between the two computing domains. In this context, the next big component in event reconstruction to be modernized is inner tracking, attracting substantial interest and investment in person power within ATLAS. The work done in this thesis plays a significant role in this effort, resulting in a competitive candidate for an end-to-end, machine learning-based and fully GPU-compatible algorithm for track reconstruction. The remaining chapters of this thesis describe its development and latest results.

2322 **Chapter 8**

2323 **Track reconstruction with Graph Neural Networks**

2324 Graph Neural Networks (GNNs) were first proposed in 2018 as an alternative track finder  
2325 to the Combinatorial Kalman Filter (CKF) [103]. Developed and tested on the TrackML  
2326 dataset [11], they demonstrated excellent physics performance and favourable scaling be-  
2327 haviour [123, 82]. Fundamentally, GNN-based algorithms represent a shift from the local  
2328 track finding approach of the CKF to a global approach. Instead of sequentially extending  
2329 a tracklet<sup>I</sup> with compatible hits on its path, as described in chapter 7, global track finding  
2330 considers simultaneously all connections between detector hits and finds those that are most  
2331 likely to belong to true particle tracks. No longer is a need to loop through a set of re-  
2332 dundant track seeds, which makes the CKF slow and requires a costly ambiguity resolution.  
2333 The GNN “looks at” all possible candidate tracks in an event at the same time, significantly  
2334 accelerating the recognition of track patterns thanks to GPU-powered parallelization. The  
2335 shift from hit finding to connection finding necessitates a change in representation of the  
2336 collision event from a point cloud to a collection of nodes and edges, the very definition of a  
2337 **graph**. This approach therefore relies on graph data structure.

2338 The work documented in this thesis builds upon that of reference [123], which examined  
2339 the physics and computing performance of the GNN on the TrackML dataset [11], and of ref-  
2340 erence [80], which made initial strides in applying the GNN to data from full ITk simulation.

---

<sup>I</sup>An incomplete track

2341 It contributes numerous developments that bring the new approach closer to the state-of-  
 2342 the-art performance. Neural network architectures undergo significant refinements. The  
 2343 algorithm is fully integrated into the official ATLAS analysis software framework [85], thus  
 2344 enabling direct performance comparison to the CKF. Finally, many components are compu-  
 2345 tationally optimized, resulting in competitive reconstruction speed. This chapter commence  
 2346 the discussion with an overview of the algorithm and the construction of graphs from de-  
 2347 tector data. Subsequent stages of the algorithm, especially the graph neural network, are  
 2348 detailed in chapters 9 and 10, and finally the results are presented in chapters 11 and 12.

## 2349 8.1 Overview

2350 The GNN-based approach, illustrated in figure 8.1 and hereafter referred to as the  
 2351 **GNN4ITk** algorithm, creates track candidates by segmenting a graph constructed from  
 2352 the collection of space points in each event. A graph  $G(V, E)$  is a mathematical structure  
 2353 consisting of a set of nodes  $V$ , and a set of pairwise connections  $E$  between these nodes. Each  
 2354 node  $v_i \in V$  represents a space point, and an edge  $e_{ij} \in E$  a hypothesis that the space points  
 2355 represented by  $v_i$  and  $v_j$  are created from successive energy deposits by the same particle.  
 2356 In addition, a ground truth graph  $G_{truth} = (V, E_{truth})$  is defined from the same set  $V$  and  
 2357 the connections between successive space points on the trajectories of all particles in the  
 2358 event, denoted by  $E_{truth}$ , oriented in the direction of increasing distance from the particle's  
 2359 production vertex. An edge  $e_{ij} \in E$  is true if it is also in the truth graph, i.e.

$$y_{ij} = 1_{[e_{ij} \in E_{truth}]}, \quad (8.1)$$

2360 and fake otherwise. A graph neural network is used to assign to every edge  $e_{ij}$  a score  
 2361  $s_{ij} = P[y_{ij} = 1]$ , representing a continuous function of the probability that the edge in  
 2362 question is true. To obtain the probability, a calibration step is sometimes needed [104]. For  
 2363 our purpose, a score threshold is selected to satisfy certain requirements on the edge efficiency  
 2364 evaluated on the validation set. Edges with scores under the threshold are eliminated, and

2365 the remaining graph is segmented into **track candidates**, collections of nodes believed to  
 2366 originate from the same particle.

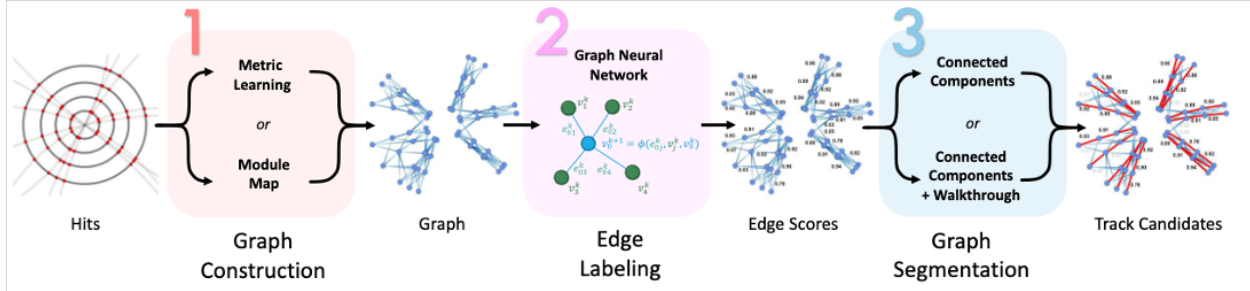


**Figure 8.1:** The GNN4ITk algorithm consists of three distinct stages. The first stage constructs a graph from the set of space points in an event, each acting as a node. The second stage identifies edges connecting consecutive nodes on a particle tracks from other edges. The last stage construct track candidates by segmenting the graph using the output of the second stage. The algorithm's output consists of individual track candidates each as a set of space points believed to belong to the same particle.

## 2367 8.2 Target, non-target particles and evaluation metrics

2368 At  $\langle \mu \rangle = 200$ , each collision event produces  $\langle N \rangle \approx 10000$  particles, the majority of  
 2369 which are of little interest to the physics program in ATLAS. They include, for example,  
 2370 low-momentum particles from background processes or particles which leave too few hits  
 2371 to be considered reconstructible. The remaining particles can be broadly categorized by  
 2372 the interaction from which they emerge. Primary particles are produced in the luminous  
 2373 area directly from proton-proton interaction and stable enough to traverse the detector,  
 2374 including protons, electrons, muons, pions, etc. Secondary particles arise from the interaction  
 2375 of primary particles with detector material, such as  $\delta$ -ray electrons and nuclear interaction  
 2376 products. As these interactions destroy information on the primary particle's kinematics,  
 2377 the CKF chain does not target secondary particles for reconstruction. In the same spirit,

throughout the GNN4ITk chain, we identify these particles prior to model training and exclude them from the loss function, as well as performance evaluation.

Since a secondary interaction occurs when the primary particle has travelled a distance from the luminous region, their vertices are considerably further from the origin than the primary counterpart. Shown on figure 8.2, the majority of primary vertex positions are located at  $v_r < 20$  cm and  $v_z < 20$  cm, in contrast to secondary vertices, whose distributions of  $v_r$  and  $v_z$  are more spread-out and with longer tails. This distinction allows us to select primary particles in training by requiring the production vertex to be within 26 cm from the origin. As we will see in chapter 11, the ATLAS reconstruction chain eliminates secondary particle tracks by applying selection cuts on the impact parameters, which are good estimates of the vertex point, of  $|z_0| \leq 20$  cm and  $|d_0| \leq 10$  cm.

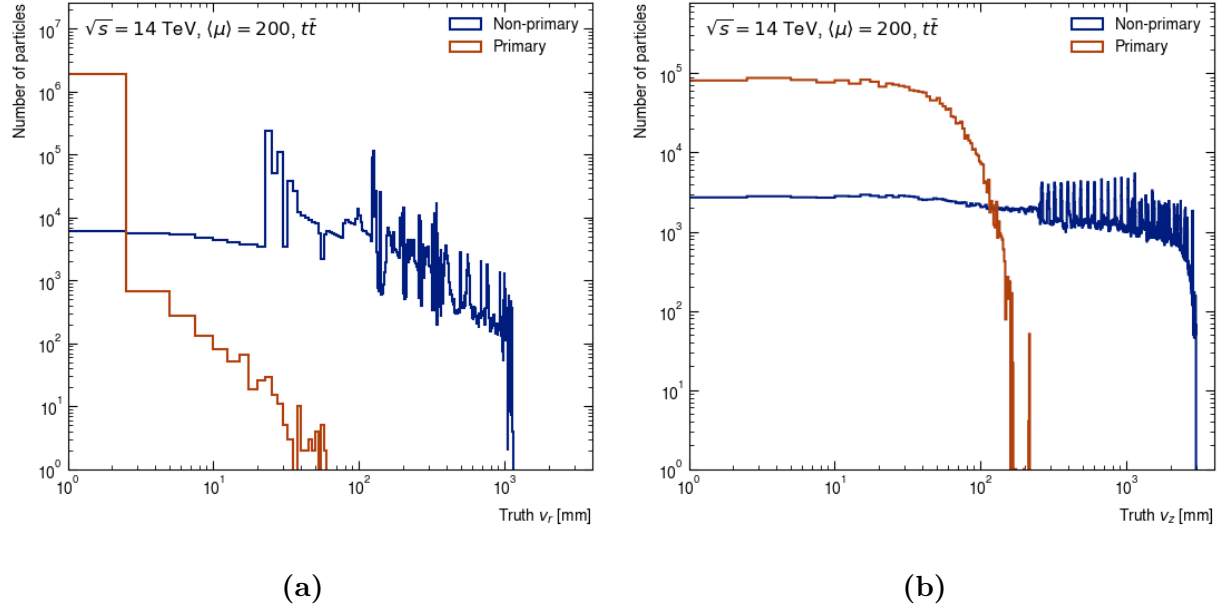


**Figure 8.2:** Distributions of the production vertex position on the transverse plane (a) and along the  $z$ -axis (b) of simulated particles in  $t\bar{t}$ -events at  $\langle\mu\rangle = 200$  for non-primary and primary particles. Primary vertices are restricted to a small region around the interaction point, whereas non-primary vertices can occur throughout the detector.

2389 As we have seen in section 6.3.2, electrons and positrons uniquely undergo significant  
 2390 energy loss due to Bremsstrahlung, and often follow trajectories that deviate from a helix.  
 2391 To guarantee good electron efficiency without compromising that of other particles, the  
 2392 ATLAS chain reconstructs electron tracks in a separate pass with a specialized parameter  
 2393 estimation technique. Similarly, we avoid training models on “irregular” electron tracks by  
 2394 excluding their contribution from the loss function.

2395 Because each simulated event is generated from one hard-scattering (HS) collision and  
 2396 on average 200 pile-up collisions (section 6.4), particles originating from soft interactions  
 2397 outnumber HS particles by about two orders of magnitude, (figure 8.3b). HS particles are  
 2398 generally more energetic; their  $p_T$  spectrum stretches up to 100 GeV, whereas that of pile-up  
 2399 particles strongly peaks at  $p_T < 1$  GeV and terminates at 20 GeV, as shown in figure 8.3a.  
 2400 As a consequence, a loss function calculated from all edges in the event is dominated by  
 2401 examples from low- $p_T$  tracks and bias the model toward pile-up particles, at the expense  
 2402 of high- $p_T$  HS particles that represent the interesting physics. This data imbalance largely  
 2403 impacts the performance, since in the presence of the magnetic field, low- $p_T$  particles have  
 2404 larger curvature and therefore different track pattern than do high- $p_T$  particles. To cope  
 2405 with this problem, we neglect the contribution to the loss function from particles of  $p_T < 1$   
 2406 GeV.

2407 In light of this discussion, we sort truth particles into two subsets by the following criteria

- 2408 1. **Target** particles: primary particles from both hard-scattering and pile-up interactions,  
 2409 which have  $p_T > 1$  GeV and  $|\eta| < 4$ , leave at least 3 hits in the tracker, are produced  
 2410 at a transverse radius  $R < 26$  cm, and are not electron nor positrons.
- 2411 2. **Non-target** particles: The rest of truth particles, including electrons and other par-  
 2412 ticles not satisfying the kinematic selection.

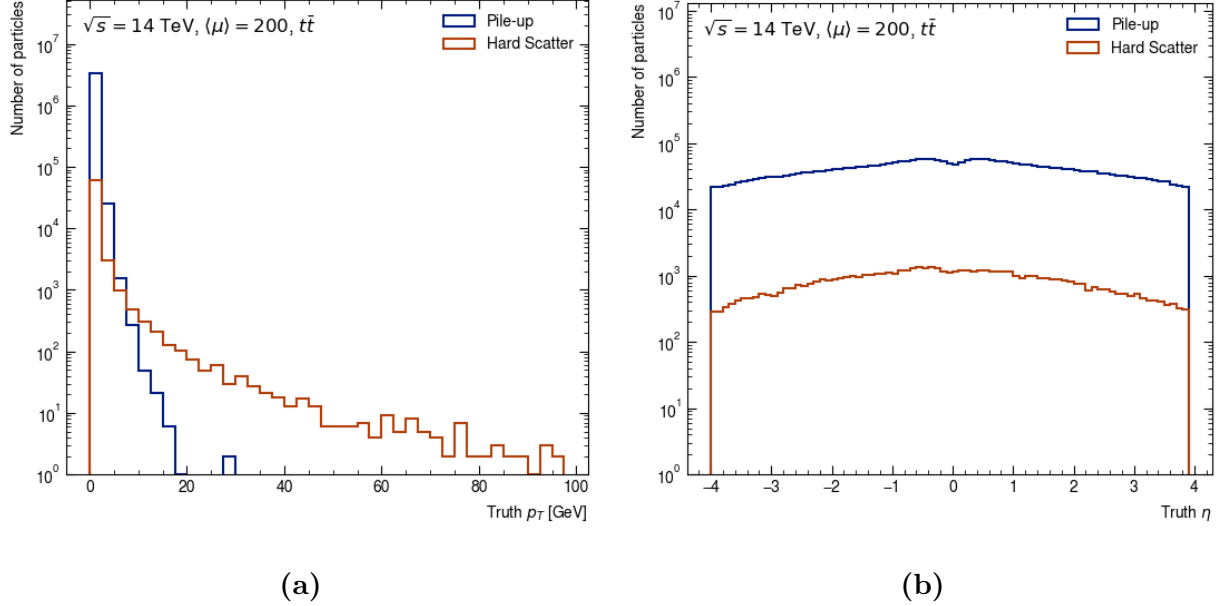


**Figure 8.3:** Distributions of transverse momentum  $p_T$  (a) and pseudorapidity (b) of simulated particles in  $t\bar{t}$ -events at  $\langle\mu\rangle = 200$  separated according into hard-scattering and pile-up particles. Soft pile-up particles have low  $p_T$ , whereas hard-scattering particles have a wider  $p_T$  distribution. The former is two orders of magnitude more abundant than the latter.

In the same manner, the subset of  $E_{truth}$  comprising exclusively connections from target particles is called the target truth edges and denoted as  $E_{truth,target}$ . A subset of non-target truth edges is defined as  $E_{truth,non-target} = E_{truth} - E_{truth,target}$ . The objective of global track finding then is to identify as many target truth edges and to misidentify as few fake edges as possible. Two metrics are defined from the edge sets to quantify these criteria. The first is the **edge efficiency**  $\epsilon$ : the fraction of target true edges present in a given edge set  $E$

$$\epsilon = \frac{|E \cap E_{truth,target}|}{|E_{truth,target}|}, \quad (8.2)$$

and the second is the **edge purity**  $\rho$ : the fraction of target true edges in  $E$ , excluding non-target true edges

$$\rho = \frac{|E_{truth,target} \cap E|}{|E - E_{truth,non-target}|}. \quad (8.3)$$

2421 High edge efficiency indicates that  $E$  contains a large proportion of target edges in the event,  
2422 while high purity means that a small proportion of  $E$  is fake edges. These definitions also  
2423 explicitly exclude non-target particles from the evaluation of model performance.

2424 **8.3 Graph construction methods**

2425 The first step of the GNN4ITk chain constructs a graph from the collision event. After  
2426 the space point formation stage, discussed in section 7.1, an event is a set of space points,  
2427 which can be considered as a graph with an empty edge set  $G_0 = (V, E = \emptyset)$ . The graph  
2428 construction stage populates  $E$  with edges, with an objective of including as many target  
2429 edges as possible, and at the same time control the total number of edges such that the  
2430 resulting graph can fit on GPU memory to train the GNN. At  $\langle\mu\rangle = 200$ , a  $t\bar{t}$  event has  
2431  $\mathcal{O}(10^5)$  space points, and a fully-connected graph, though simple, would have  $\mathcal{O}(10^{10})$  edges,  
2432 most of which are unphysical and a too expensive to process. Such a sizeable graph would  
2433 also be unable to fit on the GPU memory. Therefore, more clever methods are needed to  
2434 construct the graph. We investigate two graph construction methods: Module Map and  
2435 Metric Learning.

2436 **8.3.1 The Module Map Method**

2437 The module map is a data-driven approach to construct a graph. It is based on the  
2438 observation that a small fraction of edges in a fully-connected graph is physical, and an even  
2439 smaller fraction comes from target particles. It is therefore possible to create a list of all  
2440 pairs of detector modules connected by target particles in a large number of  $t\bar{t}$  events. By  
2441 following the path of each target particle and recording pairs of modules that it sequentially  
2442 traverses, we build up this list and call it the **Module Map**. To maximize the coverage of  
2443 possible module connections, 90000  $t\bar{t}$  simulated events described in section 6.4 are used

2444 Illustrated in figure 8.4 is an example of module map learning, in which two particles are  
 2445 observed to sequentially hit modules  $1 \rightarrow 2 \rightarrow 3 \rightarrow 4 \rightarrow 5 \rightarrow 6$  and  $3 \rightarrow 4 \rightarrow 7 \rightarrow 8 \rightarrow 9$ .  
 2446 From these particles, connections between the following pairs of modules  $(1,2)$ ,  $(2,3)$ ,  $(3,4)$ ,  
 2447  $(4,5)$ ,  $(5,6)$ ,  $(4,7)$ ,  $(7,8)$ , and  $(8,9)$  are registered to the module map (note the presence  
 2448 of two connections sharing module number **4**). As more particles are observed, the set of  
 2449 recorded connections grows, covering a wider range of module connectivity. The idea is that  
 2450 once the number of observed events is large enough, the map is saturated and becomes a  
 2451 “dictionary” of all possible module connections.

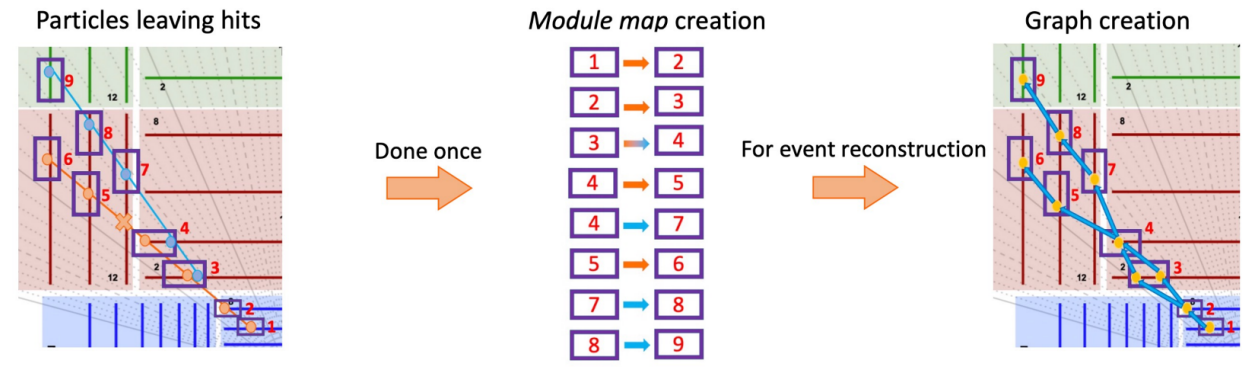


**Figure 8.4:** Principle of the Module Map method for graph construction. By observing the trajectory of target particles in 90000  $t\bar{t}$  events, a list of all pairs of detector modules sequentially traversed by a particle is built. During event reconstruction, the space points residing on the pairs of modules which appear in the module map are connected by an edge. A set of selections are applied to reduce the number of edges and eliminate outliers.

2452 When building a graph from an event *which has not been seen* by the Module Map, out  
 2453 of all possible connections between space points, only those linking pairs of modules present  
 2454 in the Module Map are admitted to become graph edges. On figure 8.4, for example, 10  
 2455 space points on 9 modules are recorded in the new event, with 2 space points present on  
 2456 module 3. The module map therefore admits connections between space points residing on  
 2457 the following module pairs:  $(1,2)$ ,  $(2,3_1)$ ,  $(2,3_2)$ ,  $(3_1,4)$ ,  $(3_2,4)$ ,  $(4,5)$ ,  $(4,7)$ ,  $(5,6)$ ,  $(7,8)$ ,  
 2458  $(8,9)$ , with subscripts indicating different space points on the same module where necessary.

2459 The module map thus allows to select a small subset of the 90 possible connections, based  
2460 on our previous observations.

2461 The same principle can be extended from pairs of modules to triplets of modules, so that  
2462 the module map is built from a list of three modules sequentially hit by a particle, and on  
2463 inference, pairs of possible connections appearing in the module map are admitted. Since  
2464 the requirement of three consecutive hits is stricter than that on two hits, the *triplet* module  
2465 map helps reduce the number of edges in the reconstructed graph compared to the simple  
2466 *doublet* module map. Nevertheless, the average number of edges in graphs constructed from  
2467 the triplet module map is still too large to process on available hardware, averaging  $\mathcal{O}(10^8)$ .

2468 On the chosen GNN architecture, we found that a GPU with 80GB memory is capable  
2469 of running the forward pass with gradient tracking on  $\sim 2 \times 10^6$  edges/graph, which is the  
2470 target of graph construction. The number of edges per event acts as a batch size which can  
2471 limit the number of trainable parameters in a neural network and its expressive power. In  
2472 addition, processing a massive graph of mostly fake edges is a computing a bottleneck. To  
2473 build leaner graphs, additional selection requirements are imposed on doublets and triplets  
2474 in the “crude” module map graphs.

2475 Edge selections are based on geometric features derived from the connected space points.  
2476 Denoting the nodes in a doublet ordered by increasing distance from the origin by  $(v_1, v_2)$ ,  
2477 and in a triplet in the same order by  $(v_1, v_2, v_3)$ , we define two categories of geometric features.

2478 1. **Doublet features** are calculated from the doublet hits connected by an edge. They  
2479 include:

2480 •  $z_0 = z_1 - r_1 \frac{z_2 - z_1}{r_2 - r_1}$ .

2481 •  $\Delta\phi = \phi_2 - \phi_1$

2482 •  $\Delta\eta = \eta_2 - \eta_1$

2483 •  $\phi_{slope} = \frac{\phi_2 - \phi_1}{r_2 - r_1}$ .

2484 These features represent several basic assumptions about the trajectory of a charged  
 2485 particle in a magnetic field. For example, the pseudorapidity  $\eta$  depends only on the  
 2486 polar angle  $\theta$  and is constant if the particle does not interact with materials. The  
 2487 distribution of  $\Delta\theta$  of two consecutive hits on a particle's path should therefore peak  
 2488 at 0 with some width  $\sigma$  resulting from detector effects.

2489 2. **Triplet features** are calculated from the doublet features of the pair of edges, resem-  
 2490 bling a second-order derivative.

- 2491 •  $\Delta\text{slope}_{xy} = \left(\frac{\Delta y}{\Delta x}\right)_{12} - \left(\frac{\Delta y}{\Delta x}\right)_{23}$   
 2492 •  $\Delta\text{slope}_{rz} = \left(\frac{\Delta z}{\Delta r}\right)_{12} - \left(\frac{\Delta z}{\Delta r}\right)_{23}$

2493 where  $\Delta u$  is the difference in variable  $u$  between the nodes indicated by the numerical  
 2494 subscript.  $\Delta\text{slope}_{xy}$  is related to the curvature of the orbit and  $\Delta\text{slope}_{rz}$  the deviation  
 2495 from a straight line over the two triplet connections.

2496 The empirical distributions of these features are established from events dedicated to the  
 2497 construction of the module map, along with a set of thresholds that defines the acceptance  
 2498 region. These thresholds are selected to eliminate as many fake edges as possible without  
 2499 rejecting true edges in the observed 90000 events. In inference, any edge failing to meet  
 2500 these thresholds is rejected. A simple choice for the acceptance region of a feature  $\xi$  is the  
 2501 whole range  $[\xi_{min}, \xi_{max}]$ , such that an inferred edge is rejected if  $\xi < \xi_{min}$  or  $\xi > \xi_{max}$ . This  
 2502 is called the **MinMax** selection. Another choice is the interval of  $[\bar{\xi} - 5\sigma_\xi, \bar{\xi} + 5\sigma_\xi]$ , where  
 2503  $\bar{\xi}$  and  $\sigma_\xi$  are respectively the sample mean and standard deviation of the feature, denoted  
 2504 the **MeanRMS** selection. Both selections are examined, and the graph construction result  
 2505 is discussed in section 8.4.

### 2506 8.3.2 The Metric Learning approach

2507 Metric Learning [112, 124, 126] is a semi-supervised machine learning technique which  
 2508 models the difference between a pair of data points. Given a sample  $X$  and corresponding  
 2509 labels  $Y$ , we seek a transformation  $f_\theta : \mathbb{R}^d \rightarrow \mathbb{R}^n$ , where  $d$  is the dimension of  $\mathbf{x} \in X$ ,  $n$   
 2510 the dimension of an embedding space and  $\theta$  a set of learnable weights. A distance metric  
 2511  $\mathcal{D} : \mathbb{R}^n \otimes \mathbb{R}^n \rightarrow [0, \infty)$  is selected to measure the difference between two data points in  
 2512 the embedding space. The objective is that for two examples  $\mathbf{x}_i, \mathbf{x}_j \in X$  and their labels  
 2513  $y_j, y_j \in Y$ , the distance  $\mathcal{D}(f_\theta(\mathbf{x}_i), f_\theta(\mathbf{x}_j))$  is small if  $y_i = y_j$  and large otherwise. After  
 2514 training, the transformation  $f$  sends data points of the same class labels to the same region in  
 2515 the embedding space, and separate those having different labels (figure 8.5). For conciseness,  
 2516 we define

$$d_\theta(\mathbf{x}_i, \mathbf{x}_j) = \mathcal{D}(f_\theta(\mathbf{x}_i), f_\theta(\mathbf{x}_j)), \quad (8.4)$$

2517 The distance metric can be any mapping that satisfies the following criteria, defined for all  
 2518  $\mathbf{z}_i, \mathbf{z}_j, \mathbf{z}_k \in \mathbb{R}^n$

- 2519 1. non-negativity:  $\mathcal{D}(\mathbf{z}_i, \mathbf{z}_j) \geq 0$
- 2520 2. symmetry:  $\mathcal{D}(\mathbf{z}_i, \mathbf{z}_j) = \mathcal{D}(\mathbf{z}_j, \mathbf{z}_i)$
- 2521 3. identity:  $\mathcal{D}(\mathbf{z}_i, \mathbf{z}_i) = 0$
- 2522 4. triangle inequality:  $\mathcal{D}(\mathbf{z}_i, \mathbf{z}_j) \leq \mathcal{D}(\mathbf{z}_i, \mathbf{z}_k) + \mathcal{D}(\mathbf{z}_k, \mathbf{z}_j)$

2523 To construct a graph using metric learning, we assume that two nodes belonging to  
 2524 different tracks differ from each other in some sense. Taking  $X$  as the set of node feature  
 2525 vector, and  $Y$  the set of the particle label, we can write  $y_{ij} = 1_{[y_i=y_j]}$ ,  $y_i \in Y$ . Through  
 2526 metric learning, the transformation weights  $\theta$  are adjusted to minimize  $d_\theta(\mathbf{x}_i, \mathbf{x}_j)$  if  $y_{ij} = 1$   
 2527 and maximize it if  $y_{ij} = 0$ .

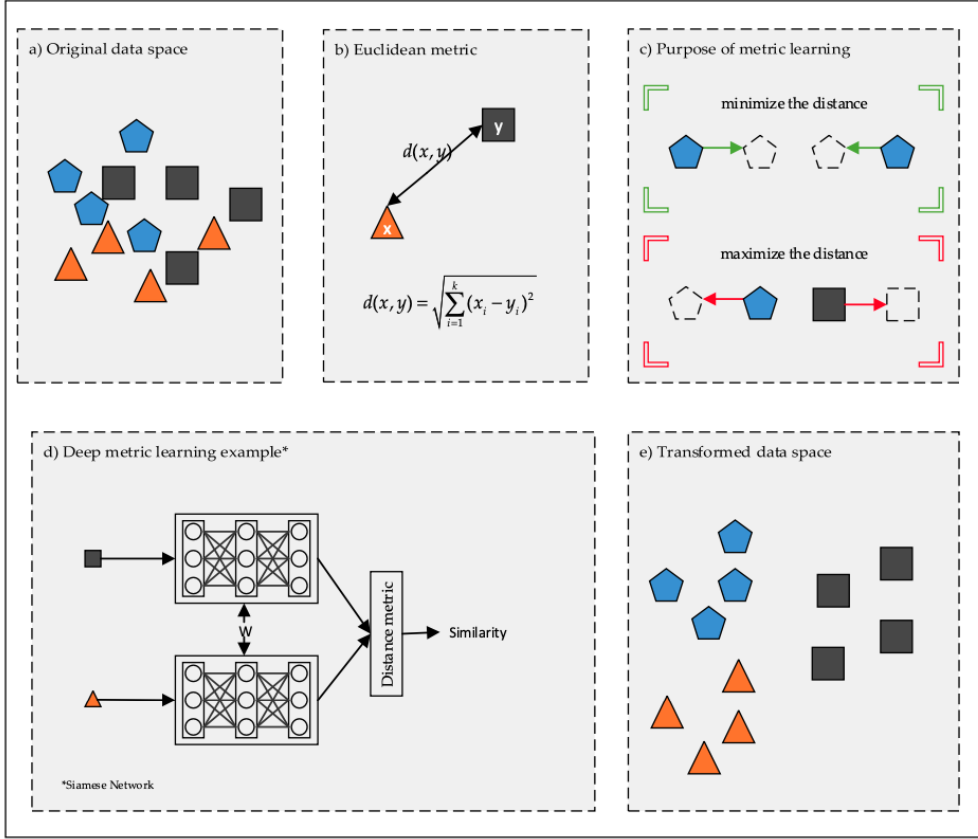


**Figure 8.5:** Principle of deep metric learning. Starting from (a) labelled data which are difficult to separate in real space, (b) a distance metric is defined to measure the similarity between data points in an embedding space, in this case a simple Euclidean distance. (c) A transformation from real to embedding space is learned, such that examples of the same class are close together, whereas those of different classes are pushed away from each other. (d) The transformation is a simple feed-forward network applied to all instances of the dataset. (e) After training, examples of different classes are well-separated, and clusterizable [124].

2528 The Euclidean distance is chosen as distance metric

$$\mathcal{D}(\mathbf{p}, \mathbf{q}) = \|\mathbf{p} - \mathbf{q}\|_2 = \sqrt{(\mathbf{p} - \mathbf{q})^2}, \quad \mathbf{p}, \mathbf{q} \in \mathbb{R}^n, \quad (8.5)$$

2529 and a simple Multi-Layer Perceptron (MLP) as the transformation  $f_\theta$ . The last ingredient  
2530 is the loss function  $\mathcal{L}(\theta)$ . There are many choices of loss function for metric learning, each

targeting a slightly different learning objective. A comprehensive summary is given in references [124, 160]. In this thesis, the simplest and most intuitive choice, called **Contrastive Loss**, is employed. Over a set of edges  $E$ , we define

$$\mathcal{L}_E(\theta) = \frac{1}{|E|} \sum_{e_{ij} \in E} l_\theta(\mathbf{x}_i, \mathbf{x}_j), \quad l_\theta(\mathbf{x}_i, \mathbf{x}_j) = y_{ij} d_\theta(\mathbf{x}_i, \mathbf{x}_j) + (1 - y_{ij}) \max\{0, r - d_\theta(\mathbf{x}_i, \mathbf{x}_j)\}. \quad (8.6)$$

For a positive pair ( $y_{ij} = 1$ ), the loss function is minimized if the distance between  $f_\theta(\mathbf{x}_i)$  and  $f_\theta(\mathbf{x}_j)$  is 0, effectively pulling together  $(\mathbf{x}_i, \mathbf{x}_j)$ . For a negative pair ( $y_{ij} = 0$ ), the loss is minimized if their distance is increased up to a margin  $r$ .  $l_\theta(\mathbf{x}_i, \mathbf{x}_j)$  becomes 0 if  $d_\theta > r$ . This margin prevents the model from enlarging the distance when the pair of nodes is sufficiently separated, focusing the attention on those that are not. The contrastive loss defined with a margin is also called the contrastive hinge loss.

Note that the loss is computed from pairs of nodes, which can be regarded as edges, but we do not have edges at this point. A training sample  $E$  must therefore be generated from the input nodes. Again, a simple choice of all  $N(N - 1)$  possible unordered pairs of node is far too many to fit on memory and would overwhelmingly contain fake edges. Instead, we construct  $E$  using a technique called hard negative mining [149]

$$E = E_{truth,target} \cup E_{hnm} \cup E_{random}, \quad (8.7)$$

where  $E_{truth,target}$  is the set of target true edges as defined in 8.2. This is truth information that comes from the training data. To generate training fake edges, a training graph is constructed in the latent space by connecting each node  $v_i \in V$  to a maximum of  $k$  closest nodes within a sphere centered at  $v_i$  of radius  $r$  using a k-Nearest-Neighbor algorithm (kNN). Note that the radius is equal to the margin. A set of edges, denoted  $E_{hnm}$ , is constructed from the training graph by finding  $n_{hnm}$  fake edges with the smallest distance in the transformed space.  $E_{hnm}$  represents the negative pairs that most resemble true pairs, so maximizing their distance is equivalent to lower-bounding the separation between all fake pairs of nodes. Finally, a set of randomly sampled edges  $E_{random}$  is added to stabilise the loss.

Hit input	Description
$r$	Global transverse radius of space point
$\phi$	Global azimuthal angle of space point
$z$	Global $z$ -coordinate of space point
$x_{CL,i}$	Global $x$ -coordinate of cluster $i$
$y_{CL,i}$	Global $y$ -coordinate of cluster $i$
$z_{CL,i}$	Global $z$ -coordinate of cluster $i$
count	Number of pixels cells contained in a cluster
charge count	Charge deposit on a pixel cluster
$\eta_{CL,loc,i}$	Module $\eta$ in local coordinate system
$\phi_{CL,loc,i}$	Module $\phi$ in local coordinate system
$\eta_{CL,glob,i}$	Module $\eta$ in global coordinate system
$\phi_{CL,glob,i}$	Module $\phi$ in global coordinate system
eta-angle	hit $\eta$ angle
phi-angle	hit $\phi$ angle
$l_x$ (LocalDirx)	Cluster shape $x$
$l_y$ (LocalDiry)	Cluster shape $y$
$l_z$ (LocalDirz)	Cluster shape $z$
LengthDirx	LengthDirx
LengthDiry	LengthDiry
LengthDirz	LengthDirz

**Table 8.1:** Input features into the Metric Learning model. See Appendix A for definitions of the variables.

Hyperparameter	Value
Hidden layers	4
Hidden dimension	1024
Embedding dimension	12
KNN	50
Margin	0.1
Weighting ratio	1.0 : 4.0

**Table 8.2:** Hyperparameters used to train the Metric Learning model.

The model was trained on an NVIDIA A100 GPU with 80 GB in memory. The train set contains 7800 simulated  $t\bar{t}$  events, each treated as a batch. An iteration over the train set (epoch) takes approximately 1 hour, and the model is trained over approximately 200 epochs.

## 8.4 Result

Shown in figure 8.6 is the averaged edge efficiency of graphs constructed with the **MinMax** and **MeanRMS** selections as a function of the pseudorapidity  $\eta^{\text{II}}$  and transverse momentum  $p_T$ . The Module Map method under both choices of edge cuts produces efficiency  $\epsilon \geq 99.5\%$  across  $\eta$ . Averaged across test events, the **MeanRMS** selection is slightly less efficient than the **MinMax** counterpart by 0.2%, due to tighter thresholds on geometric observables. The former's inefficiency is observed in the barrel region ( $|\eta| < 2$ ) and the very forward region ( $|\eta| \approx 4$ ). The slight efficiency loss comes with the benefit of building smaller graphs. The **MeanRMS** selection produces graphs having  $\langle |V| \rangle = (8.55 \pm 2.26) \times 10^5$  edges, 30% fewer than those from the latter, averaging at  $(1.22 \pm 0.31) \times 10^6$  edges.

---

<sup>II</sup>Here the pseudorapidity of an edge is defined as that of the inner node.

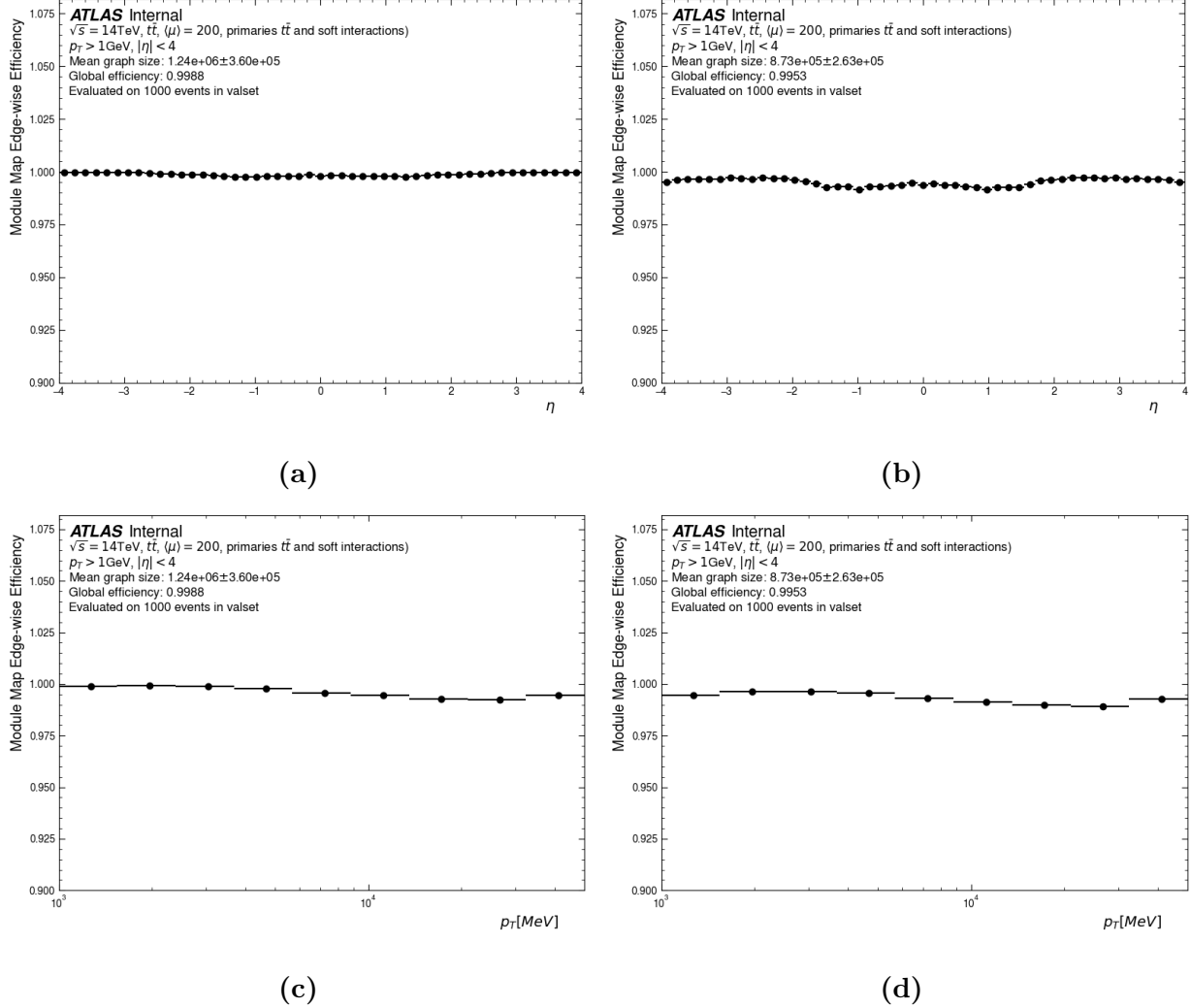


**Figure 8.6:** Graph construction efficiency of the Module Map approach as a function of  $\eta$  (upper) and  $p_T$  (lower), using the MinMax selection (left) and MeanRMS selection (right).

2568     The reduced number of edges at negligible efficiency cost is a strong advantage of the  
 2569     **MeanRMS** method. It allows the GNN to be trained with better class balance, because the  
 2570     majority of additional eliminated edges are fake or non-target, evidenced by almost identical  
 2571     efficiency values. In addition, a smaller graph leads to better latency and smaller memory  
 2572     footprint, which are important factors in inference. Therefore, graphs produced by both  
 2573     selections are examined in later stages of the reconstruction chain.

Both of the module map selections show good edge efficiency over the  $p_T$  range, reaching  $\epsilon \geq 99\%$  (figures 8.6c and 8.6d). A slight decrease is observed at the high- $p_T$  region, above  $p_T \geq 5$  GeV, which, as we will see in the next chapters, is a common occurrence in the GNN4ITk chain. It can be attributed to the rarity of high- $p_T$  particles in the training data, as discussed in section 8.2, which affects the coverage of possible module connections produced by high- $p_T$  particles. The Module Map can only create an edge in the inferred event if it has seen the same edge during its construction. In other words, in order for a true connection to appear in the inferred graph, the corresponding pair of modules must have been consecutively traversed by a particle in the training events. However, high- $p_T$  particles constitute but a small portion of final-state particles (figure 8.3a), and those observed from the training event might not cover all possible trajectories through the detector's modules. As a result, it is more likely that a high- $p_T$  connection from a target particle in an inferred event was not seen in the training events, leading to inefficiency.

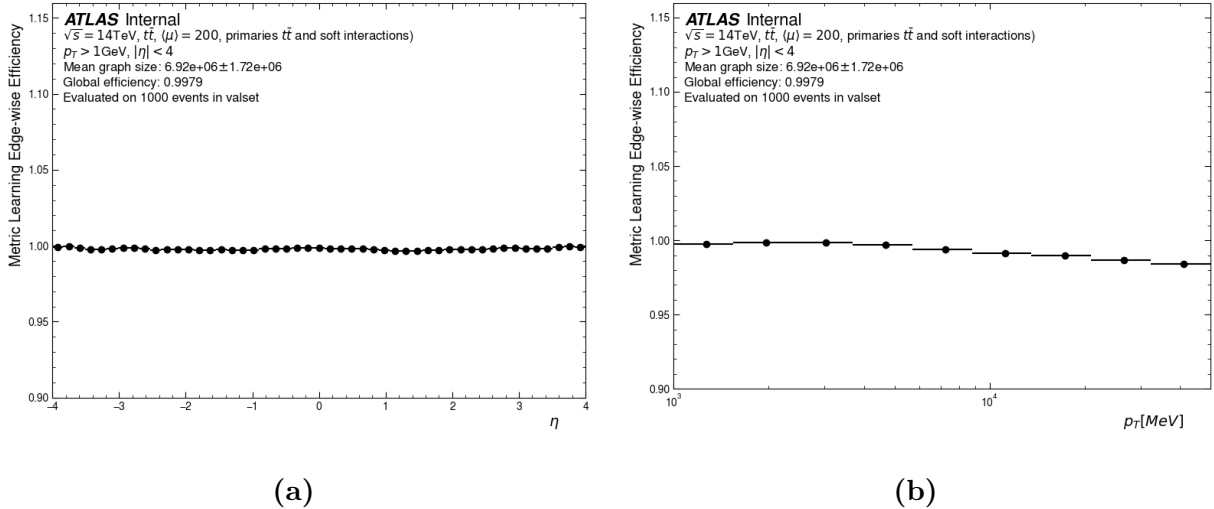


**Figure 8.7:** Graph construction efficiency of the Metric learning approach as a function of  $\eta$  (a) and  $p_T$  (b), averaged over 1000  $t\bar{t}$  events.

The efficiency of graphs constructed with the Metric Learning method as a function of  $\eta$  and  $p_T$  is shown in figure 8.7. Good edge efficiency is observed across the  $\eta$  range, averaging at 99.79%, on par with those from the Module Map under the **MinMax** selection, but with a

2590 considerably larger edge set,  $|V| = (6.92 \pm 1.72) \times 10^6$ , compared to just  $(1.24 \pm 0.36) \times 10^6$ . As  
 2591 already discussed, the increased graph size will pose a problem for the edge-classifying GNN,  
 2592 so the graph is pruned using a light-weight neural network, which will be discussed in section  
 2593 9.2. Although good efficiency is observed throughout the  $p_T$  range, a slight decrease appears  
 2594 at  $p_T > 5$  GeV, which, similar to what that of the Module Map method, can be attributed  
 2595 to small training statistics at high  $p_T$ . The metric learning model learns to minimize the  
 2596 distance between space points belonging to the same particle via an attractive term in the  
 2597 loss function (equation (8.6)), which can be rewritten as

$$\mathcal{L}_\theta = E[d_\theta] = \left( \sum_{p_T} E[d_\theta | p_T, \text{target}] P[p_T | \text{target}] P[\text{target}] \right) + E[r - d_\theta | \text{fake}] P[\text{fake}], \quad (8.8)$$

2598 where  $E[X]$  and  $P[A]$  denote unconditional expectation value and probability, and  $E[X|A]$   
 2599 and  $P[X|A]$  the conditional counterpart. The first term on the right-hand size, representing  
 2600 the attractive loss, is a sum over the  $p_T$ -dependant mean distance between nodes connected  
 2601 by a target edge, weighted by  $P[p_T | \text{target}]$ , the probability that the edge comes from a  
 2602 particle having transverse momentum  $p_T$ . As seen on figure 8.3a,  $P[p_T | \text{target}]$  decreases  
 2603 monotonically with  $p_T$ , down-weighing the loss contribution, and thus directing the attention  
 2604 away from high-momentum particles. As the curvature, which highly depends on  $p_T$ , is an  
 2605 important track pattern, the lack of high- $p_T$  examples impacts the performance of not only  
 2606 the metric learning, but also throughout the GNN4ITk algorithm.

2607 **Chapter 9**

2608 **Edge classification**

2609 Graphs constructed by both methods introduced in the last chapter contain many fake  
2610 edges. The second stage of the GNN4ITk chain labels the graph connections, so that fake  
2611 ones are removed and track candidates are built from exclusively true connections. We carry  
2612 out this task using a Graph Neural Network (GNN), which leverages the graph connectivity  
2613 to compute a score for each edge that represents the probability of being a true edge. This  
2614 chapter describes the edge classification stage, starting with a general introduction to GNNs.  
2615 Sections 9.2 and 9.3 respectively detail the filter network and the interaction network, two  
2616 edge-classifying GNN architectures investigated in this thesis, and their results.

2617 **9.1 Introduction to graph neural networks**

2618 The last 15 years have seen an explosion of deep neural networks into a major domain  
2619 of machine learning, achieving unprecedented performance on complicated tasks thanks to  
2620 increasingly available training data and computing power. An ecosystem of different network  
2621 architectures has been explored targeting different data representations. For example, Feed-  
2622 forward Neural Networks (FNNs) for tabular data, Convolutional Neural Networks (CNNs)  
2623 for 2-dimensional images, Recurrent Neural Networks (RNNs) for sequences. These archi-  
2624 tectures are effective on Euclidean, or grid-like data, but not sufficiently flexible to model  
2625 irregular non-Euclidean data structures such as graphs, which comprise entities (nodes) and

2626 their relationships (edges). In this context, **Graph Neural Networks** enable representation learning on graph-structured data by leveraging the underlying patterns in features 2627 associated with nodes and edges.

2629 Graph neural networks operate on a graph by iteratively propagating information via the 2630 edges. The representation of a node is updated based on its features and those of its direct 2631 neighbours through a learnable aggregation mechanism. The general formulation of the  $k$ -th 2632 iteration at can be written as

$$\mathbf{h}_i^k = \text{UPDATE}_k(\mathbf{h}_i^{k-1}, \text{AGGREGATE}_k(\{\mathbf{h}_j^{k-1} : j \in \mathcal{N}(v_i)\})) \quad (9.1)$$

2633 where  $\mathbf{h}_i^k$  denotes the embedding of node  $v_i$  after the  $k$ -th iteration, and  $\mathcal{N}(v_i)$  the set of 2634 neighbouring nodes of  $v_i$ . Numerous GNN architectures have been proposed, from the simple 2635 Graph Convolutional Networks (GCNs) [125], which leverage spectral graph theory to define 2636 convolution-like operations on graphs, Graph Attention Networks (GATs) [161], which introduce 2637 attention mechanisms for adaptive neighbourhood weighting, to GraphSAGE [118], and 2638 Graph Isomorphism Networks (GINs) [162], which improved expressiveness in distinguishing 2639 graph structures.

## 2640 9.2 The filter network

2641 In the previous section, we have motivated and introduced graph neural networks as 2642 the deep learning method for non-Euclidean data represented as graphs. The GNN4ITk 2643 algorithm uses graph networks to identify fake edges in the graphs built from the methods 2644 described in chapter 8.

### 2645 9.2.1 Method

2646 As discussed in 8.3.2 and shown on figure 8.7, the number of edges in a graph produced 2647 by the **Metric Learning** method is on average  $|E| = (6.92 \pm 0.17) \times 10^6$ , most of which are

2648 fake. For comparison, the number of true target edges are of  $\mathcal{O}(10^4)$ , two orders of magnitude  
 2649 fewer. Among the fake edges, we can categorize *hard* fake edges as those resembling true  
 2650 edges, for example, a connection from a source node  $i$  to a false destination node  $j'$  on  
 2651 the same detector module as the true destination node  $j$ , so that  $|\mathbf{r}_j - \mathbf{r}_{j'}| \approx 0$ . The true  
 2652 edge  $e_{ij}$  is therefore difficult to distinguish from the fake edge  $e_{ij'}$ . In contrast, *easy* fakes  
 2653 are recognizable from target true edges, such as unphysical edges randomly selected by the  
 2654 kNN.

2655 Because hard fakes are difficult to identify, it is necessary to train a deep network to  
 2656 guarantee good performance. A large graph coupled with a large network creates a bottleneck  
 2657 in inference time and resource consumption. In addition, training on both hard and easy  
 2658 fake edges directs the classifier’s attention away from hard fakes and affects the performance.  
 2659 A better strategy, therefore, is to train a shallow network on the output graphs of the Metric  
 2660 Learning to eliminate easy fakes and subsequently a deeper, more sophisticated network to  
 2661 eliminate hard fakes. The first network, designated the **Filter Network**, is described in  
 2662 this section, and the second, called the **Interaction Network**, in section 9.3.

2663 The architecture of the Filter Network is based on the GRAPH SAGE convolution pro-  
 2664 posed by reference [118], which facilitates the efficient learning of large complex graphs. The  
 2665 idea is to train a set of functions which aggregate and propagate information between dif-  
 2666 ferent depths of a node’s neighborhood. We define a  $k$ -hop neighborhood of a node as the  
 2667 subset of nodes whose shortest path to the center node proceeds through exactly  $k$  edges.  
 2668 Figure 9.1 shows an example of a **central node** and its neighborhoods with  $k = 1$  and  $k = 2$ .  
 2669 At each depth, a trainable function aggregates the features of the nodes residing within, and  
 2670 passes the aggregated features to the next depth. In the figure, the messages from nodes  
 2671 at  $k = 2$  gathered by the **green aggregator** are used to evolve the features of **nodes** at  
 2672  $k = 1$ , which are then aggregated by the **blue aggregator** and passed to the **central node**.

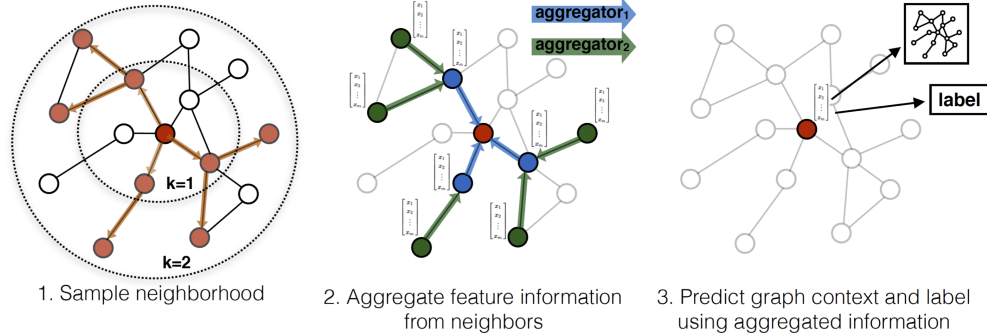


**Figure 9.1:** GRAPHSAGE sampling and aggregation mechanism. [118]

This mechanism is expressed more concretely in the pseudocode shown in algorithm 1. Each GRAPHSAGE is defined by  $K$  aggregator functions, denoted  $\text{AGGREGATE}_k$ ,  $k \in \{1, \dots, K\}$ , and a set of weight matrices  $\mathbf{W}^k$ ,  $k \in \{1, \dots, K\}$ , which propagate the aggregated information between different search depths. The aggregators must be differentiable to allow back-propagation through the search depths. Recall that the graph is defined by a set of nodes  $V$  and a set of edges  $E$ . To each node  $i \in V$  is associated a node feature vector  $\mathbf{x}_i \in \mathbb{R}^d$ . A neighbourhood function  $\mathcal{N} : v \rightarrow V$  finds other nodes directly connected to a given node  $v$ . In each step  $k$ , to each node  $v_i \in \mathcal{V}$  are aggregated the representations of other nodes in its local neighborhood  $\{\mathbf{h}_j^{k-1}\}$ , found by  $\mathcal{N}(v_i)$ , into a single vector  $\mathbf{h}_{\mathcal{N}(v_i)}^k$ . The current representation of  $v_i$  namely  $\mathbf{h}_v^{k-1}$  is concatenated with  $\mathbf{h}_{\mathcal{N}(v_i)}^k$ , and fed through an MLP represented by  $W^k$ , followed by a non-linear activation function  $\sigma$ . As this process iterates, nodes incrementally receive more information from further reaches of the graph, and their features become more expressive.

Any element-wise function is a good aggregator. However, for simplicity the **Filter** uses the mean aggregator, i.e.

$$\text{AGGREGATE}(\{\mathbf{h}_1, \dots, \mathbf{h}_N\}) = \frac{1}{N} \sum_{i=1}^N \mathbf{h}_i \quad (9.2)$$

---

**Algorithm 1:** Calculation of node embedding  $\mathbf{z}_i$  with GRAPHsAGE [118]

---

```

 $h_i^0 \leftarrow \mathbf{x}_i;$ 
for  $k \in \{1, \dots, K\}$  do
  for  $i \in \{1, \dots, |V|\}$  do
     $\mathbf{h}_{\mathcal{N}(v_i)}^k \leftarrow \text{AGGREGATE}_k(\{\mathbf{h}_j^{k-1} \forall v_j \in \mathcal{N}(v_i)\}) ;$ 
     $\mathbf{h}_i^k \leftarrow \sigma \left( \mathbf{W}^k \cdot [\mathbf{h}_v^{k-1} | \mathbf{h}_{\mathcal{N}(v_i)}^k] \right)$ 
  end
   $\mathbf{h}_i^k \leftarrow \frac{\mathbf{h}_i^k}{\|\mathbf{h}_i^k\|_2}, \forall v_i \in \mathcal{V}$ 
end

```

$\mathbf{z}_i \leftarrow \mathbf{h}_i^K \forall v_j \in \mathcal{V},$

where  $\sigma(\cdot)$  is an activation function,  $[\mathbf{x}|\mathbf{y}]$  a vector concatenation.

---

2688     The neighbourhood function  $\mathcal{N}(v)$  uniformly draws a fixed number of edges from the set  
 2689      $\{(u, v) \in \mathcal{V}\}$ , instead of using the entire 1-hop neighbourhood. Sampling limits the mem-  
 2690     ory footprint of a GRAPH SAGE operation on large graphs. Without it, the consumption  
 2691     becomes unpredictable and grows with  $|\mathcal{V}|$ . It is found in reference [118] that  $K = 2$  and  
 2692     sample sizes  $S_1 = 25$ ,  $S_2 = 10$  produce a good balance between memory and performance,  
 2693     which are used in the **Filter**.

2694     With the GRAPH SAGE mechanism defined, we can now describe the network architec-  
 2695     ture. First, the node embedding is evolved over  $L$  iterations of GRAPH SAGE to encode local  
 2696     context from a search depth at most  $K \times L$ . The embedding of two nodes  $(v_i, v_j)$  connected  
 2697     by an edge  $e_{ij} \in E$  are concatenated and fed to a decoder  $\phi : \mathbb{R}^n \times \mathbb{R}^n \rightarrow (0, 1)$  to obtain  
 2698     a score representing the probability of being a true edge. The corresponding pseudo-code is  
 2699     shown in algorithm 2.

---

**Algorithm 2:** The **Filter** network

---

```

 $\mathbf{z}_i^0 \leftarrow \mathbf{x}_i;$ 
for  $l \in \{1, \dots, L\}$  do
|  $z_i^l \leftarrow \text{GRAPH SAGE } (\mathbf{z}_i^{l-1}, \mathcal{V})$ 
end
 $\forall e_{ij} \in E : \hat{y}_{ij} \leftarrow \sigma(\mathbf{W} \cdot [\mathbf{z}_i^L | \mathbf{z}_j^L] + \mathbf{b}) \equiv \phi(\mathbf{z}_i^L, \mathbf{z}_j^L)$ 

```

---

2700     Each event is treated as a minibatch. The model weights  $\theta$  is optimized via the loss  
 2701     function  $\mathcal{L}_E(\theta)$ , defined over a set of edges  $E$  as

$$\mathcal{L}_E(\theta) = \frac{1}{|E|} \sum_{e_{ij} \in E} w_{ij} l(y_{ij}, \hat{y}_{ij}), \quad l(y, \hat{y}) = (y \log \hat{y} + (1 - y) \log(1 - \hat{y})), \quad (9.3)$$

2702     in which the edge score  $\hat{y}_{ij}$  is obtained according to algorithm 2, and the label  $y_{ij}$  is the truth  
 2703     edge label. The cost function  $l(y, \hat{y})$  is simply the cross-entropy of a binary label  $y \in \{0, 1\}$   
 2704     and a score prediction  $\hat{y} \in (0, 1)$ .

2705 Due to the large graph size, the loss function is computed from a subset of edges  $E_{train} \subset$   
2706  $E$  to avoid GPU memory overflow. The edge list is constructed in a manner similar to  
2707 equation (8.7), such that

$$E_{train} = E_{\text{truth,target}} \cup E_{\text{hnm}} \cup E_{\text{random}}. \quad (9.4)$$

2708 The difference between the training edge set of the **Metric Learning** network and that  
2709 of the **Filter** network is that the former is created on-the-fly from a kNN graph, whereas  
2710 the latter from an existing graph. In addition, the hard negatively-mined edges in this case  
2711 are defined as fake edges whose score exceeds a threshold  $Y_t = 0.5$ . This implies that  $E_{\text{hnm}}$   
2712 component of the loss punishes the network for false positive edges and ignores true negative  
2713 edges, assuming threshold  $Y_t$  is used to make predictions. In practice, we observe that the  
2714 **GRAPH SAGE** convolutions have relatively modest memory footprint even with gradient  
2715 tracking, thanks to the sampling mechanism. In contrast, the decoder consumes larger GPU  
2716 memory and can cause overflow in large graphs. Therefore, the loss function is calculated  
2717 with a memory-saving trick illustrated in algorithm 3. First, the **GRAPH SAGE** convolutions  
2718 are applied on the input graph with gradient tracking, yielding the node embedding vectors  
2719  $\mathbf{z}_i^L$  attached to a gradient compute graph. Then, the node vectors are fed to the decoder  
2720  $\phi$  **without** gradient tracking to calculate the score of **all** edges in  $E$ , which are then used  
2721 to create the training edge set  $E_{train}$  through hard-negative mining. Finally, the decoder is  
2722 invoked again, this time **with** gradient tracking and **exclusively** over  $E$ .

2723 The last ingredient is the weight  $w_{ij}$ , defined as

$$w_{ij} = \begin{cases} 1, & y_{ij} = 0 \\ 10, & (y_{ij} = 1) \wedge (e_{ij} \in E_{\text{truth,target}}) \\ 0 & (y_{ij} = 1) \wedge (e_{ij} \notin E_{\text{truth,target}}) \end{cases} \quad (9.5)$$

2724 To deal with class imbalance, true target edges are given a weight of 10 to amplify their  
2725 importance in the loss. On the other hand, the more abundant non-target edges are ignored  
2726 by giving them 0 weight.

---

**Algorithm 3:** Computation of the loss function of the **Filter** network
 

---

```

 $\mathbf{z}_i^0 \leftarrow \mathbf{x}_i;$ 
for  $l \in \{1, \dots, L\}$  do
   $//$  with gradient tracking
   $\mathbf{z}_i^l \leftarrow \text{GRAPHsAGE}(\mathbf{z}_i^{l-1}, \mathcal{V})$ 
end

begin torch.no_grad():
   $//$  Compute edge score for the whole graph without gradient tracking
   $\forall e_{ij} \in \mathcal{E} : \hat{y}_{ij} \leftarrow \phi(\mathbf{z}_i^L, \mathbf{z}_j^L);$ 
   $E_{\text{hnm}} \leftarrow \{e_{ij} \in \mathcal{E} : (\hat{y}_{ij} > Y_t) \wedge (y_{ij} = 0)\};$ 
end

 $E_{\text{train}} \leftarrow E_{\text{truth,target}} \cup E_{\text{hnm}} \cup E_{\text{random}};$ 
 $//$  Compute scores for edges in  $E$  with gradient tracking
 $\forall e_{ij} \in E_{\text{train}} : \hat{y}_{ij} \leftarrow \phi(\mathbf{z}_i^L, \mathbf{z}_j^L);$ 
 $\mathcal{L}_E(\theta) \leftarrow \frac{1}{|E|} \sum_{e_{ij} \in E} w_{ij} l(y_{ij}, \hat{y}_{ij})$ 
  
```

---

Hyperparameter	Value
GRAPHSAGE search depths (K)	2
GRAPHSAGE sample size ( $S_1, S_2$ )	(25, 10)
Number of GRAPHSAGE layers	3
Decoder hidden layers	6
Decoder hidden dimension	1024
Decoder activation function	ReLU
Learning rate	0.001
Epochs	$\approx 200$

**Table 9.1:** Hyperparameters used to train the Filter network.

2727        The Filter network takes the same input node vector as described in table 8.1, totalling 37  
 2728        features. The embedding is gradually enlarged to 1024 dimensions over 3 GRAPHSAGE con-  
 2729        volutions, and then fed to the decoder  $\phi$ . The latter is a simple MLP taking as input a con-  
 2730        catenated vector in 2048D and consisting of 6 layers of 1024 neurons with RELU nonlinearity  
 2731        [5], and a final single-neuron output layer. The network is trained with the hyperparameters  
 2732        listed in table 9.1. The training set contains 7785 events. Each full iteration over the training  
 2733        set (epoch) is followed by an evaluation epoch on a validation set of 1000 events. The model  
 2734        with the best area under the Receiver Operating Curve (ROC-AUC) is selected for inference.

### 2735        9.2.2 Results

2736        We evaluate the performance of the Filter network as described in section 8.4. By re-  
 2737        jecting edges whose score falls under a threshold, we create a filtered edge list  $E_f \subseteq \mathcal{E}$ .  
 2738        Substituting  $E_f$  for  $E$  in equations (8.2) and (8.3), we evaluate the edge efficiency and  
 2739        purity yielded by the model.

2740 Figures 9.2a 9.2b respectively show the edge efficiency as functions of the pseudorapidity  
 2741  $\eta$  and transverse momentum  $p_T$ . To maximize the efficiency, a loose score cut of 0.05 is  
 2742 applied. The model efficiency is almost flat at  $\epsilon = 1$  the entire  $\eta$  range. As a function of  
 2743 the transverse momentum, the edge efficiency slightly decreases at high  $p_T$ , when compared  
 2744 to the lower range. This might be due to the imbalance over  $p_T$  in training data. The  
 2745 majority of generated particles in each event have low  $p_T$  and follow curved trajectories, i.e.  
 2746 small radius, large curvature. High- $p_T$  tracks, on the other hand, follow more straight tracks.  
 2747 Such difference in geometry, coupled with the data imbalance, might bias the model towards  
 2748 low- $p_T$ , high-curvature tracks, and degrade the efficiency at high transverse momentum.

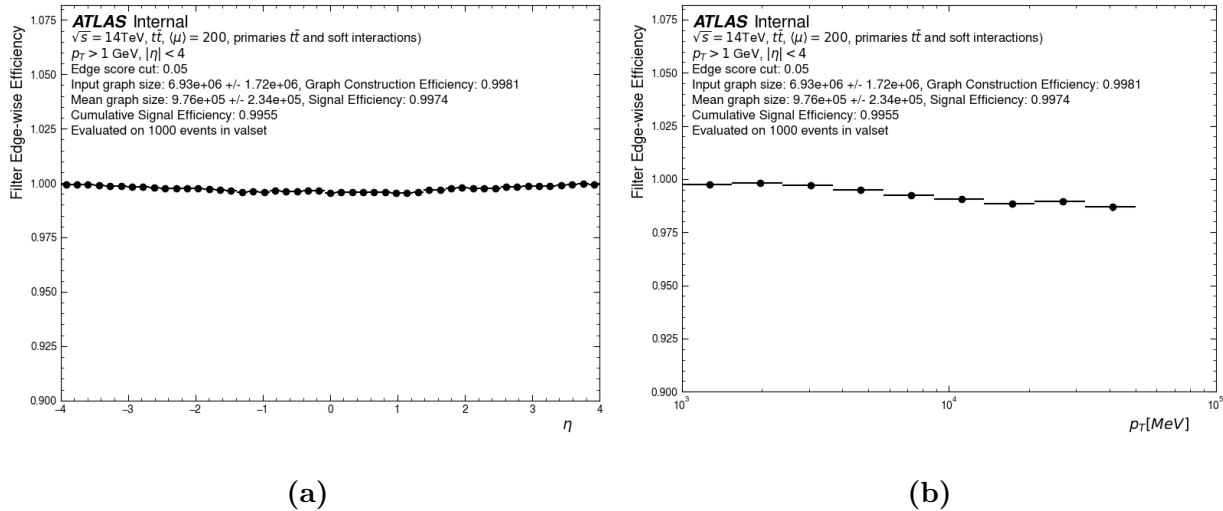


**Figure 9.2:** Edge efficiency of the Filter network on graphs constructed by the Metric Learning method as a function of  $\eta$  (a) and  $p_T$  (b).

2749 Figures 9.3a 9.3b respectively show the edge efficiency and purity as functions of the  
 2750 spherical coordinates  $(r, z)$  of the source node. These plots illustrate the variation in  $\epsilon$  and  
 2751  $\rho$  over the detector volume. 9.3a show excellent efficiency throughout the detector. Slight  
 2752 efficiency loss is observed in the outermost pixel layer and inner two layers of the strip barrel,  
 2753 where a track transitions between two sensor technologies. Overall, the edge efficiency over  
 2754 target particles is 0.996, i.e. on average 0.4 is lost per 100 target edges.

2755        The average edge purity after filtering is  $\rho = 1.48\%$ , which is not uniform throughout the  
 2756      detector. Two regions of low purity are identified. The first region with  $\rho \approx 0.4\%$  is located  
 2757      in the innermost pixel layer, closest to the interaction point. This proximity leads to a high  
 2758      density of space points, as shown in figure 9.4, and consequently a large number of possible  
 2759      random connections. This increases the chance of a misidentified fake edge and leads to low  
 2760      purity. The second region is located in the transition region between the pixel detector and  
 2761      the strip detector, and between the strip barrel and end-caps. Multiple factors play a role  
 2762      in the lowered purity, including (1) changing detector geometry, (2) accumulated material  
 2763      effects, and (3) the presence of single-cluster strip hits. A similar performance decrease is  
 2764      observed with the **Interaction Network** in the same detector region, of which a detailed  
 2765      discussion accounting for both networks will be given in section 9.3.2.

2766        Although the edge purity remains low, of  $\mathcal{O}(1\%)$ , the Filter network reduces the average  
 2767      number of edges to  $9.76 \times 10^5$ , 86% smaller than the input graph size of  $6.93 \times 10^6$ , while  
 2768      preserving the high edge efficiency from the graph construction stage. Recall that the Filter  
 2769      network aims to bring the number of edges down to a reasonable level, so it is more important  
 2770      to avoid falsely rejecting target edges than to eliminate *all* fake edges. This mission is  
 2771      reserved for a larger, more sophisticated INTERACTIONGNN introduced in the next section.

Graph Construction Method	Edge efficiency [%]	Edge Purity [%]	Number of edges
Module Map MINMAX	99.69		$1.22 \times 10^6$
Module Map MEANRMS	99.51		$8.55 \times 10^5$
Metric Learning + Filter	99.55	1.48	$9.76 \times 10^5$

**Table 9.2:** Comparison of graphs entering the INTERACTIONGNN

2772        Table 9.2 compares properties of graphs produced by Metric Learning and Filter networks  
 2773      to those produced by the Module Map method. They all have high edge efficiency, with  
 2774       $\epsilon > 99.5\%$ . The Module Map with MINMAX selection creates edges with 1.2 million edges,  
 2775      while the other methods yield fewer than 1 million edges.

2776 **9.3 The Interaction Network**

2777 In the section, a graph neural network is used to identify the majority of fake edges in  
2778 graphs constructed from either the Module Map technique, or the Metric Learning network.  
2779 Graphs from the former are directly subjected to the GNN, whereas those from the latter  
2780 are passed through a Filter network to reduce “easy” fake edges beforehand.

2781 **9.3.1 Methods**

2782 The INTERACTIONGNN architecture, proposed by Google DeepMind in 2016, is used  
2783 in this thesis [67]. It was first successfully applied to the problem of track reconstruction  
2784 by the EXATRKX project [123], delivering good tracking performance when tested on the  
2785 Particle Tracking Challenge, or commonly known as the TrackML, dataset [11]. Compared  
2786 to TrackML, our dataset represents a more realistic and complex detector geometry and  
2787 thus a greater challenge. The INTERACTIONGNN model architecture has been carefully  
2788 optimized to deal with this complexity.

2789 The model can be divided into three components: a set of encoders, a set of convolution  
2790 modules, and a decoder. In the encoding phase, a node encoder, denoted by  $\phi_{enc} : \mathbb{R}^d \rightarrow \mathbb{R}^D$   
2791 maps the features  $\mathbf{x}_i$  of node  $v_i \in V$  to a D-dimensional latent representation  $\mathbf{h}_i^0$ , such that

$$\mathbf{h}_i^0 = \phi_{enc}(\mathbf{x}_i). \quad (9.6)$$

2792 Next, an edge encoder  $\phi_e : \mathbb{R}^{2 \times D+F} \rightarrow \mathbb{R}^D$  maps the latent space node features  $(\mathbf{h}_i^0, \mathbf{h}_j^0)$   
2793 of nodes  $(v_i, v_j)$  connected by an edge  $e_{ij} \in E$ , and a set of hand-engineered edge features  
2794  $\mathbf{u}_{ij} \in \mathbb{R}^F$  to an edge feature vector  $\mathbf{k}_{ij}^0$ ,

$$\mathbf{k}_{ij}^0 = \psi_{enc}([\mathbf{h}_i^0 | \mathbf{h}_j^0 | \mathbf{u}_{ij}]) \quad (9.7)$$

2795 The custom edge features, listed in table 9.3, resemble the geometric observables defined for  
2796 the Module Map edge cuts, making  $\mathbf{u}_{ij}$  a 6-dimensional vector.

Feature	Formula
$\Delta r_{ij}$	$r_j - r_i$
$\Delta \phi_{ij}$	$\phi_j - \phi_i$
$\Delta z_{ij}$	$z_j - z_i$
$\Delta \eta_{ij}$	$\eta_j - \eta_i$
$\phi$ -slope	$\frac{\Delta \phi_{ij}}{\Delta r_{ij}}$
$r\phi$ -slope	$\frac{r_i + r_j}{2} \times \frac{\Delta \phi_{ij}}{\Delta r_{ij}}$

**Table 9.3:** Hand-engineered edge features

2797 The most important component of the INTERACTIONGNN is the graph convolution  
 2798 modules  $\{\varphi^l\}_{l=1}^L$ . They evolve the encoded node and edge features over  $L$  iterations by  
 2799 taking into account the graph connectivity. At each iteration  $l$ , the node feature  $\mathbf{h}_i^l$  of  
 2800 node  $v_i$  is computed from its feature from the previous step  $\mathbf{h}_i^{l-1}$ , and a message vector  $\mathbf{m}_i^l$   
 2801 containing information from other nodes directly connected to  $v_i$ . First, the latent feature  
 2802 vectors  $k_{ij}^{l-1}$  of edges connecting to  $v_i$  are aggregated to generate a vector  $\mathbf{m}_{i\leftarrow}^l$

$$\mathbf{m}_{i\leftarrow}^l = \text{AGGREGATE}(\{\mathbf{k}_{ji}^{l-1} \forall e_{ji} \in E\}), \quad (9.8)$$

2803 and then the aggregation is repeated on edges connecting from  $v_i$  to create a vector  $\mathbf{m}_{i\rightarrow}^l$

$$\mathbf{m}_{i\rightarrow}^l = \text{AGGREGATE}(\{\mathbf{k}_{ij}^{l-1} \forall e_{ij} \in E\}). \quad (9.9)$$

2804 The message vector  $\mathbf{m}_i^l$ , simply

$$\mathbf{m}_i^l = [\mathbf{m}_{i\leftarrow}^l | \mathbf{m}_{i\rightarrow}^l], \quad (9.10)$$

2805 is used to update the node vector by

$$\mathbf{h}_i^l = \varphi_v^l(\mathbf{h}_i^{l-1}, \mathbf{m}_i^l), \quad (9.11)$$

2806 and the updated node vector is then used to update the edge vector

$$\mathbf{k}_{ij}^l = \varphi_e^l(\mathbf{k}_{ij}^{l-1}, \mathbf{h}_i^l, \mathbf{h}_j^l). \quad (9.12)$$

2807 Equations (9.8)-(9.12) describe the message passing mechanism of the INTERACTIONGNN,  
 2808 which, analogous to the GRAPHSAGE mechanism of the Filter network, leverages the con-  
 2809nectivity on which the graph is defined to evolve the node vectors.

---

**Algorithm 4:** Message passing mechanism of the INTERACTIONGNN
 

---

```

for  $l \in \{1, \dots, L\}$  do
     $\mathbf{m}_{i\leftarrow}^l \leftarrow \text{AGGREGATE}(\{\mathbf{k}_{ji}^{l-1} \forall e_{ji} \in E\});$ 
     $\mathbf{m}_{i\rightarrow}^l \leftarrow \text{AGGREGATE}(\{\mathbf{k}_{ij}^{l-1} \forall e_{ij} \in E\});$ 
     $\mathbf{m}_i^l \leftarrow [\mathbf{m}_{i\leftarrow}^l | \mathbf{m}_{i\rightarrow}^l];$ 
     $\mathbf{h}_i^l \leftarrow \varphi_v^l(\mathbf{h}_i^{l-1}, \mathbf{m}_i^l);$ 
     $\mathbf{k}_{ij}^l \leftarrow \varphi_e^l(\mathbf{k}_{ij}^{l-1}, \mathbf{h}_i^l, \mathbf{h}_j^l);$ 
end
  
```

---

2810 However, different from GRAPHSAGE, the message passing mechanism of the INTER-  
 2811 ACTIONGNN tracks the edge vector and treats it as the message between nodes. Indeed,  
 2812 very few other GNN architectures maintain edge-level intermediate vectors, since informa-  
 2813 tion exchange between nodes can be effectuated without an explicit edge state. Because the  
 2814 number of edges in a graph is generally much larger than the number of nodes, tracking the  
 2815 gradient of an edge-level network, such as the edge updater  $\varphi_e^j$ , consumes more memory than  
 2816 that of node-level networks. However, the increased computational cost is justified by better  
 2817 expressivity. Reference [67] proposed the INTERACTIONGNN to model a multi-body physi-  
 2818 cal system, in which each node represents an object and each edge the interaction between  
 2819 these objects. As such, the node vector represents the physical state of each object, and the  
 2820 edge vector quantifies the effect an object has on another's hidden state. So naturally, the  
 2821 object state vector evolves with its previous state and the interaction as input, as seen on  
 2822 equation (9.11). This interaction itself depends not only on the current object state, but  
 2823 also on its history, so the edge updater uses its previous state, and the current object state,  
 2824 as seen in equation (9.12).

2825 The accuracy of the INTERACTIONGNN in modelling multi-body physical systems ob-  
 2826 served by reference [67] lends evidence to the effectiveness of explicitly tracking edge-level  
 2827 features following this physics intuition. In it unclear, however, how far this logic could be  
 2828 extended to other problems, or in reverse, how closely the track pattern recognition problem  
 2829 resembles an  $n$ -body system. For example, it is conceivable that since a track traces the  
 2830 evolution of a particle through the detector, hits from inner layers (the past) provide useful  
 2831 information to predict whether a hit in an outer layer (the future) belongs to the track, and  
 2832 vice versa. In this sense, the interaction between two hits, when evolved over multiple steps,  
 2833 encodes the properties of a track formed from themselves and other hits among which they  
 2834 exchange information. The network can then learn to distinguish true and fake edges by  
 2835 picking the most probable path given the hits on a particular search road. This intuition is  
 2836 in no way a *proof*. Deep neural networks are after all blackbox algorithms, whose explain-  
 2837 ability awaits further developments and lies outside the scope of this thesis. We contend  
 2838 with the assumption that the INTERACTIONGNN's success on a simplified tracking problem  
 2839 (TrackML) [123] holds potentials for a more realistic counterpart (ATLAS ITk), if given  
 2840 sufficient training data and optimization.

2841 In the final stage, the edge vector  $\mathbf{k}_{ij}^L$  is fed to a decoder  $\psi_{dec} : \mathbb{R}^D \rightarrow [0, 1]$  to compute a  
 2842 single number interpreted as the probability of being a true edge.

$$\hat{y}_{ij} = \psi_{dec}(\mathbf{k}_{ij}^L) \quad (9.13)$$

2843 The INTERACTIONGNN architecture is summarized in algorithm 5. The hidden dimension  
 2844 of all latent-space vectors is set to  $D = 128$ . A simple element-wise average is used as the  
 2845 aggregation function

$$\text{AGGREGATE} \left( \{\mathbf{k}_{ij}\}_{j=1}^N \right) = \frac{1}{N} \sum_{i=1}^N \mathbf{k}_{ij}. \quad (9.14)$$

2846 The message passing mechanism is carried out over  $L = 8$  iterations, each with a distinct set  
 2847 of node and edge updaters. All neural network submodules in the model are MLPs consisting  
 2848 of 3 layers, each containing  $M = 128$  neurons.

---

**Algorithm 5:** The INTERACTIONGNN

---

Given input graph  $G(V, E)$ , input node feature  $\mathbf{x}_i \forall v_i \in V$ ,

```

 $\mathbf{h}_i^0 \leftarrow \phi_{enc}(\mathbf{x}_i);$ 
 $\mathbf{k}_{ij}^0 \leftarrow \psi_{enc}(\mathbf{h}_i^0, \mathbf{h}_j^0);$ 
for  $l \in \{1, \dots, L\}$  do
|  $(\mathbf{h}_i^l, \mathbf{k}_{ij}^l) \leftarrow \varphi(\mathbf{h}_i^{l-1}, \mathbf{k}_{ij}^{l-1}, \{\mathbf{k}_{ij}^{l-1} \forall e_{ij} \in E\}, \{\mathbf{k}_{ji}^{l-1} \forall e_{ji} \in E\})$ 
end
 $\hat{y}_{ij} = \psi_{dec}(\mathbf{k}_{ij}^L)$ 

```

---

2849 The model weights are optimized on the edge classification objective, using the weighted  
2850 binary cross-entropy loss described in equation (9.3). Other hyperparameters related to  
2851 model training are detailed in table 9.4.

Hyperparameter	Value
Number of message passing operations	8
Hidden dimension	128
Hidden activation functions	RELU
Optimizer	ADAM
Learning rate	0.001
Epochs	$\approx 200$

**Table 9.4:** INTERACTIONGNN model specification

2852 **9.3.2 Results**

2853 Being both edge-classifying graph neural networks, the Filter and the Interaction network  
2854 are evaluated using the same metrics. Figure 9.5 shows the edge efficiency of the INTERAC-  
2855 TIONGNN as a function of the particle's pseudorapidity (left) and transverse momentum  
2856 (right). Figures 9.5a and 9.5b describes the performance on graphs from the Module Map  
2857 MeanRMS variant, whereas figures 9.5c and 9.5d those from the Metric Learning variant.

2858 The Module Map MinMax and MeanRMS variants have similar performance, so the former  
 2859 is omitted from all following figures in this chapter for brevity. The standard edge score cut  
 2860 0.5 is applied to make the binary prediction. Note, however, that this simple score cut will  
 2861 not be used to construct the final track candidate, as described in chapter 10.

2862 The INTERACTIONGNN achieves efficiency exceeding 99.5% on graphs constructed by  
 2863 both the Module Map and Metric Learning techniques. The performance is also consistently  
 2864 higher than 99% throughout the detector. Against the truth transverse momentum, a slight  
 2865 dip in efficiency is observed at high  $p_T$ . As we have seen from the discussion on the Filter  
 2866 network, the combination of low training statistics and different curvature means that edges  
 2867 from high- $p_T$  tracks receive less attention during training. As a result, the model favours the  
 2868 more abundant low- $p_T$  track edges and more often misidentifies high- $p_T$  ones. Since high- $p_T$   
 2869 tracks are more concentrated in the barrel region, a slight decrease in efficiency is observed  
 2870 in  $|\eta| < 1.5$ .

2871 It is worth noting that the GNN4ITk pipeline has been developed over several iterations  
 2872 of MC data, the most recent of which is described in reference [81], on a dataset of 1780  
 2873  $t\bar{t}$ -events. The cumulative edge efficiency achieved in this thesis is 99.04% for the **Mean-**  
 2874 **RMS** variant, higher than the previous result of 98.2%. The enhanced performance can be  
 2875 attributed to an optimized model architecture, and a larger training dataset, in particular  
 2876 7800 event versus 1600 in reference [81].

2877 The edge efficiency as a function of the  $(z, r)$ -coordinates of the inner hit, shown in figure  
 2878 9.6, illustrates the spatial distribution of misidentified true edges. Similar to the case of the  
 2879 Filter network, pockets of edge inefficiency as low as 96% are observed on the outermost pixel  
 2880 layer and near the edges of barrel strip layers, where a trajectory passes from one sensor  
 2881 technology or geometry to another. It is clear that both graph neural networks perform  
 2882 better in the pixel detector than in the the strip detector. The degraded performance can be  
 2883 attributed to a number of factors. First, accumulated material effects change the geometry of

2884 the orbit and increase the chance of an edge deviating from the pattern observed on the inner  
 2885 layers and being deemed incompatible with other true edges. Second, the transition between  
 2886 one sensor technology to another creates heterogeneity in both the geometric representation  
 2887 of the local coordinates, which is part of the input features and their resolution, as described  
 2888 in section 7.1. Yet despite the inherently heterogeneous data, all models employed in this  
 2889 thesis are homogeneous in architecture, which, though generally sufficient for their purpose,  
 2890 cannot predict well the cases where the heterogeneity can provide useful discrimination.  
 2891 Third, the hit inefficiency in space point formation, also described in section 7.1, means that  
 2892 true particle tracks are more likely to pass a strip layer without a hit when constructed from  
 2893 space points. Learning from these tracks, the GNNs may tolerate or even encourage layer-  
 2894 skipping edges in the strip detector, at the detriment of some true edges not well featured  
 2895 in the training data. We will return to the third issue in chapter 11, as it has an even  
 2896 larger implication on the tracking performance. In general, the training input data into the  
 2897 GNN4ITk contains shortcomings that are not optimal for learning and processing the output  
 2898 track candidates, to be addressed in future work.

2899 The edge purity as a function of the  $(z, r)$ -coordinates of the inner hit, shown in figure  
 2900 9.7, paints a similar picture as the efficiency distribution. On graphs from the MeanRMS  
 2901 variant, an average purity of 95.3% is achieved with noticeable variations over the detector  
 2902 regions. Model predictions are more pure in the pixel detector than in the strip detector,  
 2903 with pockets of impurity as high as 25% at the edges of the strip barrel. When compared  
 2904 to the input graphs, which average to  $\rho < 0.1\%$  and  $\mathcal{O}(10^6)$  edges in all variants (see table  
 2905 9.2), a purity level of  $\sim 95\%$  in graphs of  $\mathcal{O}(10^4)$  edges represents a significant rate of fake  
 2906 rejection. Nevertheless, the residual impurity creates challenges to the construction of track  
 2907 candidates, which is the focus of chapter 10.

2908 A comparison in performance of the three GNN4ITk variants is provided in table 9.5. The  
 2909 Module Map MinMax variant displays the best performance in both efficiency and purity,  
 2910 followed by the MeanRMS and the Metric Learning variants. The edge-based efficiency and

Graph Construction Method	Edge efficiency [%]	Edge Purity	Number of edges
Module Map <b>MinMax</b>	99.40	95.64	$2.53 \times 10^4$
Module Map <b>MeanRMS</b>	99.04	95.34	$2.48 \times 10^4$
Metric Learning + Filter	99.55		$9.76 \times 10^5$

**Table 9.5:** Performance of the INTERACTIONGNN across three graph construction methods.

2911 purity are useful in developing machine learning models. However, in production settings,  
2912 the performance must be evaluated using Athena [85], the main software analysis framework  
2913 of ATLAS.

2914 As such, the next step of the GNN4ITk pipeline partitions a graphs whose edges have been  
2915 scored by the GNN into track candidates, which are then fed into Athena. Track parameters  
2916 are estimated and other important metrics are computed in a unified framework for both  
2917 the CKF- and the GNN-based track finders. The graph segmentation step is presented in  
2918 the next chapter, and the tracking performance in chapter 11.

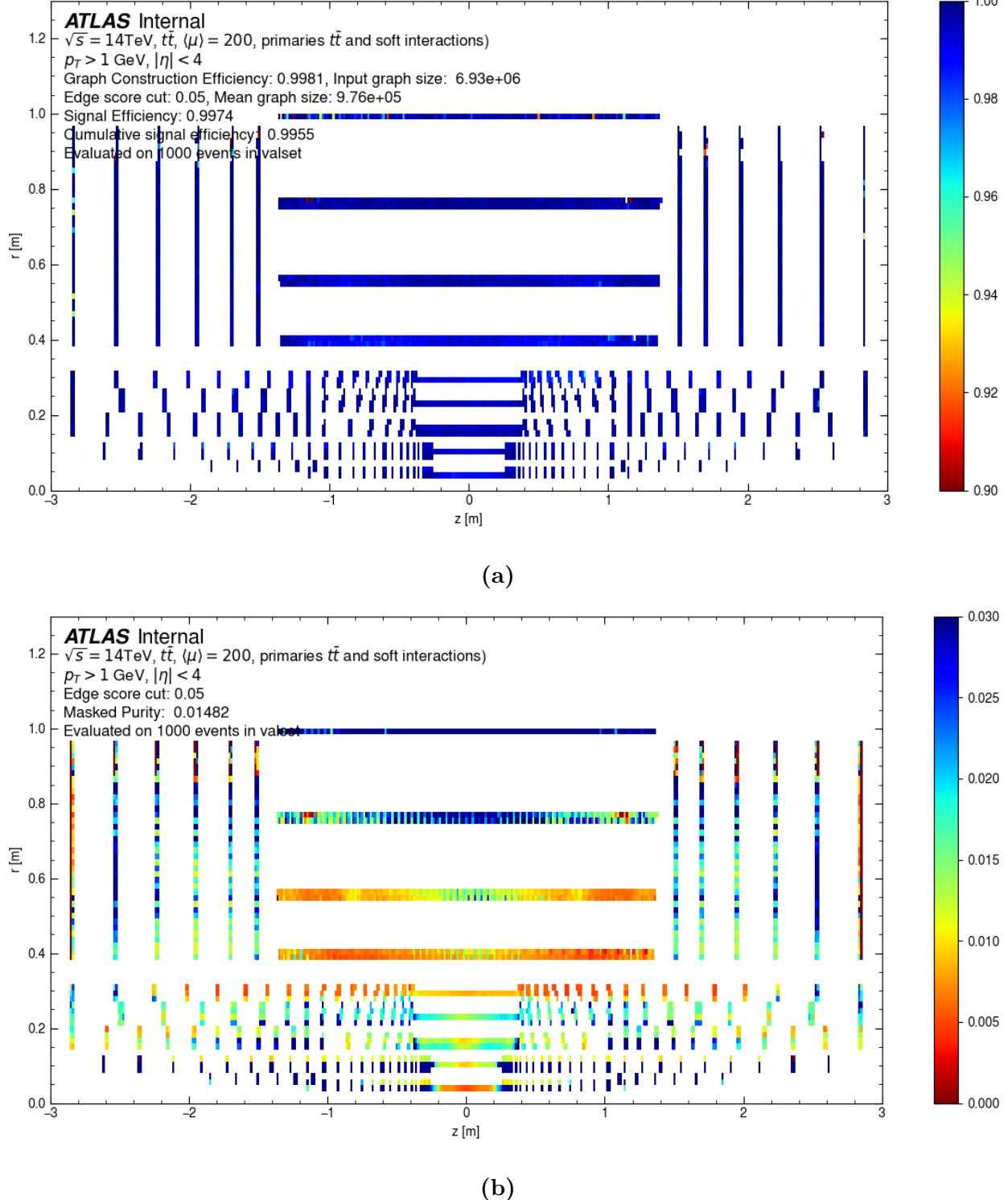


**Figure 9.3:** Edge efficiency (a) and purity (b) of the Filter network on graphs constructed by the Metric Learning method as functions of the  $(z, r)$ -coordinates of the inner hit.

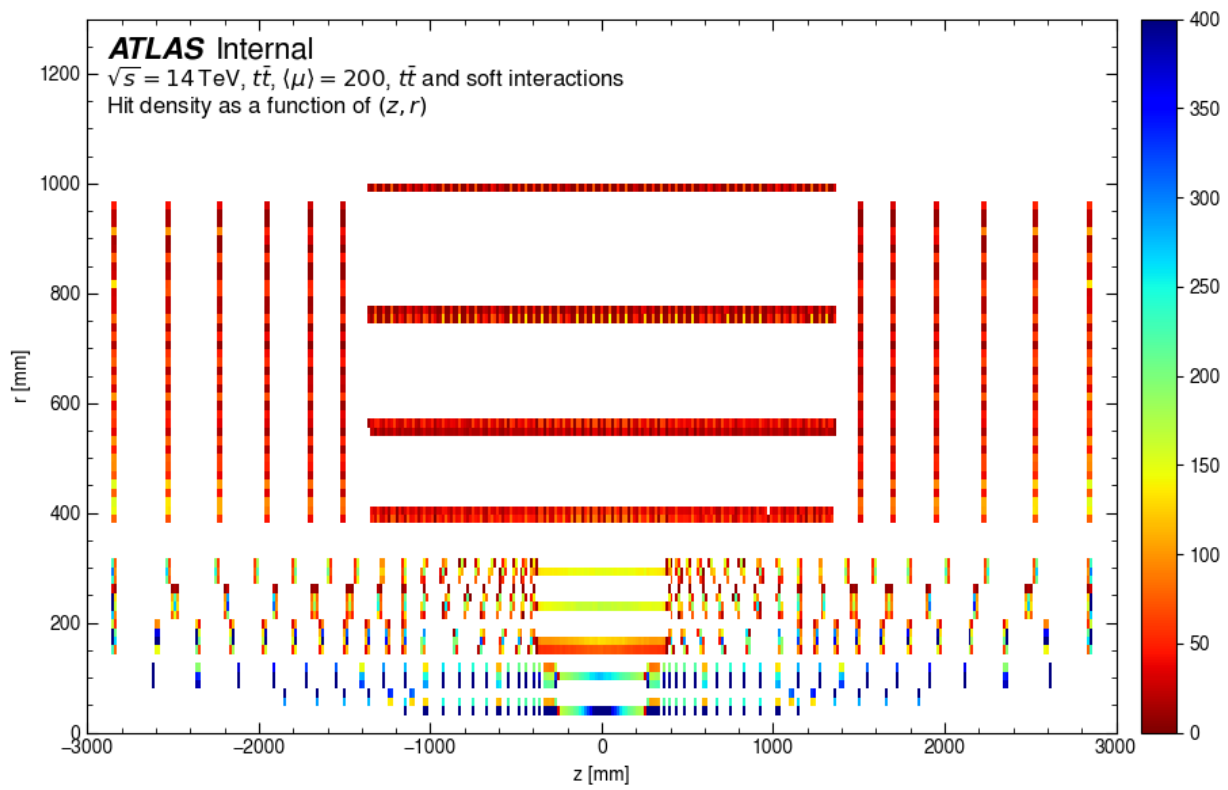


**Figure 9.4:** The number of space points per  $(z, r)$ -bin averaged over 50  $t\bar{t}$  events. The binwidth is 15 mm in both  $z$ - and  $r$ -direction.

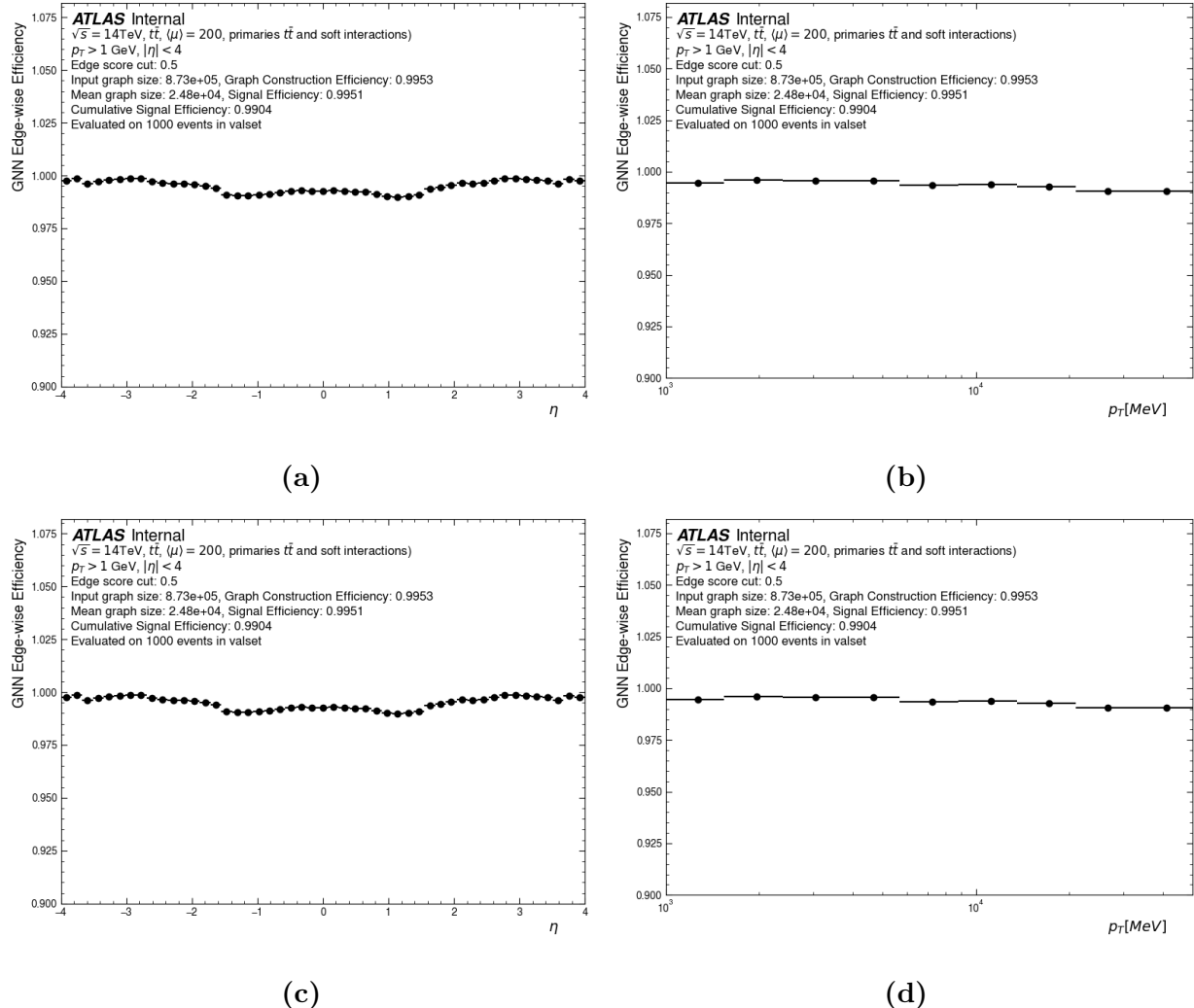


**Figure 9.5:** Edge efficiency of the INTERACTIONGNN as a function of  $\eta$  (left) and  $p_T$  (right), evaluated on graphs created using the Module Map method with MeanRMS (upper) and MinMax selections (lower).

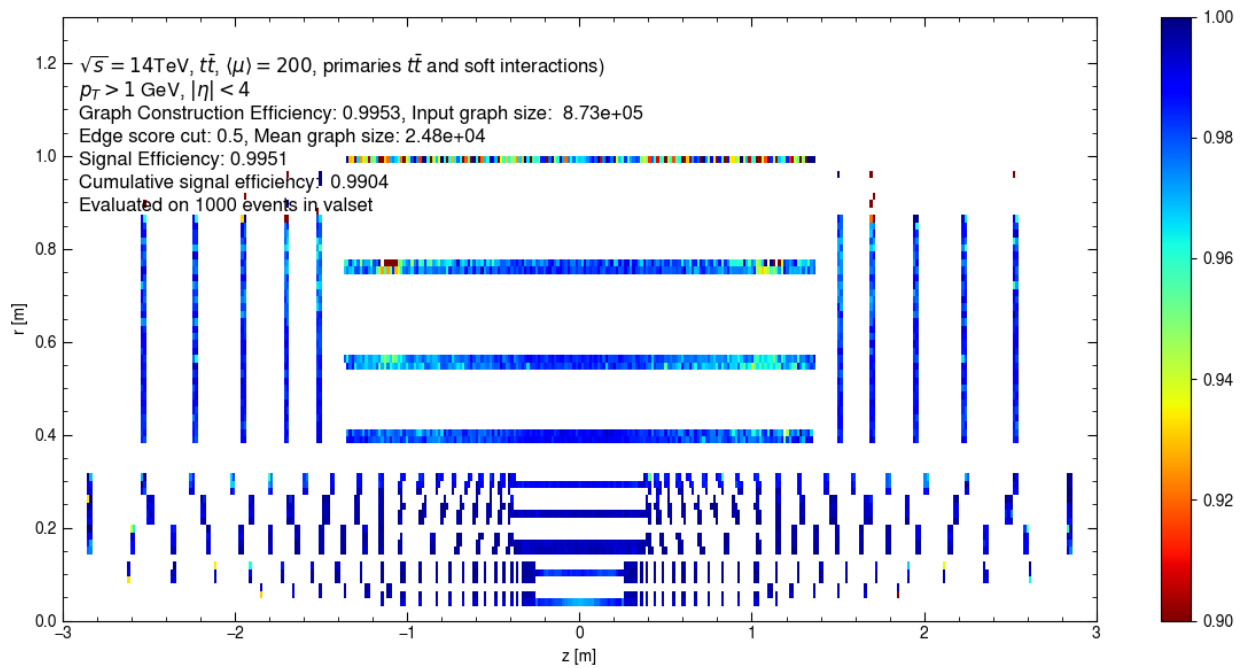


**Figure 9.6:** Edge efficiency of the INTERACTIONGNN on graphs constructed by the **Module Map MeanRMS** as a function of the  $(z, r)$ -coordinates of the inner hit.

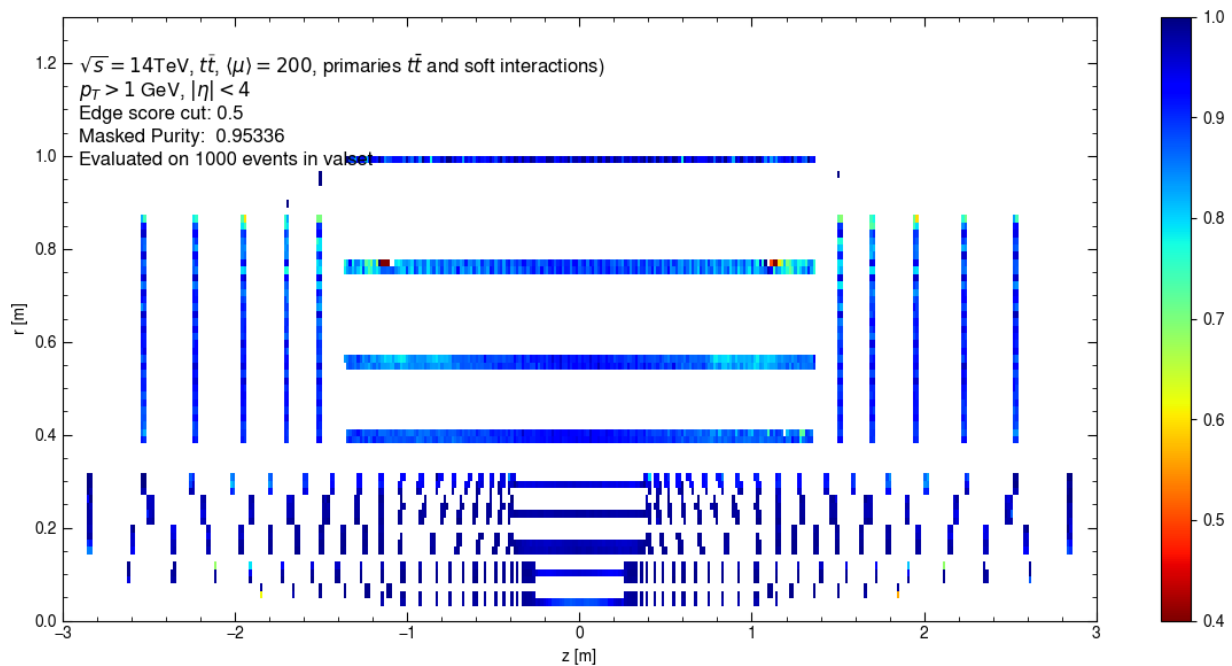


**Figure 9.7:** Edge purity of the INTERACTIONGNN on graphs constructed by the **Module Map MeanRMS** as a function of the  $(z, r)$ -coordinates of the inner hit.

2919 **Chapter 10**

2920 **Graph segmentation**

2921 Given a set of scored edges, the last stage of the pipeline segments them into individual  
2922 track candidates. There are several methods to carry out this task. The simplest case  
2923 applies a score threshold to eliminate edges believed to be fake, and treats the remaining  
2924 connected subgraphs as track candidates. This approach, called **Connected Component**,  
2925 ignores the directionality of graph edges. At the other edge of complexity, the edge direction  
2926 is retained and exploited to make heuristic segmentation decisions. A subgraph is traversed  
2927 outward from a source node—one with no incoming edges, selecting the longest path to form a  
2928 track candidate. This method is called **Walkthrough**. Both approaches are detailed in this  
2929 chapter, starting with the simple Connected Component. The track candidates constructed  
2930 by the Walkthrough algorithm are used to evaluate tracking performance in chapter 11.

2931 **10.1 Connected components**

2932 The simplest and most intuitive method of track building involves pruning the graph  
2933 of edges that are deemed fake. Assigned to each edge by the GNN is a score  $s \in [0, 1]$   
2934 representing the probability that it is a true edge. A binary label is obtained from a threshold  
2935  $s_{cut}$ , which reflects the level of confidence one desires in a prediction of a positive edge

$$\hat{y}_{ij} = \mathbb{1}_{s_{ij} > s_{cut}}. \quad (10.1)$$

2936 The threshold is typically set to  $s_{cut} = 0.5$  in typical classification problems. However, the  
 2937 score cut in our problem needs not follow this convention. Figure 10.1 shows the score  
 2938 distribution of the GNN on graphs constructed with Metric Learning method, categorized  
 2939 by the true label. We observe an excellent separation between target and fake edges. 99.6%  
 2940 of fake edges have score lower than 0.01, with the highest among other bins contributing  
 2941 < 0.1%. On the other hand, 99.7% of target edges get score higher than 0.01. This means  
 2942 that even a loose  $s_{cut} = 0.01$  eliminates 99.6% fake edges and retains 99.7% target edges.  
 2943 The edge efficiency and fake reduction of several other cuts are shown in table 10.1. It is  
 2944 obvious that the edge efficiency decreases, while the fake reduction increases with tightening  
 2945 score cut. It is also clear that for our purpose, we lose too much efficiency at  $s_{cut} = 0.5$ ,  
 making it sub-optimal. A score cut of  $s_{cut} = 0.01$  is chosen to label the graph edges.

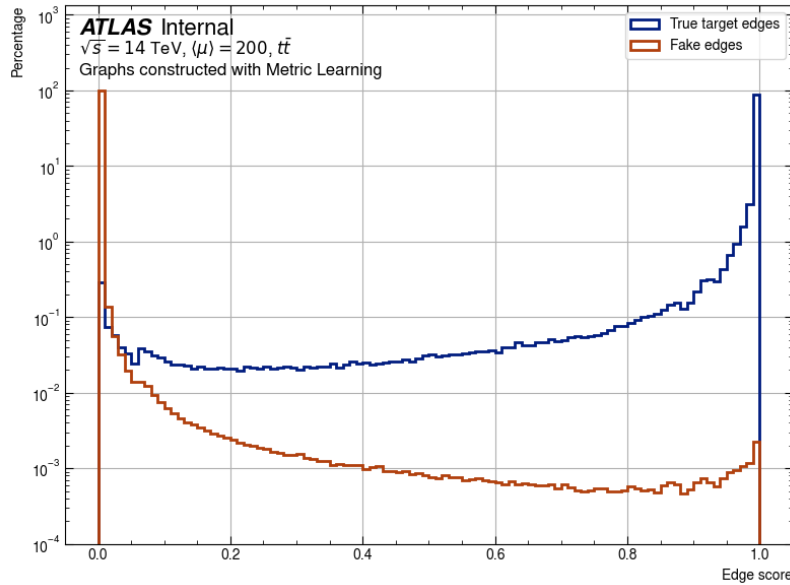


**Figure 10.1:** A distribution of the GNN edge classification scores. 200 graphs constructed using the Metric Learning approach are used.

2946

2947 Illustrated in figure 10.2, the elimination of fake edges results in the segmentation of the  
 2948 input graph into subgraphs which are not connected to the rest of the graph. Mathematically,

2949 the segmented graph can be written as

$$G(V, E) = \bigcup_{i=1}^M G(V_i, E_i) \quad (10.2)$$

2950 where for any pair  $i \neq j$ ,  $i \in [M]$ ,  $j \in [M]$ ,

$$V_i \cap V_j = \emptyset, \quad E_i \cap E_j = \emptyset \quad (10.3)$$

2951 figure 10.2a, shows a simplified input graph to the GNN, which contains two color-coded  
2952 tracks: a **green** track with 4 hits labelled  $\{1, 2, 3, 4\}$ , a **blue** track with 3 hits labelled  
2953  $\{5, 6, 7\}$ ; and a single **violet** hit labelled  $\{8\}$ . Hits and true edges from a track share the  
2954 same color. Fake edges are shown in **red**. Note that the colours represent truth information  
2955 available only for evaluation. During inference, the GNN **ideally** gives **fake** edges a low score,  
2956 and true edges a high score. After eliminating edges whose score falls belows  $s_{cut} = 0.01$ , we  
2957 are left with three correctly segmented subgraphs, each containing all hits from the parent  
2958 particle. Every node in each subgraph has at most 1 incoming and 1 outgoing edge, creating  
2959 a single path from the innermost to the outermost hit <sup>1</sup>. These graphs, designated simply  
2960 connected components, are labelled as track candidates.

Score cut	Edge efficiency [%]	Fake reduction [%]
0.01	99.71	99.58
0.02	99.63	99.72
0.05	99.50	99.82
0.1	99.35	99.89
0.2	99.12	99.93
0.5	98.42	99.97

**Table 10.1:** Edge efficiency and fake reduction rate at representative values of GNN edge score cut.

---

<sup>1</sup>Note that all input edges point in the direction of increasing distance from the IP

Because of its simplicity, **Connected Component** is fast and widely available in many Python libraries. We use the NETWORKX library[115] to implement the segmentation, which has a GPU backend called Nx-CUGRAPH. The latter allows the GNN-labelled graph which already resides on the GPU during inference to be segmented without being moved to the CPU, avoiding data transfer overheads.

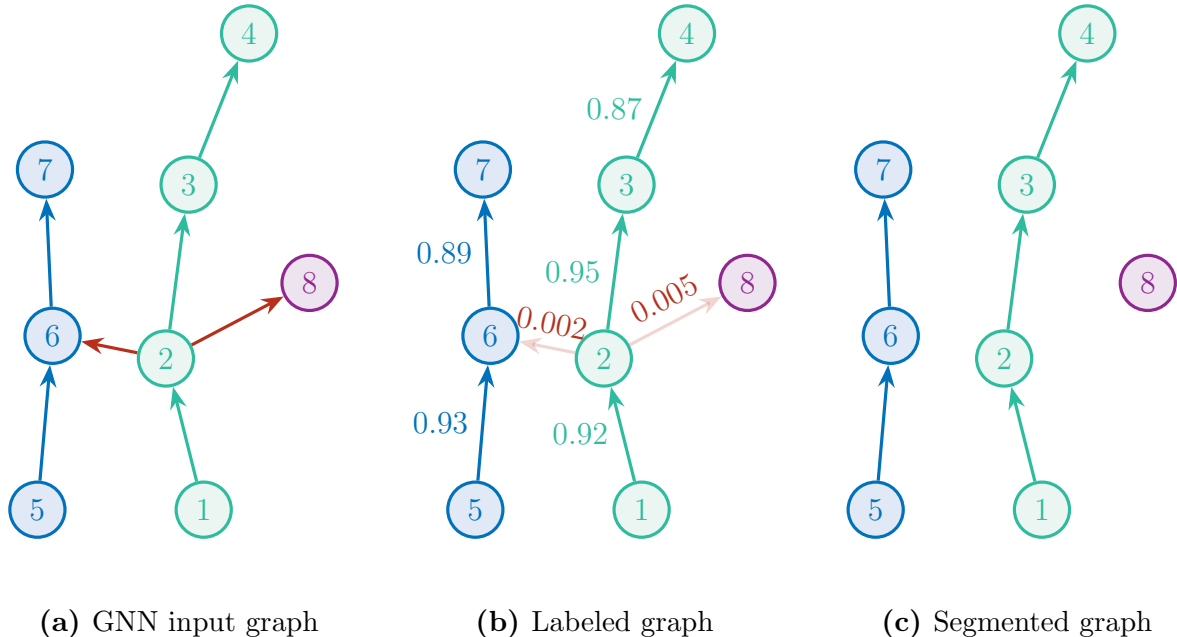


**Figure 10.2:** Illustration of the Connected Component method. (a) The input graph contains two particle tracks and a single hits, all color-coded. The three objects are merged by two fake edges in red. (b) Edges whose score falls under a threshold is eliminated. (c) The remaining connected components are considered as track candidates.

It is perhaps not surprising that connected component alone is not sufficient to build track candidates with sufficient reconstruction efficiency, which is why its description emphasizes on an ideal GNN labelling. We already see from figure 10.1 that this is not the case. Aside from the inefficiency associated with the rejection of true edges with  $\hat{y} < 0.01$ , 0.42% of the fake edges still remain after the edge cut. Despite their small population, residual fake edges create a non-negligible number of non-simple subgraphs, with whom the method is not equipped to deal. These non-simple subgraphs occur then true tracks are merged by

2973 a misclassified fake edge, creating an object that fails to represent any of the underlying  
2974 particle. We will examine this problem in greater details and its treatment in the next  
2975 section.

2976 **10.2 The Walkthrough algorithm**

2977 Non-simple subgraphs are a big drawback of the Connected Component approach. Their  
2978 topology can range from a random hit being wrongly connected to an otherwise good track,  
2979 to several tracks being merged together. With the only tuneable parameter being the GNN  
2980 edge score cut, it undergoes a trade-off between the edge efficiency and the fake edge rate. A  
2981 high score cut decreases the efficiency but also the number of fake edges, thus reducing the  
2982 occurrence of non-simple subgraphs. This edge efficiency reduction, however, often results  
2983 in strong impact on the tracking efficiency of high- $p_T$  particles due to their small proportion.  
2984 To avoid compromising high- $p_T$  tracks, we must contend with a loose score cut and resolve  
2985 the ensuing merged tracks.

2986 The Walkthrough algorithm is constructed as a solution to this issue. It still relies on the  
2987 Connected Component method to quickly construct simple track candidates. On non-simple  
2988 subgraphs, however, it considers both the directionality and the GNN edge score to isolate  
2989 merged tracks. The main idea is to traverse all possible paths starting from the source nodes  
2990 and to identify the longest paths which do not share any node with each other. The edge  
2991 score is used to resolve ambiguity when multiple paths have the same lengths, and other  
2992 subtle cases.

2993 First, all cycles in the form  $u \rightarrow \dots \rightarrow v \rightarrow \dots \rightarrow u$  are removed. Although by construc-  
2994 tion graph edges always point in the direction of increasing distance from the interaction  
2995 point, a loop can occur when three or more equidistant nodes are connected in a manner  
2996 such as  $v_1 \rightarrow v_2 \rightarrow v_3 \rightarrow v_1$ , in which case one of the edge is randomly flipped to remove the  
2997 loop. The removal of loops enables a topological sort  $f : V \rightarrow \mathbb{N}$  of nodes in the subgraph,

2998 such that for every directed edge  $u \rightarrow v$ ,  $f(u) < f(v)$ . The sorting places all nodes that have  
 2999 no incoming edges at the top, which are isolated into a set of starting nodes. Thanks to the  
 3000 loop removal and the edge orientation, this set is guaranteed non-empty. Each starting node  
 3001 becomes a seed for iterative track building.

3002 Space points are sequentially added to the seed path, guided by the GNN edge score.  
 3003 Two thresholds on edge score are defined. The first, denoted  $s_{min}$ , is the minimum score of  
 3004 an edge via which the path may be extended. The second, denoted  $s_{add}$  and always larger  
 3005 than  $s_{min}$ , is the minimum score to create an alternative path. With these thresholds, three  
 3006 distinct scenarios can be identified.

- 3007 1. A unique outgoing edge exists from the starting node. This is the trivial case. The  
 3008 receiving node is added to the path and becomes the next starting node (figure 10.3a),
- 3009 2. Multiple outgoing edges stem from the starting node, among which the highest score  
 3010  $s_{max} \leq s_{add}$ . The edge with the highest score is uniquely chosen and its receiving node  
 3011 becomes the next starting node (figure 10.3b),
- 3012 3. Multiple outgoing edges stem from the starting node, and  $s_{max} \geq s_{add}$ . All edges with  
 3013  $s > s_{add}$  are admitted to create multiple parallel paths, each now starting from the  
 3014 corresponding receiving node (figure 10.3c).

3015 In these scenarios, the scores of all considered edges must exceed  $s_{min}$ . This local procedure  
 3016 is repeated until all paths reach a terminal node, from which no outgoing edge stems. In  
 3017 the end, every encounter of scenario (3) creates at least two track paths. To resolve the  
 3018 ambiguity, we select the longest path. Thus, from a given starting node, we obtain a single  
 3019 track candidate, whose node are removed from the parent subgraph. This prevents space  
 3020 points from being shared among multiple track candidates. Nodes from the globally rejected  
 3021 paths, and locally rejected nodes can be reused to build track candidates from other starting  
 3022 nodes.

3023        Nevertheless, ambiguity may still arise when multiple globally longest paths are identified  
3024      from a starting node, as illustrated in figure 10.4. The path traversing via the edge of  
3025      highest score is then chosen as the track candidate in such case. In the figure, the path  
3026       $1 \rightarrow 2 \rightarrow 3 \rightarrow 4 \rightarrow 5$  is selected, since  $s_{23} > s_{26}$ . Nodes (5, 6, 7) are returned to the  
3027      subgraph to build subsequent paths. With the Walkthrough technique, the track finding  
3028      part of the GNN4ITk algorithm is concluded. The final product of graph segmentation is  
3029      simple a set of track candidates. Each candidate is a list of space points ordered by their  
3030      distance from the origin. Equivalently, the CKF also creates a collection of track candidates,  
3031      which are subjected to an ambiguity resolution step to reduce the number of shared hits  
3032      and fake tracks, as described in chapter 7. Different from GNN-built tracks, CKF tracks  
3033      by construction “live” in Athena as a link in the event reconstruction chain, and more  
3034      importantly, are equipped with the track parameters. From an engineering point of view,  
3035      it is crucial to treat GNN-built track candidates in Athena, so that they can rejoin the  
3036      chain and be ready for downstream tasks. This also enables an apple-to-apple performance  
3037      comparison of both track finders in the same environment, which is presented in the next  
3038      chapter.

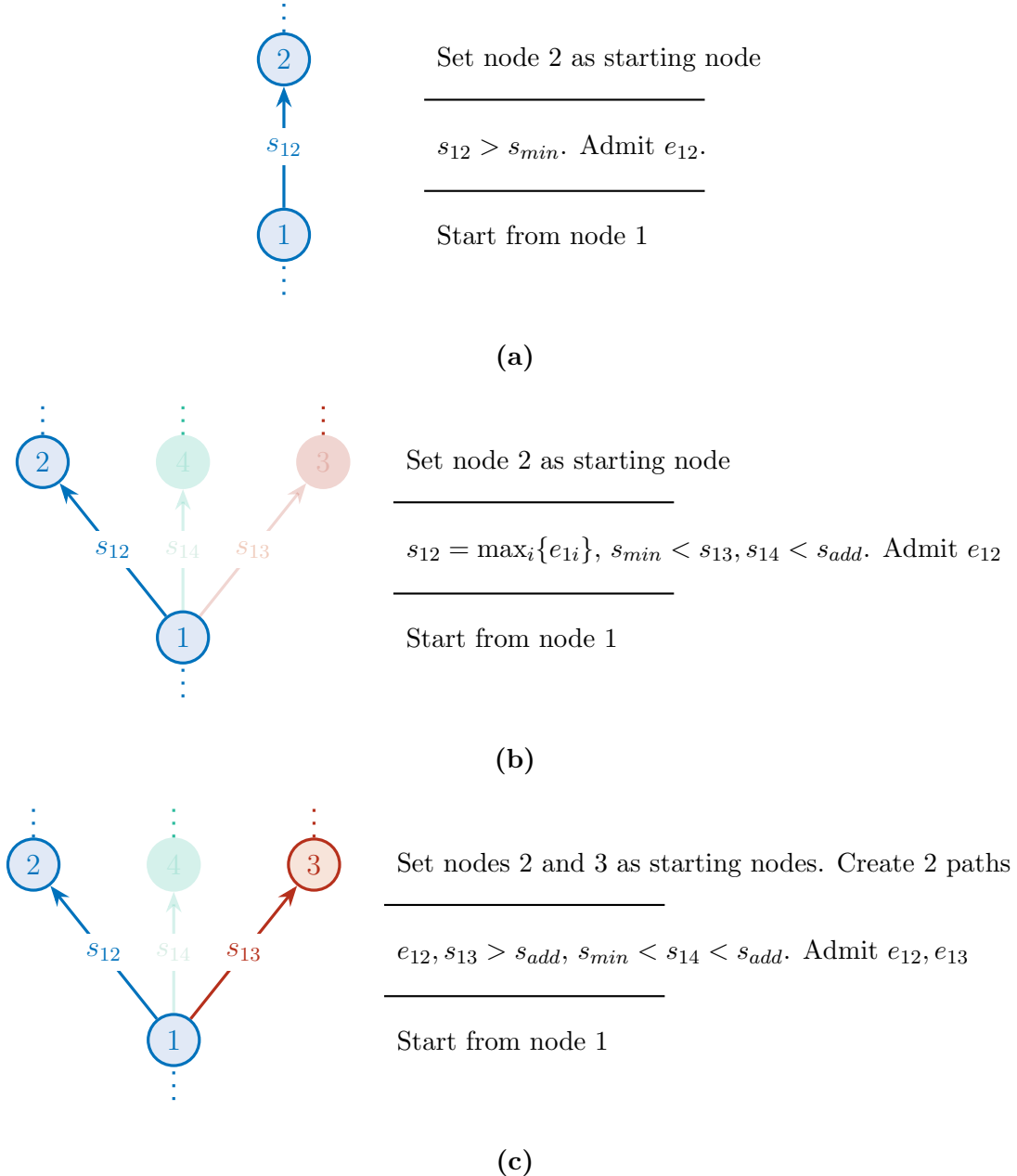


**Figure 10.3:** Different scenarios encountered by the Walkthrough algorithm. (a) A starting node as a single outgoing edge. (b) The starting node has several outgoing edges  $\{e_{12}, e_{13}, e_{14}\}$ . Edge  $e_{12}$  has the highest score, and neither lower-score edges exceed the minimum score  $s_{add}$  to create an alternative path. Only edge  $e_{12}$  is admitted. (c) The starting node has several outgoing edges  $\{e_{12}, e_{13}, e_{14}\}$ , in which  $e_{12}$  and  $e_{13}$  exceed  $s_{add}$ . Two candidate paths stemming from the junction are considered, the longer of which is admitted.

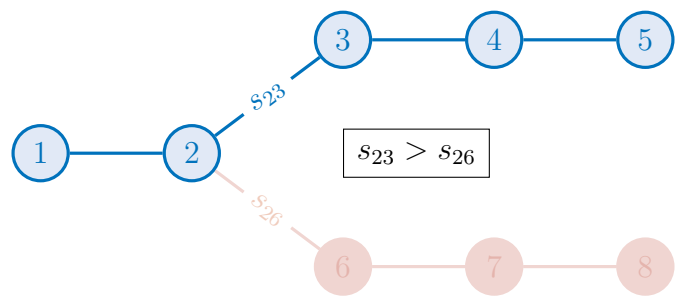


**Figure 10.4:** An ambiguity occurs when two candidate paths have equal lengths. The path stemming from the higher edge score at the junction is selected.

3039    **Chapter 11**

3040    **Track reconstruction performance**

3041    Track reconstruction identifies a track candidate as the digital realization of a particle  
3042    trajectory. In the GNN-based chain, after graph segmentation, a track candidate is a list of 3-  
3043    dimensional estimates of the intersections between a trajectory and different detector layers.  
3044    The analysis of tracking performance starts with the extraction of track parameters by a  
3045     $\chi^2$ -fit over on the measurements contained in the candidate. These parameters characterize  
3046    the impact parameters and the momentum of the particle, which are crucial information for  
3047    downstream tasks in event reconstruction. We have described the principles of track fitting  
3048    in section 7.2. The parameter extraction in this chapter closely follows this description, with  
3049    a small number of adaptations described in section 11.1.

3050    To evaluate the tracking efficiency, fake rate, and parameter resolution, fitted tracks  
3051    are matched to generator-level truth particles, which must satisfy a number of criteria on  
3052    reconstructibility and kinematics. Section 11.2 describes the matching procedure and the  
3053    metrics under which the performance is assessed.

3054    Finally, section 11.3 is an apple-to-apple comparison between GNN4ITk and CKF track-  
3055    ing performance.

3056 **11.1 Extraction of track parameters**

3057 As mentioned in section 7.2, the tracking model used in ATLAS considers the local  
3058 coordinates of individual clusters as measurements. A GNN track candidate, however, is a  
3059 list of space points reconstructed from these clusters, according to section 7.1. To carry out  
3060 the fit, the space points are first matched to their corresponding clusters. A pixel space point  
3061 is matched to a unique pixel cluster, while a strip space point is matched to two strip clusters,  
3062 each from one side of a barrel stave or an endcap petal (see section 6.1). The building block  
3063 of track candidates is a major difference between the GNN-based and the current tracking  
3064 algorithm, which has implications in the interpretation of results.

3065 To fully characterize a charged particle’s trajectory in a magnetic field, the parametriza-  
3066 tion must specify its global position, momentum and charge at any given point. Various  
3067 conventions satisfy this requirement. In the offline analysis framework of ATLAS, the fol-  
3068 lowing track parametrization convention is chosen as part of the Event Data Model (EDM)  
3069 [7]

$$\mathbf{x} = (l^{(1)}, l^{(2)}, \phi, \theta, q/p)^T \quad (11.1)$$

3070 where  $(l^{(1)}, l^{(2)})$  denote the coordinates of the intersection between the measuring surface  
3071 and the trajectory in the local frame of reference,  $\phi \in [-\pi, \pi]$  and  $\theta \in [0, \pi]$  respectively the  
3072 azimuthal angle and the polar angle in the global frame of the current location, and  $q/p$  the  
3073 inverse momentum signed by the particle charge. The track parameters vary continuously  
3074 along the trajectory, and the measurements are “snapshots” taken at the active layers that it  
3075 traverses. The local coordinates  $(l^{(1)}, l^{(2)})$  take different meaning depending on the measur-  
3076 ing surface. For example, on a disk, they are the polar coordinates  $(l^{(1)}, l^{(2)}) = (R_{loc}, \phi_{loc})$  of  
3077 the cluster, while on a plane, they are given in Cartesian coordinates  $(l^{(1)}, l^{(2)}) = (X_{loc}, Y_{loc})$ .  
3078 The perigee parametrization, shown in figure 11.1, is an imaginary cylindrical surface par-  
3079 allel to the global  $z$ -axis and passing through the point of closest approach to the origin<sup>I</sup>.

---

3077<sup>I</sup>This point is defined as the perigee, hence the designation.

3080 The local parameters  $(l^{(1)}, l^{(2)}) = (d_0, z_0)$  are respectively the transverse and longitudinal  
 3081 impact parameters, which, along with other global parameters estimated at this position,  
 3082 are reported as *the* track parameters of the corresponding hypothetical particle. The perigee  
 3083 parameters are the quantity denoted by  $\mathbf{x}_0$  in the discussion in 7.2.

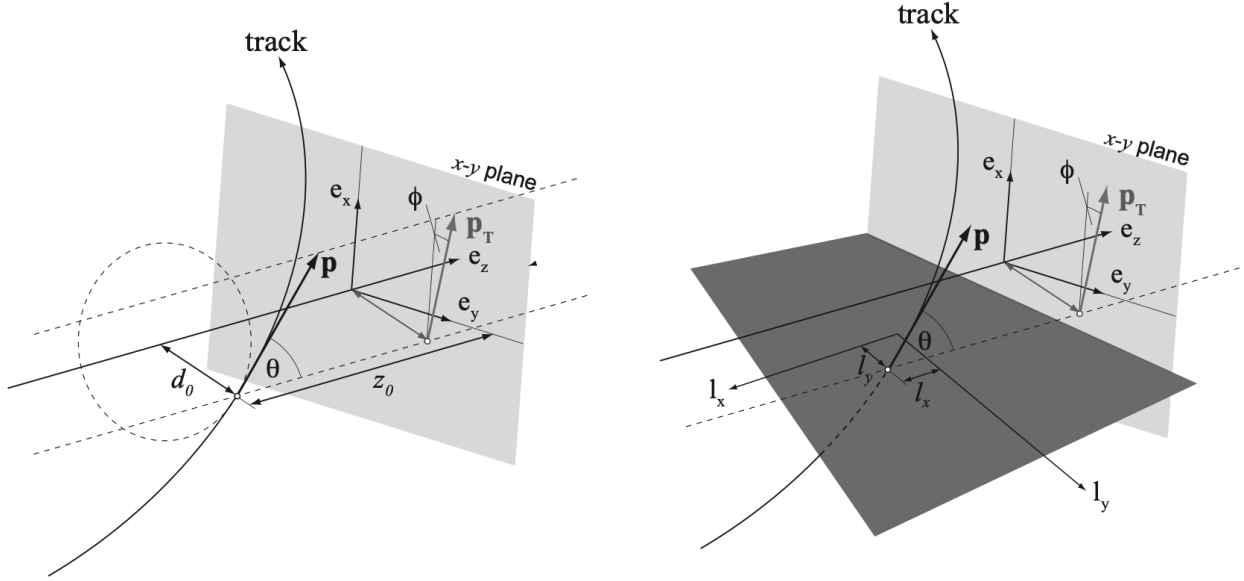


**Figure 11.1:** A track represented in two different parametrizations, both being particular instances of the general ATLAS parametrization in equation (11.1). The perigee parametrization (left) is defined with respect to the global  $z$ -axis, while the planar parametrization (right) is defined with respect to the coordinate axes of a local measuring surface [97].

3084 Thanks to this parametrization, the measurement model is a simple identity projection  
 3085 of the first two track parameter parameters. The  $i$ -th measurement on track is given by

$$\mathbf{m}_i = \mathbf{H}_i \mathbf{x}_i = \begin{bmatrix} 1 & 0 & 0 & 0 & 0 \\ 0 & 1 & 0 & 0 & 0 \end{bmatrix} \begin{bmatrix} l^{(1)} \\ l^{(2)} \\ \phi \\ \theta \\ q/p \end{bmatrix} = \begin{bmatrix} l^{(1)} \\ l^{(2)} \\ \phi \\ \theta \\ q/p \end{bmatrix}. \quad (11.2)$$

3086 The measurement uncertainty is codified in the covariance matrix

$$[\mathbf{V}_i]_{jk} = \begin{cases} \sigma^2(l_i^{(j)}), & i = j \\ \rho(l_i^{(j)}, l_i^{(k)}), & j \neq k \end{cases} \quad (11.3)$$

3087 which is a block of the covariance matrix of the track parameters

$$[\mathbf{C}_i]_{jk} = \begin{cases} \sigma^2(\mathbf{x}_i^{(j)}), & j = k \\ \rho(\mathbf{x}_i^{(j)}, \mathbf{x}_i^{(k)}), & j \neq k \end{cases} \quad (11.4)$$

3088 where  $\mathbf{x}^{(i)}$  is the  $i$ -th component of the track parameters,  $\sigma^2(X)$  the variance of  $X$  and  
3089  $\rho(X, Y)$  the covariance of  $X$  and  $Y$ .

3090 Given the track state  $\mathbf{x}$  and a covariance  $\mathbf{C}$  at any point on the trajectory, an estimate  
3091 of the state at another point  $\mathbf{x}'$  can be obtained by numerically integrating the EOM, as  
3092 described in section 11.1. If the position of  $\mathbf{x}'$  coincides with a sensitive element, an expected  
3093 value of the corresponding measurement could be derived using equation (11.2), allowing to  
3094 write the measurement error as a function of  $\mathbf{x}$ . Repeating this process, taking  $\mathbf{x}$  as the  
3095 initial value, we can define the measurement error of the entire track candidate and optimize  
3096 for  $\mathbf{x}$ .

3097 Let  $M = \{\mathbf{m}_1, \dots, \mathbf{m}_N\}$  be the set of all clusters matched to the track candidate. The  
3098 cost function can be written as a function of an initial state  $\mathbf{x}$  as

$$\boxed{\mathcal{L}_M(\mathbf{x}, \vartheta) = \frac{1}{2} \sum_{i=1}^N [\mathbf{m}_i - \mathbf{H}_i f_i(\mathbf{x}, \vartheta)]^T \mathbf{V}_i^{-1} [\mathbf{m}_i - \mathbf{H}_i f_i(\mathbf{x}, \vartheta)] + \frac{1}{2} \sum_{j=1}^J \frac{\vartheta_j^2}{\sigma^2(\vartheta_j)}}, \quad (11.5)$$

3099 in which, as discussed in section 7.2, the set of angles  $\{\vartheta_j\}$  is included to model small-  
3100 angle multiple scatterings due to interaction with the detector material. These angles are  
3101 assumed to be normally distributed with mean  $\langle \vartheta_j \rangle = 0$  and variance estimated by the  
3102 Highland formula (6.14). It is important to note that these scattering angles are floated as  
3103 fit parameters, but they are constrained by the variances  $\sigma^2(\vartheta_j)$  which are functions of the  
3104 trajectory and therefore the initial state  $\mathbf{x}$ .

3105 Since the cost function is no longer linear, an analytical solution to the equation

$$\nabla \mathcal{L}_M(\mathbf{x}, \vartheta) = 0 \quad (11.6)$$

3106 does not exist. Instead, it must be numerically minimized, starting from some initial value  
3107  $\tilde{\mathbf{x}}$ . To estimate  $\tilde{\mathbf{x}}$ , a circle fit using the conformal map method is performed over the  $(x, y)$   
3108 coordinates the first three space points of the track candidate. This procedure is described  
3109 in reference [119]. The crude estimate is fed into the optimizer, along with the cost function  
3110 to obtain a globally optimal estimate  $\hat{\mathbf{x}}$  of the track parameters.

$$\hat{\mathbf{x}} = \min_{\mathbf{x}} \mathcal{L}_M(\mathbf{x}, \vartheta) \quad (11.7)$$

## 3111 11.2 Track matching and performance metrics

3112 In simple terms, tracking performance is evaluated by answering the following questions

- 3113 1. **Efficiency:** How many *relevant* truth particles are reconstructed?
- 3114 2. **Fake rate:** How many tracks are created but represent no truth particles?
- 3115 3. **Track quality:** How well does a reconstructed track represent the corresponding truth  
3116 particle?

3117 Since all three items compare tracks to particles, it is necessary to match the reconstructed  
3118 track candidates and truth-level particles. It is for this reason that the evaluation can only  
3119 be done with Monte-Carlo simulation where truth information is available.

3120 **Definition 11.1** The tracking efficiency ( $\epsilon_{track}$ ) is the fraction of prompt particles associated  
3121 with track candidates passing some quality selection.

$$\epsilon_{track} = \frac{N_{reco}}{N_{truth}}, \quad (11.8)$$

3122 in which  $N_{truth}$  is the number of particle passing a set of reconstructibility criteria, and  $N_{reco}$   
3123 the number of those matched to a “good” track candidate.

3124 It is important to distinguish the tracking efficiency the edge efficiency defined in equation  
3125 (8.2). The former is defined on the set of truth particles, while the latter the set of edges  
3126 between space points reconstructed from truth particles. While the edge efficiency is useful in  
3127 machine learning development, only the tracking efficiency is meaningful in the performance  
3128 presented in this chapter, and, to a larger extent, in the ATLAS event reconstruction chain.

3129 A matched track candidate is required to have a high matching probability with the  
3130 particle in question, defined as follows.

3131 **Definition 11.2** Matching probability  $P_m(A, B)$ : Let  $A$  denote both a track candidate and  
3132 the set of clusters it contains, and  $B$  those of a particle. The matching probability between  
3133 track  $A$  and particle  $B$  is the weighted fraction of clusters contained in  $A$  that are in common  
3134 with  $B$ .

$$P_m(A, B) = \frac{2|(A \cap B)_{pix}| + |(A \cap B)_{strip}|}{2|A_{pix}| + |A_{strip}|}, \quad (11.9)$$

3135 where  $S_{pix}$  and  $S_{strip}$  respectively denote the subsets of pixel and strip clusters of set  $S$ .

Intuitively, a track candidate has a high probability of matching to a particle if the majority of its hits originate from that particle. The factor of 2 gives a doublet the weight to a pixel cluster, because it provides a 2D measurement of the track, whereas a strip cluster provides only 1<sup>II</sup>. A track  $A$  is said to be matched to a particle  $B$  if its matching probability

$$P_m(A, B) > 0.5.$$

3136 Tracks candidates that are not matched to any particle are said to be fake. The fake rate is  
3137 thus defined as follows.

---

<sup>II</sup>Remember that it takes 2 measurements (2 clusters) from a double-sided strip layer to form a 3D space point.

3138 **Definition 11.3** The fake rate  $F_{track}$  is the fraction of reconstructed track candidates having  
3139 the highest matching probability not exceeding 0.5

$$F_{track} = \frac{1}{N_{track}} \sum_{i=1}^{N_{track}} \mathbb{I}_{[\max_j P_m(A_i, B_j) \leq 0.5]} = \frac{N_{fake}}{N_{track}}, \quad (11.10)$$

3140 where  $\mathbb{I}$  is the indicator function.

3141 Definitions 11.1 and 11.3 thus answer questions (1) and (2).

3142 The track quality is a comparison between the properties of truth particles, including  
3143 momentum, cluster composition, and impact parameters, to those of the matched track  
3144 candidate. The track properties are estimated by the track fit described in 11.1. Most  
3145 important among them are the track parameter resolution, defined as

$$\sigma(\mathbf{x}^{(i)}) = \left| \mathbf{x}_{reco}^{(i)} - \mathbf{x}_{truth}^{(i)} \right|. \quad (11.11)$$

### 3146 11.3 Results

3147 The tracking performance of the GNN-based algorithm is presented in this section. Track  
3148 candidates constructed from 1000  $t\bar{t}$  events at  $\langle \mu \rangle = 200$  using the GNN4ITk algorithm are  
3149 processed in ATHENA<sup>III</sup>. These are the same events used to evaluate the individual stages of  
3150 the GNN-based pipeline presented in chapters 8 and 9. We implemented a new component,  
3151 denoted `InDetGNNTracking`, in ATHENA to interface between the GNN-based track builder  
3152 and the current event reconstruction chain [85]. The same events are fed to the Kalman  
3153 Filter under the configuration outlined in ref. [95]. Tracking performance is evaluated using  
3154 the standard `InDetPhysValMonitoring` tool in the software framework.

3155 As mentioned in definition 11.1, track candidates must pass a set of quality selections to  
3156 be considered for truth-particle matching. In production, the same selections are applied to

---

IIIThe ATLAS offline analysis framework

3157 reconstructed tracks before submitting them to downstream reconstruction stages. Reference  
3158 [95] studies the expected tracking performance of the ITk at  $\langle \mu \rangle = 200$  under the CKF, for  
3159 which a set of such selection criteria is optimized. These  $\eta$ -dependent criteria, shown in  
table 11.1, are hereafter referred to as the **nominal cuts**. Among these requirements, a hole

Requirements	Pseudorapidity interval		
	$ \eta  \leq 2.0$	$2.0 <  \eta  \leq 2.6$	$2.6 <  \eta  < 4.0$
Number of clusters	$\geq 9$	$\geq 8$	$\geq 7$
Number of holes	$\leq 2$	$\leq 2$	$\leq 2$
Number of pixel clusters	$\geq 1$	$\geq 1$	$\geq 1$
$p_T$ [MeV]	$> 900$	$> 400$	$> 400$
$ d_0 $ [mm]	$< 2.0$	$< 2.0$	$< 10.0$
$ z_0 $ [cm]	$< 20.0$	$< 20.0$	$< 20.0$

**Table 11.1:** Nominal track selection criteria featured in reference [95].

3160  
3161 is defined as the absence of a cluster between the first and the last hit on track, when the  
3162 interpolated trajectory intersects a layer of active sensors.  $p_T$ ,  $d_0$  and  $z_0$  are respectively the  
3163 transverse momentum, the transverse and longitudinal impact parameters, as described in  
3164 section 11.1. The dependence on  $\eta$  accounts for the difference in detector layout and material  
3165 distribution, and helps maintain uniform reconstruction efficiency throughout the detector.

3166 It is important to note that the CKF and the GNN-based algorithm are two different  
3167 techniques running on different event-level inputs, the former directly consuming the recorded  
3168 clusters while the latter using space points formed from these clusters, adding an extra layer  
3169 of abstraction. As mentioned in section 7.1, there exists by construction cluster inefficiency  
3170 amongst the reconstructed space points. In other words, assuming a particle generates at  
3171 least one lone cluster in the strip detector, even a track perfectly reconstructed<sup>IV</sup> from space  
3172 points cannot recuperate the lone clusters. This issue also leads to an increase in the average

---

<sup>IV</sup>that is, containing all of the particle's space points and no space points from other particles

3173 number of holes on track, because every lone cluster that is not the outermost cluster of the  
 3174 particle contributes an additional hole, on top of those caused by detector or algorithmic  
 3175 inefficiency. Consequently, the first two criteria in table 11.1 on the number of clusters and  
 3176 holes would likely penalize an algorithm based on space point because of information lost in  
 3177 its input rather than its inherent inefficiency. We thus examine a second set of selections,  
 denoted **relaxed cuts** and shown in table 11.2. In particular, compare to the nominal

Requirements	Pseudorapidity interval		
	$ \eta  \leq 2.0$	$2.0 <  \eta  \leq 2.6$	$2.6 <  \eta  < 4.0$
<b>Number of clusters</b>	$\geq 7$	$\geq 7$	$\geq 7$
<b>Number of holes</b>	$\leq 4$	$\leq 4$	$\leq 4$
Number of pixel clusters	$\geq 1$	$\geq 1$	$\geq 1$
$p_T$ [MeV]	$> 900$	$> 400$	$> 400$
$ d_0 $ [mm]	$< 2.0$	$< 2.0$	$< 10.0$
$ z_0 $ [cm]	$< 20.0$	$< 20.0$	$< 20.0$

**Table 11.2:** Relaxed selections adapted to GNN-based tracks. Modified criteria with respect to those in table 11.1 are highlighted in boldface. The rest is identical to reference [95].

3178  
 3179 cuts, the minimum number of clusters is decreased to 7 and the maximum number of holes  
 3180 increased to 4 for pseudo rapidity range  $-2.6 \leq \eta \leq 2.6$ . All particle traversing this region  
 3181 intersect the strip detector and may produce lone clusters, as shown in figure 7.4. The  
 3182 selections on tracks having  $|\eta| > 2.6$  are identical to those in table 11.1, since this region  
 3183 features exclusively pixel sensors.

3184 **11.3.1 Reconstruction performance of the GNN-based algorithm  
3185 under nominal and relaxed track selections**

3186 In this section, we compare the tracking performance of the GNN-based algorithm under  
3187 the **nominal** and the **relaxed** selections. This discussion will shed light on the effect of  
3188 cluster inefficiency and justify the relaxation in selection cuts.

3189 Shown in figure 11.2a is the tracking efficiency of the GNN4ITk chain in the **Module**  
3190 **Map MeanRMS** variant. Other graph construction techniques slightly differ in numerical  
3191 value but maintain the same trend. The efficiency under the relaxed selections selections  
3192 is significantly higher than that under the nominal selections. It follows that the algorithm  
3193 produces a number of track candidates which are matchable to a target truth particle but  
3194 contain an insufficient number of cluster or an excess number of holes to pass the nominal  
3195 selections. The relaxed selections allow these candidates to enter truth matching, so a larger  
3196 proportion of particles are reconstructed, yielding better efficiency.

3197 The difference is clearly visible in the particle pseudorapidity range  $|\eta| < 2.6$ , whereas  
3198 no difference in the range  $|\eta| > 2.6$  is observed. A strong correlation between the truth  
3199 pseudorapidity, the number of lone clusters, and the efficiency gain with relaxed selection  
3200 emerges when we consider together figures figure 7.4 and 11.2a. For  $|\eta| < 2.6$ , lone clusters  
3201 appear in the particle's trajectory, reaching up to one lone cluster per track near  $|\eta| = 2.0$ .  
3202 Correspondingly, the efficiency in this region benefits from allowing fewer hits and more  
3203 holes in the track candidate. For  $|\eta| > 2.6$ , the particle stays entirely in the pixel detector,  
3204 thus generating no lone cluster. No efficiency gain from relaxed selections is observed in  
3205 this region, implying that without lone clusters, the reconstructed track candidate contains  
3206 fewer missing hits than it would otherwise. Almost all pixel-only candidates passing other  
3207 selection cuts have at most 2 holes, so they gain nothing from further increase in maximum  
3208 hole count. The logical conclusion of these observation is that the excess holes and deficient

3209 clusters on tracks containing strip clusters are largely due to hit inefficiency in the put rather  
 3210 than algorithmic inefficiency of the GNN-based track maker.

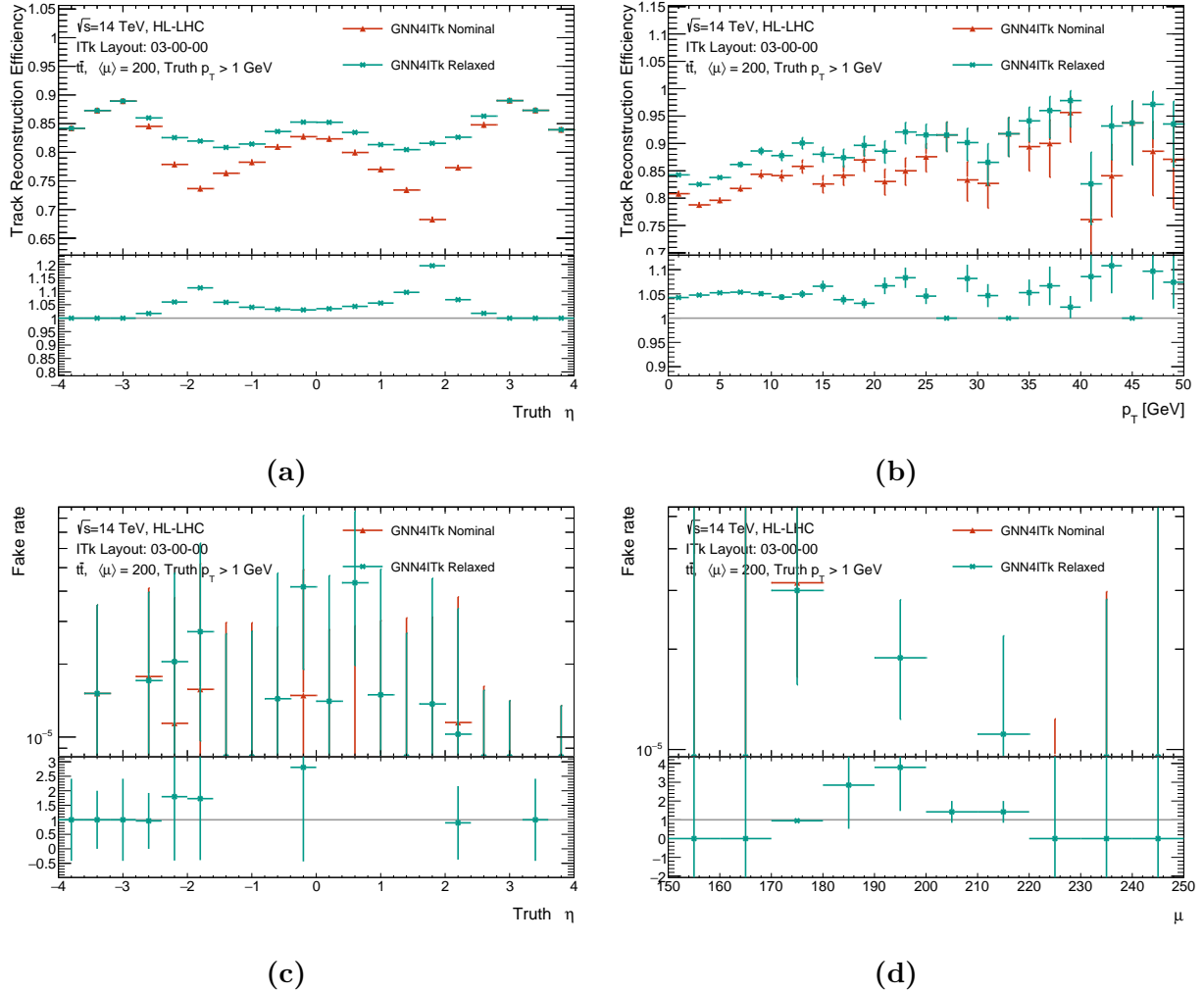


**Figure 11.2:** A comparison of the GNN-based track candidates selected by the nominal and the relaxed criteria in representative performance metrics. Top plots show the efficiency as functions of the truth pseudorapidity  $\eta$  (a) and transverse momentum  $p_T$  (b). Bottom plots show the rate of fake tracks as functions of  $\eta$  (c) and the pile-up level  $\mu$  (d).

3211 Efficiency and fake rate are typically in a trade-off relationship, such that to increase  
 3212 efficiency, one often admits more track candidates by loosening some selection criteria, poten-  
 3213 tially allowing those constructed from randomly associated hits. Fake tracks at best consume

extra computing resources and at worse introduce bias to event- and object-level parameters, such as the missing transverse momentum  $p_{T,miss}$  which is estimated as the compliment of the total visible transverse momentum. As parameter biases from the tracker accumulate throughout the reconstruction chain, it is particularly important to control the number of fake tracks. In fact, the nominal cuts in table 11.1 are optimized with a primary objective of limiting the fake rate [95].

Despite the increased efficiency, no explosion in the number fake tracks is observed with the relaxed cuts. Shown in figure 11.2c, the average fake rate under both the nominal and the relaxed selections is of  $\mathcal{O}(10^{-5})$ , i.e. every 10000 track candidates contain  $\mathcal{O}(1)$  fake track. Considering that the track builder produces about 2000 tracks per event, this fake rate implies that both sets of cuts can filter all fake candidates in the majority of events. Table 11.3 shows the total number of fake candidates among 1000 test  $t\bar{t}$ -events produced by the GNN- and CKF-based track builders under the two sets of selections. While the relaxed cuts increase the number of fake by a factor of 9 for the CKF, only a factor of 2 is observed for the GNN, in addition to its small absolute values. Therefore, for the CKF, requiring track candidates to satisfy the requirements in table 11.1 is *essential* to limit fake tracks and maintain good efficiency. On the other hand, for the GNN4ITk, a relaxation in the minimum number of hits and the maximum number of holes in the strip region ( $|\eta| < 2.6$ ) is necessary to cope with the input hit inefficiency, yet still guarantees low fake rate, thus achieving an optimal performance.

Track selection	GNN4ITk	CKF
Nominal	11	130
Relaxed	22	1205

**Table 11.3:** The total number of reconstructed tracks by the GNN4ITk and the CKF chains having matching probability less than 0.5 over 1000  $t\bar{t}$  events.

These factors when considered together justify the evaluation of GNN-based tracking performance at relaxed selections, and the CKF-based performance at the nominal selections. In light of this discussion, we propose to apply a minimally modified set of cuts, shown in table 11.4 to all tracks built by the GNN-based algorithm.

Requirements	Pseudorapidity interval		
	$ \eta  \leq 2.0$	$2.0 <  \eta  \leq 2.6$	$2.6 <  \eta  < 4.0$
Number of clusters	$\geq 7$	$\geq 7$	$\geq 7$
Number of holes	$\leq 4$	$\leq 4$	$\leq 2$
Number of pixel clusters	$\geq 1$	$\geq 1$	$\geq 1$
$p_T$ [MeV]	$> 900$	$> 400$	$> 400$
$ d_0 $ [mm]	$< 2.0$	$< 2.0$	$< 10.0$
$ z_0 $ [cm]	$< 20.0$	$< 20.0$	$< 20.0$

**Table 11.4:** Minimally modified selections adapted to GNN-based tracks. Modified criteria with respect to those in table 11.1 are highlighted in boldface. The rest is identical to reference [95].

### 11.3.2 Reconstruction efficiency

In this section, we compare the reconstruction efficiency of the three variants of the GNN-based algorithm to that of the CKF. Track candidates produced by the former are required to pass the quality cuts in table 11.4, and those produced by the latter are required to pass the cuts in table 11.1. The tracking efficiency as functions of the truth  $\eta$  and  $p_T$  are respectively shown in figures 11.3a and 11.3b. The bottom plot in each figure shows the ratio between each of the GNN-based curves to the CKF-based curve.

The tracking efficiency varies as a function of truth pseudorapidity. All reconstruction algorithms reach the maximum efficiency at  $|\eta| = 0$  and  $\eta = 3.0$ , and minimum at  $|\eta| = 1.8$ , symmetric around  $\eta = 0$ . These variations are strongly correlated to the detector material encountered by the particle on its path, illustrated on figure 6.8c. The total radiation length

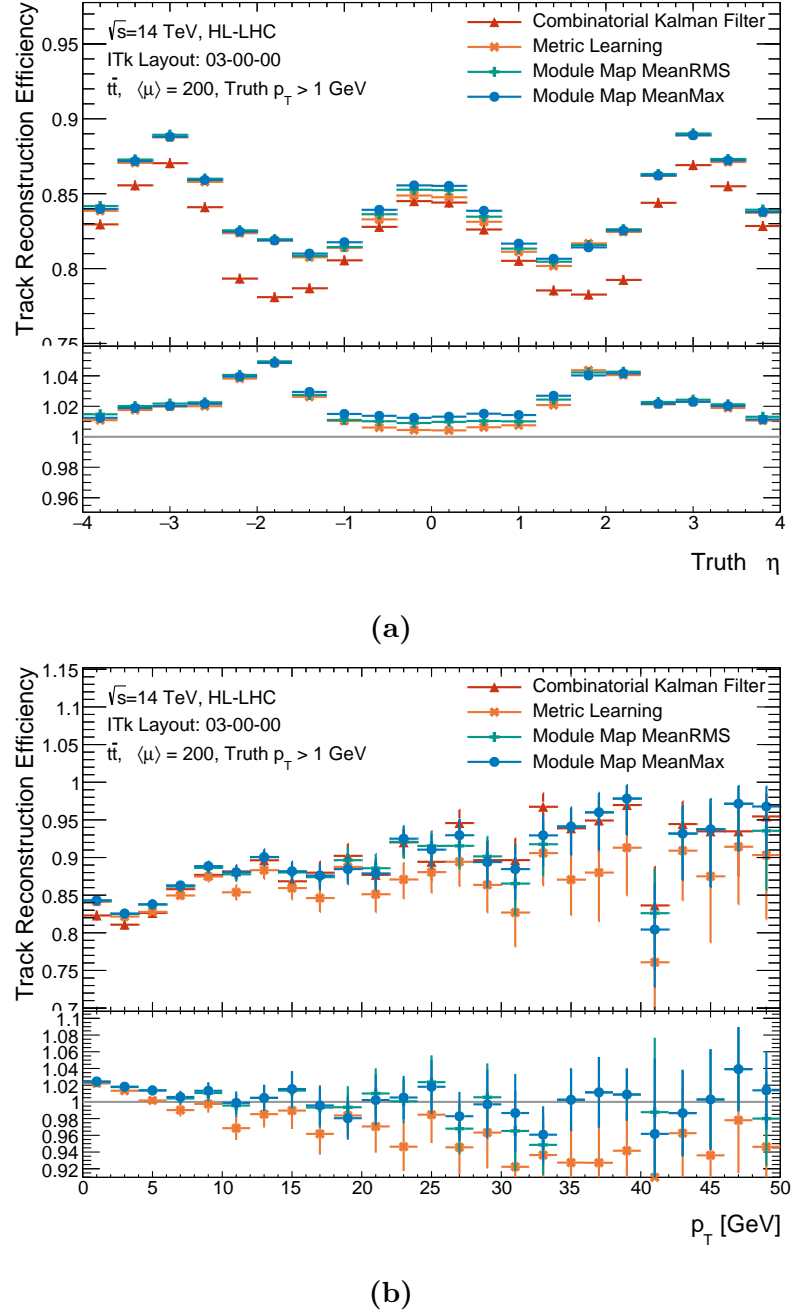


**Figure 11.3:** Tracking efficiency as functions of the truth pseudorapidity  $\eta$  (a) and transverse momentum  $p_T$  (b). The bottom plots show the ratio of the GNN-based curves to the CKF-based curve.

3249 traversed by a particle before reaching the minimum number of hits to be reconstructible is  
 3250 lowest at  $|\eta| = 0$  and  $|\eta| = 3.0$  and peaks at  $|\eta| = 1.5$ . Since material effects randomly direct  
 3251 the real trajectory away from an ideal helix, particles travelling through more material tend  
 3252 to have more hits deviating considerably from their expected position. For the CKF, this  
 3253 means that incorporating the correct hit could significantly increase the total  $\chi^2$ , leading to  
 3254 an early termination of the hit-finding sequence and subsequently the track candidate failing  
 3255 the selection cuts. On the other hand, trained on data which contain these “irregular”  
 3256 connections, the GNN is observed to tolerate large deviations, but the constructed track  
 3257 candidate could still be ruled out by the global  $\chi^2$  fit.

3258 Among the GNN-based trackers, the best efficiency is observed in the Module Map Min-  
 3259 Max variant, followed closely by the MeanRMS variant. All three variants yield similar  
 3260 efficiency at low transverse momentum ( $p_T < 5$  GeV), but start to diverge at high  $p_T$ . The  
 3261 Metric Learning variant is slightly less efficient than the Module Map variants for  $p_T > 5$   
 3262 GeV. On the pseudorapidity spectrum, it has lower efficiency in the strip barrel in the range  
 3263  $|\eta| < 1$ , but otherwise identical to the other GNN-based variants. These observations are  
 3264 explain by the fact that high- $p_T$  particles are more likely to have small pseudorapditiy and  
 3265 concentrate in the barrel region. Graph construction using the Metric Learning is less efficient  
 3266 than the Module Map at high  $p_T$ , as shown in figure 9.2a, and the inefficiency accumulates  
 3267 throughout the pipeline, leading to the observed degradation in tracking efficiency.

3268 All variants of the GNN4ITk algorithm produce tracking efficiency exceeding that of the  
 3269 CKF when plotted as a function of  $\eta$ , in which each bin is the conditional efficiency averaged  
 3270 over all particle momenta. On the  $p_T$  spectrum, however, it is clear that the improvement  
 3271 is not evenly distributed. All of the efficiency improvement occurs on particles with low  
 3272  $p_T$ , as seen on the ratio plot of figure 11.3b, the performance at high  $p_T$  is largely similar  
 3273 to that of the CKF. High- $p_T$  particles are rare, as they commonly originate from the hard-  
 3274 scattering collision, and concentrate around the barrel region. The absence of efficiency  
 3275 improvement at high  $p_T$  partially explains the comparatively smaller efficiency boost near

3276  $\eta = 0$ . In contrast, low- $p_T$  particles constitute the majority of target particles, orders of  
3277 magnitude more abundant than their high- $p_T$  counterparts, and are distributed quite evenly  
3278 throughout the detector, which explains the excess efficiency in all  $\eta$  bins on figure 11.3a.

3279 Though not simply related, tracking efficiency is determined by the edge-level efficiency  
3280 encountered the results of previous chapters. The impact of the uneven  $p_T$  distribution in  
3281 training data on edge-level performance was already seen in section 9.2.2. All models in the  
3282 GNN4ITk are trained on data which predominantly features low- $p_T$  tracks. They learn to  
3283 minimize the classification loss of true edges from these tracks, possibly at the expense of the  
3284 other less abundant particles. As discussed in section 9.3.2, increasing the weight of high- $p_T$   
3285 edges in the loss function proves ineffective. For now, despite the degradation in the edge  
3286 efficiency, the efficiency of the GNN-based tracker at high momentum matches that of the  
3287 CKF in absolute terms. Increasing the per-edge performance of the pipeline at high  $p_T$  is a  
3288 priority for future work.

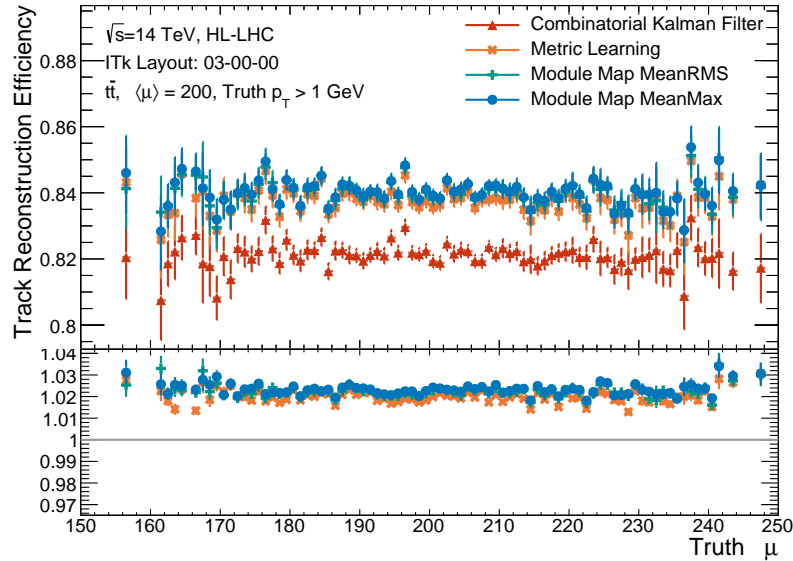


**Figure 11.4:** Tracking efficiency as a function of the pile-up level  $\langle \mu \rangle$ . The bottom plots show the ratio of the GNN-based curves to the CKF-based curve.

3289       Figure 11.4 shows the tracking efficiency as a function of truth pile-up level. The tracking  
 3290       efficiency is found to be stable over a range of pile-up from  $\mu = 160$  to  $\mu = 240$ . The GNN-  
 3291       based track builders are on average 84% efficiency, while the CKF is 82%. No degradation  
 3292       is observed with increased pile-up.

3293       **11.3.3 Track fake rate**

3294       The proportion of track candidates without a matching truth particle as functions of  
 3295       the truth pseudorapidity and pile-up is shown in figures 11.5a and 11.5b. While both the  
 3296       GNN4ITk and the CKF have fake rate order  $\mathcal{O}(10^{-5})$ , the former produces fewer fake tracks  
 3297       than the latter. As seen in table 11.3, the total number of fake tracks from the GNN is  
 3298       approximately 1/6 of those from the CKF. Despite more truth particles are reconstructed  
 3299       by the GNN than by the CKF, evidenced by the better efficiency, only track candidates  
 3300       matched to these particles are created in excess. In other words, we achieve higher efficiency  
 3301       without paying the cost of building more low-quality, unassociated tracks. It lends support  
 3302       to the use of selection criteria that are adapted to a specific algorithm of interest, rather  
 3303       than rigidly adopting a predetermined working point optimized for a different one.

3304       Given the small number of fake tracks, it is difficult to examine their spatial distribution  
 3305       and variation with pile-up, the latter being of particular importance. This is due to the  
 3306       small number of  $t\bar{t}$  events used in evaluation. Future work may address this problem with a  
 3307       larger test sample.

### 3308 11.3.4 Parameter resolution

3309     Track parameter resolution quantifies how well the reconstructed track candidate rep-  
 3310     resents the underlying truth particle, and is thus an important aspect of tracking. It is  
 3311     evaluated by comparing the parameters at the perigee surface extracted from the global  $\chi^2$   
 3312     fit discussed in section 11.1 and the corresponding truth value using equation 7.11. In MC  
 3313     simulation, the truth impact parameters are specified by the primary vertex position, and  
 3314     the truth kinematics the momentum at the vertex. The are generated along the particles  
 3315     and stored for tracking validation.

3316     The resolution of the longitudinal ( $z_0$ ) and transverse ( $d_0$ ) impact parameters of the  
 3317     track candidates produced by both the GNN- and CKF-based algorithms is shown in figure  
 3318     11.6. The vertical axis in these plots displays the number of matched track–particle pairs  
 3319     normalized to unity. All track builders show a spectrum peaking at  $\sigma(d_0) = 0$  and  $\sigma(z_0) = 0$ .  
 3320     In general, the GNN-based algorithms produce a larger proportion of tracks whose resolution  
 3321     concentrates around 0 for both impact parameters than does the CKF. Despite having higher  
 3322     efficiency, i.e. reconstructing more particles, the GNN-based track candidates are less tail-  
 3323     heavy. In other words, the excess tracks found by the GNN4ITk are overwhelmingly good-  
 3324     quality tracks accurately characterizing the impact parameters of the underlying particle.  
 3325     The distributions from the two Module Map variants appear similar, while that of the Metric  
 3326     Learning variant is slightly more tail-heavy.

3327     The good resolution observed for the GNN-based algorithm can be explained by the  
 3328     efficiency in finding the hit on the innermost pixel layer, which provides a strong constraint  
 3329     on the impact parameters. Figure 11.7 shows the number innermost pixel hits as a function  
 3330     of track pseudorapidity. The Module Map variants build tracks with the same average  
 3331     number of innermost pixel hits as does the CKF, with tracks in the barrel region having  
 3332      $\langle N_{pix,innermost} \rangle = 1$ . The Metric Learning variant is slightly less hit-efficient in the barrel,  
 3333     which would explain its lower resolution.

Another measure of resolution is the RMS of the core of the distribution of the difference between the reconstructed and true values of the parameter. Figures 11.8 and 11.9 respectively show the RMS of the  $(d_{0,reco} - d_{0,truth})$  distribution and the the  $(z_{0,track} - z_{0,truth})$  distribution, measured in  $\mu\text{m}$ , as a function of  $\eta$ . Over the entire  $\eta$  range, the resolution of the Module Map variants is in good agreement with that of the CKF, while that of the Metric Learning is slightly degraded in the barrel region. Here we can clearly observe the correlation between the number of innermost pixel hits and the impact parameter resolution, as the degradation occurs where the former quantity is the most deficient among the the Metric Learning track candidates.

The transverse momentum resolution as a histogram is shown in figure 11.10a and as a function of  $\eta$  in figure 11.10b. Unlike the other parameters' resolution, the dimensionless transverse momentum resolution is computed as

$$\sigma(p_T) = p_{T,truth} \times \left( \frac{q}{p_{T,reco}} - \frac{q}{p_{T,truth}} \right).$$

3343 While other track parameters are directly obtained from the  $\chi^2$  fit, the transverse momentum  
 3344 is derived from the total momentum  $p$  and the azimuthal angle  $\theta$  in the ATLAS parametriza-  
 3345 tion (equation (11.1)). There is no straightforward relationship between its resolution and  
 3346 elements of the global fit. However, given that it is derived from fit parameter  $q/p$ , whose  
 3347 uncertainty is driven by material interaction, one expects lower  $p_T$  resolution with more  
 3348 detector material encountered on the trajectory. This effect is observed on figure 11.10b,  
 3349 viewed in tandem with figure 6.8a, which shows the material budget traversed by a straight  
 3350 track in radiation length as a function of the particle's pseudorapidity. The total radiation  
 3351 length increases generally with  $\eta$ , so the closer to the beamline is the particle, the more its  
 3352 energy—and thus momentum—is eroded, weakening the constraints on  $p_T$ . In consequence,  
 3353 the  $p_T$  resolution decreases monotonically with  $\eta$ .

3354 The transverse momentum is proportional to the radius of the curved trajectory, which in  
 3355 turn is geometrically constrained by the hits found between the outermost hits of the track  
 3356 candidate<sup>V</sup>. Therefore, the  $p_T$  resolution generally improves with the number of measure-  
 3357 ments and degrades with the number of holes of the track candidate. In light of this principle,  
 3358 the difference in  $p_T$  resolution between the GNN4ITk and the CKF may be elucidated. On  
 3359 figure 11.10b, the observed  $p_T$  resolution of the GNN4ITk is similar to that of the CKF in  
 3360 the all-pixel region, for  $|\eta| > 2.6$ . Both algorithms find relatively long tracks in this region,  
 3361 having on average 13–14 hits, shown in figure 11.11a. Track candidates from the GNN4ITk  
 3362 are slightly shorter than those from the CKF. However, these the former contains on average

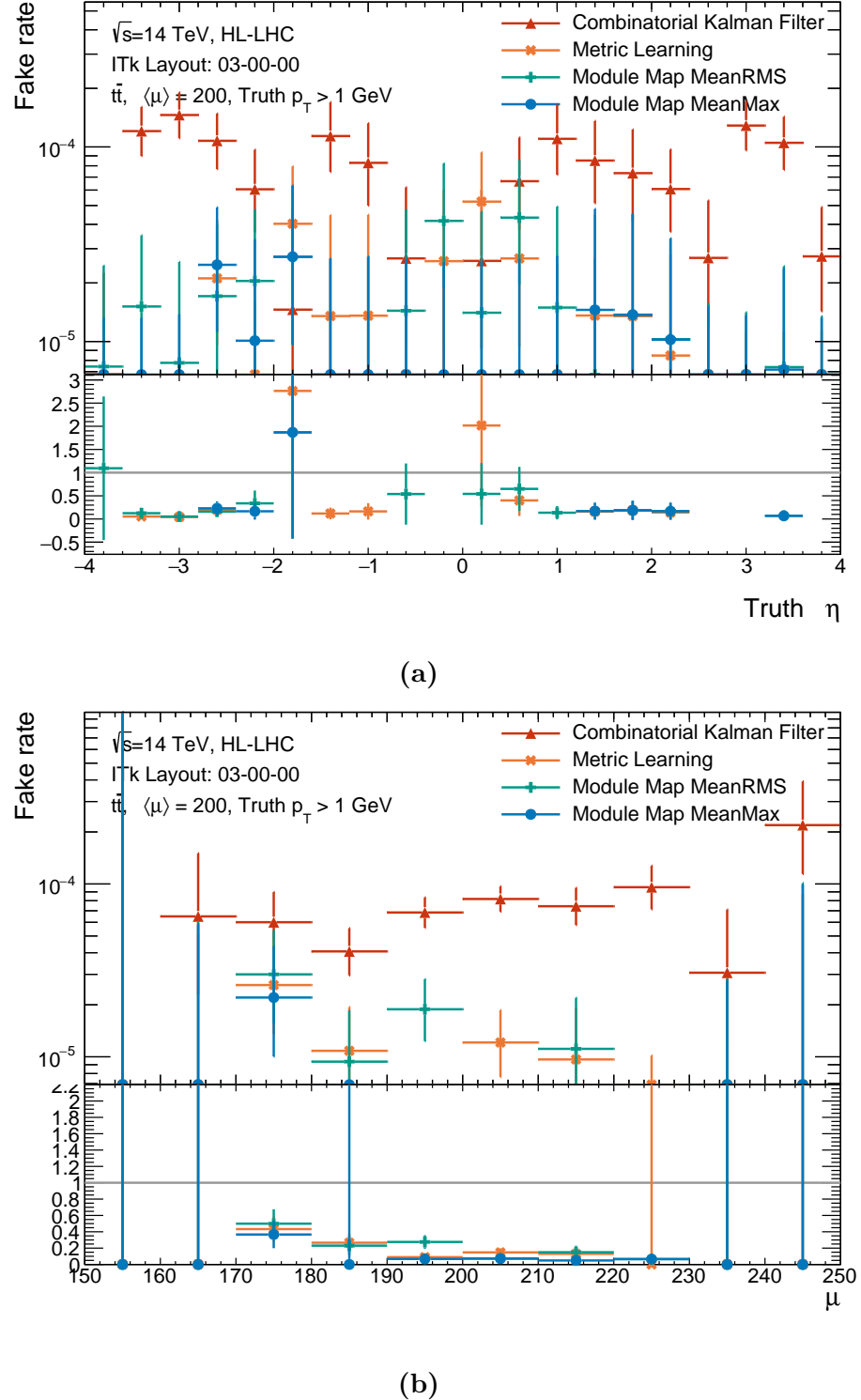
---

<sup>V</sup>Intuitively, imagine fitting a circle passing through two outermost points. If no intermediate points exists, any of infinitely many possible circles is equally likely, hence null constraint. If an intermediate measurement exists with some measurement error, the closer a circle passes by the points, the more likely hit is. More intermediate measurements provide better constraining power, hence better resolution.

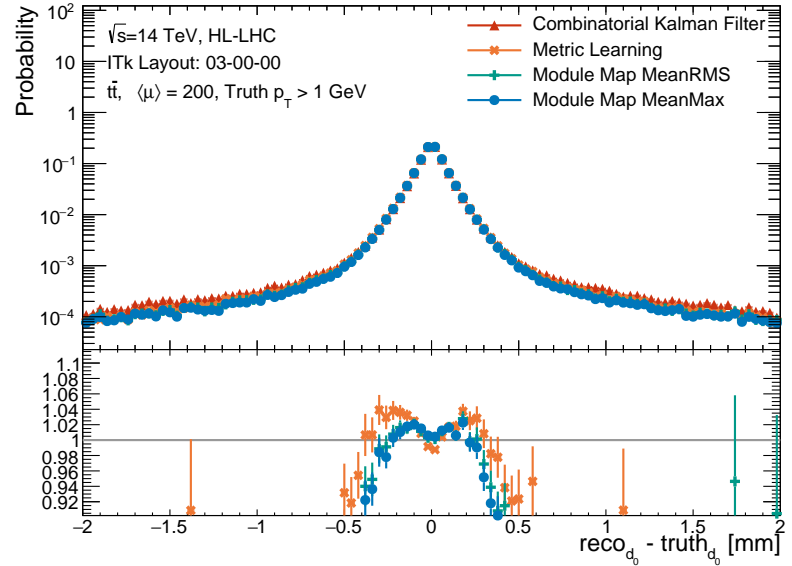
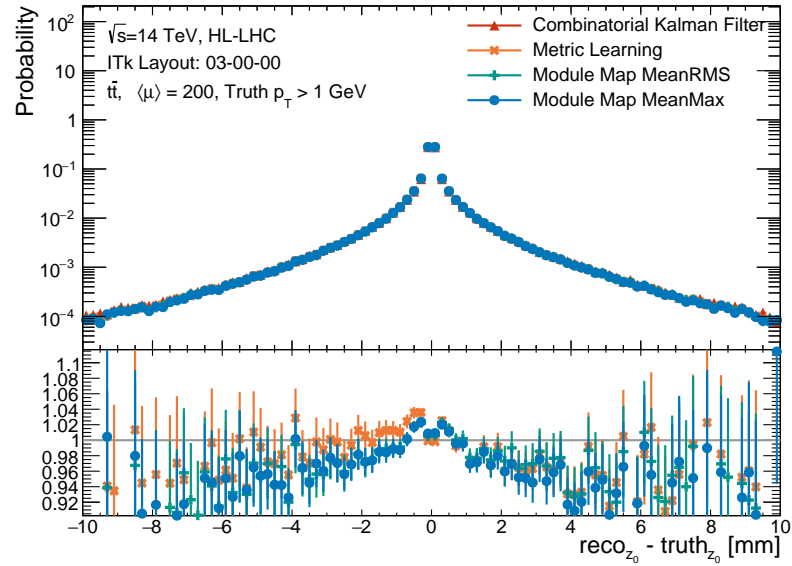
3363 fewer holes, as seen on figure 11.11b. In other words, pixel-only GNN-tracks are shorter,  
3364 but skip fewer layers than do the CKF counterparts. Though not simply quantifiable, these  
3365 factors have opposite impacts on the  $p_T$  resolution and likely yield similar performance in  
3366 this region in effect.

3367 On the other hand, in the barrel ( $|\eta| < 2$ ) and transition regions ( $2 < |\eta| < 2.6$ ), the  $p_T$   
3368 resolution of all GNN-based variants is lower than that of the CKF. The RMS width of the  
3369  $\sigma(p_T)$ -distribution from the GNN4ITk is at worst 8% larger than from CKF. In this region,  
3370 the GNN-based tracks contain fewer clusters and more holes than the CKF-based tracks. The  
3371 gap is particularly pronounced in the strip detector, due to the presence of single clusters. In  
3372 the barrel, despite the same average number of pixel clusters and negligible numbers of pixel  
3373 holes, the GNN4ITk finds about 90% the average number of strip hits found by the CKF,  
3374 and leaves up to 5 times the number of holes left by the latter. In the transition region,  
3375 this trend repeats. The combination of cluster deficiency and enrichment of holes explains  
3376 the degraded  $p_T$  resolution in this region. In general, the GNN, being trained on incomplete  
3377 data, performs worse than the CKF does in the strip detector. In addition, the relaxed track  
3378 selection cuts in  $|\eta| < 2.6$ -range allow short and layer-skipping GNN tracks to pass through,  
3379 contributing to their increased abundance. This is the trade-off we make in exchange for  
3380 better efficiency.

3381 In accordance with our discussion on figure 11.10b, the  $\eta$ -independent GNN-based dis-  
3382 tributions of  $\sigma(p_T)$  is manifestly wider than corresponding CKF-based distribution. The tail-  
3383 heavy histograms verify that the GNN4ITk yields lower  $p_T$  resolution than does the CKF.  
3384 Notably, the GNN-based distributions are not symmetric around  $\sigma(p_T) = 0$ , but instead  
3385 leaning more heavily toward positive values of  $\sigma(p_T)$ . Although occurring with low statis-  
3386 tics, this asymmetry is apparent and merits further investigation. We hypothesize that the  
3387 asymmetric distribution of strip holes observed in figure 11.11d could contribute to this  
3388 phenomenon, but more careful inspection is needed.



**Figure 11.5:** The proportion of reconstructed tracks reconstructed by the GNN4ITk and CKF chains having matching probability less than 0.5 as a function of the track pseudorapidity  $\eta$  (a) and the truth pile-up (b). The bottom plots show the ratio of the GNN-based curves to the CKF-based curve.

(a) Transverse impact parameter resolution  $\sigma(d_0)$ (b) Longitudinal impact parameter resolution  $\sigma(z_0)$ 

**Figure 11.6:** Transverse (a) and longitudinal (b) impact parameter resolution shown as histograms of  $\sigma(d_0)$  and  $\sigma(z_0)$  respectively. Note that the resolution of parameter  $x$  is inversely proportional to  $\sigma(x)$ .

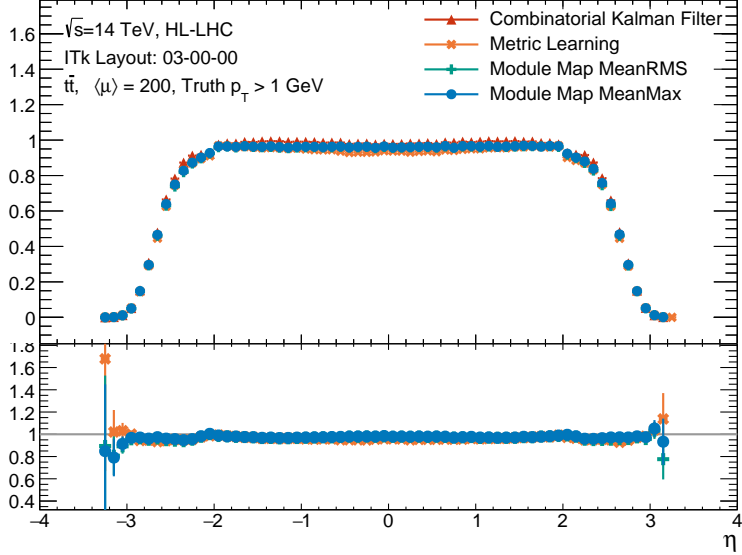


**Figure 11.7:** The number of hits from the inner most pixel layer as a function of reconstructed pseudorapidity  $\eta$ .

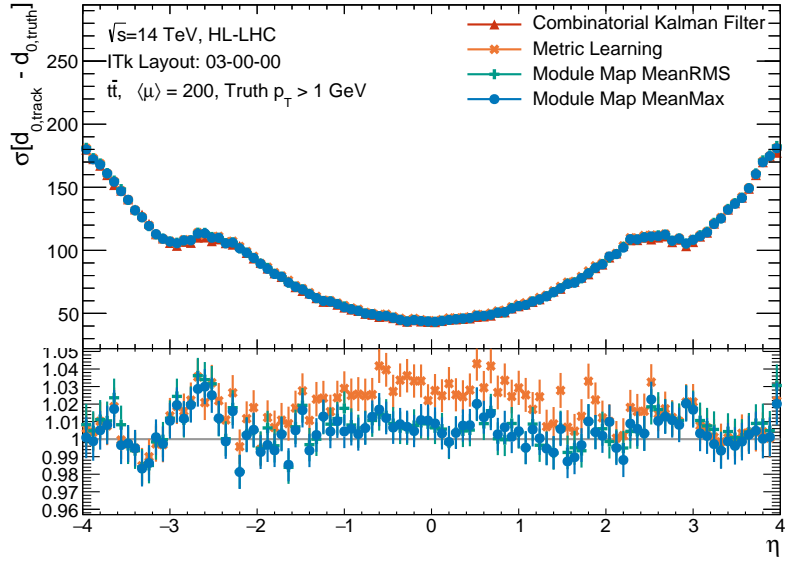


**Figure 11.8:** Transverse impact parameter resolution  $\sigma(d_0)$  of as a function of truth  $\eta$ , evaluated on tracks reconstructed by the GNN4ITk and the CKF chains. The bottom plots show the ratio of the GNN-based curves to the CKF-based curve.

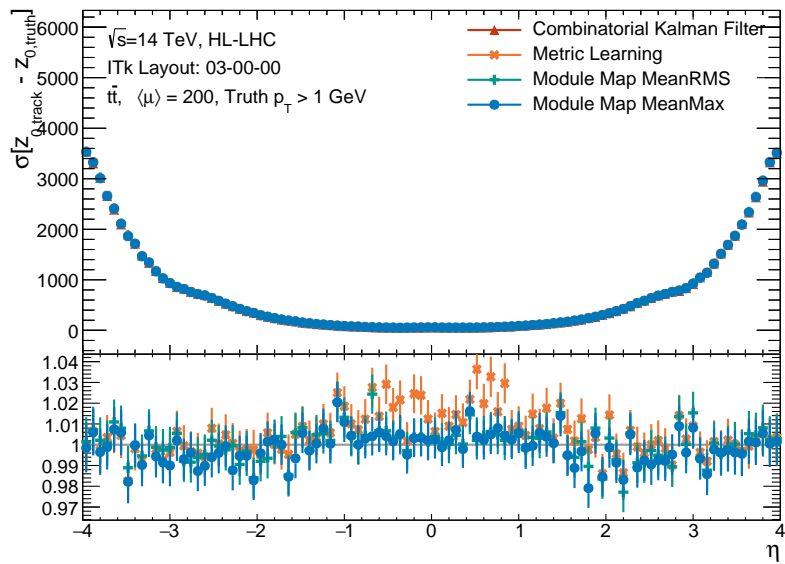
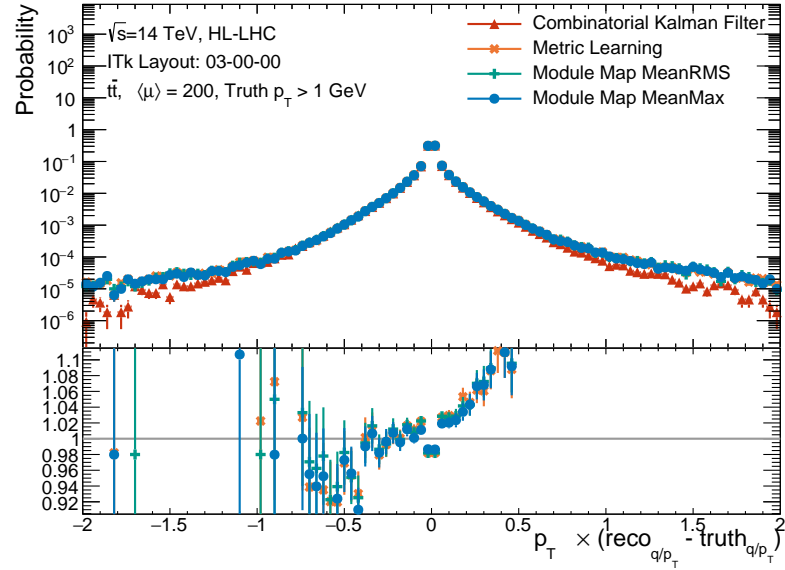
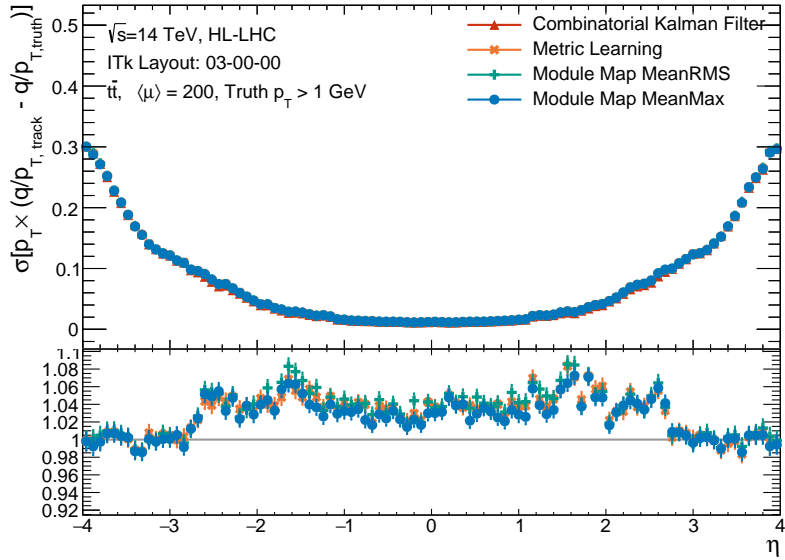


**Figure 11.9:** Longitudinal impact parameter resolution  $\sigma(z_0)$  of as a function of truth  $\eta$ , evaluated on tracks reconstructed by the GNN4ITk and the CKF chains. The bottom plots show the ratio of the GNN-based curves to the CKF-based curve.

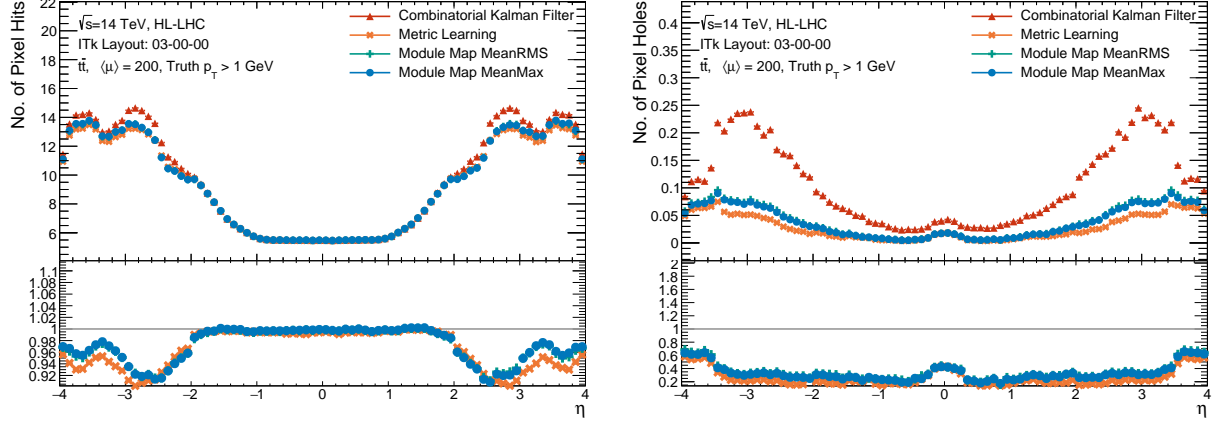


(a) Transverse momentum resolution  $p_T \times \left( \frac{q}{p_{T,reco}} - \frac{q}{p_{T,truth}} \right)$

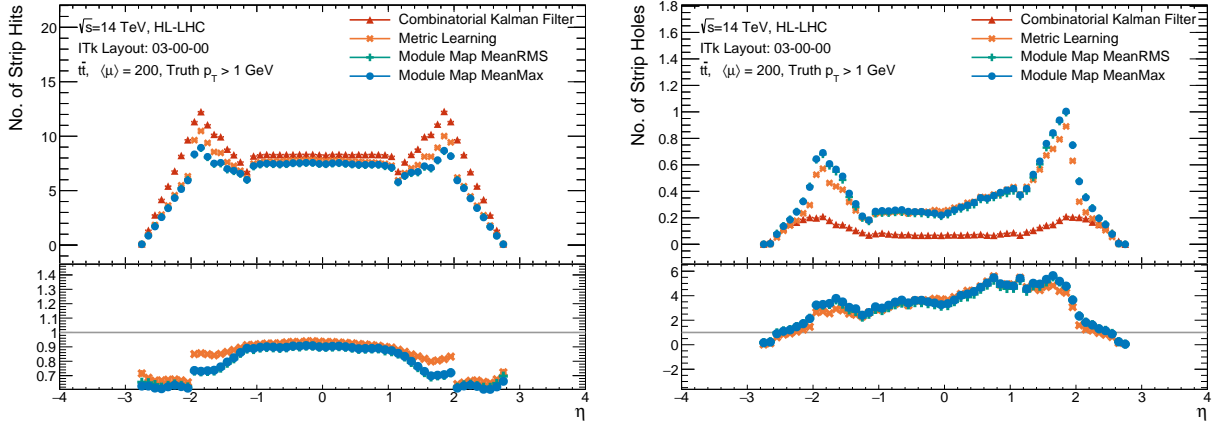


(b) Transverse momentum resolution  $p_T \times \left( \frac{q}{p_{T,reco}} - \frac{q}{p_{T,truth}} \right)$  as a function of  $\eta$

**Figure 11.10:** Transverse momentum resolution shown as a histogram of  $\sigma(p_T)$  (a) and a function of the truth pseudorapidity  $\eta$  (b).



(a) Average number of pixel clusters on selected track candidates. (b) Average number of pixel holes on selected track candidates.



(c) Average number of strip clusters on selected track candidates. (d) Average number of strip holes on selected track candidates

**Figure 11.11:** Hit content of selected track candidates, demonstrated by the average number pixel clusters (a), pixel holes (b), strip clusters (c) and strip holes (d). These quantities are shown as functions of the reconstructed pseudorapidity  $\eta$ .

3389 **Chapter 12**

3390 **Computational performance**

3391 In the previous chapter, we have shown that the GNN4ITk pipeline achieves tracking  
3392 performance competitive to that of the CKF chain. An equally important aspect of a track  
3393 reconstruction algorithm, as previously stated, is speed and resource consumption. After all,  
3394 the bottleneck caused by the current CPU-intensive track finder under HL-LHC conditions  
3395 is the primary motivation to develop a GPU-based alternative. In this regard, this thesis  
3396 documents the first attempt to evaluate and optimize the computing performance on full-  
3397 simulation data with realistic ITk geometry. In comparison, previous publications have either  
3398 focused entirely on the physics performance [76, 81], or evaluated computing performance  
3399 on an open dataset based on simplified geometry [123]. This chapter presents a number  
3400 of techniques to accelerate the edge classification inference, the key part of the GNN4ITk  
3401 algorithm. The most recent results on the pipeline latency is summarized and discussed with  
3402 respect to that of the CKF.

3403 It should be noted, however, that the computational performance of this technique un-  
3404 dergoes rapid developments, and thus this chapter aims to provide a snapshot of the progress  
3405 at the time of writing, rather than the finished product. A fully optimized algorithm will  
3406 likely be different from its present status. As such, we will identify several directions both  
3407 currently undertaken and for future studies.

3408 **12.1 An inference pipeline**

3409 As shown in figure 8.1 and explained in chapters 8, 9, and 10, the GNN4ITk is a multi-  
3410 stage algorithm, in which the output from one stage becomes the input to the next. It is  
3411 natural that these stages are developed and optimized independently. In production, the data  
3412 must flow seamlessly through all stages to avoid unnecessary overhead from intermediate I/O  
3413 and data transfer between CPU and GPU memories. [A figure here to illustrate this] The  
3414 data containing space point input is prepared by reading and preprocessing an event already  
3415 save on disk, then transferred to the GPU only once. It stays on the GPU, gets treated in  
3416 sequence by the models, yielding a collection of track candidates, each as an array of hit  
3417 indices. After the track building stage, the output transferred back to the CPU for track fit,  
3418 and the GPU memory liberated to process the next event.

3419 An inference pipeline in PYTHON, as a part of our R&D software framework, was de-  
3420 veloped to evaluate the latency at each stage of the algorithm and the overall inference  
3421 time.

3422 **12.2 Neural Network optimization techniques**

3423 Graph neural networks are the key engine for pattern recognition in the GNN4ITk  
3424 pipeline. They are also the easiest to accelerate, as many techniques are well established  
3425 and integrated into standard PYTHON libraries. We detail in this section two optimizations  
3426 which in combination significantly enhance the inference speed of the INTERACTIONGNN,  
3427 starting with Automated Mixed Precision, followed by Ahead-Of-Time compilation.

### 3428 12.2.1 Automatic mixed precision (AMP)

3429 Reduced precision is a common technique in machine learning to enhance latency and  
3430 reduce memory footprint. A number represented by binary form is characterized by three  
3431 components, namely the sign, the exponent, and the mantissa, each of which is quantified  
3432 by a number of bits, depending on the data format. The sign, represented by a single bit,  
3433 is self-explanatory. The exponent determines the range of the number that a particular  
3434 format can represent, and the mantissa the precision with which a number is characterized.  
3435 The more bits are dedicated to the exponent, the wider is the range. Similarly, the more  
3436 bits reserved for the mantissa, the more decimal points a number can have. By default,  
3437 arithmetic operations employed in training neural networks are done in FP32, or single-  
3438 precision. In this format, a number is represented by 32 bits. The first bit is dedicated for  
3439 the sign, the next 8 bits for the exponent, and the remaining 23 bits for the digits that make  
3440 up the number. The 8 exponential bits can represent numbers from 0 to 256, thus enabling  
3441 a logarithmic<sup>1</sup> range of  $[-126, 127]$ , with some values reserved for special numbers such as  
3442 infinities, NaNs, etc. Roughly speaking, the 23 mantissa bits allow to express numbers with  
3443 lower threshold of  $2^{-23}$  in precision.

3444 However, during inference, such a wide range and high precision may not be necessary to  
3445 achieve good accuracy, since no gradient calculation, which is prone to numerical explosion  
3446 and vanishing, takes place. If the network output is stable under smaller bit widths, it is  
3447 possible to decrease memory footprint, improve computational efficiency, and reduce power  
3448 consumption by simply lowering the precision. We examine the latency and accuracy of  
3449 the INTERACTIONGN under FP16, or half-precision, in comparison to the baseline single-  
3450 precision. [Figure]

---

<sup>1</sup>base 2

### 3451 12.2.2 Ahead-Of-Time (AOT) compilation

3452 Compilation is a mechanism to optimize the performance and deployability of deep learn-  
3453 ing models by transforming dynamic PYTHON code into an intermediate representation that  
3454 can be efficiently executed. PYTORCH [141]’s eager execution model is highly expressive and  
3455 user-friendly but also incurs significant overhead due to the dynamic nature of PYTHON  
3456 and the interpreter. Ahead-of-time compilation addresses this limitation by capturing, trans-  
3457 forming, and optimizing the execution of PYTORCH models at runtime, thereby delivering  
3458 substantial speedups while maintaining full compatibility with native PYTHON constructs.

3459 Under the hood, PYTORCH performs a series of sophisticated transformations to analyze  
3460 the computational graph<sup>II</sup> for efficient execution on both CPUs and GPUs. The first step  
3461 translates the model into a graph of symbolic functional transformations (FX), in which  
3462 each node represents the sequence of computations. The FX nodes are then converted  
3463 into a lower-level representation that reflects the underlying tensor operations, followed by  
3464 partitioning the FX graph into subgraphs suitable for kernel fusion. A large contribution to  
3465 the overall acceleration comes from merging multiple pointwise and elementwise operations  
3466 in each FX subgraph into a single kernel, reducing memory reads/writes and kernel launch  
3467 overhead. As a simple example, consider a series of three computations shown in algorithm  
6. Without compilation, they are executed separately, starting with the exponent, followed

---

**Algorithm 6:** An example of eager computation

---

Given input  $x$

$x \leftarrow \exp(x);$

$x \leftarrow x + 3;$

$x \leftarrow \text{ReLU}(x)$

---

3468

3469 by the addition, and finally the activation, each step consuming an intermediate memory

---

<sup>II</sup>A model is essentially a computational graph, to be distinguished from the graph data on which it operates.

buffer and dispatch. With compilation, however, they are fused into a single kernel yielding a

---

**Algorithm 7:** Compiled computation

---

```
Given input x
for (i=0; i < N; ++i) {
    out[i] = relu( exp( x[i] ) + 3.0 );
}
```

---

3470

single-step computation instead of three separate ones, thus eliminating intermediate tensor allocations and kernel launch overhead. Further miscellaneous optimizations are carried out, and finally GPU-backend code is emitted for use. Remarkably, this complex analysis is entirely automated by PYTORCH, such that minimal code change is needed to compile an eager model. As this is an active area of development, further optimizations will likely become available.

3477 **12.3 Optimized performance**

3478 The computational efficiency gain from reduced precision and compilation of the INTER-  
 3479 ACTIONGNN is measured on three GPU platforms: the NVIDIA A100 Tensor Core GPUs  
 3480 with 40GB and 80GB memory, and the more advanced H100 model with 80GB memory.  
 3481 These measurements are conducted on the same 1000  $t\bar{t}$  events used in the previous chapter.  
 3482 The baseline corresponds to eager computation with no optimization. The improvement  
 3483 over the baseline automatic mixed precision (AMP) and compilation is separately measured.  
 3484 Because the two techniques are completely independent, we can perform the inference on  
 3485 a compiled model under reduced precision, compounding their effects. The combined im-  
 3486 provement is also measured. The average execution time and peak memory consumption as  
 3487 functions of the optimization method are shown in figure 12.1.

3488 The baseline configuration shows a latency of  $\approx 600$  ms/event on the A100 platform,  
 3489 and 264 ms/event on the H100 platform. The H100's better performance is due to enhanced

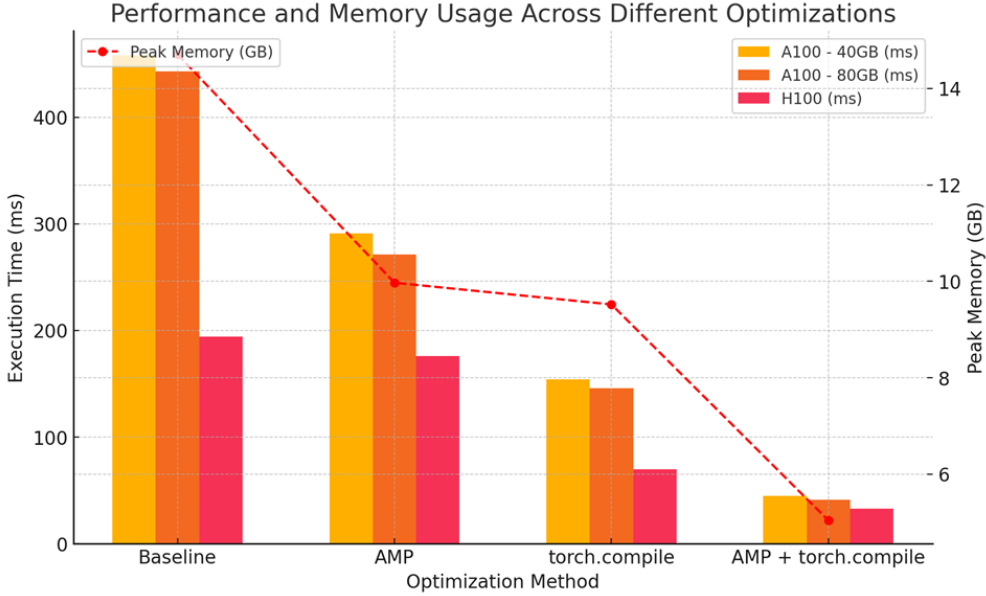


**Figure 12.1:** Computational efficiency of the INTERACTIONGNN in terms of the execution time (left vertical axis) and peak memory (right vertical axis), measured using the baseline configuration, and configuration optimized with automated mixed precision (AMP), Ahead-of-time computation (AOT), and a combination of the two techniques. All measurements use graphs constructed with the Module Map MinMax method.

3490 floating-point operation efficiency on FP32, namely 67 TFLOPS compared to 19.5 TFLOPS  
 3491 on the A100. Under reduced precision, the latency is reduced by approximately 1/3 compared  
 3492 to the baseline on the A100, reaching on average 391 ms/event (40GB) and 362 ms/event  
 3493 (80GB), but only by a small margin on the H100, reaching 239 ms/event. With AOT  
 3494 compilation, the execution time is enhanced to  $\approx$  200 ms/event on both A100 platforms,  
 3495 and 92 ms/event on the H100. Under the combined effect of both techniques, the execution  
 3496 time is significantly reduced to  $\leq$  60 ms/event across all platform.

3497 Table 12.1 shows the improvement in inference speed with respect to eager computation  
 3498 at full precision of each optimization. The A100 and H100 platforms respectively benefit  
 3499 from up to an 11x and 6x boost in efficiency. Remarkably, while the next-generation H100  
 3500 outperforms the older A100-80GB by a factor of 2.25 in speed, this gap is shrunk to 1.40 by

3501 these optimizations. The larger enhancement of the A100 is an important benefit, because  
 3502 it is less expensive and power hungry than the new-generation counterpart, and hence more  
 3503 suitable for budget-constrained scientific computing. Interestingly, the performance boost  
 3504 delivered by the combined technique exceeds the product of the two underlying factors.

Optimization	A100-40GB	A100-80GB	H100-80GB
AMP	1.57	<b>1.63</b>	1.10
Compilation	2.97	<b>3.02</b>	2.77
Combined	9.69	<b>10.58</b>	5.92

**Table 12.1:** Latency improvement over eager computation at full precision of each optimization, measured using the baseline configuration, and configurations optimized with automated mixed precision (AMP), AOT compilation, and a combination of both techniques. All measurements use graphs constructed with the Module Map MeanRMS method.

3505 Similarly, the peak memory consumption is significantly improved with the combined  
 3506 optimization. Shown in figure 12.1, the peak consumption on the A100 decreases from  
 3507 19.16GB in the baseline to 6.48GB in the combined configuration, a factor of almost 3  
 3508 smaller. Thanks to the reduced memory footprint, it becomes possible to simultaneously  
 3509 fit several events on the GPU and enhance the inference throughput, a logical next step for  
 3510 future computational optimization. This direction is being explore using a *inference-as-a-*  
 3511 *service* approach, which optimizes the GPU utilization by batching multiple inference events  
 3512 and processing at the same time [163].

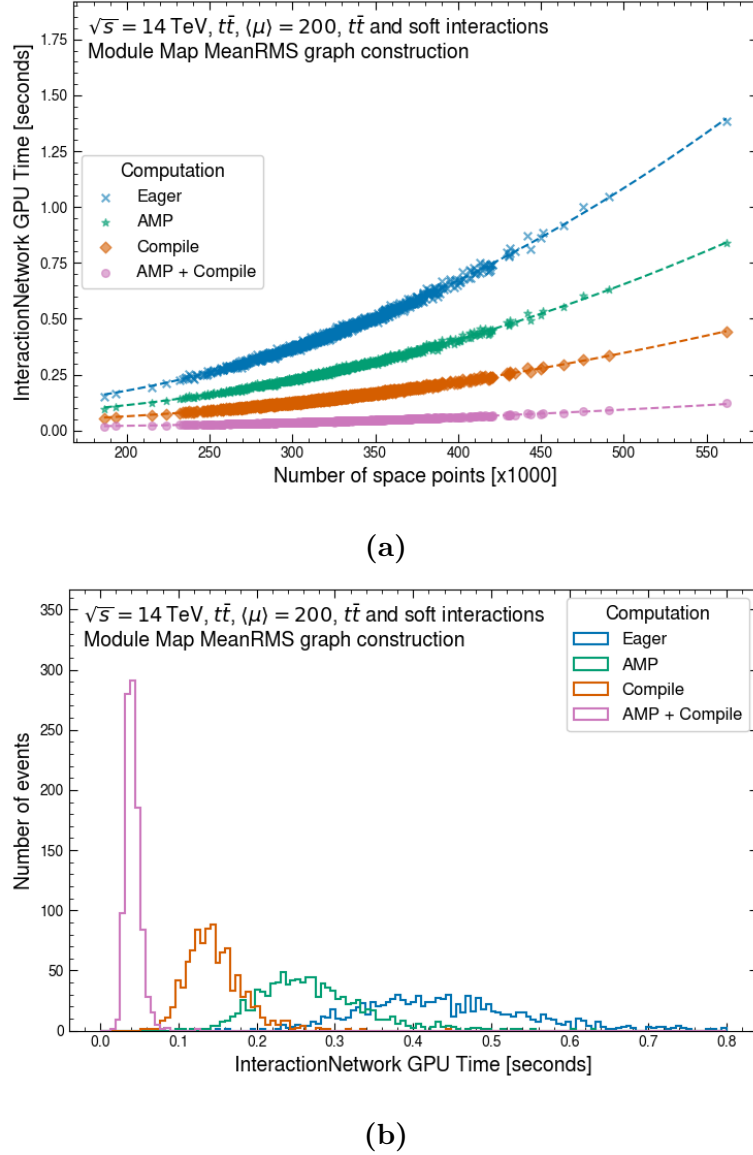


**Figure 12.2:** GPU time of the INTERACTIONGNN as a function of the number of space points in a  $t\bar{t}$  event (a) and as a histogram (b), measured using the baseline configuration, and configurations optimized with automated mixed precision (AMP), AOT compilation, and a combination of both techniques. Each dashed line in (a) displays the best-fit second-order polynomial to the corresponding configuration. The fitted coefficients are exhibited in table 12.2. All measurements are performed on an NVIDIA-A100 GPU with 80 GB of memory, using graphs constructed with the Module Map MeanRMS method.

Computation	A	B	C
Eager	5.56	$-8.73 \times 10^{-1}$	$1.30 \times 10^{-1}$
AMP	3.36	$-5.40 \times 10^{-1}$	$8.87 \times 10^{-2}$
Compile	1.73	$-2.67 \times 10^{-1}$	$4.76 \times 10^{-2}$
AMP + Compile	0.457	$-7.95 \times 10^{-2}$	$1.87 \times 10^{-2}$

**Table 12.2:** The coefficients of a second-order polynomial fit to the GPU time shown in figure 12.2 for each optimization technique. The GPU time  $t$  in units of seconds is assumed to depend on  $x = \frac{|V|}{10^6}$ , where  $V$  is the set of nodes, as  $t = Ax^2 + Bx + C$ .

3513        The event-level GPU run time as a function of the event size measured in the number of  
 3514        space points (graph nodes) along its best-fit second-order polynomial is shown in figure 12.2a,  
 3515        and the fitted coefficients in table 12.2. The majority of events contain 250,000 to 425,000  
 3516        nodes, and their GPU time exhibits a well-defined scaling behaviour with respect to the  
 3517        number of space points in the event. The dependence on space point number of GPU time  
 3518        scales quadratically, with a small linear component. Events far from the distribution core  
 3519        are well-described by the fitted curve, and no significant outliers are observed. The scaling  
 3520        behaviour is significantly improved with each optimization technique. In comparison to that  
 3521        of eager execution, the execution time of the combined AMP and Compilation execution  
 3522        scales much slower with event size, which is approximately proportional to true pile-up.  
 3523        This is evident, given the second-order coefficient of obtained from the latter  $A_{AMP+Compile} =$   
 3524        0.457, being an order of magnitude smaller than former's corresponding coefficient  $A_{Eager} =$   
 3525        5.56. The execution time of the optimized code is thus not only small but also stays small  
 3526        over the typical range of pile-up.

3527        The latency reduction from these computational optimizations is also evident from both  
 3528        the mean and spread of the GPU time distribution observed in each scenario, demonstrated  
 3529        in figure 12.2b. In the combined optimization, the distribution averages to  $42 \pm 9$  ms, with  
 3530        a range of 103 ms, while in the eager baseline, the distribution centers at  $443 \pm 117$  ms, with

3531 a range of 1231 ms. The former only peaks at a lower latency, it is also much narrower  
 3532 than the latter. This weak scaling makes the computation less susceptible to large events  
 3533 outside the core distribution, as shown in figure 12.2a above  $|V| = 4.5 \times 10^5$ .

3534 **12.4 Pipeline computational performance**

3535 The average latency of each stage in the GNN4ITk algorithm is shown in table 12.3,  
 3536 along with the average total execution time. The edge classification stage is measured with  
 3537 combined AMP and AOT optimization in all three variants. Among the stages, graph  
 3538 segmentation is the slowest, contributing nearly 60% of the total run time, while graph  
 3539 construction and edge classification each account for 20%. The difference in latency can be  
 3540 attributed to the different hardware on which these stages take place. Graph construction  
 3541 in the Module Map method is carried out on the GPU, by means of a custom CUDA  
 3542 kernel that highly parallelizes many steps of the algorithm. Edge classification leverages a  
 3543 graph neural network whose building blocks (the feed-forward multi-layer perceptron) are  
 3544 natively suitable to run on the GPU, and further benefit from the optimizations detailed in  
 3545 section 12.2. As a result, both stages are optimized for and performed on the GPU, and  
 3546 are thus massively accelerated. In comparison, the Walkthrough algorithm used in graph  
 3547 segmentation, originally conceived as an *ad hoc* routine, contains many loops and logical  
 3548 IF-THEN statements (see section 10.2), and is thus difficult to parallelize. Although much  
 3549 effort has been put into optimizing the current implementation, a mechanism redesign that  
 3550 prioritizes parallelizability is necessary to accelerate it on the GPU and bring the entire  
 3551 GNN4ITk algorithm onto a single hardware architecture. As of writing, a CUDA-based  
 3552 version of the Walkthrough is under development, promising better latency in the future.

3553 Of the two graph construction approaches, Module Map is significantly faster than Metric  
 3554 Learning. The former is carried out by a custom CUDA-kernel which maximally parallelizes  
 3555 all steps of the graph creation on the GPU, most notably the MERGE/JOIN operations of data

Stage	Latency [ms/event]		
	MeanRMS	MinMax	Metric Learning
Graph construction	$41 \pm 10$	$41 \pm 11$	$932 \pm 92$
Edge classification	$42 \pm 9$	$53 \pm 12$	$47 \pm 10$
Graph segmentation	$120 \pm 93$	$120 \pm 93$	
Total	$203 \pm 94$		

**Table 12.3:** Per-event run time of each stage in the GNN4ITk algorithm. The latency of graph construction and edge classification is evaluated on an NVIDIA-A100 GPU with 80GB of memory, and of graph segmentation on the AMD EPYC 7763 CPU, using graphs constructed with the Module Map MeanRMS method.

frames, which consume considerable computation on the CPU but are greatly accelerated on the GPU [156]. On the other hand, the latter’s graph construction latency is the sum of the metric learning and filter steps, both of which, as of writing, have not been optimized. The metric learning step suffers from a lengthy kNN search in high a 12-dimensional space, and the filter step operates on large graphs of  $|V| \sim 6 \times 10^6$  edges. These shortcomings are however optimizable, and methods to address them are being investigated. In the edge classification step, both graph construction approaches demonstrate similar speed, ranging from 42 to 53 ms/event. Their difference in latency is evident from the average graph size, with  $|E|_{\text{MinMax}} > |E|_{\text{ML}} > |E|_{\text{MeanRMS}}$ , and correspondingly  $t_{\text{MinMax}} > t_{\text{ML}} > t_{\text{MeanRMS}}$ , where  $E$  is the edge set and  $t$  the latency. In the graph segmentation step, after fake edges are removed by a loose GNN score cut, the remaining graphs have similar edge set among the three variants, and their track building time is largely in accordance.

A comparison between the GNN- and the CKF-based track finders in terms of computing performance is unfortunately not straightforward. The two algorithms by design operates on different hardware, the CKF on CPUs and the GNN on GPUs. The lack of a common benchmark is the main challenge, which stems from differences in architecture, programming

models, and performance goals. For example, CPUs are optimized for low-latency execution of sequential tasks with a control flow, whereas GPUs for high-throughput executions of parallelized code. These factors complicate the establishment of a fair and standardized metrics across the computing platforms. CPU performance is usually measured by the latency per task, and GPU performance by FLoating-point Operations Per Second (FLOPS). Of course, one could naively compare the per-event latency of the two algorithms, and immediately runs into the question: ***which*** latency? As we have seen in the previous section, the GNN latency varies widely with different GPU platforms, and the most performant platform may not be the choice for production infrastructure, giving little significance to this comparison. Quoting the latency of the CKF on different CPUs suffers from the same problem.

Ultimately, the latency alone is insufficient to make a decision on the tracking technology in HL-HLC. It is not enough to answer the question “*How fast can we reconstruct tracks?*”, but **How much does it cost to reach a certain event/second throughput using each algorithm?** Therefore, a cost analysis taking into account all factors such as procurement, inherent throughput, latency, energy consumption, etc. is needed. It necessitates investigations much deeper than the scope of the scope of this thesis. For the moment, we refrain from making a direct comparison in computing performance between the two track finders.

## 12.5 Toward computational performance in production environment

The result in section 12.4 representing the current computational performance of the GNN4ITk algorithm, is obtained from inference in a development environment. Most of the source code is implemented in PYTHON, and deep-learning models are written with PYTORCH. The Module Map, though implemented in C++ and CUDA, is incorporated via

3597 a python-binding into the inference pipeline. The Walkthrough mechanism, though highly  
3598 optimized by Just-In-Time compiling many components in a manner similar to C++ using  
3599 NUMBA[128], is still implemented in PYTHON code. As a syntactically simple language rich  
3600 in well-supported libraries, PYTHON is suitable for research and development, but it is not  
3601 the language of choice for production systems, which prioritize computational performance.  
3602 In fact, the legacy analysis software and the future tracking toolkit employed by ATLAS are  
3603 both written in C++. Therefore, table 12.3 serves as the algorithm’s baseline latency, not  
3604 measurements in a realistic production environment. As compiled C++ code is typically  
3605 faster than the corresponding PYTHON code, we expect even better performance than so far  
3606 demonstrated.

3607 Further developments are needed to achieve competitive computing performance. The  
3608 entire pipeline must be implemented in C++ and ported to ATHENA[85], enabling measure-  
3609 ments and optimizations in production environment. All three stages of the Module Map  
3610 variant have been integrated into the ACTS framework [153], which will become the tracking  
3611 component of the ATLAS software. The graph construction stage of the Metric Learning  
3612 remains to be accelerated and integrated. The slowest component of this step is the k-  
3613 nearest-neighbor search which takes  $\approx 400$  ms/event, due to the rather large 12-dimensional  
3614 embedding space. A possible method is to reduce the embedding dimensions by encourag-  
3615 ing one or more dimensions to take a constant value using an extra loss term in training.  
3616 During inference, the kNN search can ignore these dimension in the distance calculation,  
3617 and therefore save time. The large number of edges, likely due to the current method being  
3618 sub-optimal, is also a huge bottleneck, requiring a filter step to eliminate easy fake edges.  
3619 As Metric Learning is a mature technique of machine learning, more sophisticated models  
3620 can better discriminate target hits from background, allowing to build smaller graphs and  
3621 possibly bypass the Filter step.

## 3622 Chapter 13

### 3623 Conclusion

3624 This thesis presents a combination of a wide range of searches targeting experimental sig-  
 3625 natures with and without a missing transverse momentum  $E_T^{\text{miss}}$  and an interpretation in the  
 3626 context of a Two-Higgs-Doublet Model extended by a pseudo-scalar mediator (2HDM+ $a$ )  
 3627 between the visible and dark sectors. The searches use up to  $139 \text{ fb}^{-1}$  of proton-proton  
 3628 collision data at a center-of-mass energy  $\sqrt{s} = 13 \text{ TeV}$  recorded by the ATLAS detector  
 3629 during LHC Run 2 between 2015 and 2018. The most sensitive analyses, including searches  
 3630 for large  $E_T^{\text{miss}}$  produced in association with a leptonically decaying  $Z$ -boson ( $E_T^{\text{miss}} + Z(\ell\ell)$ )  
 3631 and with a SM Higgs boson decaying to a pair of  $b$ -quarks ( $E_T^{\text{miss}} + h(b\bar{b})$ ), and a search for  
 3632 associated production of a top and a bottom quarks with a charged Higgs boson decaying to  
 3633 a top and a bottom quark ( $tbH^\pm(tb)$ ) are statistically combined, and constraints from other  
 3634 searches are overlaid in the summary. No significant deviations from SM predictions are  
 3635 observed, and 95% confidence-level upper limits on the 2HDM+ $a$  for a variety of benchmark  
 3636 scenarios, including those based on the recommendations of the LHC Dark Matter Working  
 3637 Group and several new ones exploring the model's rich phenomenology, are established.

3638 Large regions of the parameter space are excluded, thanks to the combined sensitivity  
 3639 of the  $E_T^{\text{miss}} + X$  and  $tbH^\pm(tb)$  signatures. The  $E_T^{\text{miss}} + Z(\ell\ell)$  and  $E_T^{\text{miss}} + h(b\bar{b})$  searches  
 3640 drive the sensitivity in at high heavy Higgs boson mass ( $m_A = m_H = m_{H^\pm}$ ), while the  
 3641  $tbH^\pm(tb)$  search is most sensitive at low  $m_A$  across the full mediator mass ( $m_a$ ) range. The  
 3642 latter also extends the exclusion region in  $\tan\beta$  across all  $m_a$ . The statistically combined

3643 result provides better sensitivity to the 2HDM+ $a$  than that derived from each individual  
 3644 search. This analysis represents an improvement over the summary based on  $36\text{ fb}^{-1}$  of data  
 3645 from LHC Run 1, by statistically combining the  $t\bar{H}^\pm(t\bar{b})$  channel which was previously not  
 3646 considered, by including new benchmark scenarios, and by incorporating a larger amount  
 3647 of data. Nevertheless, a large part of the parameter space remains unexcluded and awaits  
 3648 future analyses using larger datasets.

3649 In general, the sensitivity of searches for BSM signals, as well as precision measurements  
 3650 of SM processes is statistically constrained. The High Luminosity Large Hadron Collider  
 3651 (HL-LHC) promises an order of magnitude increase in collision data compared to that ac-  
 3652 quired over the three nominal LHC Runs, which would greatly benefits all physics programs  
 3653 at each of the general-purpose experiments. Nevertheless, reaching this goal requires consid-  
 3654 erable upgrades in event reconstruction. Charged-particle track reconstruction, in particular,  
 3655 faces numerous challenges from the increased expected pile-up multiplicity ( $\langle\mu\rangle$ ), for which  
 3656 a GPU-based new algorithm is a potential solution. We investigate an algorithm based on  
 3657 Graph Neural Networks (GNNs) for tracking under HL-LHC conditions. Using  $t\bar{t}$  collision  
 3658 event simulated simulated at  $\langle\mu\rangle = 200$  with realistic ITk layout, we optimized all stages  
 3659 of the algorithm, including graph construction, edge classification and graph segmentation.  
 3660 Compared to previous publications, this thesis demonstrates a comprehensive apple-to-apple  
 3661 comparison to the traditional technique in important tracking metrics, as well as measure-  
 3662 ments and optimizations of the computing performance.

3663 The efficiency on target particles in  $t\bar{t}$  samples of exceeds that of the Combinatorial  
 3664 Kalman Filter (CKF) at low transverse momentum  $p_T$ , and is competitive at high  $p_T$ . At  
 3665 the same time, the proportion of track candidates having the highest matching probability  
 3666 less than 50% is significantly reduced. Good impact parameter resolution is observed, but  
 3667 the momentum resolution has yet to reach the same level of CKF. The fastest configuration  
 3668 of the algorithm, in which the first two stages are carried out on the GPU and the last on  
 3669 the CPU, has a total run time of  $\approx 200$  ms/event.

Despite the impressive performance, future work is need to improve and demonstrated the algorithm. First, the object-level performance must be evaluated to understand potential impacts on the reconstruction and identification of various physics objects. For example, the efficiency and parameter resolution of tracks inside  $b$ -quark jets is an indicator of  $b$ -tagging performance, whereas samples containing single muons, electrons, and pions help isolate the performance when various levels of material interactions are involved, as we as track quality at fixed transverse momenta. Single-cluster hits should also be reintroduced into the track candidates constructed by the GNN-chain to improve momentum resolution. Second, all stages the algorithm must be implemented to run on the GPU and fully integrated into Athena via the ACTS framework. In particular, the graph segmentation which runs on the CPU and the metric learning technique based on costly kNN searches are identified as bottlenecks, which ongoing developments will address. Other incremental improvements, such as model size reduction and quantization, could shave away both inference time and memory consumption, enhancing algorithmic frugality and economic competitiveness.

3684

## APPENDIX

3685

### Definition of hit-level training variables

3686       Lorem ipsum dolor sit amet, consectetuer adipiscing elit. Ut purus elit, vestibulum ut,  
3687   placerat ac, adipiscing vitae, felis. Curabitur dictum gravida mauris. Nam arcu libero,  
3688   nonummy eget, consectetuer id, vulputate a, magna. Donec vehicula augue eu neque. Pel-  
3689   lentesque habitant morbi tristique senectus et netus et malesuada fames ac turpis egestas.  
3690   Mauris ut leo. Cras viverra metus rhoncus sem. Nulla et lectus vestibulum urna fringilla  
3691   ultrices. Phasellus eu tellus sit amet tortor gravida placerat. Integer sapien est, iaculis  
3692   in, pretium quis, viverra ac, nunc. Praesent eget sem vel leo ultrices bibendum. Aenean  
3693   faucibus. Morbi dolor nulla, malesuada eu, pulvinar at, mollis ac, nulla. Curabitur auctor  
3694   semper nulla. Donec varius orci eget risus. Duis nibh mi, congue eu, accumsan eleifend,  
3695   sagittis quis, diam. Duis eget orci sit amet orci dignissim rutrum.

## APPENDIX Track fit

3696

3697

3698     Track reconstruction identifies a track candidate as a digital realization of a particle  
 3699    trajectory in the detector. In many cases, a track candidate could simply be a set of detector  
 3700    measurements, which by itself does not provide any useful physical information about the  
 3701    trajectory. Only by fitting a track model through these measurements can we extract a set of  
 3702    track parameters that describe the momentum and impact parameters of the particle. This  
 3703    chapter describes elements of track fitting using the Least-Square Method and the Kalman  
 3704    Filter in ATLAS, laying the foundation for the discussion in subsequent chapters.

### 3705   A.1 Basic concepts

3706     Aside from the set of measurements, track fitting considers the following essential ele-  
 3707    ments

- 3708     • A description of the detector: This detector geometry must include the precise loca-  
 3709       tion, dimensions, and orientation of every sensor, allowing the estimation of the track  
 3710       state projected on the local coordinates of the sensor plane, as well as the intrinsic  
 3711       uncertainty associated with its measurements. In addition, a distribution of inactive  
 3712       materials must also be given, as they interact with the particle to accurately model  
 3713       deviations from an ideal trajectory caused by interactions with these mate-  
 3714       rials.

- 3715     • A track model describing the particle trajectory given the detector setup. For example,  
 3716       in a homogeneous magnetic field, an analytical solution to the equation of motion  
 3717       describing a helical orbit is obtained from the equation of motion which specifies the  
 3718       location of the particle at time  $t$  given the initial location  $\mathbf{r}_0$  and momentum  $\mathbf{p}_0$  at time  
 3719        $t_0$ . The magnetic field in ATLAS is far too complex for such an analytical solution to  
 3720       exist. In addition, interactions with detector material deviate the trajectory further  
 3721       from a perfect helix, and, as a result, the track model must be obtained from numerical  
 3722       integrations.

3723   A helical track is represented by a set of track parameters, denoted by

$$\mathbf{x} = \mathbf{x}(s) \quad (\text{A.1})$$

3724   The choice of parametrization varies from one experiment to another. In ATLAS, tracks are  
 3725   parametrized by 5 parameters

$$\mathbf{x} = (\theta, \phi, p, d_0, z_0) \quad (\text{A.2})$$

3726   in which  $(\theta, \phi, p)$  represents the momentum in spherical coordinates, and  $(d_0, z_0)$  respectively  
 3727   specifies the longitudinal and polar impact parameters. The track state can evolve non-  
 3728   trivially as the particle interacts with detector materials on its flight path, which is why it  
 3729   is written as a function of a free parameter  $s$  denoting, in our case, the arc length. When

3730   In general, track parameters are not directly measurable. Instead, only their projection on  
 3731   the surface of discrete sensor elements are experimentally available. At the  $i$ -th intersection  
 3732   of the track with a detector module, we denote the track state as  $\mathbf{x}_i$ , the corresponding  
 3733   measurement vector as  $\mathbf{m}_i \in \mathbb{R}^d$ , and assume a measurement mapping function  $h_i : \mathbb{R}^5 \rightarrow \mathbb{R}^n$ .  
 3734   This mapping depends on the sensor device encounter at  $i$ , e.g. a pixel module makes  
 3735   a measurement different from that of a strip module, and thus corresponds to a different  
 3736   mapping function. The  $i$ -th measurement vector is given by

$$\mathbf{m}_i = h_i(\mathbf{x}_i) + \mathbf{e}_i \quad (\text{A.3})$$

3737 Just like any measured quantity,  $\mathbf{m}_i$  is a random variable, assumed to be the sum of the  
3738 deterministic projection  $h_i(\mathbf{x}_i)$  and a noise model  $\mathbf{e}_i$  describing the intrinsic uncertainty of  
3739 the detector.

3740 With these definitions, track fitting is reduced to finding a transformation  $F : \mathbb{R}^d \rightarrow \mathbb{R}^5$   
3741 that maps the measurements  $\{\mathbf{m}\}$  back to the track parameters, such that the estimated  
3742 track state is unbiased and has minimum variance

$$\hat{\mathbf{x}} = F(\mathbf{m}), \quad E[\hat{\mathbf{x}}] = \mathbf{x}, \quad \mathbf{V}(\hat{\mathbf{x}}_i) = \min_F E[(\hat{\mathbf{x}} - \mathbf{x})^2] \quad (\text{A.4})$$

3743 The linear least square method makes, in addition to the non-bias and minimum variance  
3744 requirements, an assumption that the measurement model is a linear function of the track  
3745 parameters, namely

$$\mathbf{m} = \mathbf{Hx} + \mathbf{e}. \quad (\text{A.5})$$

3746 Assuming an inverse transform exists, we make an ansatz that it is also linear

$$\hat{\mathbf{x}} = F(\mathbf{m}) = \mathbf{Fm} = \mathbf{F}(\mathbf{Hx} + \mathbf{e}) = \mathbf{FHx} + \mathbf{Fe} \quad (\text{A.6})$$

3747 It is worth noting that this assumption only holds for a careful choice of parametrization. In  
3748 ATLAS, the track parameters and measurement model are selected such that a linear model  
3749 always applies. From the requirement that the estimate be unbiased, we have

$$E[\hat{\mathbf{x}}] = \mathbf{FHx} + \mathbf{FE}[\mathbf{e}] = \mathbf{FHx} = \mathbf{x} \Rightarrow \mathbf{FH} = \mathbf{I} \quad (\text{A.7})$$

3750 The sum of variance of  $\hat{\mathbf{x}}$  can be written as the trace of the covariance matrix

$$\begin{aligned} \mathbf{V}(\hat{\mathbf{x}}) &= \text{Tr}[E[(\hat{\mathbf{x}} - \mathbf{x})(\hat{\mathbf{x}} - \mathbf{x})^T]] \\ &= \text{Tr}[E[((\mathbf{FH} - \mathbf{I})\mathbf{x} + \mathbf{Fe})((\mathbf{FH} - \mathbf{I})\mathbf{x} + \mathbf{Fe})^T]] \\ &= \text{Tr}[\mathbf{FE}[\mathbf{ee}^T]\mathbf{F}^T] \end{aligned} \quad (\text{A.8})$$

3751 in which we have substituted equation A.6. The minimum variance principle thus states that  
3752 the transformation  $\mathbf{F}$  is one that minimizes the right-hand side of equation A.8 subjected to

<sup>3753</sup> the constraint of equation in A.7. The cost function to be minimized can be written using a  
<sup>3754</sup> Lagrange multiplier

$$J = \frac{1}{2} \text{Tr}[\mathbf{F}\mathbf{R}\mathbf{F}^T] + \text{Tr}[(\Lambda(\mathbf{F}\mathbf{H} - \mathbf{I}))], \quad \mathbf{R} = E[\mathbf{e}\mathbf{e}^T]. \quad (\text{A.9})$$

<sup>3755</sup> Differentiating with respect to  $\mathbf{F}$  and to  $\Lambda$  and setting to 0, we get

$$\frac{\partial J}{\partial \mathbf{F}} = \frac{1}{2}\mathbf{F}(\mathbf{R} + \mathbf{R}^T) + \Lambda^T \mathbf{H}^T = \mathbf{F}\mathbf{R} + \Lambda^T \mathbf{H}^T = 0 \Rightarrow \mathbf{F} = -\Lambda^T \mathbf{H}^T \mathbf{R}^{-1} \quad (\text{A.10})$$

<sup>3756</sup> Solving for  $\Lambda$  from the constraint,

$$\mathbf{F}\mathbf{H} = -\Lambda^T \mathbf{H}^T \mathbf{R}^{-1} \mathbf{H} = \mathbf{I} \Rightarrow -\Lambda^T = (\mathbf{H}^T \mathbf{R}^{-1} \mathbf{H})^{-1}, \quad (\text{A.11})$$

<sup>3757</sup> and substituting into equation A.10, we get the inverse transform

$$\boxed{\mathbf{F} = (\mathbf{H}^T \mathbf{R}^{-1} \mathbf{H})^{-1} \mathbf{H}^T \mathbf{R}^{-1}}, \quad (\text{A.12})$$

<sup>3758</sup> and covariance of the residual

$$\mathbf{P} = E[(\hat{\mathbf{x}} - \mathbf{x})(\hat{\mathbf{x}} - \mathbf{x})^T] = \mathbf{F}\mathbf{R}\mathbf{F}^T = (\mathbf{H}^T \mathbf{R}^{-1} \mathbf{H})^{-1} \mathbf{H}^T ((\mathbf{H}^T \mathbf{R}^{-1} \mathbf{H})^{-1} \mathbf{H}^T \mathbf{R}^{-1})^T. \quad (\text{A.13})$$

<sup>3759</sup> A similar result can be gotten by considering the experimental estimate of the covariance  
<sup>3760</sup>  $\mathbf{e}\mathbf{e}^T$

$$\text{Tr}[\overline{\mathbf{e}\mathbf{e}^T}] = \frac{1}{n} \sum_{i=1}^n (\mathbf{m}_i - \mathbf{H}\mathbf{x}_i)^T \mathbf{R}_i^{-1} (\mathbf{m}_i - \mathbf{H}\mathbf{x}_i) = \quad (\text{A.14})$$

## APPENDIX Bibliography

- [1] Tomohiro Abe et al.,  
*LHC Dark Matter Working Group: Next-generation spin-0 dark matter models*,  
Phys. Dark Univ. **27** (2020) 100351, arXiv: 1810.09420 [hep-ex]  
(cit. on pp. 28, 43, 46–48, 51, 85, 101).
- [2] Daniel Abercrombie et al., *Dark Matter benchmark models for early LHC Run-2 Searches: Report of the ATLAS/CMS Dark Matter Forum*,  
Phys. Dark Univ. **27** (2020) 100371, ed. by Antonio Boveia, Caterina Doglioni,  
Steven Lowette, Sarah Malik, and Stephen Mrenna, arXiv: 1507.00966 [hep-ex]  
(cit. on p. 40).
- [3] O. Aberle et al.,  
*High-Luminosity Large Hadron Collider (HL-LHC): Technical design report*,  
CERN Yellow Reports: Monographs, Geneva: CERN, 2020,  
URL: <https://cds.cern.ch/record/2749422> (cit. on p. 16).
- [4] Danyer Perez Adan, *Dark Matter searches at CMS and ATLAS*, 2023,  
arXiv: 2301.10141 [hep-ex], URL: <https://arxiv.org/abs/2301.10141>  
(cit. on p. 15).
- [5] Abien Fred Agarap, *Deep Learning using Rectified Linear Units (ReLU)*, 2019,  
arXiv: 1803.08375 [cs.NE], URL: <https://arxiv.org/abs/1803.08375>  
(cit. on p. 155).

- 3782 [6] S. Agostinelli et al., GEANT4 – *a simulation toolkit*,  
 3783 Nucl. Instrum. Meth. A **506** (2003) 250 (cit. on pp. 51, 99).
- 3784 [7] P F Åkesson et al., *ATLAS Tracking Event Data Model*, tech. rep.,  
 3785 All figures including auxiliary figures are available at  
 3786 <https://atlas.web.cern.ch/Atlas/GROUPS/PHYSICS/PUBNOTES/ATL-SOFT-PUB-2006-004>: CERN, 2006, URL: <https://cds.cern.ch/record/973401>  
 3787 (cit. on p. 181).
- 3788 [8] Simone Alioli, Paolo Nason, Carlo Oleari, and Emanuele Re,  
 3789 *A general framework for implementing NLO calculations in shower Monte Carlo*  
 3790 *programs: the POWHEG BOX*, JHEP **06** (2010) 043, arXiv: 1002.2581 [hep-ph]  
 3791 (cit. on p. 113).
- 3792 [9] J. Alwall et al., *The automated computation of tree-level and next-to-leading order*  
 3793 *differential cross sections, and their matching to parton shower simulations*,  
 3794 JHEP **07** (2014) 079, arXiv: 1405.0301 [hep-ph] (cit. on p. 49).
- 3795 [10] Federico Ambrogi et al.,  
 3796 *MadDM v.3.0: a Comprehensive Tool for Dark Matter Studies*,  
 3797 Phys. Dark Univ. **24** (2019) 100249, arXiv: 1804.00044 [hep-ph]  
 3798 (cit. on pp. 86, 88).
- 3799 [11] Anaderi et al., *TrackML Particle Tracking Challenge*,  
 3800 <https://kaggle.com/competitions/trackml-particle-identification>,  
 3801 Kaggle, 2018 (cit. on pp. 129, 158).
- 3802 [12] Spyros Argyropoulos and Ulrich Haisch,  
 3803 *Benchmarking LHC searches for light 2HDM+a pseudoscalars*,  
 3804 SciPost Phys. **13** (2022) 007, arXiv: 2202.12631 [hep-ph] (cit. on pp. 47, 48).
- 3805 [13] ATLAS Collaboration, *ATLAS b-jet identification performance and efficiency*  
 3806 *measurement with  $t\bar{t}$  events in  $pp$  collisions at  $\sqrt{s} = 13 \text{ TeV}$* ,  
 3807 Eur. Phys. J. C **79** (2019) 970, arXiv: 1907.05120 [hep-ex] (cit. on p. 52).

- 3809 [14] ATLAS Collaboration,  
 3810 *ATLAS data quality operations and performance for 2015–2018 data-taking*,  
 3811 JINST **15** (2020) P04003, arXiv: 1911.04632 [physics.ins-det] (cit. on p. 48).
- 3812 [15] ATLAS Collaboration,  
 3813 *ATLAS flavour-tagging algorithms for the LHC Run 2 pp collision dataset*, (2022),  
 3814 arXiv: 2211.16345 [physics.data-an] (cit. on p. 52).
- 3815 [16] ATLAS Collaboration, *ATLAS Inner Detector: Technical Design Report, Volume 1*,  
 3816 ATLAS-TDR-4; CERN-LHCC-97-016, 1997,  
 3817 URL: <https://cds.cern.ch/record/331063> (cit. on p. 34).
- 3818 [17] ATLAS Collaboration, *ATLAS Inner Detector: Technical Design Report, Volume 2*,  
 3819 ATLAS-TDR-5, CERN-LHCC-97-017, 1997,  
 3820 URL: <https://cds.cern.ch/record/331064> (cit. on p. 34).
- 3821 [18] ATLAS Collaboration,  
 3822 *ATLAS Inner Tracker Pixel Detector: Technical Design Report*,  
 3823 ATLAS-TDR-030; CERN-LHCC-2017-021, 2017,  
 3824 URL: <https://cds.cern.ch/record/2285585> (cit. on pp. 96, 102, 103).
- 3825 [19] ATLAS Collaboration,  
 3826 *ATLAS Inner Tracker Strip Detector: Technical Design Report*,  
 3827 ATLAS-TDR-025; CERN-LHCC-2017-005, 2017,  
 3828 URL: <https://cds.cern.ch/record/2257755> (cit. on pp. 96, 99, 100, 111).
- 3829 [20] ATLAS Collaboration, *ATLAS Muon Spectrometer: Technical Design Report*,  
 3830 ATLAS-TDR-10; CERN-LHCC-97-022, CERN, 1997,  
 3831 URL: <https://cds.cern.ch/record/331068> (cit. on p. 39).
- 3832 [21] ATLAS Collaboration, *ATLAS Pythia 8 tunes to 7 TeV data*,  
 3833 ATL-PHYS-PUB-2014-021, 2014, URL: <https://cds.cern.ch/record/1966419>  
 3834 (cit. on pp. 50, 113).

- 3835 [22] ATLAS Collaboration,  
 3836 *Combination of searches for invisible decays of the Higgs boson using 139 fb<sup>-1</sup> of*  
 3837 *proton-proton collision data at  $\sqrt{s} = 13$  TeV collected with the ATLAS experiment,*  
 3838 (2023), arXiv: 2301.10731 [hep-ex] (cit. on pp. 53, 64).
- 3839 [23] ATLAS Collaboration, *Constraints on mediator-based dark matter and scalar dark*  
 3840 *energy models using  $\sqrt{s} = 13$  TeV pp collision data collected by the ATLAS detector,*  
 3841 JHEP **05** (2019) 142, arXiv: 1903.01400 [hep-ex]  
 3842 (cit. on pp. 47, 48, 79, 82, 84, 85).
- 3843 [24] ATLAS Collaboration, *Constraints on new phenomena via Higgs boson couplings*  
 3844 *and invisible decays with the ATLAS detector*, JHEP **11** (2015) 206,  
 3845 arXiv: 1509.00672 [hep-ex] (cit. on p. 64).
- 3846 [25] ATLAS Collaboration, *Constraints on spin-0 dark matter mediators and invisible*  
 3847 *Higgs decays using ATLAS 13 TeV pp collision data with two top quarks and missing*  
 3848 *transverse momentum in the final state*, (2022), arXiv: 2211.05426 [hep-ex]  
 3849 (cit. on p. 64).
- 3850 [26] ATLAS Collaboration, *Electron and photon performance measurements with the*  
 3851 *ATLAS detector using the 2015–2017 LHC proton–proton collision data*,  
 3852 JINST **14** (2019) P12006, arXiv: 1908.00005 [hep-ex] (cit. on p. 52).
- 3853 [27] ATLAS Collaboration, *Electron and photon reconstruction and performance in*  
 3854 *ATLAS using a dynamical, topological cell clustering-based approach*,  
 3855 ATL-PHYS-PUB-2017-022, 2017, URL: <https://cds.cern.ch/record/2298955>  
 3856 (cit. on p. 52).
- 3857 [28] ATLAS Collaboration, *Fast Track Reconstruction for HL-LHC*,  
 3858 ATL-PHYS-PUB-2019-041, 2019, URL: <https://cds.cern.ch/record/2693670>  
 3859 (cit. on pp. 127, 128).

- 3860 [29] ATLAS Collaboration,  
 3861 *Improvements in  $t\bar{t}$  modelling using NLO+PS Monte Carlo generators for Run 2,*  
 3862 ATL-PHYS-PUB-2018-009, 2018, URL: <https://cds.cern.ch/record/2630327>  
 3863 (cit. on p. 67).
- 3864 [30] ATLAS Collaboration, *Jet energy scale and resolution measured in proton–proton*  
 3865 *collisions at  $\sqrt{s} = 13$  TeV with the ATLAS detector*, Eur. Phys. J. C **81** (2020) 689,  
 3866 arXiv: 2007.02645 [hep-ex] (cit. on p. 52).
- 3867 [31] ATLAS Collaboration,  
 3868 *Jet reconstruction and performance using particle flow with the ATLAS Detector*,  
 3869 Eur. Phys. J. C **77** (2017) 466, arXiv: 1703.10485 [hep-ex] (cit. on p. 52).
- 3870 [32] ATLAS Collaboration, *Local Hadronic Calibration*, ATL-LARG-PUB-2009-001-2,  
 3871 ATL-COM-LARG-2008-006, ATL-LARG-PUB-2009-001, 2008,  
 3872 URL: <https://cds.cern.ch/record/1112035> (cit. on p. 53).
- 3873 [33] ATLAS Collaboration, *Luminosity determination in  $pp$  collisions at  $\sqrt{s} = 13$  TeV*  
 3874 *using the ATLAS detector at the LHC*, ATLAS-CONF-2019-021, 2019,  
 3875 URL: <https://cds.cern.ch/record/2677054> (cit. on p. 70).
- 3876 [34] ATLAS Collaboration,  
 3877 *Measurement of the tau lepton reconstruction and identification performance in the*  
 3878 *ATLAS experiment using  $pp$  collisions at  $\sqrt{s} = 13$  TeV*, ATLAS-CONF-2017-029,  
 3879 2017, URL: <https://cds.cern.ch/record/2261772> (cit. on p. 53).
- 3880 [35] ATLAS Collaboration,  
 3881 *Measurements of top-quark pair single- and double-differential cross-sections in the*  
 3882 *all-hadronic channel in  $pp$  collisions at  $\sqrt{s} = 13$  TeV using the ATLAS detector*,  
 3883 JHEP **01** (2021) 033, arXiv: 2006.09274 [hep-ex] (cit. on p. 67).
- 3884 [36] ATLAS Collaboration, *Muon reconstruction performance of the ATLAS detector in*  
 3885 *proton–proton collision data at  $\sqrt{s} = 13$  TeV*, Eur. Phys. J. C **76** (2016) 292,  
 3886 arXiv: 1603.05598 [hep-ex] (cit. on p. 52).

- 3887 [37] ATLAS Collaboration,  
 3888 *Object-based missing transverse momentum significance in the ATLAS Detector,*  
 3889 ATLAS-CONF-2018-038, 2018, URL: <https://cds.cern.ch/record/2630948>  
 3890 (cit. on p. 55).
- 3891 [38] ATLAS Collaboration,  
 3892 *Observation of electroweak production of two jets in association with an isolated*  
 3893 *photon and missing transverse momentum, and search for a Higgs boson decaying*  
 3894 *into invisible particles at 13 TeV with the ATLAS detector,*  
 3895 Eur. Phys. J. C **82** (2021) 105, arXiv: 2109.00925 [hep-ex] (cit. on p. 64).
- 3896 [39] ATLAS Collaboration, *Performance of missing transverse momentum reconstruction*  
 3897 *with the ATLAS detector using proton–proton collisions at  $\sqrt{s} = 13 \text{ TeV}$ ,*  
 3898 Eur. Phys. J. C **78** (2018) 903, arXiv: 1802.08168 [hep-ex] (cit. on p. 53).
- 3899 [40] ATLAS Collaboration,  
 3900 *Reconstruction, Energy Calibration, and Identification of Hadronically Decaying Tau*  
 3901 *Leptons in the ATLAS Experiment for Run-2 of the LHC,*  
 3902 ATL-PHYS-PUB-2015-045, 2015, URL: <https://cds.cern.ch/record/2064383>  
 3903 (cit. on p. 53).
- 3904 [41] ATLAS Collaboration, *Search for  $t\bar{t}H/A \rightarrow t\bar{t}t\bar{t}$  production in the multilepton final*  
 3905 *state in proton–proton collisions at  $\sqrt{s} = 13 \text{ TeV}$  with the ATLAS detector,* (2022),  
 3906 arXiv: 2211.01136 [hep-ex] (cit. on pp. 53, 67).
- 3907 [42] ATLAS Collaboration,  
 3908 *Search for associated production of a Z boson with an invisibly decaying Higgs boson*  
 3909 *or dark matter candidates at  $\sqrt{s} = 13 \text{ TeV}$  with the ATLAS detector,*  
 3910 Phys. Lett. B **829** (2021) 137066, arXiv: 2111.08372 [hep-ex]  
 3911 (cit. on pp. 16, 53, 54, 64).

- 3912 [43] ATLAS Collaboration, *Search for charged Higgs bosons decaying into a top quark*  
 3913 *and a bottom quark at  $\sqrt{s} = 13 \text{ TeV}$  with the ATLAS detector*, JHEP **06** (2021) 145,  
 3914 arXiv: 2102.10076 [hep-ex] (cit. on pp. 16, 53, 66).
- 3915 [44] ATLAS Collaboration, *Search for dark matter in events with a hadronically decaying*  
 3916 *vector boson and missing transverse momentum in pp collisions at  $\sqrt{s} = 13 \text{ TeV}$*   
 3917 *with the ATLAS detector*, JHEP **10** (2018) 180, arXiv: 1807.11471 [hep-ex]  
 3918 (cit. on pp. 53, 65).
- 3919 [45] ATLAS Collaboration, *Search for dark matter in events with missing transverse*  
 3920 *momentum and a Higgs boson decaying into two photons in pp collisions at*  
 3921  *$\sqrt{s} = 13 \text{ TeV}$  with the ATLAS detector*, JHEP **10** (2021) 013,  
 3922 arXiv: 2104.13240 [hep-ex] (cit. on pp. 53, 59).
- 3923 [46] ATLAS Collaboration, *Search for dark matter produced in association with a Higgs*  
 3924 *boson decaying to tau leptons at  $\sqrt{s} = 13 \text{ TeV}$  with the ATLAS detector*, (2023),  
 3925 arXiv: 2305.12938 [hep-ex] (cit. on pp. 53, 60, 62).
- 3926 [47] ATLAS Collaboration,  
 3927 *Search for dark matter produced in association with a single top quark and an*  
 3928 *energetic W boson in  $\sqrt{s} = 13 \text{ TeV}$  pp collisions with the ATLAS detector*, (2022),  
 3929 arXiv: 2211.13138 [hep-ex] (cit. on pp. 53, 61).
- 3930 [48] ATLAS Collaboration, *Search for dark matter produced in association with a single*  
 3931 *top quark in  $\sqrt{s} = 13 \text{ TeV}$  pp collisions with the ATLAS detector*,  
 3932 Eur. Phys. J. C **81** (2020) 860, arXiv: 2011.09308 [hep-ex] (cit. on pp. 61, 78, 80).
- 3933 [49] ATLAS Collaboration,  
 3934 *Search for dark matter produced in association with a Standard Model Higgs boson*  
 3935 *decaying into b-quarks using the full Run 2 dataset from the ATLAS detector*,  
 3936 JHEP **11** (2021) 209, arXiv: 2108.13391 [hep-ex] (cit. on pp. 16, 53, 56, 58).

- 3937 [50] ATLAS Collaboration, *Search for dark matter produced in association with bottom*  
 3938 *or top quarks in  $\sqrt{s} = 13 \text{ TeV}$  pp collisions with the ATLAS detector,*  
 3939 Eur. Phys. J. C **78** (2018) 18, arXiv: 1710.11412 [hep-ex] (cit. on pp. 53, 65, 66).
- 3940 [51] ATLAS Collaboration,  
 3941 *Search for Higgs boson decays into a pair of pseudoscalar particles in the  $b\bar{b}\mu\bar{\mu}$  final*  
 3942 *state with the ATLAS detector in pp collisions at  $\sqrt{s} = 13 \text{ TeV}$ ,*  
 3943 Phys. Rev. D **105** (2021) 012006, arXiv: 2110.00313 [hep-ex] (cit. on pp. 53, 69).
- 3944 [52] ATLAS Collaboration, *Search for Higgs boson decays to beyond-the-Standard-Model*  
 3945 *light bosons in four-lepton events with the ATLAS detector at  $\sqrt{s} = 13 \text{ TeV}$ ,*  
 3946 JHEP **06** (2018) 166, arXiv: 1802.03388 [hep-ex] (cit. on pp. 53, 69).
- 3947 [53] ATLAS Collaboration, *Search for Higgs bosons decaying into new spin-0 or spin-1*  
 3948 *particles in four-lepton final states with the ATLAS detector with  $139 \text{ fb}^{-1}$  of pp*  
 3949 *collision data at  $\sqrt{s} = 13 \text{ TeV}$* , JHEP **03** (2021) 041, arXiv: 2110.13673 [hep-ex]  
 3950 (cit. on pp. 53, 69).
- 3951 [54] ATLAS Collaboration, *Search for Higgs bosons decaying to aa in the  $\mu\mu\tau\tau$  final*  
 3952 *state in pp collisions at  $\sqrt{s} = 8 \text{ TeV}$  with the ATLAS experiment,*  
 3953 Phys. Rev. D **92** (2015) 052002, arXiv: 1505.01609 [hep-ex]  
 3954 (cit. on pp. 53, 69, 87).
- 3955 [55] ATLAS Collaboration,  
 3956 *Search for invisible Higgs-boson decays in events with vector-boson fusion signatures*  
 3957 *using  $139 \text{ fb}^{-1}$  of proton–proton data recorded by the ATLAS experiment,*  
 3958 JHEP **08** (2022) 104, arXiv: 2202.07953 [hep-ex] (cit. on p. 64).
- 3959 [56] ATLAS Collaboration,  
 3960 *Search for new phenomena in events with an energetic jet and missing transverse*  
 3961 *momentum in pp collisions at  $\sqrt{s} = 13 \text{ TeV}$  with the ATLAS detector,*  
 3962 Phys. Rev. D **103** (2021) 112006, arXiv: 2102.10874 [hep-ex]  
 3963 (cit. on pp. 53, 63, 64).

- 3964 [57] ATLAS Collaboration, *Search for the Higgs boson produced in association with a*  
 3965 *vector boson and decaying into two spin-zero particles in the  $H \rightarrow aa \rightarrow 4b$  channel*  
 3966 *in  $pp$  collisions at  $\sqrt{s} = 13$  TeV with the ATLAS detector*, JHEP **10** (2018) 031,  
 3967 arXiv: 1806.07355 [hep-ex] (cit. on pp. 53, 69).
- 3968 [58] ATLAS Collaboration, *Search for top-squark pair production in final states with one*  
 3969 *lepton, jets, and missing transverse momentum using  $36\text{ fb}^{-1}$  of  $\sqrt{s} = 13$  TeV  $pp$*   
 3970 *collision data with the ATLAS detector*, JHEP **06** (2018) 108,  
 3971 arXiv: 1711.11520 [hep-ex] (cit. on pp. 53, 66).
- 3972 [59] ATLAS Collaboration, *Studies on top-quark Monte Carlo modelling for Top2016*,  
 3973 ATL-PHYS-PUB-2016-020, 2016, URL: <https://cds.cern.ch/record/2216168>  
 3974 (cit. on p. 113).
- 3975 [60] ATLAS Collaboration, *Summary of ATLAS Pythia 8 tunes*,  
 3976 ATL-PHYS-PUB-2012-003, 2012, URL: <https://cds.cern.ch/record/1474107>  
 3977 (cit. on p. 51).
- 3978 [61] ATLAS Collaboration, *The ATLAS Simulation Infrastructure*,  
 3979 Eur. Phys. J. C **70** (2010) 823, arXiv: 1005.4568 [physics.ins-det]  
 3980 (cit. on p. 51).
- 3981 [62] ATLAS Collaboration, *The ATLAS Tau Trigger in Run 2*, ATLAS-CONF-2017-061,  
 3982 2017, URL: <https://cds.cern.ch/record/2274201> (cit. on p. 60).
- 3983 [63] ATLAS Collaboration, *The simulation principle and performance of the ATLAS fast*  
 3984 *calorimeter simulation FastCaloSim*, ATL-PHYS-PUB-2010-013, 2010,  
 3985 URL: <https://cds.cern.ch/record/1300517> (cit. on p. 51).
- 3986 [64] E. A. Bagnaschi et al., *Supersymmetric dark matter after LHC Run 1*,  
 3987 Eur. Phys. J. C **75** (2015) 500, arXiv: 1508.01173 [hep-ph] (cit. on p. 85).
- 3988 [65] Pierre Baldi, Kyle Cranmer, Taylor Faucett, Peter Sadowski, and Daniel Whiteson,  
 3989 *Parameterized neural networks for high-energy physics*,  
 3990 Eur. Phys. J. C **76** (2016) 235, arXiv: 1601.07913 [hep-ex] (cit. on p. 68).

- 3991 [66] Gaetano Barone, *ATLAS silicon microstrip tracker operation and performance*,  
 3992 Nuclear Instruments and Methods in Physics Research Section A: Accelerators,  
 3993 Spectrometers, Detectors and Associated Equipment **732** (2013) 57, Vienna  
 3994 Conference on Instrumentation 2013, ISSN: 0168-9002, URL:  
 3995 <https://www.sciencedirect.com/science/article/pii/S0168900213007171>  
 3996 (cit. on p. 34).
- 3997 [67] Peter W. Battaglia, Razvan Pascanu, Matthew Lai, Danilo Rezende, and  
 3998 Koray Kavukcuoglu,  
 3999 *Interaction Networks for Learning about Objects, Relations and Physics*, 2016,  
 4000 arXiv: 1612.00222 [cs.AI], URL: <https://arxiv.org/abs/1612.00222>  
 4001 (cit. on pp. 158, 160, 161).
- 4002 [68] Martin Bauer, Ulrich Haisch, and Felix Kahlhoefer,  
 4003 *Simplified dark matter models with two Higgs doublets: I. Pseudoscalar mediators*,  
 4004 JHEP **05** (2017) 138, arXiv: 1701.07427 [hep-ph]  
 4005 (cit. on pp. 43, 44, 46, 47, 50, 78, 82).
- 4006 [69] K. G. Begeman, A. H. Broeils, and R. H. Sanders,  
 4007 *Extended rotation curves of spiral galaxies: Dark haloes and modified dynamics*,  
 4008 MNRAS **249** (1991) 523 (cit. on p. 15).
- 4009 [70] G. Bertone, D. Hooper, and J. Silk,  
 4010 *Particle dark matter: evidence, candidates and constraints*,  
 4011 Phys. Rept. **405** (2005) 279 (cit. on p. 15).
- 4012 [71] H. A. Bethe, *Molière's Theory of Multiple Scattering*, Phys. Rev. **89** (6 1953) 1256,  
 4013 URL: <https://link.aps.org/doi/10.1103/PhysRev.89.1256> (cit. on p. 110).
- 4014 [72] Pierre Billoir, *Track fitting with multiple scattering: A new method*,  
 4015 Nuclear Instruments and Methods in Physics Research **225** (1984) 352,  
 4016 ISSN: 0167-5087, URL:

- 4017            <https://www.sciencedirect.com/science/article/pii/0167508784902746>  
 4018            (cit. on p. 122).
- 4019 [73] L. Blanquart et al., *FE-I2: a front-end readout chip designed in a commercial*  
 4020            *0.25-/spl mu/m process for the ATLAS pixel detector at LHC*,  
 4021            IEEE Transactions on Nuclear Science **51** (2004) 1358 (cit. on p. 33).
- 4022 [74] G.C. Branco et al., *Theory and phenomenology of two-Higgs-doublet models*,  
 4023            Physics Reports **516** (2012) 1, ISSN: 0370-1573,  
 4024            URL: <http://dx.doi.org/10.1016/j.physrep.2012.02.002> (cit. on p. 28).
- 4025 [75] Matthew R. Buckley, David Feld, and Dorival Goncalves,  
 4026            *Scalar Simplified Models for Dark Matter*, Phys. Rev. D **91** (2015) 015017,  
 4027            arXiv: 1410.6497 [hep-ph] (cit. on p. 40).
- 4028 [76] Jared Dynes Burleson et al.,  
 4029            *Physics Performance of the ATLAS GNN4ITk Track Reconstruction Chain*,  
 4030            tech. rep., CERN, 2023, URL: <https://cds.cern.ch/record/2882507>  
 4031            (cit. on p. 208).
- 4032 [77] Jon Butterworth et al., *PDF4LHC recommendations for LHC Run II*,  
 4033            J. Phys. G **43** (2016) 023001, arXiv: 1510.03865 [hep-ph] (cit. on p. 70).
- 4034 [78] Matteo Cacciari, Gavin P. Salam, and Gregory Soyez, *FastJet user manual*,  
 4035            Eur. Phys. J. C **72** (2012) 1896, arXiv: 1111.6097 [hep-ph] (cit. on p. 52).
- 4036 [79] Matteo Cacciari, Gavin P. Salam, and Gregory Soyez,  
 4037            *The anti-kt jet clustering algorithm*, JHEP **04** (2008) 063,  
 4038            arXiv: 0802.1189 [hep-ph] (cit. on p. 52).
- 4039 [80] Sylvain Caillou et al., *ATLAS ITk Track Reconstruction with a GNN-based pipeline*,  
 4040            tech. rep., CERN, 2022, URL: <https://cds.cern.ch/record/2815578>  
 4041            (cit. on p. 129).

- 4042 [81] Caillou, Sylvain et al.,  
 4043 *Physics Performance of the ATLAS GNN4ITk Track Reconstruction Chain*,  
 4044 EPJ Web of Conf. **295** (2024) 03030,  
 4045 URL: <https://doi.org/10.1051/epjconf/202429503030> (cit. on pp. 163, 208).
- 4046 [82] Nicholas Choma et al.,  
 4047 *Track Seeding and Labelling with Embedded-space Graph Neural Networks*, 2020,  
 4048 arXiv: 2007.00149 [physics.ins-det],  
 4049 URL: <https://arxiv.org/abs/2007.00149> (cit. on p. 129).
- 4050 [83] James M. Cline, Kimmo Kainulainen, and Axel P. Vischer, *Dynamics of*  
 4051 *two-Higgs-doublet violation and baryogenesis at the electroweak phase transition*,  
 4052 Physical Review D **54** (1996) 2451, ISSN: 1089-4918,  
 4053 URL: <http://dx.doi.org/10.1103/PhysRevD.54.2451> (cit. on p. 28).
- 4054 [84] James M. Cline and Pierre-Anthony Lemieux,  
 4055 *Electroweak phase transition in two Higgs doublet models*,  
 4056 Phys. Rev. D **55** (6 1997) 3873,  
 4057 URL: <https://link.aps.org/doi/10.1103/PhysRevD.55.3873> (cit. on p. 28).
- 4058 [85] ATLAS Collaboration, *Athena*, version 21.0.127, 2021,  
 4059 URL: <https://doi.org/10.5281/zenodo.4772550> (cit. on pp. 130, 165, 186, 220).
- 4060 [86] The ATLAS Collaboration, *ATLAS HL-LHC Computing Conceptual Design Report*,  
 4061 tech. rep., CERN, 2020, URL: <https://cds.cern.ch/record/2729668>  
 4062 (cit. on p. 126).
- 4063 [87] The ATLAS Collaboration, *ATLAS pixel detector electronics and sensors*,  
 4064 Journal of Instrumentation **3** (2008) P07007,  
 4065 URL: <https://dx.doi.org/10.1088/1748-0221/3/07/P07007> (cit. on p. 34).
- 4066 [88] The ATLAS Collaboration, *ATLAS Software and Computing HL-LHC Roadmap*,  
 4067 tech. rep., CERN, 2022, URL: <https://cds.cern.ch/record/2802918>  
 4068 (cit. on p. 127).

- 4069 [89] The ATLAS Collaboration,  
4070 *AtlFast3: The Next Generation of Fast Simulation in ATLAS*,  
4071 Computing and Software for Big Science **6** (2022), ISSN: 2510-2044,  
4072 URL: <http://dx.doi.org/10.1007/s41781-021-00079-7> (cit. on p. 127).
- 4073 [90] The ATLAS Collaboration,  
4074 *Combination and summary of ATLAS dark matter searches interpreted in a 2HDM*  
4075 *with a pseudo-scalar mediator using 139 fb<sup>-1</sup> of  $\sqrt{s} = 13$  TeV pp collision data*,  
4076 Science Bulletin **69** (2024) 3005, ISSN: 2095-9273, URL:  
4077 <https://www.sciencedirect.com/science/article/pii/S2095927324003992>  
4078 (cit. on pp. 40, 48–50, 53, 75, 77, 80, 81, 83, 86, 88).
- 4079 [91] The ATLAS Collaboration,  
4080 *Jet reconstruction and performance using particle flow with the ATLAS Detector*,  
4081 The European Physical Journal C **77** (2017) 466,  
4082 URL: <https://doi.org/10.1140/epjc/s10052-017-5031-2> (cit. on p. 127).
- 4083 [92] The ATLAS Collaboration,  
4084 *Software Performance of the ATLAS Track Reconstruction for LHC Run 3*,  
4085 Computing and Software for Big Science **8** (2024), ISSN: 2510-2044,  
4086 URL: <http://dx.doi.org/10.1007/s41781-023-00111-y> (cit. on p. 93).
- 4087 [93] The ATLAS Collaboration,  
4088 *The ATLAS Experiment at the CERN Large Hadron Collider*,  
4089 Journal of Instrumentation **3** (2008) S08003,  
4090 URL: <https://dx.doi.org/10.1088/1748-0221/3/08/S08003> (cit. on p. 37).
- 4091 [94] The ATLAS collaboration,  
4092 *A neural network clustering algorithm for the ATLAS silicon pixel detector*,  
4093 Journal of Instrumentation **9** (2014) P09009,  
4094 URL: <https://dx.doi.org/10.1088/1748-0221/9/09/P09009> (cit. on p. 115).

- 4095 [95] The ATLAS collaboration, *Expected tracking performance of the ATLAS Inner*  
 4096 *Tracker at the High-Luminosity LHC*, Journal of Instrumentation **20** (2025) P02018,  
 4097 URL: <https://dx.doi.org/10.1088/1748-0221/20/02/P02018>  
 4098 (cit. on pp. 96, 98, 99, 101, 111, 113, 186–188, 191, 192).
- 4099 [96] Edvige Corbelli and Paolo Salucci,  
 4100 *The Extended Rotation Curve and the Dark Matter Halo of M33*,  
 4101 Mon. Not. Roy. Astron. Soc. **311** (2000) 441, arXiv: astro-ph/9909252  
 4102 (cit. on p. 15).
- 4103 [97] T G Cornelissen et al.,  
 4104 *Updates of the ATLAS Tracking Event Data Model (Release 13)*, tech. rep.,  
 4105 All figures including auxiliary figures are available at  
 4106 <https://atlas.web.cern.ch/Atlas/GROUPS/PHYSICS/PUBNOTES/ATL-SOFT-PUB-2007-003>: CERN, 2007, URL: <https://cds.cern.ch/record/1038095>  
 4108 (cit. on p. 182).
- 4109 [98] Glen Cowan, Kyle Cranmer, Eilam Gross, and Ofer Vitells,  
 4110 *Asymptotic formulae for likelihood-based tests of new physics*,  
 4111 Eur. Phys. J. C **71** (2011) 1554, arXiv: 1007.1727 [physics.data-an]  
 4112 (cit. on pp. 71, 72), Erratum: Eur. Phys. J. C **73** (2013) 2501.
- 4113 [99] Celine Degrande, Maria Ubiali, Marius Wiesemann, and Marco Zaro,  
 4114 *Heavy charged Higgs boson production at the LHC*, JHEP **10** (2015) 145,  
 4115 arXiv: 1507.02549 [hep-ph] (cit. on p. 50).
- 4116 [100] Celine Degrande et al., *UFO - The Universal FeynRules Output*,  
 4117 Comput. Phys. Commun. **183** (2012) 1201, arXiv: 1108.2040 [hep-ph]  
 4118 (cit. on p. 49).
- 4119 [101] Abdelhak Djouadi, Manuel Drees, and Jean-Loic Kneur,  
 4120 *Neutralino dark matter in mSUGRA: Reopening the light Higgs pole window*,  
 4121 Phys. Lett. B **624** (2005) 60, arXiv: hep-ph/0504090 [hep-ph] (cit. on p. 85).

- <sup>4122</sup> [102] Arnaud Duperrin,  
<sup>4123</sup> *Flavour tagging with graph neural networks with the ATLAS detector*, tech. rep.,  
<sup>4124</sup> 6 pages, 2 figures, 1 table, Presented at DIS2023: XXX International Workshop on  
<sup>4125</sup> Deep-Inelastic Scattering and Related Subjects, Michigan State University, USA,  
<sup>4126</sup> 27-31 March 2023: CERN, 2023, arXiv: 2306.04415,  
<sup>4127</sup> URL: <https://cds.cern.ch/record/2860610> (cit. on p. 128).
- <sup>4128</sup> [103] Steven Farrell et al., *Novel deep learning methods for track reconstruction*, 2018,  
<sup>4129</sup> arXiv: 1810.06111 [hep-ex], URL: <https://arxiv.org/abs/1810.06111>  
<sup>4130</sup> (cit. on p. 129).
- <sup>4131</sup> [104] Di Feng, Ali Harakeh, Steven L. Waslander, and Klaus Dietmayer, *A Review and*  
<sup>4132</sup> *Comparative Study on Probabilistic Object Detection in Autonomous Driving*,  
<sup>4133</sup> IEEE Transactions on Intelligent Transportation Systems **23** (2022) 9961,  
<sup>4134</sup> ISSN: 1558-0016, URL: <http://dx.doi.org/10.1109/TITS.2021.3096854>  
<sup>4135</sup> (cit. on p. 130).
- <sup>4136</sup> [105] Jonathan L. Feng,  
<sup>4137</sup> *Dark Matter Candidates from Particle Physics and Methods of Detection*,  
<sup>4138</sup> Ann. Rev. Astron. Astrophys. **48** (2010) 495 (cit. on p. 15).
- <sup>4139</sup> [106] Stefano Frixione, Paolo Nason, and Carlo Oleari, *Matching NLO QCD computations*  
<sup>4140</sup> *with parton shower simulations: the POWHEG method*, JHEP **11** (2007) 070,  
<sup>4141</sup> arXiv: 0709.2092 [hep-ph] (cit. on p. 113).
- <sup>4142</sup> [107] Stefano Frixione and Bryan R. Webber,  
<sup>4143</sup> *Matching NLO QCD computations and parton shower simulations*,  
<sup>4144</sup> JHEP **06** (2002) 029, arXiv: hep-ph/0204244 (cit. on p. 113).
- <sup>4145</sup> [108] Lars Fromme, Stephan J. Huber, and Michael Seniuch,  
<sup>4146</sup> *Baryogenesis in the two-Higgs doublet model*,  
<sup>4147</sup> Journal of High Energy Physics **2006** (2006) 038,  
<sup>4148</sup> URL: <https://dx.doi.org/10.1088/1126-6708/2006/11/038> (cit. on p. 28).

- 4149 [109] R. Frühwirth, *Application of Kalman filtering to track and vertex fitting*,  
 4150 Nuclear Instruments and Methods in Physics Research Section A: Accelerators,  
 4151 Spectrometers, Detectors and Associated Equipment **262** (1987) 444,  
 4152 ISSN: 0168-9002, URL:  
 4153 <https://www.sciencedirect.com/science/article/pii/0168900287908874>  
 4154 (cit. on p. 122).
- 4155 [110] K. Funakubo, A. Kakuto, and K. Takenaga, *The Effective Potential of Electroweak  
 4156 Theory with Two Massless Higgs Doublets at Finite Temperature*,  
 4157 Progress of Theoretical Physics **91** (1994) 341, ISSN: 1347-4081,  
 4158 URL: <http://dx.doi.org/10.1143/ptp/91.2.341> (cit. on p. 28).
- 4159 [111] Paul Gessinger-Befurt, *Development and improvement of track reconstruction  
 4160 software and search for disappearing tracks with the ATLAS experiment*,  
 4161 Doctoral Dissertation: Johannes Gutenberg-Universität Mainz, 2021  
 4162 (cit. on pp. 115–117).
- 4163 [112] Benyamin Ghojogh, Ali Ghodsi, Fakhri Karray, and Mark Crowley,  
 4164 *Spectral, Probabilistic, and Deep Metric Learning: Tutorial and Survey*, 2022,  
 4165 arXiv: 2201.09267 [stat.ML], URL: <https://arxiv.org/abs/2201.09267>  
 4166 (cit. on p. 139).
- 4167 [113] John F. Gunion and Howard E. Haber,  
 4168 *The CP conserving two Higgs doublet model: The Approach to the decoupling limit*,  
 4169 Phys. Rev. D **67** (2003) 075019, arXiv: [hep-ph/0207010](https://arxiv.org/abs/hep-ph/0207010) (cit. on p. 41).
- 4170 [114] H.E. Haber and G.L. Kane,  
 4171 *The search for supersymmetry: Probing physics beyond the standard model*,  
 4172 Physics Reports **117** (1985) 75, ISSN: 0370-1573, URL:  
 4173 <https://www.sciencedirect.com/science/article/pii/0370157385900511>  
 4174 (cit. on p. 28).

- 4175 [115] Aric A. Hagberg, Daniel A. Schult, and Pieter J. Swart,  
 4176 “Exploring Network Structure, Dynamics, and Function using NetworkX”,  
 4177 *Proceedings of the 7th Python in Science Conference*,  
 4178 ed. by Gaël Varoquaux, Travis Vaught, and Jarrod Millman,  
 4179 Pasadena, CA USA, 2008 11 (cit. on p. 174).
- 4180 [116] Ulrich Haisch and Giacomo Polesello,  
 4181 *Searching for heavy Higgs bosons in the  $t\bar{t}Z$  and  $t\bar{b}W$  final states*,  
 4182 JHEP **09** (2018) 151, arXiv: 1807.07734 [hep-ph] (cit. on p. 47).
- 4183 [117] Francis Halzen and Alan Douglas Martin,  
 4184 *Quarks and leptons: An introductory course in modern particle physics*,  
 4185 John Wiley, 2016 (cit. on p. 19).
- 4186 [118] William L. Hamilton, Rex Ying, and Jure Leskovec,  
 4187 *Inductive Representation Learning on Large Graphs*, 2018,  
 4188 arXiv: 1706.02216 [cs.SI], URL: <https://arxiv.org/abs/1706.02216>  
 4189 (cit. on pp. 148–152).
- 4190 [119] M. Hansroul, H. Jeremie, and D. Savard,  
 4191 *Fast circle fit with the conformal mapping method*,  
 4192 Nuclear Instruments and Methods in Physics Research Section A: Accelerators,  
 4193 Spectrometers, Detectors and Associated Equipment **270** (1988) 498,  
 4194 ISSN: 0168-9002, URL:  
 4195 <https://www.sciencedirect.com/science/article/pii/016890028890722X>  
 4196 (cit. on p. 184).
- 4197 [120] Virgil L. Highland, *Some practical remarks on multiple scattering*,  
 4198 Nuclear Instruments and Methods **129** (1975) 497 (cit. on p. 110).
- 4199 [121] G. Hinshaw et al., *Nine-Year Wilkinson Microwave Anisotropy Probe (WMAP)*  
 4200 *Observations: Cosmological Parameter Results*, *Astrophys. J. Suppl.* **208** (2013) 19,  
 4201 arXiv: 1212.5226 [astro-ph.CO] (cit. on p. 15).

- 4202 [122] Michael Joyce, Tomislav Prokopec, and Neil Turok,  
 4203     *Nonlocal electroweak baryogenesis. II. The classical regime*,  
 4204     Physical Review D **53** (1996) 2958, ISSN: 1089-4918,  
 4205     URL: <http://dx.doi.org/10.1103/PhysRevD.53.2958> (cit. on p. 28).
- 4206 [123] Xiangyang Ju et al.,  
 4207     *Performance of a geometric deep learning pipeline for HL-LHC particle tracking*,  
 4208     The European Physical Journal C **81** (2021) 876,  
 4209     URL: <https://doi.org/10.1140/epjc/s10052-021-09675-8>  
 4210     (cit. on pp. 129, 158, 161, 208).
- 4211 [124] Mahmut KAYA and Hasan Şakir BİLGE, *Deep Metric Learning: A Survey*,  
 4212     Symmetry **11** (2019), ISSN: 2073-8994,  
 4213     URL: <https://www.mdpi.com/2073-8994/11/9/1066> (cit. on pp. 139–141).
- 4214 [125] Thomas N. Kipf and Max Welling,  
 4215     *Semi-Supervised Classification with Graph Convolutional Networks*, 2017,  
 4216     arXiv: 1609.02907 [cs.LG], URL: <https://arxiv.org/abs/1609.02907>  
 4217     (cit. on p. 148).
- 4218 [126] Brian Kulis, 2013 (cit. on p. 139).
- 4219 [127] M. Laine and K. Rummukainen, *Two Higgs doublet dynamics at the electroweak*  
 4220     *phase transition: a non-perturbative study*, Nuclear Physics B **597** (2001) 23,  
 4221     ISSN: 0550-3213, URL:  
 4222     <https://www.sciencedirect.com/science/article/pii/S0550321300007367>  
 4223     (cit. on p. 28).
- 4224 [128] Siu Kwan Lam, Antoine Pitrou, and Stanley Seibert,  
 4225     “Numba: a LLVM-based Python JIT compiler”,  
 4226     *Proceedings of the Second Workshop on the LLVM Compiler Infrastructure in HPC*,  
 4227     LLVM ’15, Austin, Texas: Association for Computing Machinery, 2015,

- 4228 ISBN: 9781450340052, URL: <https://doi.org/10.1145/2833157.2833162>
- 4229 (cit. on p. 220).
- 4230 [129] D. J. Lange, *The EvtGen particle decay simulation package*,  
4231 Nucl. Instrum. Meth. A **462** (2001) 152 (cit. on p. 113).
- 4232 [130] Gerald R. Lynch and Orin I. Dahl, *Approximations to multiple Coulomb scattering*,  
4233 Nuclear Instruments and Methods in Physics Research Section B: Beam Interactions  
4234 with Materials and Atoms **58** (1991) 6 (cit. on p. 110).
- 4235 [131] R Mankel,  
4236 *Pattern recognition and event reconstruction in particle physics experiments*,  
4237 Reports on Progress in Physics **67** (2004) 553, ISSN: 1361-6633,  
4238 URL: <http://dx.doi.org/10.1088/0034-4885/67/4/R03> (cit. on p. 122).
- 4239 [132] A. D. Martin, W. J. Stirling, R. S. Thorne, and G. Watt,  
4240 *Parton distributions for the LHC*, Eur. Phys. J. C **63** (2009) 189,  
4241 arXiv: 0901.0002 [hep-ph] (cit. on p. 51).
- 4242 [133] Olivier Mattelaer,  
4243 *On the maximal use of Monte Carlo samples: re-weighting events at NLO accuracy*,  
4244 Eur. Phys. J. C **76** (2016) 674, arXiv: 1607.00763 [hep-ph] (cit. on p. 51).
- 4245 [134] Mikolaj Misiak and Matthias Steinhauser, *Weak radiative decays of the B meson*  
4246 *and bounds on  $M_{H^\pm}$  in the Two-Higgs-Doublet Model*,  
4247 Eur. Phys. J. C **77** (2017) 201, arXiv: 1702.04571 [hep-ph] (cit. on p. 46).
- 4248 [135] G. Moliere, *Theory of the scattering of fast charged particles. 2. Repeated and*  
4249 *multiple scattering*, Z. Naturforsch. A **3** (1948) 78 (cit. on p. 110).
- 4250 [136] Gert Moliere, *Theorie der Streuung schneller geladener. Teichen I. Einzelstreuung*  
4251 *am abgeschilderten Coulomb-Feld*. Z. Zeitsch. f. Naturforsch. **2a** (2014) 133  
4252 (cit. on p. 110).

- 4253 [137] Paolo Nason,  
 4254     *A new method for combining NLO QCD with shower Monte Carlo algorithms,*  
 4255     JHEP **11** (2004) 040, arXiv: hep-ph/0409146 (cit. on p. 113).
- 4256 [138] NNPDF Collaboration, Richard D. Ball, et al., *Parton distributions with LHC data,*  
 4257     Nucl. Phys. B **867** (2013) 244, arXiv: 1207.1303 [hep-ph] (cit. on p. 113).
- 4258 [139] Priscilla Pani and Giacomo Polesello,  
 4259     *Dark matter production in association with a single top-quark at the LHC in a*  
 4260     *two-Higgs-doublet model with a pseudoscalar mediator,*  
 4261     Phys. Dark Univ. **21** (2018) 8, arXiv: 1712.03874 [hep-ph] (cit. on pp. 48, 80).
- 4262 [140] Particle Data Group, P.A. Zyla, et al., *Review of Particle Physics,*  
 4263     PTEP **2020** (2020) 083C01 (cit. on pp. 28, 104, 106, 109, 112).
- 4264 [141] Adam Paszke et al.,  
 4265     *PyTorch: An Imperative Style, High-Performance Deep Learning Library*, 2019,  
 4266     arXiv: 1912.01703 [cs.LG], URL: <https://arxiv.org/abs/1912.01703>  
 4267 (cit. on p. 211).
- 4268 [142] Joao Pequenao, “Computer generated image of the whole ATLAS detector”, 2008,  
 4269     URL: <https://cds.cern.ch/record/1095924> (cit. on p. 31).
- 4270 [143] Michael E. Peskin, *An introduction to quantum field theory*, CRC Press, 2018  
 4271 (cit. on p. 19).
- 4272 [144] R. L. Plackett, *A Historical Note on the Method of Least Squares*,  
 4273     Biometrika **36** (1949) 458, ISSN: 00063444, 14643510,  
 4274     URL: <http://www.jstor.org/stable/2332682> (visited on 05/22/2025)  
 4275 (cit. on p. 121).
- 4276 [145] Planck Collaboration,  
 4277     *Planck 2018 results. I. Overview and the cosmological legacy of Planck*,  
 4278     Astron. Astrophys. **641** (2020) A1, arXiv: 1807.06205 [astro-ph.CO]  
 4279 (cit. on p. 15).

- 4280 [146] Alexander L. Read, *Presentation of search results: the CL<sub>S</sub> technique*,  
 4281 J. Phys. G **28** (2002) 2693 (cit. on p. 72).
- 4282 [147] M Regler, R Fruhwirth, R K Bock, H Grote, and D Notz,  
 4283 *Cambridge monographs on particle physics, nuclear physics and cosmology: Data*  
 4284 *analysis techniques for high-energy physics series number 11*, en, 2nd ed.,  
 4285 Cambridge monographs on particle physics, nuclear physics and cosmology,  
 4286 Cambridge, England: Cambridge University Press, 2000 (cit. on p. 122).
- 4287 [148] D. Robinson, *The atlas semi-conductor tracker operation and performance*,  
 4288 Nuclear Instruments and Methods in Physics Research Section A: Accelerators,  
 4289 Spectrometers, Detectors and Associated Equipment **699** (2013) 139 (cit. on p. 35).
- 4290 [149] Joshua Robinson, Ching-Yao Chuang, Suvrit Sra, and Stefanie Jegelka,  
 4291 *Contrastive Learning with Hard Negative Samples*, 2021,  
 4292 arXiv: 2010.04592 [cs.LG], URL: <https://arxiv.org/abs/2010.04592>  
 4293 (cit. on p. 141).
- 4294 [150] Azriel Rosenfeld and John L. Pfaltz,  
 4295 *Sequential Operations in Digital Picture Processing*, J. ACM **13** (1966) 471,  
 4296 ISSN: 0004-5411, URL: <https://doi.org/10.1145/321356.321357> (cit. on p. 115).
- 4297 [151] Bruno Rossi and Kenneth Greisen, *Cosmic-Ray Theory*,  
 4298 Reviews of Modern Physics **13** (1941) 240 (cit. on p. 110).
- 4299 [152] V. C. Rubin et al., *Rotational properties of 21 SC galaxies with a large range of*  
 4300 *luminosities and radii, from NGC 4605 (R=4kpc) to UGC 2885 (R=122kpc)*,  
 4301 Astrophysical Journal **238** (1980) 471 (cit. on p. 15).
- 4302 [153] Andreas Salzburger et al., *acts-project/acts: v41.0.0*, version v41.0.0, 2025,  
 4303 URL: <https://doi.org/10.5281/zenodo.15260074> (cit. on pp. 128, 220).
- 4304 [154] Matthew Dean Schwartz, *Quantum Field Theory and the standard model*,  
 4305 Cambridge University Press, 2014 (cit. on p. 19).

- 4306 [155] William T. Scott,  
 4307 *The Theory of Small-Angle Multiple Scattering of Fast Charged Particles*,  
 4308 Rev. Mod. Phys. **35** (2 1963) 231,  
 4309 URL: <https://link.aps.org/doi/10.1103/RevModPhys.35.231> (cit. on p. 110).
- 4310 [156] Ahmedur Rahman Shovon, Landon Richard Dyken, Oded Green, Thomas Gilray,  
 4311 and Sidharth Kumar, “Accelerating Datalog applications with cuDF”,  
 4312 *2022 IEEE/ACM Workshop on Irregular Applications: Architectures and Algorithms*  
 4313 (*IA3*), 2022 41 (cit. on p. 218).
- 4314 [157] Torbjörn Sjöstrand et al., *An introduction to PYTHIA 8.2*,  
 4315 Comput. Phys. Commun. **191** (2015) 159, arXiv: 1410.3012 [hep-ph]  
 4316 (cit. on pp. 49, 113).
- 4317 [158] The NNPDF Collaboration, Richard D. Ball, et al.,  
 4318 *Parton distributions for the LHC run II*, JHEP **04** (2015) 040,  
 4319 arXiv: 1410.8849 [hep-ph] (cit. on pp. 50, 113).
- 4320 [159] Virginia Trimble, *Existence and Nature of Dark Matter in the Universe*,  
 4321 Ann. Rev. Astron. Astrophys. **25** (1987) 425 (cit. on p. 15).
- 4322 [160] R. L. Vasilev and A. G. D'yakonov,  
 4323 *Deep Metric Learning: Loss Functions Comparison*,  
 4324 Doklady Mathematics **108** (2023) S215,  
 4325 URL: <https://doi.org/10.1134/S1064562423701053> (cit. on p. 141).
- 4326 [161] Petar Veličković et al., *Graph Attention Networks*, 2018,  
 4327 arXiv: 1710.10903 [stat.ML], URL: <https://arxiv.org/abs/1710.10903>  
 4328 (cit. on p. 148).
- 4329 [162] Keyulu Xu, Weihua Hu, Jure Leskovec, and Stefanie Jegelka,  
 4330 *How Powerful are Graph Neural Networks?*, 2019, arXiv: 1810.00826 [cs.LG],  
 4331 URL: <https://arxiv.org/abs/1810.00826> (cit. on p. 148).

- [4332] [163] Haoran Zhao et al., *Track reconstruction as a service for collider physics*, 2025,  
[4333] arXiv: 2501.05520 [physics.ins-det],  
[4334] URL: <https://arxiv.org/abs/2501.05520> (cit. on p. 214).